Rotating Orthogonal Polarization Imaging

by

Qun Zhu, BEng.

Thesis submitted to the University of Nottingham for the degree of

Doctor of Philosophy

September 2009

The University of Nottingham

To my family.

Abstract

Non-invasively characterizing the polarization properties of tissues has potential for *in vivo* clinical applications such as monitoring the healing state of wounds and burns. Conventional methods, which measure the polarization difference of a tissue and usually involve a co-polarized detection, are either restricted by a sample's surface reflections or can only be performed in off-axial systems with the use of matching fluid and a glass plate applied to the sample's surface. In this thesis a new technique called rotating orthogonal polarization imaging (*ROPI*) is presented.

The technique involves illumination in a single polarization state and detection in the orthogonal polarization state in a coaxial system. Synchronously rotating both the illumination and orthogonal detection states can provide a polarization difference image that is free from surface reflections and sensitive to the polarization property of a target embedded within a scattering medium.

The basic theoretical principle of the technique is demonstrated using Mueller calculus. Monte Carlo (*MC*) simulations are used to simulate the ideal performance when detecting a polarizing target embedded in a scattering medium at different depths. Tissue phantom experiments also investigate the imaging of a polarizing target embedded within a scattering medium at different depths using manual rotation of polarisers and liquid crystal tunable filters.

ROPI is far more effective than conventional polarization difference imaging due to the significant reduction in surface reflections. The technique is sensitive to polarizing

targets embedded at depths of up to 17 mean free paths within the medium. Accurate

quantification of dichroism is difficult due to scattering that occurs between the target

and the exit surface of the medium.

In addition, preliminary measurements of the linear dichroism of different real tissues

(bovine tendon, lamb tendon, chicken breast and human skin) and a tissue engineered

tendon orientated at two orthogonal directions are demonstrated.

It should be noted that the majority of simulation and tissue phantom results that are

presented in this thesis are for performing *ROPI* for polarizing targets embedded in a

scattering solution. Much further work is required before the technique can be taken

into clinical practice. Issues such as image alignment and the inversion of the data to

produce clinically useful images still need to be addressed.

Publications arising from this Thesis

The following papers and conference presentations have been based on part of this work:

Papers:

Morgan S. P., Zhu Q., Stockford I. M. and Crowe J. A. Rotating Orthogonal Polarization Imaging. *Optics Letters*, 2008, vol. 33, No. 13, pp. 1503-1505.

Zhu Q., Stockford I. M. Crowe J. A. and Morgan S. P. Experimental and Theoretical Evaluation of Rotating Orthogonal Polarization Imaging. *Journal of Biomedical Optics*, 2009, vol. 14, No. 3, p. 034006.

Zhu Q., Stockford I. M. Crowe J. A. and Morgan S. P. Liquid Crystal Based Rotating Orthogonal Polarization Imaging System. *Journal of Innovative Optical Health Sciences*, 2009, vol. 2, No. 3, p. 00055.

Conferences:

Morgan S. P., Zhu Q., Stockford I. M. and Crowe J. A. Rotating Orthogonal Polarization Imaging for Tissue Imaging. *Optics in Tissue Engineering and Regenerative Medicine II*, San Jose, CA, USA, 2008.

Mather M. L., Morgan S. P., Crowe J. A., Morris D. E., Zhu Q., Notingher I., Zoladek A., Kee J. (Loughborough Univ.) and Johnson P. (Intercytex) Raman Spectroscopy and Rotating Orthogonal Polarization Imaging for Non-Destructive Testing of Collagen Deposition in Tissue Engineered Skin Substitutes. *Optics in Tissue Engineering and Regenerative Medicine III*, San Jose, CA, USA, 2009.

Press:

Pollitt M. Boldly Going Where No Mass Spectrometer Has Gone Before. *The Guardian*, Thursday, 6 September, 2007. Guardian Article.

http://www.guardian.co.uk/science/2007/sep/06/research.gadgets

Acknowledgements

Nottingham
September 2009

Qun Zhu

Table of Contents

Chapter 1

Introduction and Review

1.1 Motivation and Background

Polarized light has many applications in biomedical optics. It has been demonstrated to be capable of providing coarse optical sectioning which can be useful in characterizing superficial tissue [1; 2; 3; 4; 5]. In addition, many tissue types are known to have polarization properties that affect the polarization state of light, such as linear dichroism in sickled red blood cells [6], linear birefringence in collagen [7], muscle fibres and retina [8] and chiral rotation (i.e. circular birefringence or optical activity) in glucose molecules [9] and amino acids [8].

Non-invasively characterizing the polarization properties of tissues has potential for *in vivo* clinical applications such as monitoring the healing state of wounds and burns. In arthroscopic surgery the alignment of collagen within tendons and ligaments can be measured through its polarization properties (birefringence and dichroism). In sickle cell anaemia, red blood cells polymerize and become linearly dichroic when they are deoxygenated [6]. Other potential applications include skin cancer diagnosis, plastic surgery, connective tissue disorders, endoscopy and monitoring of tissue engineered structures in bioreactors.

Characterizing the polarization properties of tissues usually involves polarization difference imaging of the tissues (i.e. polarized light illumination and subtraction of the

co- and cross- polarized detections). For clinical convenience, imaging in the back-scattered direction (i.e. reflection mode) is usually performed. However, in this case, the co-image is often dominated by surface reflections at the air-tissue interface which obscures the polarization information from deeper tissue [1; 5; 10]. Therefore, accurate quantitative measurements of polarization difference signals are severely hampered by surface reflections.

It is well known that illuminating with linearly polarized light and detecting in the orthogonal (cross) polarization state can be used to reduce the effect of surface reflections and improve image quality in tissue imaging [11; 12; 13]. This has been applied frequently in dermatoscopy [13] and in capillaroscopy [11] (imaging the micro-vasculature) and is often used in machine vision [14] and photography [12]. When imaging the micro-vasculature this technique is known as orthogonal polarization spectral (*OPS*) imaging [11]. However, this does not permit quantification of the polarization properties of the underlying tissue as effective measurements can only be performed in the orthogonal polarization channel. Two alternative methods of reducing the effect of surface reflections are side-stream dark field (*SSDF*) illumination [15] and dark field epi-illumination (*DFEI*) [16] where source and detection are spatially and angularly displaced to remove the effects of surface reflections. The main limitation of these methods is the low light levels seen in the images, which results in the tissues requiring very strong illumination and thereby potentially damaging the tissues. *SSDF* is also usually performed in close proximity to the sample.

In addition, *Jacques et al* [1] proposed the application of matching fluid and a glass plate to the tissue surface, combined with off-axis detection, to overcome the surface reflection problem. In this case the surface reflected light is specularly reflected away

from the detector by the glass plate. However, in many applications (e.g. endoscopy and assessment of wound healing), the use of matching fluid and a glass plate is not appropriate and more importantly compression of the tissue can alter its optical and physical properties. *Morgan* and *Stockford*[5] proposed a subtraction of circular and linear polarization states in which the reversal of the helicity of surface reflected circularly polarized light allows it to be differentiated from polarization maintaining light that enters the tissue. *Boulbry et al*[10] have suggested an ellipsometric approach to measure polarization difference signals. This involves an out-of-plane illumination technique, which is similar to *DFEI*, to minimise the effect of surface reflections; however, it also involves comparatively sophisticated instrumentation. More details about the methods discussed above to overcome the effect of surface reflections will be given in subsection 1.4.2.

In this thesis, a new technique which is capable of providing quantitative measurements of the polarization properties of scattering media such as tissue and is free from surface reflections is presented. Our group has termed the technique rotating orthogonal polarization imaging (*ROPI*). The technique involves illumination in a single polarization state and detection in the orthogonal polarization state. Synchronously rotating both the illumination and orthogonal detection states provides an image free from surface reflections that is sensitive to the polarization properties of the underlying scattering medium. There may be some parallel commercial work into this technique being undertaken [17], but the results presented here provide the first, to the best of our knowledge, successful demonstration of the technique.

In this chapter, a general introduction of the technique illustrating the basic principles of applying *ROPI* is provided in section 1.2. This is followed by a review of previous

work that is relevant to this study. It includes modelling light propagation in scattering media in section 1.3 and polarization analysis of scattering media in section 1.4. Finally, a thesis overview is given.

1.2 *ROPI* Introduction

ROPI is a novel technique to quantitatively measure the polarization properties of scattering media free from the effects of surface reflections. In this section, the basic principles of applying *ROPI* are described and illustrated by examples.

The technique involves illumination in a single polarization state and detection in the orthogonal polarization state. Synchronously rotating both the illumination and orthogonal detection states can provide a polarization difference image that is free from surface reflections and sensitive to the polarization property of a target embedded within a scattering medium. Depending on whether the polarization property and orientation of the target are known, the number of illumination and detection cases and the synchronously rotating angle for each case will be different.

For the known cases, there is only one rotation required, and for instance, for measuring linear dichroism and linear birefringence, which have been studied in this work, the synchronously rotating angle will be 90° and 45° respectively (note that the illumination and detection are maintained linearly polarized at 90°, they are rotated together). The basic principle of applying *ROPI* for measuring linear dichroism within a scattering medium is illustrated in figures 1.1 and 1.2.

Figure 1.1 demonstrates the principle of *ROPI* while figure 1.2 provides the typical photon trajectories generated from applying *ROPI* within a scattering medium for a

single randomly polarized illumination, where the variations of the colours indicate the modification of the polarization state of the trajectories. As figure 1.1 shows, the first image is obtained when light illuminates the scattering medium in a linear polarization state and detection is performed in the orthogonal state. By synchronously rotating both the illumination and orthogonal detection by 90°, another image is obtained. As figure 1.2 shows, for each imaging case, light that is reflected by the surface or is weakly scattered within the superficial scattering medium, maintains its original polarization state and is rejected by the cross-polarized detection (paths P_1 and P_2). Light that has been multiply scattered within the medium becomes randomly polarized and back-illuminates the target (path P_3). Similar to *OPS* systems [11], this provides an image free from surface reflections. If the target possesses linear dichroism then the randomly polarized field which back-illuminates the target has polarization information superimposed upon it.
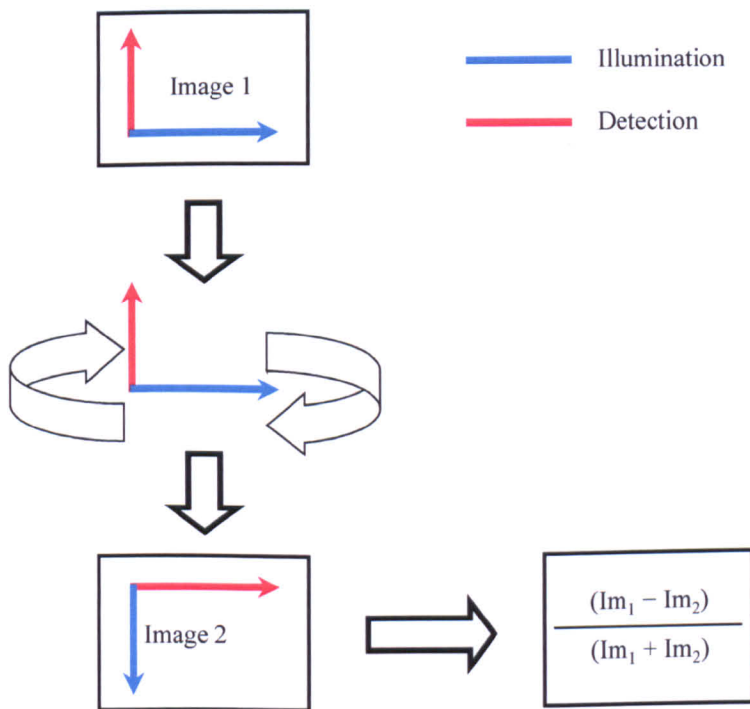
Figure 1.1: The basic principle of applying ROPI for forming images.
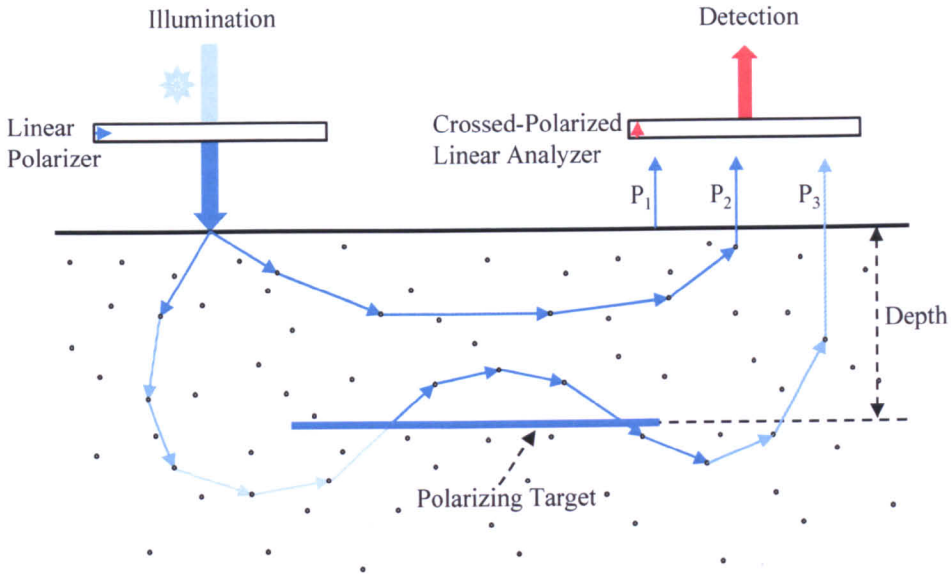
Figure 1.2: Typical photon trajectories in ROPI for a randomly polarized illumination. P_1 and P_2 are respectively a surface reflection and a weakly scattered component which are rejected as they maintain the original polarization state. P_3 is a path that has its polarization state modified by the target. Variations of the colours suggest modifications of polarization states of the trajectories.

As discussed, the conventional way to analyze this polarization information superimposed by the target would be to perform co- and cross- polarised detections but the co-polar channel is dominated by surface reflections. This means that it is not possible to quantitatively extract the polarization information superimposed by the target. For *ROPI*, as figure 1.1 shows, as both the images are obtained with orthogonal detection, a normalised polarization difference image of these two cases can provide a polarization sensitive image of the medium that is free from surface reflections.

Similarly, for measuring linear birefringence, the principle is the same as that illustrated above except for synchronously rotating the orthogonal illumination and detection by 45° rather than 90° to obtain the second image. In addition, if it is assumed that the light that back-illuminates the target is randomly polarized then it should also

be noted that the technique is only sensitive to linear dichroism and not birefringence. This is because a purely birefringent medium introduces a phase change into a randomly polarized field which produces another randomly polarized field with no additional information. A Mueller matrix explanation of this effect and a mathematical evaluation of the principles of those *ROPI* measurements through Mueller calculus will be provided in detail in chapter 2.

The case of performing *ROPI* measurements without knowing the polarization properties and orientation of the target embedded within a scattering medium has not been fully investigated within this thesis. However, in order to perform the measurements, at least three orthogonal polarization detections over the range of $[0^o, 90^o]$ are necessary.

1.3 Modelling of Light Propagation in Scattering Media

Modelling the behaviour of light propagation through a scattering medium is useful in developing optical techniques for biomedical applications. This enables ideal evaluations of both the performance of a technique and may be useful for inversion. There are various modelling approaches which have been developed and in this section, three generally used computational models of light migration in scattering media are reviewed. As a review of modelling techniques has been provided extensively elsewhere [18; 19; 20; 21; 22]; only a brief review of the basic theory is presented. However, as a modified Monte Carlo (*MC*) model is extensively applied in this study, more detail about the basic *MC* model will be provided.

1.3.1 Radiative Transport Theory

In general, as a complete electromagnetic defined wave, the interaction of light with scattering media can be either analytically represented by *Maxwell's* equation or modelled by using geometric optics [18; 23]. However, due to the many inhomogeneities that can occur in a scattering medium such as atmospheric phenomena (e.g. cloud, fog) and biological tissue, the number of distinct interactions is very large and light propagation through the medium tends to be easier to model as a forward migration via a series of scattering events rather than a wave or ray propagation. Therefore, it is desirable and would be more practical to consider the interactions based on transport theory [23; 24; 25] which interprets light as a particle rather than an electromagnetic disturbance. The radiative transport equation (*RTE*) or *Boltzmann* equation [25] which is given as equation 1.1 provides a representation of such behaviour.

$$
\left(\frac{1}{c_n} \frac{\partial}{\partial t} + \hat{s} \cdot \nabla \right) I(r, \hat{s}, t) =
$$
$$
-\mu_t I(r, \hat{s}, t) + \frac{\mu_s}{4\pi} \iint_{4\pi} I(r, \hat{s}, t) p(\hat{s}, \hat{s}') d\omega' + \varepsilon(r, \hat{s}, t) \tag{1.1}
$$

The equation describes propagation of a continuous wave (*CW*) within a medium in terms of radiative flux density $I(r, \hat{s}, t)$ which is defined as the energy at a point r along the direction of a unit vector $\hat{s}$, per unit time, per unit solid angle, per unit area perpendicular to the $\hat{s}$ vector in $Wm^{-2}sr^{-1}$. As it is given, the left hand side of the equation represents the diffuse intensity as a function of time at a point r in space in the direction of $\hat{s}$, where c_n is the light speed in the medium. The first term on the right hand side represents the decrease of incident light intensity due to the absorption and scattering, where μ_t is the extinction coefficient and $\mu_t = \mu_s + \mu_a$, in which re-

spectively μ_s and μ_a are scattering and absorption coefficients. The second term represents the contributions from other directions due to diffuse scattering, where ω is the solid angle and $p(\hat{s}, \hat{s}')$ is the phase function, which provides the probability of a photon scattering from direction $\hat{s}$ to $\hat{s}'$ and satisfies the normalisation condition as given in equation 1.2[23]. $p(\hat{s}, \hat{s}') = 1$ represents isotropic scattering.

$$\frac{1}{4\pi} \int_{4\pi} p(\hat{s}, \hat{s}') \, d\omega = 1 \qquad (1.2)$$

The last term $\varepsilon(r, \hat{s}, t)$ is the source function which defines the characteristics of the source in terms of its temporal and spatial emittance at the point r at time t for photons travelling in the direction, $\hat{s}$.

The *RTE* is an approximation to *Maxwell's* equations, which provides a strict mathematical description of the light propagation within a scattering medium and has been successfully applied in biological tissues[18] under the condition of elastic scattering. This approach implies the assumption that the distance between scatterers is much larger than the incident light wavelength. In addition, it also has been successfully applied for modelling light transport in diffuse media, turbulence in the earth's atmosphere and neutron transport[26]. However, the *RTE* does not take into account electromagnetic wave properties such as polarization and particle properties such as inelastic collisions. Moreover, it is apparent that the complexity of the *RTE* expression requires a full definition of the interactions of light with heterogeneous media providing a non-trivial solution for even simple scattering sample geometries. Therefore, in order to be able to extend its applications and simplify the solution of *RTE*, various analytical and numerical approximations have been proposed.

The most widely used methods are the diffusion approximation (analytical) and the *MC* modelling (numerical). Those two methods, especially the *MC* modelling which is modified to be applied in this study, will be discussed in the next two subsections respectively.

1.3.2 Diffusion Approximation

For highly scattering media where the reduced scattering coefficient, μ_s', is much greater than the absorption coefficient, μ_a, i.e. $\mu_s' \gg \mu_a$, a widely applied approximation to the radiative transport theory is the assumption that the scattering of the light propagation is diffuse [27]. By further assuming that the radiance is weakly anisotropic, the scattering is isotropic and the source is an isotropic point emitter, the approximation to the radiance *I* can be obtained by the simple summation of the photon density, $\phi(r,t)$, and the photon flux, $J(r,t)$, [28] which are respectively quoted in equations 1.3 and 1.4. Therefore, the *RTE* provided in equation 1.1 can be simplified as a diffusion approximation equation quoted as in equation 1.5, which is a more manageable expression and can be solved either iteratively or analytically [25; 27; 28; 29]. The mathematical consequences of these assumptions and a more detailed derivation of the diffusion equation obtained from the deterministic *RTE* can be found in [25; 27; 28].

$$\phi(r,t) = \int_{4\pi} I(r,t,\hat{s}) \, d^2\hat{s} \tag{1.3}$$

$$J(r,t) = \int_{4\pi} \hat{s} I(r,t,\hat{s}) \, d^2\hat{s} \tag{1.4}$$

$$\frac{1}{c_n}\frac{\partial \phi(r,t)}{\partial t} + D\nabla^2 \phi(r,t) = -\mu_a \phi(r,t) + S(r,t) \tag{1.5}$$

Here $S(r,t)$ is the modified source term and the diffusion coefficient, D, which indicates the spatial rate of diffusion, is defined as:

$$D = \frac{1}{3\left(\mu_a + \mu_s'\right)} \tag{1.6}$$

The diffusion equation has been widely applied for modelling light propagation in tissues [18]. However, it cannot be used to express the light transport within a medium near to the source, near to the surface, near to the boundary and in anisotropic tissues [29]. In such circumstances, higher order approximations of the *RTE* and the boundary conditions [30] may be required. Moreover, as is discussed, the diffusion approximation is only valid in highly scattering media when scattering dominates absorption, which is appropriate for non-pigmented skin according to [31]. Finally, the diffusion equation is not able to model polarization and hence it cannot be applied for modelling the *ROPI* technique in this study.

1.3.3 Monte Carlo Modelling

As has been discussed above, although a widely used analytical solution to the *RTE* for modelling light propagation in scattering media, the diffusion approximation equation may only be applied to specific geometries [29]. Thereby, a more flexible modelling solution is desired for solving forward and inverse radiation transfer problems [24] for more complex geometries which are more appropriate to practical cases with arbitrary configurations and boundary conditions. The standard Monte Carlo (*MC*) modelling method, which is based on a technique proposed initially by *Metropolis* and *Ulam* [32], provides a numerical solution [33; 34] to the *RTE*. The main idea is the use of a stochastic approach to model multivariate physical phenomena. The method simu-

lates photon transport in scattering media by recording histories of random migrations of individual photons that are influenced by both scattering and absorption interactions from their input into the modelled media until their absorption or output.

Standard Monte Carlo

In the biomedical field, the standard *MC* model was first introduced into the area of laser-tissue interactions by *Wilson* and *Adam* [35] in 1983 and further developed by *Forester* and *Godfrey* [36] for modelling the physical process of light propagation in turbid media. However, the model was infrequently used as it took neither the fact that light could be internally reflected off a boundary nor the anisotropy of the tissue into account. A *MC* model that included the provision of anisotropy and internal reflection was developed by *Prahl* [37] in 1988, and has since gone through several improvements and been widely used to simulate light transport in tissues for various applications [21; 22; 38; 39; 40; 41; 42; 43; 44; 45]. The model was released into the public domain in 1992 by *Wang et al* [46].

A detailed description of the standard *MC* model for simulating light propagation within a scattering medium has been provided elsewhere [38; 46; 47]; therefore, only a brief description of how the model works and steps considered vital will be emphasized here.

As the flow chart shown elsewhere [38] described, the light transport is performed stochastically on a photon-by-photon basis. Once a photon is launched with an initial direction and location, it is moved a distance, Δs, to where a photon-particle interaction (it may be scattered, absorbed, internally reflected or transmitted out of the medium) occurs and its direction is changed according to the *Henyey-Greenstein* phase function [48] after the interaction has happened. The photon is repeatedly moved until

it either escapes from or is absorbed by the medium. At each interaction, the position of the photon (in Cartesian coordinates) and its intensity is recorded. This process is repeated until the desired number of photons have been propagated. The recorded reflection, transmission, and absorption profiles will approach true values (for a medium with the specified optical properties) as the number of photons propagated approaches infinity.

The vital steps of the modelling are emphasized as follows. Details of other steps such as moving the photon, internal reflection, photon absorption and layer transitions can be found elsewhere [38; 46; 47].

➤ *Photon Initialization*

Photons are launched into a scattering medium one by one with initial directions and locations depending on the application. Normally, a large number of photons are required to produce meaningful results. In order to reduce the number of photons necessary to achieve the desired accuracy for *MC* calculation, a simple variance reduction technique named 'implicit photon capture' which was firstly implemented by *Kahn*[49] is used to improve the efficiency. This technique allows one to equivalently propagate many photons as a packet along a particular pathway simultaneously. Generally at each interaction, only one photon follows each pathway and the photon may be either absorbed or scattered. If a photon packet followed each pathway then some portion of the packet would be absorbed. The size of each photon packet is called the weight (w) and initially it is set to unity.

➤ *Propagation Distance*

The distance that a photon will travel at each photon-particle interaction is represented by the step size, Δs, which is a randomly generated number and calculated as:

$$\Delta s = -ln\xi \cdot mfp \tag{1.7}$$

where ξ is a uniformly distributed random variable with the interval of [0, 1] obtained each time it is evaluated from the *Mersenne Twister* random generator[50]. *mfp* is the mean free path which is the mean distance between interactions and calculated as:

$$mfp = \frac{1}{\mu_s} \tag{1.8}$$

➤ *Photon Direction*

The longitudinal angle, θ, and the azimuthal angle, ϕ, are applied as direction parameters for determining the direction of the photon at each movement. The longitudinal angle, θ, which is distributed between 0 and π is drawn from the *Henyey-Greenstein* phase function[48] and it is calculated as:

$$cos\theta = \begin{cases} \dfrac{1}{2g}\left[1 + g^2 - \left(\dfrac{1 - g^2}{1 - g + 2g\xi}\right)^2\right] & \text{for } g \neq 0 \\ 2\xi - 1 & \text{for } g = 0 \end{cases} \tag{1.9}$$

Obviously, the longitudinal angle, θ, is distributed depending on g as well, which is the anisotropy of the medium and $g = \langle cos\theta \rangle$ (i.e. the average of the cosine of the longitudinal angle, θ) which varies from -1 to 1. If $g = 1$, this indicates the scattering is directly forward and if $g = 0$, it indicates the scattering is isotropic.

The azimuthal angle, ϕ, which is independent of the phase function and uniformly distributed between 0 and 2π is determined by:

$$\phi = 2\pi\xi \tag{1.10}$$

➢ *Photon Termination*

As the variance reduction technique, implicit photon capture, is applied for the model, a photon packet will be never be completely absorbed and hence will be propagated continuously even with very little weight until it escapes the medium. As propagating a photon packet with a minuscule weight yields only little information, it is more efficient to terminate photons whose weight falls below a threshold, w_t, while the energy in the system is conserved. A technique known as roulette [51; 52] is specifically designed for such a circumstance, which allows photons to be terminated in an unbiased manner and mathematically is represented as:

$$w' = \begin{cases} 0 & if \ \xi > 1/m \\ mw & if \ \xi \leq 1/m \end{cases} \quad (when \ w \leq w_t) \qquad (1.11)$$

where $1/m$ is the chance that the photon will survive the roulette.

MC modelling is arguably the most widely used method of modelling light propagation in scattering media, because of its main advantage in that the modelled geometry can be easily modified to satisfy complex configurations appropriate to practical cases. However, as a stochastic process, the main drawback of applying the *MC* model is that a large number of photons are required to be modelled to form a physical representation that is statistically significant and hence, a large amount of running time and storage memory on the computing system will be consumed. Thereby, several methods which are known as variance reduction techniques have been developed to accelerate the calculations [52; 53; 54]. The most popular one which has also been applied for this study is to operate the *MC* calculations in parallel on a computer network [53].

The basic idea is to break the whole model into many sub-simulations as each photon packet run is independent. Therefore, the large number of photons required to be run

can be grouped as many sub-groups and run on different computers in parallel rather than just running on a single computer in series. Obviously, the more computers are used the faster the run and the storage needed is also distributed. More information about this parallel processing can be found elsewhere [55; 56], where the processing has been described in detail.

Polarized Light Monte Carlo

As has been discussed, as radiative transport theory treats photons as particles rather than an electromagnetic wave; the standard *MC* model records only the histories of a simulated photon's positions and optical contrast. It is only able to provide the distributions (temporal, spatial and angular) of the absorbed, transmitted or reflected photons but not the assessment of wave properties such as polarization states of the photons. As polarized light has great potential applications in the biomedical field, which will be reviewed in next section, it is useful to simulate polarized light propagation in scattering media. Thereby, polarized light Monte Carlo (*PMC*) models which incorporate and are able to track information concerning the polarization states of propagating light have been developed based on the standard *MC* model and are widely applied in the biomedical field including this work.

The basic idea of the *PMC* technique is to simulate the propagation of polarized light in scattering media and be able to track the polarization properties of each photon packet which has been affected by the characteristic of the media. Mathematically, this is achieved by incorporating the Stokes vector and the Mueller matrix, which provides a complete description of the polarization properties of the light (photons) and the media [57] respectively, into the standard *MC* model. This is based on *Mie* theory [58; 59] which is applied to model the single scattering events (i.e. the photon-

particle interactions in the medium). More details about how to develop a *PMC* model from the standard *MC* model and how the polarization state is adjusted in the *Mie* scattering regime at each photon-collision have been fully provided elsewhere [60; 61; 62] and thus will not be given here. However, development and applications of *PMC* models are briefly reviewed as follows.

Light polarization states after multiple scattering were first calculated using a *MC* method by *Kattawar* and *Plass* in 1967 [63] for the studies of haze and clouds. Since then, many studies have been carried out on *PMC* models and their applications. *Bruscaglioni et al* [64] applied a *PMC* model to analyze changes in polarization of light pulses transmitted through turbid media. *Ambirajan* and *Look* [65] developed a backward *PMC* model for slab geometry with circularly polarized light where they studied the degree of polarization of the diffuse light. *Hielscher et al* [66] were the first to develop a *PMC* based method to determine 16 elements of the diffuse backscattering Mueller matrix [57] through 49 measurements by varying polarization states of the incident beam and the analyser of the diffusely backscattered light. Afterwards, the matrix was successively re-calculated by *Kattawar et al* [67], *Rakovic et al* [60] and *Bartel* and *Hielsher* [61] based on efficiency improved *PMC* models and further compared with experimental results obtained from a suspension of polystyrene spheres.

Furthermore, *Cote* and *Vitkin* [68] developed a three dimensional *PMC* model to study optically active molecules in turbid media. *Wang* and *Wang* [69] used a *PMC* model to simulate light propagation in birefringent media. *Yao* [70] developed a *PMC* technique to study subsurface polarization imaging of scattering media with absorption, scattering and reflective objects embedded within using both linearly and circularly polarized incident light.

Within our group, since the basic *PMC* model initially was developed by *Chang et al* [71] for single layer backscattering imaging studies, it has been further developed for different biomedical studies. It has been applied by *Stockford et al* for the study of characterising layered scattering media using polarized light [72; 73] and by *Lu et al* for simulating propagation of polarized and un-polarized light through an infinite slab, spectroscopy cuvette and a multilayered medium [74; 75]. In addition, the model has also been modified for application in this study [76; 77]. Since the basic *PMC* model has been presented in detail [71], a brief description of the model will be given in chapter 3, focusing mainly on the modifications made specifically for this work.

1.4   Polarization Analysis of Scattering Media

Related to *ROPI*, a brief review of eliminating surface reflections has been provided in section 1.1. In this section, a further review of relevant work is provided. Different categories of light obtained through different polarized detections from a scattering medium in reflection mode with different polarized illuminations are presented in subsection 1.4.1. Various polarization techniques that have been applied to examine scattering media, including the elimination of surface reflections are reviewed in subsection 1.4.2.

1.4.1   Light Categories of Polarization Detection

According to previous studies [5; 73; 78; 79; 80] through assessment of the degree of polarization (*DOP*) of the emerging light, it is found that the polarization state of illuminating light will be gradually randomized by a scattering medium. Un-scattered or

weakly scattered light maintains its original polarization state whereas multiple scattered light is randomly polarized and contributes equally to both co-polarization and cross-polarization states. The polarization states of reflected and backscattered light from a scattering medium with illuminations of linearly and circularly polarized light are graphically showed in figure 1.3 [5]. The categories of those light detected by using co- and cross-polarization states are summarized in table 1.1 [5].
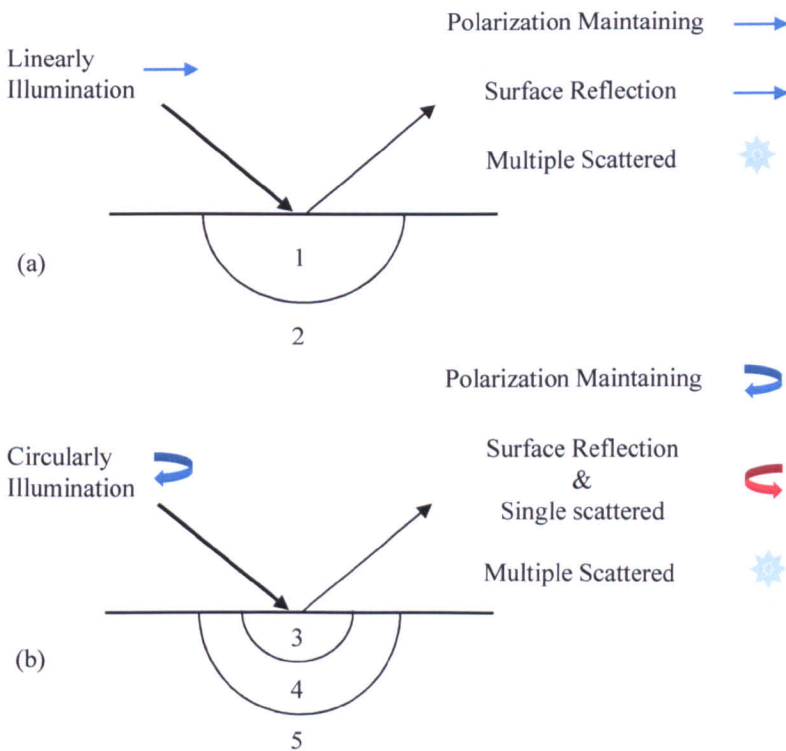
Figure 1.3: Illustration of different light obtained from a scattering medium in reflection mode with (a) linearly and (b) circularly polarized illumination. Polarization maintaining light is localized in regions 1 and 4 while multiple scattered light in regions 2 and 5. Single scattered circular light is localized in region 3. [5]

In the case of linearly polarized illumination (figure 1.3a), both the surface reflection and the light that only undergoes relatively few scattering events (i.e. propagates in region 1 which is close to the surface of the medium) maintain the original polarization state. Therefore, those two light categories can only contribute to the co-polarized

detection (channel 1). Light that travels a greater distance (region 2) will be randomly polarized and thus contributes equally to both the co-and cross-polarized detections (channels 1 and 2).

In the case of circularly polarized illumination (figure 1.3b), the surface reflection and the light that is almost immediately backscattered (i.e. single scattered or mirror reflection) upon entering the scattering medium (region 3) have the helicity of the incoming circular polarization reversed. Thereby, these two components can only be detected by the orthogonal circularly polarized channel 4. The light that undergoes a series of forward scattering events (region 4) maintains its initial polarization state and will be detected only by the co-circularly polarized channel 3. Finally, the light that experiences multiple scattering in the scattering medium (region 5) will be randomly polarized and contribute equally to both channels 3 and 4.

Channel	Illumination	Detection	Category of Light
1	Linear	Co Linear	Surface Reflection & Linear Polarization Maintaining & Multiple Scattering
2	Linear	Cross Linear	Multiple Scattering
3	Circular	Co Circular	Circular Polarization Maintaining & Multiple Scattering
4	Circular	Cross Circular	Surface Reflection & Single Scattering (Flipped Helicity) & Multiple Scattering

Table 1.1: Categories of light obtained from the four different polarization channels from a scattering medium in reflection mode.

Similarly, the different categories of light obtained in transmission mode with linearly and circularly polarized illuminations have also been studied [62; 74]. However, this is not reviewed here as this study only concentrates on the reflection mode.

1.4.2 Polarization Techniques

Polarized light has many applications in biomedical optics. As shown above, by applying linearly polarized illumination, along with being capable of removing surface reflections (which has been briefly reviewed in section 1.1), simple subtraction of co- and cross-polarized detections (channel1−channel2) removes the multiple scattered background and enables the weakly scattered component to be extracted. Polarization gating has been demonstrated as a simple and effective method of improving image resolution and extracting light that has propagated only within superficial tissue [1; 2; 3; 4]. This is useful in characterizing superficial tissue and can potentially be used to diagnose skin lesions such as burns, wounds and even skin cancer.

For instance, this was demonstrated by *Demos* and *Alfano* [2] using linearly polarized light. Images in the polarization states co- and cross-polarized to the illumination were recorded from the back of a human hand using off-axis detection in order to reduce surface reflections. The polarization maintaining light, which only went through the shallow tissue, was extracted by performing a simple subtraction of the co-polar and cross-polar channels. Furthermore, *Jacques et al* [1] tried to remove both the multiply scattered light and the tissue surface reflections. This was to provide sensitivity to near subsurface regions. The extraction of polarization maintaining components was performed via a subtraction of the co- and cross-polar images as in [2]. The effect of surface reflections was overcome by the use of a flat glass plate and matching fluid

to the tissue surface (which ensure a flat surface) and combined with off-axis detection to avoid the specularly reflected light. However, as discussed in section 1.1, this method has a drawback of possibly altering the tissue's optical and physical properties as the tissue is compressed by the use of a glass plate and matching fluid. The study also attempted to remove the effect of non-uniform illumination by normalising the extracted polarization maintaining light by the total randomly polarized intensity on a pixel-by-pixel basis. Although this provided a representation of the variation of scattering, the effect due to pigmentation would be removed as well. As pigmentation plays an important role in lesion diagnosis[81], it is debatable whether the application of this processing is appropriate in the diagnosis of pigmented lesions.

As demonstrated, both of the above techniques [1; 2] were capable of removing the multiple scattered components and extracting only the weakly scattered light from superficial tissue by using linearly polarized light. However, such techniques could only perform with off-axis detections in order to avoid contributions from the samples' surface reflections. *Morgan* and *Stockford*[5] described a method of extracting light that had propagated only within superficial tissue while removing surface reflections by use of only polarized light subtraction with coaxial detection. This often simplifies systems; for example, in endoscopy, illumination and detection can use the same fiber bundle. As the table 1.1 shows, this method involved using both linearly and circularly polarized light and was achieved by performing the subtraction of channels 2 and 3 rather than purely using linearly polarized light (channels 1 and 2). The key to the successful removal of both surface reflections and multiply scattered components is to note that the use of circularly polarized light discriminates between weakly scattered light (channel 3) and surface reflections (channel 4). The linearly polarized case does not make this discrimination and both components would be backscattered into

the linear co-polar channel. Therefore, the extraction of circular polarization maintaining components through the subtraction of channels 2 and 3 should result in an image localised in depth and containing no surface reflection components as both the channels contain no surface reflections.

In addition, *Ramella-Roman et al* [82] demonstrated a polarized imaging method, which is based on out-of-plane polarized illumination with polarization-sensitive detection, to extract subsurface features with elimination of both surface reflections and multiply scattered components. This involves two measurements using the out-of-plane polarized setup where the source and detection are spatially displaced at an inclination angle, $\theta = 45^o$, with respect to the normal direction of the sample surface, and the azimuthal angle of illumination, ϕ, is movable. With the illumination orientated at the same polarization state, one measurement, which is similar to channel 2 shown in table 1.1, is taken with $\phi = 0^o$ (i.e. azimuthal direction is aligned with the detection) and the detection in cross-polarized in order to remove surface reflections. The other measurement is taken with $\phi > 50^o$, which was found to best minimise surface reflections in co-polarized detection. A simple subtraction of these measurements was shown to be capable of providing subsurface features free from both surface reflections and multiply scattered light. However, as discussed, this method involves illumination of a sample in different positions for the same assessment. Hence, the detected signals might be from different sources and so the subsurface features obtained might be unreliable.

Boulbry et al [10] further presented an ellipsometric approach which is based on hemispherical backscattering for the assessment of superficial skin lesions. This involves comparatively sophisticated instrumentation and the use of out-of-plane illumination as in [82] to minimise the effect of skin's surface reflections. The instrumentation in-

cludes two systems. The polarized light sources which are distributed on a hemi-spherical shell can provide illumination in and out of plane at three different wave-lengths and sixteen different directions. The Stokes vector imaging system is composed of two liquid crystal variable retarders, a fixed polarizer and a *CCD* camera. This is used to obtain Stokes vector images where each image is obtained by using seven different retardance combinations. The polarized components (in the superficial tissue) can then be separated from the un-polarized components (from deep in the tissue) via performing a decomposition of the Stokes vector generated from a multiplication of a matrix (4×7) with a Stokes vector image (7-element). Depending on the applications, different behaviours can be observed by using different combinations of the illumination directions and wavelengths.

As mentioned in section 1.1, the technique of *OPS* imaging[11] can be used to reduce the effect of surface reflections and improve image quality in tissue imaging. This involves illuminating with linearly polarized light and detecting in the orthogonal (cross) polarization state. The technique has been shown to be capable of imaging the microvasculature from human sublingual sites in great detail in terms of contrast and sharpness under clinical conditions. This results in the capability to measure the vessels' diameters and blood flow velocities and thus provides diagnostic assessment for human microvascular pathologies. However, due to movements of the *OPS* device, the tissue and flowing red blood cells, which introduce image blurring, images cannot always be obtained optimally. Also because of image blurring, it is difficult to observe the granular nature of flowing blood cells in larger vessels, especially during continuous flow, which results in difficulties in measuring the blood flow velocities. Moreover, as has been discussed in section 1.1, this technique is not able to provide quantification of the polarization properties of the underlying tissue.

In addition, also as introduced in section 1.1, the technique of *SSDF* imaging [15], which is a stroboscopic *LED* ring-based imaging modality, is an alternative method of reducing the effect of surface reflections via applying illumination from the sides of detection. Compared to the *OPS* technique, a magnifying (5 or 10×) lens system which projects the image onto a video camera is introduced into *SSDF*. It is an improved method of observing the human microcirculation, which allows the observations in even greater detail in terms of contrast and sharpness, at the bedside. Also, the light sources provides pulsed illumination in synchrony with the *CCD* frame rate in order to improve the imaging of moving components such as flowing red blood cells. As has been discussed in section 1.1, the drawback of this technique is that relatively strong illumination to the tissues is required, which can cause damage to the tissues. Another limitation of *SSDF* is that the probe needs to be close to the tissue surface to ensure appropriate spatial filtering. Furthermore, this technique is also not able to provide quantification of the polarization properties of the underlying tissue as polarization is not involved.

Studies by *Morgan* and *Ridgway* [79] and *MacKintosh et al* [80] presented a 'polarization memory' discussion of different polarization states. This effect described how an initial polarization state is maintained over varying numbers of scattering events dependent on the illumination polarization state and the scatterer size. It was found that when the scatterer diameter, d, is greater than the incident wavelength, $(d \gg \lambda)$, then circular polarization is maintained for more scattering events than with linear polarization. The opposite was found for the small particles $(d \ll \lambda)$. This is due to the increase of backward scattering which results in many circularly polarized photons experiencing a flip in helicity and thus depolarising from the initial state.

Recently, a study by *Gomes et al* [83] tried to measure changes of mucosal (i.e. superficial) blood supply *in vivo* using linear polarization gating (i.e. subtraction of channels 1 and 2 in table 1.1) spectroscopy to detect colonic neoplasia. It was found that there was increased blood supply spatially around precancerous adenomatous lesions. This is known as the field effect and suggested that measurements could be taken anywhere in the colon to detect cancer, not just the cancerous site itself.

For culturing tissues, as proper cell alignment leads to optimum tissue strength, successful development of cultured tissues is heavily influenced by cell alignment within the tissue scaffold. Therefore, *Gladish* and *Duncan* [84], has developed a spectral polarimetry system to extract spectral polarization properties of light that had been scattered by the cultured tissues to provide feedback for proper cell alignment.

In addition, *Wood et al* [85] demonstrated the first *in vivo* use of a Mueller matrix decomposition method for polarization based characterization of tissue. Mueller matrices for polarized light transmitted through the collagenase-treated tissue were measured. The individual constituent polarization properties of the tissue were then extracted through polar matrix decomposition. Large decreases in birefringence and depolarization were seen in the collagenase-treated region due to the destruction of collagen. This indicated the potential of the method to monitor the organization and structural anisotropy of tissue.

1.5   Thesis Overview

As has been discussed, non-invasively characterizing the polarization properties of tissues has potential for *in vivo* clinical applications such as monitoring the healing

state of wounds and burns. This thesis aims to present a new polarization imaging technique, *ROPI*, which is capable of providing quantitative measurements of the polarization properties of scattering media such as tissue with free surface reflections.

In comparison with conventional polarization difference measurements, which normally involve co-polarized detections and thus are restricted by surface reflection; *ROPI* has the advantages of performing quantitative measurements not only free from surface reflections but also in coaxial detection, which often simplifies systems. For instance, in endoscopy, illumination and detection can use the same fiber bundle. Throughout the entire thesis, the *ROPI* technique will be fully evaluated through quantitatively measuring linear dichroism and linear birefringence of a target underlying scattering media using theoretical calculus, *MC* simulations and various experiments.

In chapter 2, the principles of applying *ROPI* for quantitatively measuring linear dichroism and linear birefringence of a target underlying a scattering medium will be developed mathematically based on Mueller calculus in chapter 2. These first provide an ideal prediction of the responses and second show the factors that affect the measurements. In addition, this provides a set of criteria to judge the simulation and experimental results.

In chapter 3, the *MC* simulations of applying the technique for performing the measurements validated in chapter 2 with different ideal conditions will be presented. The model, which is modified based on a general *PMC* model to simulate *ROPI*, will also be introduced. These will provide the ideal results of the measurements which will be compared with and hence used to assess the experimental results.

For practical evaluations, the *ROPI* measurements will be demonstrated via phantom experiments. These will be further performed in two different systems. One is the standard system which is based on Glan-Thompson (*GT*) polarisers while the other one is based on liquid crystal variable retarders (*LCVR*). The main difference between the systems is that the polarization states of illuminations and detections are controlled manually in the standard system and electrically in the *LCVR* one.

The standard system is simple and stable. Therefore, the experimental investigations of the *ROPI* technique will be mainly demonstrated using this system. The experiments will be performed in both reflection and transmission modes. However, as *ROPI* applications are preferred in reflection mode, only those experiments that cannot be performed in reflection will be performed in transmission for further evaluation. In addition, preliminary *ROPI* measurements of different real and engineered tissues are demonstrated as well. Chapter 4 will concentrate on presenting the system design and calibrations, and chapter 5 will provide all the experimental measurements.

The *LCVR* system is more convenient and faster; however, it is also less stable and more complicated. As the system is controlled automatically, the *ROPI* measurements performed in this system will mainly demonstrate an essentially forward step towards realisation of the technique for clinical applications. Both the system design and measurements will be provided in chapter 6.

Chapter 7 compares the same measurements obtained from ideal simulations and phantom experiments in the two different systems. Finally, a summary of the study along with suggestions for future work and final conclusions are presented in chapter 8.

Chapter 2

Theoretical Principles of Applying *ROPI*

2.1 Introduction

In order to evaluate the *ROPI* technique, it is useful to demonstrate the theoretical basis of the technique prior to performing Monte Carlo (*MC*) simulations and phantom experiments. In this chapter the theory, which is based on Mueller calculus, is introduced.

Stokes vectors and Mueller matrices can be used to mathematically represent polarized light and optical components respectively [57]. By performing Mueller calculus (multiplication of Stokes vectors and Mueller matrices), the new polarization state of light, which has been affected by passing through optical components, can be mathematically represented. Therefore, by applying this approach to analyse *ROPI*, it allows one to demonstrate the measurement process and also to identify the factors that affect the results. In addition, it is also useful as it provides a set of criteria to judge the simulation and experimental results.

This chapter aims to mathematically demonstrate the theoretical principles of applying *ROPI* for measuring linear dichroism and linear birefringence. Stokes vectors, Mueller matrices and Mueller calculus will be firstly introduced in section 2.2. This is followed by the mathematical foundations for ideally performing *ROPI* measurements

to detect linear dichroism and linear birefringence in sections 2.3 and 2.4 respectively. Finally, a summary is given in section 2.5.

2.2 Stokes Vectors, Mueller Matrices and Mueller Calculus

Generally, any polarization phenomenon can be mathematically described by either a single interaction or a series of interactions of light's polarization state with either a single optical component or a set of optical components. The polarization state of light can be represented by either Stokes vectors or Jones vectors and optical components can be represented by either Mueller matrices or Jones matrices. In this study, only Stokes vectors and Mueller matrices are used as they allow consideration of light which is not fully polarized. More details about Jones vectors and matrices can be found elsewhere [86; 87]. In this section, Stokes vectors, Mueller matrices and Mueller calculus which mathematically represent polarization interactions are briefly introduced.

Stokes Vectors

Stokes vectors are used to mathematically represent the polarization state of light. The definition of a general Stokes vector is presented in equation 2.1 [57]. Where $E_{//}$ and $E_{\perp}$ are the electric field components parallel and perpendicular to the plane of reference respectively. * denotes the complex conjugate, and $\langle \rangle$ denotes the time average of the contained variable.

The first Stokes parameter, I, represents the intensity of light, Q expresses the tendency to be horizontally polarized, U indicates the tendency of light to be linearly po-

larized at 45°, and V provides the tendency to have right handed circular polarization. After normalization to the intensity, I, then Q, U and V all vary from -1 to 1. This means that Q varies from vertically polarized (i.e. -1) to horizontally polarized (i.e. 1); U varies from $-45°$ polarized to $45°$ polarized and V varies from left handed circularly polarized through different degrees of elliptical polarization from left handed to right handed until totally right handed circularly polarized.

$$\begin{bmatrix} S_0 \\ S_1 \\ S_2 \\ S_3 \end{bmatrix} = \begin{bmatrix} I \\ Q \\ U \\ V \end{bmatrix} = \begin{bmatrix} \langle E_{//}E_{//}^* + E_\perp E_\perp^* \rangle \\ \langle E_{//}E_{//}^* - E_\perp E_\perp^* \rangle \\ \langle E_{//}E_\perp^* + E_{//}^* E_\perp \rangle \\ \langle i(E_{//}E_\perp^* - E_{//}^* E_\perp) \rangle \end{bmatrix} \tag{2.1}$$

For completely polarized light, the Stokes parameters satisfy equation 2.2 and for partially polarized light, the Stokes parameters satisfy equation 2.3. In addition, the degree of polarization of light $(0 \le P \le 1)$ is defined by equation 2.4. This parameter can be used to indicate the following states [88]:

- If $P = 0$, the light is randomly polarized;

- If $P = 1$, the light is completely polarized;

- If $0 < P < 1$, the light is partially polarized and the larger the P, the greater the degree of polarization.

$$I^2 = Q^2 + U^2 + V^2 \tag{2.2}$$

$$I^2 > (Q^2 + U^2 + V^2) > 0 \tag{2.3}$$

$$P = \frac{(Q^2 + U^2 + V^2)^{\frac{1}{2}}}{I} \tag{2.4}$$

The Stokes vector for the general form of linearly polarized light is given in equation 2.5. Some commonly used Stokes vectors for polarized light in different states are listed in table 2.1.

$$
\begin{bmatrix} I \\ Q \\ U \\ V \end{bmatrix} = \begin{bmatrix} 1 \\ \cos 2\zeta \\ \sin 2\zeta \\ 0 \end{bmatrix}
\tag{2.5}
$$

where ζ is the azimuthal orientation of linearly polarized light, which determines the linear polarization state of the light and varies from 0 to π.

$\begin{bmatrix} 1 \\ 1 \\ 0 \\ 0 \end{bmatrix}$ Horizontal linearly polarized; $\begin{bmatrix} 1 \\ -1 \\ 0 \\ 0 \end{bmatrix}$ Vertical linearly polarized;

$\begin{bmatrix} 1 \\ 0 \\ 1 \\ 0 \end{bmatrix}$ 45° linearly polarized; $\begin{bmatrix} 1 \\ 0 \\ -1 \\ 0 \end{bmatrix}$ -45° linearly polarized;

$\begin{bmatrix} 1 \\ 0 \\ 0 \\ 1 \end{bmatrix}$ Right-hand circularly polarized; $\begin{bmatrix} 1 \\ 0 \\ 0 \\ -1 \end{bmatrix}$ Left-hand circularly polarized;

$\begin{bmatrix} 1 \\ 0 \\ 0 \\ 0 \end{bmatrix}$ Randomly polarized or natural light.

Table 2.1: Commonly found Stokes vectors of polarized light in different states.

Mueller Matrices

The Mueller matrix is a 4 × 4 matrix, which can mathematically represent the effect of an optical component or medium on the polarization state of incident light [57]. Therefore, any optical component or media could be represented by an exclusive Mueller matrix. For example, the general form of the Mueller matrices for diattenuators $\left(\bar{M}_D\right)$ and retarders $\left(\bar{M}_R\right)$ are given in equations 2.6 [89] and 2.7 [90] respectively.

$$\bar{M}_D = \frac{T_1 + T_2}{2} \times$$

$$\begin{bmatrix} 1 & K_1\cos(2\varphi) & K_1\sin(2\varphi) & 0 \\ K_1\cos(2\varphi) & K_2+(1-K_2)\cos^2(2\varphi) & (1-K_2)\cos(2\varphi)\sin(2\varphi) & 0 \\ K_1\sin(2\varphi) & (1-K_2)\cos(2\varphi)\sin(2\varphi) & K_2+(1-K_2)\sin^2(2\varphi) & 0 \\ 0 & 0 & 0 & K_2 \end{bmatrix} \quad (2.6)$$

$$\left(K_1 = (T_1 - T_2) / (T_1 + T_2) \quad \& \quad K_2 = 2\sqrt{T_1 T_2} / (T_1 + T_2)\right)$$

where T_1 and T_2 are the transmittances of the diattenuator along the major and minor axes respectively and φ is the azimuthal orientation of the diattenuator and varies from 0 to π.

$$\bar{M}_R =$$

$$\begin{bmatrix} 1 & 0 & 0 & 0 \\ 0 & \cos^2(2\theta)+\sin^2(2\theta)\cos\delta & (1-\cos\delta)\sin(2\theta)\cos(2\theta) & -\sin(2\theta)\sin\delta \\ 0 & (1-\cos\delta)\sin(2\theta)\cos(2\theta) & \sin^2(2\theta)+\cos^2(2\theta)\cos\delta & \cos(2\theta)\sin\delta \\ 0 & \sin(2\theta)\sin\delta & -\cos(2\theta)\sin\delta & \cos\delta \end{bmatrix} (2.7)$$

where θ is the azimuthal orientation of the fast axis of the retarder, which determines the polarization state of the retarder and varies from 0 to π. δ is the retardance (i.e. phase delay in wavelengths).

$$\frac{1}{2}\begin{bmatrix} 1 & 1 & 0 & 0 \\ 1 & 1 & 0 & 0 \\ 0 & 0 & 0 & 0 \\ 0 & 0 & 0 & 0 \end{bmatrix}$$ *LP* orientated at 0°; $$\frac{1}{2}\begin{bmatrix} 1 & -1 & 0 & 0 \\ -1 & 1 & 0 & 0 \\ 0 & 0 & 0 & 0 \\ 0 & 0 & 0 & 0 \end{bmatrix}$$ *LP* orientated at 90°;

$$\frac{1}{2}\begin{bmatrix} 1 & 0 & 1 & 0 \\ 0 & 0 & 0 & 0 \\ 1 & 0 & 1 & 0 \\ 0 & 0 & 0 & 0 \end{bmatrix}$$ *LP* orientated at 45°; $$\frac{1}{2}\begin{bmatrix} 1 & 0 & -1 & 0 \\ 0 & 0 & 0 & 0 \\ -1 & 0 & 1 & 0 \\ 0 & 0 & 0 & 0 \end{bmatrix}$$ *LP* orientated at -45°;

$$\begin{bmatrix} 1 & 0 & 0 & 0 \\ 0 & 1 & 0 & 0 \\ 0 & 0 & 0 & 1 \\ 0 & 0 & -1 & 0 \end{bmatrix}$$ *QWP* orientated at 0°; $$\begin{bmatrix} 1 & 0 & 0 & 0 \\ 0 & 1 & 0 & 0 \\ 0 & 0 & 0 & -1 \\ 0 & 0 & 1 & 0 \end{bmatrix}$$ *QWP* orientated at 90°;

$$\begin{bmatrix} 1 & 0 & 0 & 0 \\ 0 & 0 & 0 & -1 \\ 0 & 0 & 1 & 0 \\ 0 & 1 & 0 & 0 \end{bmatrix}$$ *QWP* orientated at 45°; $$\begin{bmatrix} 1 & 0 & 0 & 0 \\ 0 & 0 & 0 & 1 \\ 0 & 0 & 1 & 0 \\ 0 & -1 & 0 & 0 \end{bmatrix}$$ *QWP* orientated at -45°;

$$\begin{bmatrix} 1 & 0 & 0 & 0 \\ 0 & 1 & 0 & 0 \\ 0 & 0 & -1 & 0 \\ 0 & 0 & 0 & -1 \end{bmatrix}$$ *HWP* orientated at 0° / 90°;

$$\begin{bmatrix} 1 & 0 & 0 & 0 \\ 0 & -1 & 0 & 0 \\ 0 & 0 & 1 & 0 \\ 0 & 0 & 0 & -1 \end{bmatrix}$$ *HWP* orientated at 45° / -45°.

Table 2.2: Commonly found Mueller matrices for LP, QWP and HWP.

From these general cases, the Mueller matrix for a linear polariser (*LP*) (diattenuator

with $T_1 = 1$ and $T_2 = 0$), a quarter-wave plate (*QWP*) (retarder with $\delta = \pi/2$) and a

half-wave plate (*HWP*) (retarder with $\delta = \pi$) at an arbitrary azimuthal orientation can

be derived as *LP* ($\bar{M}_{LP}$), *QWP* ($\bar{M}_{QWP}$) and *HWP* ($\bar{M}_{HWP}$), which are given in equa-

tions 2.8, 2.9 and 2.10 respectively [57]. More specific commonly found Mueller ma-

trices for *LP*, *QWP* and *HWP* are given in table 2.2.

$$\bar{M}_{LP} = \frac{1}{2} \begin{bmatrix} 1 & \cos 2\varphi & \sin 2\varphi & 0 \\ \cos 2\varphi & \cos^2 2\varphi & \sin 2\varphi \cos 2\varphi & 0 \\ \sin 2\varphi & \sin 2\varphi \cos 2\varphi & \sin^2 2\varphi & 0 \\ 0 & 0 & 0 & 0 \end{bmatrix} \tag{2.8}$$

$$\bar{M}_{QWP} = \begin{bmatrix} 1 & 0 & 0 & 0 \\ 0 & \cos^2 2\theta & \sin 2\theta \cos 2\theta & -\sin 2\theta \\ 0 & \sin 2\theta \cos 2\theta & \sin^2 2\theta & \cos 2\theta \\ 0 & \sin 2\theta & -\cos 2\theta & 0 \end{bmatrix} \tag{2.9}$$

$$\bar{M}_{HWP} = \begin{bmatrix} 1 & 0 & 0 & 0 \\ 0 & \cos 4\theta & \sin 4\theta & 0 \\ 0 & \sin 4\theta & -\cos 4\theta & 0 \\ 0 & 0 & 0 & -1 \end{bmatrix} \tag{2.10}$$

Additional Mueller matrices of relevance to this work are the mirror and rotation

Mueller matrices. These are applied as part of the polarized *MC* model. The mirror

Mueller matrix $\left(\bar{M}_{mirror} \right)$ subject to the condition of normal incidence is given in

equation 2.11. The rotation Mueller matrix $\left(\bar{R}_\vartheta \right)$ which rotates either any Stokes vec-

tors or any other Mueller matrices for a certain azimuthal angle (ϑ) in the range of

$[-\pi/2, \pi/2]$ is given in equation 2.12. The formulas for rotating a Stokes vector

$\left(\bar{S}_0\right)$ and a Mueller matrix $\left(\bar{M}_0\right)$ for a rotation angle ϑ are given in equations 2.13 and 2.14 respectively (note the minus sign of ϑ is used).

$$\bar{M}_{mirror} = \begin{bmatrix} 1 & 0 & 0 & 0 \\ 0 & 1 & 0 & 0 \\ 0 & 0 & -1 & 0 \\ 0 & 0 & 0 & -1 \end{bmatrix} \tag{2.11}$$

$$\bar{R}_\vartheta = \begin{bmatrix} 1 & 0 & 0 & 0 \\ 0 & \cos 2\vartheta & \sin 2\vartheta & 0 \\ 0 & -\sin 2\vartheta & \cos 2\vartheta & 0 \\ 0 & 0 & 0 & 1 \end{bmatrix} \tag{2.12}$$

$$\bar{S}_\vartheta = \bar{R}_{-\vartheta}\bar{S}_0 \tag{2.13}$$

$$\bar{M}_\vartheta = \bar{R}_{-\vartheta}\bar{M}_0\bar{R}_\vartheta \tag{2.14}$$

Mueller Calculus

Mueller calculus is a matrix method for manipulating Stokes vectors and Mueller matrices, i.e. it mathematically describes how the polarization state of light is affected by optical components or media that light illuminates. Light which is randomly polarized or partially polarized must be treated using Mueller calculus while fully polarized light can be treated with either Mueller calculus or the simpler Jones calculus. Furthermore, incoherent light normally must be treated with Mueller calculus while coherent light generally must be treated with Jones calculus as the latter works with amplitude rather than intensity of light. Most work in this area applies Mueller calculus [74; 90; 91] and this is the approach followed here.

To determine the polarization influence of such an optical component or medium on the incident illumination, the Stokes vector of the illumination is multiplied by the

appropriate Mueller matrix [57]. If a beam of light is initially in the state, $\bar{S}_i$, and then passes through an optical component, $\bar{M}$, and emerging in a state, $\bar{S}_o$, then it is written as [86]:

$$\bar{S}_o = \bar{M}\bar{S}_i \tag{2.15}$$

If a beam of light sequentially passes through optical components, $\bar{M}_1$, followed by $\bar{M}_2$ then $\bar{M}_3$, $\bar{S}_o$ is written as:

$$\bar{S}_o = \bar{M}_3\bar{M}_2\bar{M}_1\bar{S}_i \tag{2.16}$$

In addition, because matrix multiplication is not commutative, it is important to stress that in general:

$$\bar{M}_3\bar{M}_2\bar{M}_1\bar{S}_i \neq \bar{M}_1\bar{M}_2\bar{M}_3\bar{S}_i \tag{2.17}$$

An example of Mueller calculus to show the influence of a 45° polarized *LP* on the horizontal linearly polarized incident light is expressed as:

$$\frac{1}{2}\begin{bmatrix} 1 \\ 0 \\ 1 \\ 0 \end{bmatrix} = \frac{1}{2}\begin{bmatrix} 1 & 0 & 1 & 0 \\ 0 & 0 & 0 & 0 \\ 1 & 0 & 1 & 0 \\ 0 & 0 & 0 & 0 \end{bmatrix}\begin{bmatrix} 1 \\ 1 \\ 0 \\ 0 \end{bmatrix} \tag{2.18}$$

This means that the influence of a 45° polarized *LP* on the horizontal linearly polarized incident light is to change the polarization state of the incident light from horizontal to +45° linearly polarized as represented as a Stokes vector on the left hand side of equation 2.18.

2.3 Mathematical Foundation for Measuring Linear Dichroism

In this section, Mueller calculus is used to demonstrate the principle of *ROPI* measuring the linear dichroism (or strictly speaking at a single wavelength, linear diattenuation) of an object within a scattering medium. This provides guidelines for performing the *ROPI MC* simulations and phantom experiments presented in the next four chapters.

The linear dichroism (linear diattenuation), D_L, is defined by equation 2.19 (relative to a reference orientation). This means the linear dichroism is the intensity difference signal between two orthogonal linear polarization detections, normalised by the sum of those two intensities. ξ is the orientation of the analyser[86].

$$D_L = \frac{I(\xi) - I(\xi + \pi/2)}{I(\xi) + I(\xi + \pi/2)} \tag{2.19}$$

The appropriate Mueller calculus is now presented using this definition and the description of *ROPI* given in chapter 1. For demonstration of the technique, consider the block diagram for a proposed imaging arm of the *ROPI* phantom experimental setup shown in figure 2.1 (the complete setup will be provided in figure 4.1, chapter 4):
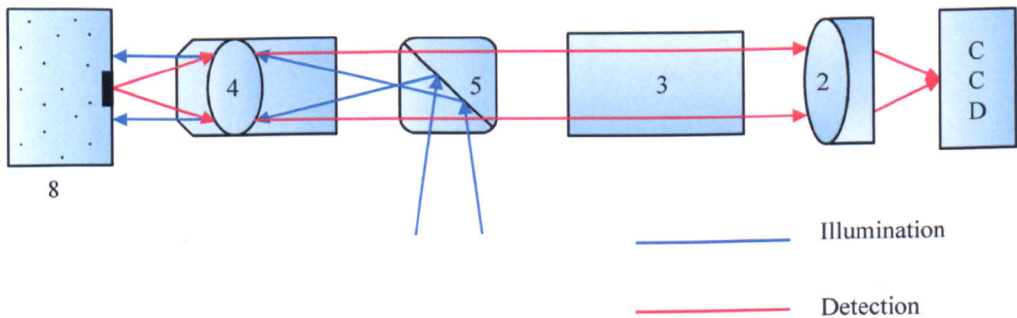
Figure 2.1: Imaging arm of the ROPI phantom experimental setup.

where 2) is a positive achromatic lens; 3) is a Glan-Thompson linear polariser which is always set cross polarized to the illumination; 4) is an infinite conjugate objective which has magnification of $\times 4$ and $NA=0.1$; 5) is a cube beam splitter orientated at 45°; CCD is a detector camera and 8) is the sample which is a scattering medium with a dichroic component embedded within it.

The following initial assumptions are made to demonstrate the main principles of using the technique to measure linear dichroism;

1). Surface reflections are completely eliminated as the detection is orthogonal to the illumination.

2). The majority of light undergoes many scattering events before being backscattered and therefore becomes completely depolarized hence the initial state can be ignored.

3). When this randomly polarized component back-illuminates the sub-surface dichroic component, the tendency to a linear polarization state imposed depends on the properties of that component.

4). The dichroic component is assumed to be close to the surface of the sample; therefore this imposed information is retained in the backscatter from the medium.

To extract the information regarding the presence of linear dichroism using *ROPI*, measurements are taken in two orthogonal detection polarization states for use in equation 2.19. It should be noted that these assumptions (also made in capillaroscopy [11]) greatly simplify the derivation. There is clearly a conflict of sorts between assumptions 2) and 4). However, deviations from these initial assumptions are thoroughly discussed later.

From figure 2.1, the randomly polarized light which is assumed to back-illuminate the target is represented by the Stokes vector, $\bar{S}_i$:

$$\bar{S}_i = \begin{bmatrix} 1 \\ 0 \\ 0 \\ 0 \end{bmatrix} \qquad (2.20)$$

Since the Mueller matrix of a general diattenuator, $\bar{M}_D$, is as defined in equation 2.6, the Stokes vector representing light emerging from the sample, $\bar{S}_s$, is given as:

$$\bar{S}_s = \bar{M}_D \bar{S}_i = \begin{bmatrix} \dfrac{T_1 + T_2}{2} \\ \dfrac{T_1 - T_2}{2}\cos(2\varphi) \\ \dfrac{T_1 - T_2}{2}\sin(2\varphi) \\ 0 \end{bmatrix} \qquad (2.21)$$

where again, T_1 and T_2 are the transmittances of the diattenuator along the major and minor axes respectively and φ is the azimuthal angle of the diattenuator. This state is assumed to be maintained until emergence at the sample's surface.

From the partial *ROPI* phantom experimental setup shown in figure 2.1, assuming the optical components of the objective, beam splitter, positive achromatic lens and *CCD* camera are ideal, the only optical component that affects the polarization state of emerging light from the sample is the Glan-Thompson linear polariser. The Mueller matrix of an arbitrarily orientated linear polariser, $\bar{M}_{LP}$, is defined in equation 2.8; therefore, with an orientation angle, φ_1, the detection light, $\bar{S}_d$, after the Glan-Thompson polarizer (i.e. analyser) is performed as:

$$\bar{S}_d = \bar{M}_{LP}\bar{S}_s =$$

$$\begin{bmatrix} K_3 + K_4\cos(2\varphi_1)\cos(2\varphi) + K_4\sin(2\varphi_1)\sin(2\varphi) \\ K_3\cos(2\varphi_1) + K_4\cos^2(2\varphi_1)\cos(2\varphi) + K_4\sin(2\varphi_1)\cos(2\varphi_1)\sin(2\varphi) \\ K_3\sin(2\varphi_1) + K_4\sin(2\varphi_1)\cos(2\varphi_1)\cos(2\varphi) + K_4\sin^2(2\varphi_1)\sin(2\varphi) \\ 0 \end{bmatrix} \quad (2.22)$$

$$\left(K_3 = (T_1 + T_2)/4 \quad \& \quad K_4 = (T_1 - T_2)/4 \right)$$

As a result, the intensities detected in orthogonal linear polarization states (i.e. analyzers at φ_1 and $\varphi_1 + \pi/2$) are given by equations 2.23 and 2.24 respectively:

$$I(\varphi_1) = K_3 + K_4\cos(2\varphi_1)\cos(2\varphi) + K_4\sin(2\varphi_1)\sin(2\varphi) \qquad (2.23)$$

$$\begin{aligned} I(\varphi_1 + \pi/2) \\ &= K_3 + K_4\cos(2\varphi_1 + \pi)\cos(2\varphi) + K_4\sin(2\varphi_1 + \pi)\sin(2\varphi) \qquad (2.24) \\ &= K_3 - K_4\cos(2\varphi_1)\cos(2\varphi) - K_4\sin(2\varphi_1)\sin(2\varphi) \end{aligned}$$

According to equation 2.19, the determined value of linear dichroism, D_L, relative to the angle, φ_1, is therefore given by:

$$\begin{aligned} D_L &= \frac{I(\varphi_1) - I(\varphi_1 + \pi/2)}{I(\varphi_1) + I(\varphi_1 + \pi/2)} \\[2mm] &= \frac{T_1 - T_2}{T_1 + T_2}\left\{\cos(2\varphi_1)\cos(2\varphi) + \sin(2\varphi_1)\sin(2\varphi)\right\} \\[2mm] &= \frac{T_1 - T_2}{T_1 + T_2}\cos\left\{2(\varphi_1 - \varphi)\right\} \\[2mm] &= \frac{T_1 - T_2}{T_1 + T_2}\cos(\Delta\gamma) \qquad \text{where } \Delta\gamma = 2(\varphi_1 - \varphi) \end{aligned} \qquad (2.25)$$

From equation 2.25, it can be seen that the linear dichroism, D_L, varies cosinusoidally from a minimum of 0 when $\Delta\gamma = 90°$ to a maximum of $(T_1 - T_2)/(T_1 + T_2)$ when

$\Delta\gamma = 0°$, which means the linear dichroism depends on the difference between azimuthal angles of the diattenuator and analyzing polariser and the transmittances of the diattenuator along the major and minor axes. Therefore, for the most commonly considered case (in this research) when the target is orientated horizontally ($\varphi = 0°$) and

$\varphi_1 = 0°$, the linear dichroism, D_L, is:

$$D_L = \frac{T_1 - T_2}{T_1 + T_2} \qquad (2.26)$$

This means to measure the linear dichroism of a diattenuator embedded within a scattering medium by applying *ROPI*, with an ideal analyser and alignment to the fast axes of the diattenuator for one of the detection channels, the linear dichroism, D_L, only depends on the transmittances of the diattenuator along the major and minor axes. If a diattenuator with properties, $T_1 = 1$ and $T_2 = 0$ (i.e. a linear polariser), is chosen, D_L will be detected as a maximum which is 1; otherwise, it varies from a minimum, which is 0, to 1 depending on the values of T_1 and T_2. It should be noted that this ideal case is considered in this study for characterization purposes. However, in practice, the orientation of the polarizing component will be unknown and therefore equation 2.25 should be used. For the characterization described later, a piece of sheet polariser with a good extinction ratio ($T_2/T_1 = 10^{-4}$) is chosen.

2.4 Mathematical Foundation for Measuring Linear Birefringence

Linear birefringence is a property relating to the introduction of a phase difference between two orthogonal electric fields ($E_{//}$ and $E_{\perp}$) of polarized light due to axes

with different refractive indices. In this section, the Mueller calculus representation demonstrating the application of *ROPI* for measuring linear birefringence in a scattering medium is mathematically described.

In the previous section which determined the linear dichroism of a sample, the signal was provided by the difference in transmission along the major and minor axes of the component as shown in equation 2.25. For a linear birefringent sample, the parameter providing the polarization signal is the retardance, δ. If the same assumptions are applied as were introduced in the previous section, *ROPI* measurement of linear birefringence within scattering media is not possible. This is shown in the following analysis.

For the sample shown in figure 2.1 for a linear birefringence measurement, consider the Mueller matrix for the most general birefringent component $\left(\bar{M}_R\right)$ as in equation 2.7. Back-illumination of this component with randomly polarized light $\left(\bar{S}_i\right)$ shown in equation 2.20, results in the following Stokes vector representing light emerging from the sample $\left(\bar{S}_s\right)$:

$$\bar{S}_s = \bar{M}_R \bar{S}_i = \bar{M}_R \begin{bmatrix} 1 \\ 0 \\ 0 \\ 0 \end{bmatrix} = \begin{bmatrix} 1 \\ 0 \\ 0 \\ 0 \end{bmatrix} \qquad (2.27)$$

This clearly also represents randomly polarized light. Therefore, it is clear that this randomly polarized back-illumination component cannot be used to extract information regarding the sample's linear birefringence.

However, assumption 2) in the previous section states that all light is depolarized before interaction with the sample. Practically, this is not always the case (especially for superficial targets) and some of the initial polarization information will be retained. For the purposes of this analysis, fully linearly polarized light is used. The general Mueller matrix of linearly polarized illumination $(\bar{S}_i)$ with an arbitrary azimuthal orientation angle, ζ_1, is shown as:

$$\bar{S}_i = \begin{bmatrix} 1 \\ \cos(2\zeta_1) \\ \sin(2\zeta_1) \\ 0 \end{bmatrix} \tag{2.28}$$

If such a polarization $(\bar{S}_i)$ back-illuminates a birefringent component $(\bar{M}_R)$, the following polarization state emerges from the sample resulting in $(\bar{S}_s)$:

$$\bar{S}_s = \bar{M}_R \bar{S}_i =$$
$$\begin{bmatrix} 1 \\ \cos(2\zeta_1)\left[\cos^2(2\theta)+\sin^2(2\theta)\cos\delta\right]+\sin(2\zeta_1)\left[(1-\cos\delta)\sin(2\theta)\cos(2\theta)\right] \\ \cos(2\zeta_1)\left[(1-\cos\delta)\sin(2\theta)\cos(2\theta)\right]+\sin(2\zeta_1)\left[\sin^2(2\theta)+\cos^2(2\theta)\cos\delta\right] \\ \cos(2\zeta_1)\sin(2\theta)\sin\delta-\sin(2\zeta_1)\cos(2\theta)\sin\delta \end{bmatrix} \tag{2.29}$$

Detection of this light emerging from the sample $(\bar{S}_s)$ through a linear polarizer (i.e. analyser) ($\bar{M}_{LP}$ shown in equation 2.8) whose polarization state, $(\zeta_1+\pi/2)$, is orthogonal to the illumination state, (ζ_1), can be represented by the Mueller calculus shown in equation 2.30. The intensity, $I(\zeta_1+\pi/2)$, of the detected light, $(\bar{S}_d)$, thereby can be obtained as given in equation 2.31.

$$\bar{S}_d = \bar{M}_{LP}\bar{S}_s \tag{2.30}$$

$$I(\zeta_1 + \pi/2) = \frac{1}{2}\left\{\begin{array}{c} 1 \\ -\cos^2(2\zeta_1)\left[\cos^2(2\theta) + \sin^2(2\theta)\cos\delta\right] \\ -\sin^2(2\zeta_1)\left[\sin^2(2\theta) + \cos^2(2\theta)\cos\delta\right] \\ -2\cos(2\zeta_1)\sin(2\zeta_1)\left[(1 - \cos\delta)\sin(2\theta)\cos(2\theta)\right] \end{array}\right\} \tag{2.31}$$

For the second *ROPI* channel with illumination (ζ_2) in a plane orthogonal to ζ_1

where $\zeta_2 = \zeta_1 + \pi/2$, and detecting orthogonal to the illumination, the second channel

intensity, $I(\zeta_2 + \pi/2)$, is obtained as:

$$I(\zeta_2 + \pi/2)$$

$$= \frac{1}{2}\left\{\begin{array}{c} 1 \\ -\cos^2(2\zeta_2)\left[\cos^2(2\theta + \pi) + \sin^2(2\theta + \pi)\cos\delta\right] \\ -\sin^2(2\zeta_2)\left[\sin^2(2\theta + \pi) + \cos^2(2\theta + \pi)\cos\delta\right] \\ -2\cos(2\zeta_2)\sin(2\zeta_2)\left[(1 - \cos\delta)\sin(2\theta + \pi)\cos(2\theta + \pi)\right] \end{array}\right\}$$

$$= \frac{1}{2}\left\{\begin{array}{c} 1 \\ -\cos^2(2\zeta_1 + \pi)\left[\cos^2(2\theta) + \sin^2(2\theta)\cos\delta\right] \\ -\sin^2(2\zeta_1 + \pi)\left[\sin^2(2\theta) + \cos^2(2\theta)\cos\delta\right] \\ -2\cos(2\zeta_1 + \pi)\sin(2\zeta_1 + \pi)\left[(1 - \cos\delta)\sin(2\theta)\cos(2\theta)\right] \end{array}\right\}$$

$$= \frac{1}{2}\left\{\begin{array}{c} 1 \\ -\cos^2(2\zeta_1)\left[\cos^2(2\theta) + \sin^2(2\theta)\cos\delta\right] \\ -\sin^2(2\zeta_1)\left[\sin^2(2\theta) + \cos^2(2\theta)\cos\delta\right] \\ -2\cos(2\zeta_1)\sin(2\zeta_1)\left[(1 - \cos\delta)\sin(2\theta)\cos(2\theta)\right] \end{array}\right\} \tag{2.32}$$

It can be clearly shown from equations 2.31 and 2.32 that using these two orthogonal

illumination states $(\zeta_1$ and $\zeta_2 = \zeta_1 + \pi/2)$ and detecting the cross-polar channels does

not provide any information concerning the linear birefringence. This is due to the

difference of these two intensities, which is used to represent the linear birefringence,

being 0 as:

$$I(\zeta_1 + \pi/2) = I(\zeta_2 + \pi/2) \tag{2.33}$$

To examine the sensitivity to birefringence, further consider two arbitrarily selected azimuthal orientations (ψ_1 and ψ_2) of illuminating polarization ($\bar{S}_i$ in equation 2.5). Following the same Mueller calculus applied above (equations 2.29 and 2.30) with detection provided orthogonal to each of these illumination states (i.e. $\bar{M}_{LP}$ shown in equation 2.8 at $\psi_1 + \pi/2$ and $\psi_2 + \pi/2$), the intensity difference between the detections, $I_{sig}(\psi_1 - \psi_2)$, can be obtained as:

$$
\begin{aligned}
&I_{sig}(\psi_1 - \psi_2) \\
&= I(\psi_1 + \pi/2) - I(\psi_2 + \pi/2) \\
&= \frac{1}{2}\left\{(1 - \cos\delta)\left[\begin{array}{l}\left(\cos^2(2\theta) - \sin^2(2\theta)\right)\left(\cos^2(2\psi_2) - \cos^2(2\psi_1)\right) \\ + 2\sin(2\theta)\cos(2\theta)\left(\sin(2\psi_2)\cos(2\psi_2) - \sin(2\psi_1)\cos(2\psi_1)\right)\end{array}\right]\right\}
\end{aligned}
\tag{2.34}
$$

As equation 2.34 shows, clearly the value of $I_{sig}(\psi_1 - \psi_2)$ depends on the retardance (δ), and the azimuthal orientation (θ) of the birefringent component and the azimuthal orientation of the two illuminating polarization states (ψ_1 and ψ_2). This demonstrates that some sensitivity to birefringence is available. In order to show how the variation is dependent on those parameters (δ, θ, ψ_1 and ψ_2), a further investigation of equation 2.34 was performed. However, the investigation will be provided in appendix A in detail. Only the conclusion of the investigation is presented here.

It is found that the absolute intensity difference, $|I_{sig}(\psi_1 - \psi_2)|$, varies sinusoidally from a minimum of 0 to a maximum of 1 depending on the values of δ, α and $\Delta\psi$. Where ($\alpha = \psi_1 - \theta$) and ($\Delta\psi = \psi_2 - \psi_1$) are the azimuthal orientation differences between the first illumination and the birefringent component and between the two

illuminations respectively. The maximum values are obtained when $\delta = n\pi$ (n=1, 3, 5,

7 $\cdots$), $\alpha = n\pi/4$ (n=0, 1, 2, 3 $\cdots$) and $\Delta\psi = n\pi/4$ (n=1, 3, 5, 7 $\cdots$).

This firstly indicates that linear birefringence measurements with *ROPI* are possible

(equation 2.34). This is due to the intensity difference resultant from passing through

a birefringent component. Secondly, in order to measure the maximum linear bire-

fringence: (i) two linearly polarized illumination channels are required and the differ-

ence in azimuthal orientation between the illuminations must be 45°±n90° (n=0, 1, 2,

3 $\cdots$); (ii) the difference in azimuthal orientation between the first illumination and the

birefringent component must be 0°±n45° (n=0, 1, 2, 3 $\cdots$); (iii) the retardance of the

birefringent component must be 180° which is a *HWP* in practice. In any other cases,

linear birefringence would vary between 0 and 1.

Finally, to accommodate the difference in illumination intensities between measure-

ments, it is necessary to normalise the subtraction (equation 2.34). Therefore, the re-

sultant difference signal is divided by the sum of the two channels. This is the final

definition of linear birefringence $\left(B_L \right)$ applied in this study for *ROPI* measurements,

which is given as:

$$
\begin{aligned}
B_L &= \frac{I_{sig}\left(\psi_1 - \psi_2\right)}{I_{sig}\left(\psi_1 + \psi_2\right)} \\[2ex]
&= \frac{I\left(\psi_1 + \pi/2\right) - I\left(\psi_2 + \pi/2\right)}{I\left(\psi_1 + \pi/2\right) + I\left(\psi_2 + \pi/2\right)}
\end{aligned}
\tag{2.35}
$$

where ψ_1 and ψ_2 are the azimuthal orientations of two illuminations applied (i.e. $\bar{S}_i$

in equation 2.5 at ψ_1 and ψ_2). $\psi_1 + \pi/2$ and $\psi_2 + \pi/2$ which are orthogonal to the

illuminations represent the two azimuthal orientations applied for the analyser (i.e.

$\bar{M}_{LP}$ shown in equation 2.8 at $\psi_1 + \pi/2$ and $\psi_2 + \pi/2$).

2.5 Summary

This section mainly focuses on the theoretical foundations of *ROPI* towards meas-urement of linear dichroism and linear birefringence within a scattering medium. The principles developed in this section are important as it not only demonstrates the *ROPI* technique but also will provide a valuable evaluation tool in later parts of this study. In addition, it also provides a set of ideal criteria against which to judge the simulation and experimental results.

Firstly, Stokes vectors, Mueller matrices and Mueller calculus were briefly introduced and commonly used Stokes vectors and Mueller matrices were presented. This was followed by demonstrating the mathematical foundations of *ROPI* measurement of linear dichroism and linear birefringence within a scattering medium.

In conclusion, when applying *ROPI* to measure linear dichroism and linear birefrin-gence within a scattering medium, the following principles need to be applied:

For measuring the maximum linear dichroism:

➢ Two illumination polarization states must be orthogonal to each other;

➢ The polarization state of the component embedded within the medium must be aligned to one of the illumination polarization states;

➢ Follow the calculations given in equation 2.19.

For measuring the maximum linear birefringence:

➢ The polarization states of illumination before back-illuminating the component embedded within the medium must be maintained;

➢ The two illumination polarization states must be $45° \pm n90°$ (n=0, 1, 2, 3 ⋯) to each other;

➢ The retardance of the birefringent component embedded within the medium must be $180°$;

➢ The azimuthal orientation of the birefringent component must be $0° \pm n45°$ (n=0, 1, 2, 3 ⋯) to one of the illuminations azimuthal orientation;

➢ Follow the calculations given in equation 2.35.

Chapter 3

ROPI Monte Carlo Simulations

3.1 Introduction

In chapter 2, the theoretical principles of applying the *ROPI* technique for measuring linear dichroism and linear birefringence within scattering media were demonstrated using Mueller calculus. For the purpose of evaluating the *ROPI* technique under ideal conditions, a Monte Carlo (*MC*) model has been developed to simulate different quantitative measurements within a scattering medium using *ROPI*. This model is introduced and described in detail in this chapter. The presented simulations include examination of different polarizing targets (dichroic and birefringent) embedded within the scattering medium in different orientations and at different depths. Different pairs of orthogonally polarized illumination and detection states are applied. In addition to its use for an ideal evaluation of the technique, the model is also used to investigate non-ideal situations such as the evaluation of imperfect targets. These simulation results provide useful comparisons to the results generated from the phantom experiments which will be described in chapters 5 and 6.

As reviewed in chapter 1, a basic *MC* model based on *Mie* scattering theory [58; 59] can be used to simulate polarized light propagating from a point source through a scattering medium. This has been widely applied for investigating the optical properties of

scattering media in biomedical optics research [65; 69]. Within our group, a fully polarized *MC* model has been developed and described in detail by *Chang et al* [71] and then further evaluated and presented by *Stockford et al* [72; 73] and *Lu* [74]. Therefore only a brief description of the model will be provided here.
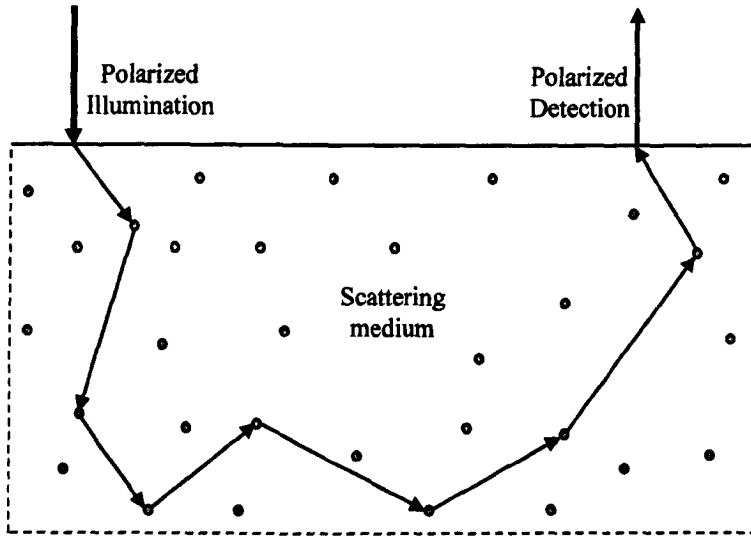
Figure 3.1: Illustration of a basic Monte Carlo simulation of a polarized photon travelling within a scattering medium.

As shown in figure 3.1 in reflection mode, the basic model simulates the propagation of individual polarized photons through a scattering medium and tracks changes including polarization state, position, travelling direction and distance at each scattering event. Photons trajectories are terminated either when they exceed a predefined distance within the medium or when they emerge from the medium. From the records of many photon trajectories, one can build up the spatial, temporal, and angular distributions of light emerging in different polarization states from a scattering medium. Absorption can be added post-simulation through application of the microscopic *Beer-Lambert* law [8]. The mismatch in refractive index at the boundary of medium-air interface is taken into account by either reflecting all those photons greater than or equal to the critical angle back into the medium or otherwise allowing them to leave

the medium with transmitted angles following *Snell's* law [86]. This is used for the purpose of simplifying and speeding up the simulations; since it is only an approximation to *Fresnel's* law [86] which is an ideal and accurate way but too complicated to be fully applied to model the mismatch boundary condition [92]. An alternative approximation to *Fresnel's* law, which involves a probabilistic approach to decide if the photons are to be transmitted or reflected, is introduced by *Prahl et al* [38] and more details about the comparison between applying those approximations and *Fresnel's* law can be found elsewhere [37].

As figure 3.1 shows, the basic *MC* model implements illumination with a pencil beam at a single point without any objects embedded within the scattering medium and it only detects spatially or temporally resolved intensity. It is not able to form images. In order to simulate the *ROPI* system, an imaging model with full field illumination and a polarizing target embedded within a scattering medium is necessary. Based on the existing *MC* model, three modifications are needed to enable the model to simulate the *ROPI* technique. The first modification is to allow full field illumination to be realised. The second allows the insertion of a polarizing target into the scattering medium and the third allows representation of the appropriate imaging system.

This chapter will concentrate on these three modifications of the model and the presentation and analysis of the results obtained. Firstly, in section 3.2, the modified *MC* model in reflection mode applied in this study is described and discussed. Section 3.3 presents the *ROPI MC* simulations of quantitatively measuring linear dichroism of a polarizing target embedded within a scattering medium at different depths. Section 3.4 demonstrates similar analysis for a birefringent target. Finally, a summary and discussion of the chapter is given in section 3.5.

3.2 Description of the Monte Carlo Model

In this section, the modified *MC* model developed in this study to simulate different *ROPI* quantitative measurements within a scattering medium is introduced and described in detail. The description will concentrate on the three modifications that enable the model to simulate the *ROPI* technique. The limitations and verifications of the model are also discussed.

3.2.1 Modifications and Simulation Algorithm

Modification 1: Full Field Illumination

In order to simulate *ROPI*, conversion of the existing single point illumination *MC* model to achieve full field illumination is required. One option would be to simply run many different simulations scanning the single point illumination within the illumination area point-by-point. However, in practice with typically one million photons per illumination point, this would take approximately 1.6 hours per point. For a small area such as 100*points* × 100*points*, this would take more than 660 days to simulate an object embedded at only one depth and polarization state; hence it is clearly not practical to implement this approach. An alternative approach, as applied here, is to implement the existing single point illumination scheme but to extend it to realise full field illumination by indexing the photon path laterally to all illumination positions within the incident area. This allows representation of full field illumination using a single ~1.6 hour simulation.

As shown in figure 3.2, the model requires a polarizing target to be embedded within the scattering medium at a depth of *D*. (Presentation of this modification is performed

in the next part.) Trajectory *A* (solid red line) is a typical scattering photon path within a scattering medium obtained from running the basic *MC* simulation with a single photon illumination at the central position ($x=0$, $y=0$, $z=0$) of the illumination area. Assuming the rest of the point simulations run within the illumination area have the same trajectories (A_{-n} to A_n, dashed blue lines) as *A*, the full field illumination can be achieved post-simulation by laterally indexing the trajectory *A* around the illumination area with a step size, *s*, until all the illumination points are covered. This indexing process means that full field illumination can be represented by running a single simulation rather than running multiple simulations at all the points within the illumination area, significantly reducing the simulation time.
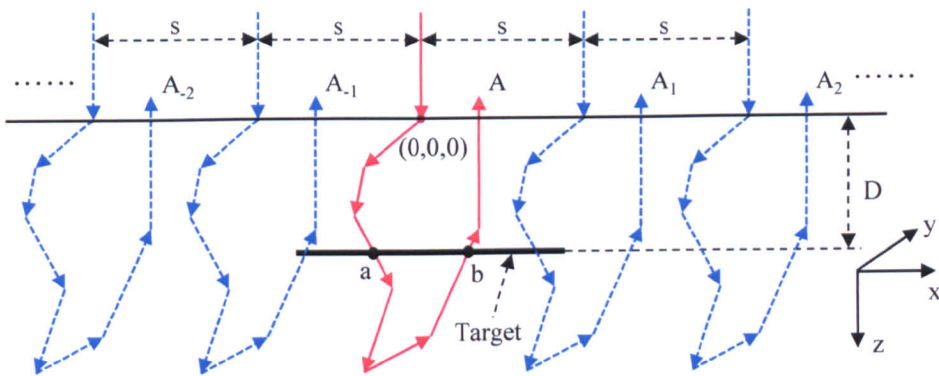
Figure 3.2: Index process for modification of the basic MC model from single point illumination to full field illumination.

In order to efficiently simulate the full field illumination, it is found that setting $s = mfp/4$ provides sufficient sampling at the illumination plane. This is to match the geometry of the detection array as will be discussed in subsection 3.2.3. The assumption that the trajectories A_{-n} to A_n at different illumination points have the same photon path is clearly an approximation. As the simulations are dependent on the analysis of millions of photons; the cumulative effect is of interest rather than individual photon paths. If the assumption can be made that a single simulation is statistically stable

then this is a reasonable assumption when extended to all points within the illumination area.

Modification 2: Inserting a Polarizing Target within a Scattering Medium

For the case of simulating an absorbing object embedded within a scattering medium with a *MC* model, monitoring the effect of indexing the illumination position is simplified from the polarizing case required here. This case as applied in [5, 72] is considered initially as it is instructive for development of the polarizing target model.

To monitor the interaction of a photon with a (particular) absorbing target, an array of counters is required with each element representing a point within the illumination field. For every event during the propagation of a photon which results in transit through the specified depth of the target, the indexed lateral location of the photon is determined for each element in the counter array. If this indexed position would result in a target interaction, the appropriate counter is increased and propagation continued.

However for the case of a polarizing target embedded, as the polarization state of a photon changes when it passes through the polarizing target, it is not sufficient to simply record a target interaction as in the previous case (for an absorbing target for example). A modification of the photon's parameters is also required, which would impact on the polarization properties at subsequent target interactions. Thereby, this provides a problem when using the indexing method for achieving full field illumination as, depending on the width of the target and the relative position of the illumination and the target, some photons will have interacted with the target and some will not. This results in different trajectories being obtained for different illumination points and hence, the assumption made that all indexing illumination points have the same photon trajectory is unreasonable.

A method developed to overcome this problem is illustrated in figure 3.3, which repeatedly applies a splitting process for the trajectory of a photon each time it passes through the target plane. Each time a photon crosses the target plane, the photon trajectory is split into two paths; the first is for the case that the target is present (upon which the target Mueller matrix is applied) and the second is for the case that the target is absent. When the photon emerges from the medium, rather than as normally recording one trajectory for the photon, this provides multiple trajectories depending on the number of interactions of the photon with the target plane are recorded. Each trajectory contains different combined effects of polarization states modified by the target.
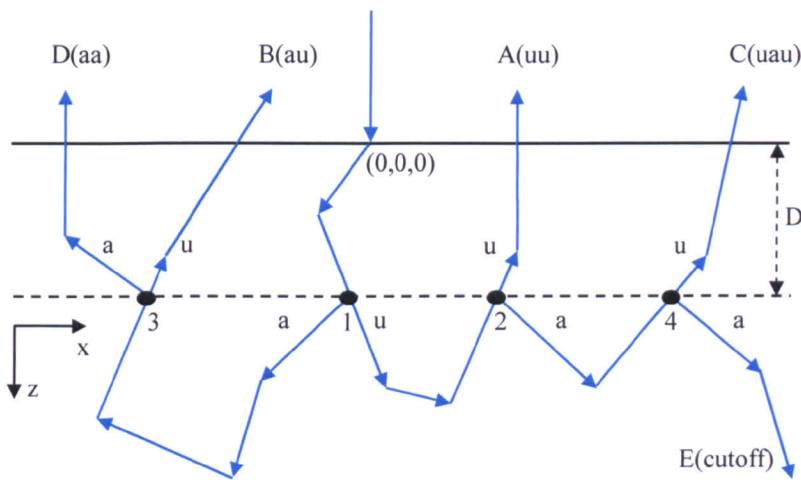
Figure 3.3: Illustration of the splitting process applied for modifying the MC model to allow the insertion of a polarizing target within a scattering medium.

Figure 3.3 illustrates the generation of multiple trajectories from a single photon simulation through applying the splitting process. As it is shown, each photon illuminates the medium at point $(0, 0, 0)$, and when the photon initially passes through the depth D where the target is located, the first position at the crossing point '1' in the x direction is recorded. The photon is then split into the two trajectories labelled as 'a'

meaning affected by the target and 'u' meaning unaffected by the target. The interaction of the photon with the polarizing target modifies the polarization state of the photon through the Mueller calculus described in chapter 2. This process will be repeated for multiple crossings of the target plane until all the splitting trajectories either emerge from the medium or travel too far to be cut off. As the photon is attenuated through interaction with the target, it was also found that 20 crossings allowed convergence of the results, which will be discussed more in section 3.2.3. In addition, the label '1, 2, 3······' indicates the crossing points at the target depth in sequence; 'A, B, C······' labels the trajectories generated for the photon simulated in sequence and the combinations of 'a' and 'u' represents combination of the effects of the polarization states being modified by the target for each trajectory from all the crossings in sequence.

For each point in the illumination, only the photon trajectory with the appropriate combination of target interactions is selected from those multiple trajectories depending on the relative location and geometry of the target. This approach leads to a computationally efficient MC simulation with full field illumination and a polarizing target embedded within the scattering medium.

Modification 3: Imaging System Representation

The basic MC model detects the positions of emergence of backscattered photons and their propagation directions. In order to simulate the $ROPI$ system, it is therefore necessary to modify the model to image a target within a scattering medium located at different depths and distribute the detected backscattered photons into different pixels in a 2-D detector. This model must also account for the numerical aperture (NA) of the objective lens which determines the range of photon angles that can be collected.
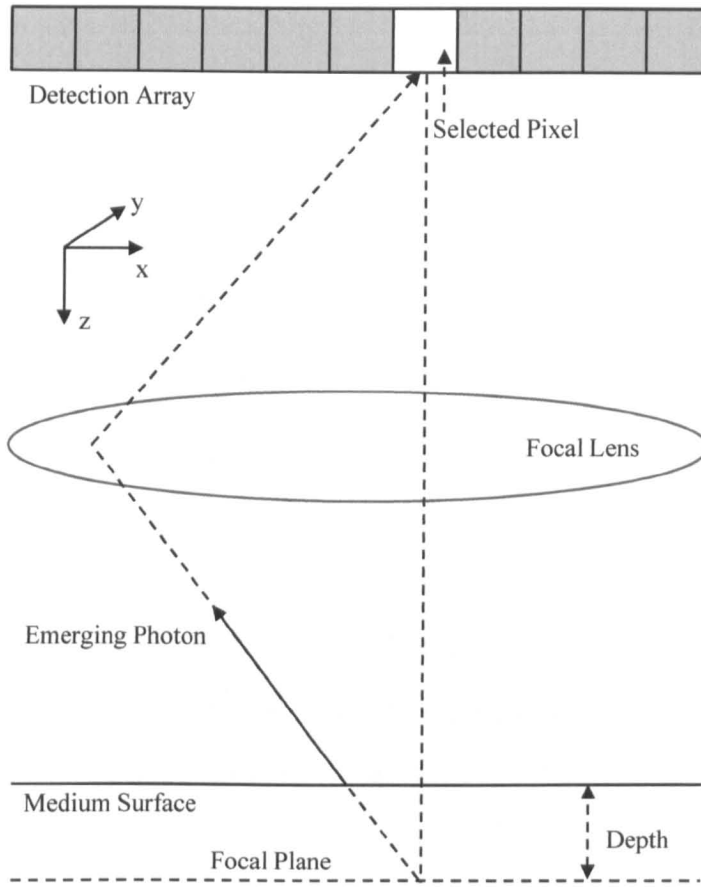
Figure 3.4: Illustration of the imaging formation applied for modifying the MC model to be able to form images within a scattering medium.

The modelled imaging system is presented in figure 3.4. This is represented here in only the x and z dimensions for illustrative purposes. However, implementation clearly includes consideration of both x and y lateral dimensions. The focal plane of the imaging system corresponds to the depth of the target located within a scattering medium, which can be varied as the target depth is changed. The imaging is performed by a lens such that an image of the focal plane is obtained at the detector. An image is formed by firstly recording the angle of emergence of each photon at the medium surface then back-propagating the emerging photon along the emerging angle to the focal plane of the imaging optics. The intensity of the photon is then stored in the identified position in the detection array as illustrated.

Combining the three modifications detailed here allows full field imaging of polarizing targets in scattering media and therefore realistic simulation of the *ROPI* system. The whole simulation algorithm with flow charts is provided in appendix B.

3.2.2 Scattering Medium and Targets

In this subsection, the scattering medium's properties and the targets used in this study for the *ROPI MC* simulations are presented.

In order to be able to compare the *MC* simulation results with the experimental phantom results (which will be performed in chapters 5 and 6), the scattering medium matches that used in the experiments. The optical and physical properties of the scattering medium used for the simulations are shown in table 3.1.

Parameters	Values
$g = <cos(\theta)>$	0.938
$\mu_s = N\sigma_s = NQ_sA$	$20~mm^{-1}$
Q_s	3.373
μ_a	$3.0\times10^{-4}~mm^{-1}$
$mfp = 1/\mu_s$	0.05 mm
n_m	1.332
n_p	1.572
d	1.4 μm
λ	632.8 nm

Table 3.1: Optical and physical properties of the scattering medium applied for ROPI MC simulations in reflection mode.

μ_s is the scattering coefficient of the scattering medium at a wavelength of 632.8nm. It is defined as the probability of photon scattering in a medium per unit path length [8]

and is the factor that expresses the attenuation caused by scattering. For a single scatterer, the scattering cross section, σ_s, which indicates the scattering capability, is related to its geometric cross-sectional area, $A = \pi(d/2)^2$, through the dimensionless scattering efficiency Q_s: $\sigma_s = Q_s A$, where d is the particle diameter. For a medium containing many scatterers with number density (the number of particles per unit volume), N, the scattering coefficient can be calculated as the total cross-sectional area for scattering per unit volume:

$$\mu_s = N\sigma_s \qquad (3.1)$$

For the *Mie* scattering case, where the light wavelength is similar or smaller to the particle diameter, light interacts with a particle over the scattering cross-sectional area that is larger than the geometric cross-sectional area.

g is the scattering anisotropy factor which is defined as the mean scattering angle ($<\cos(\theta)>$) and represents the direction followed by a photon after a scattering event; θ is the scattering angle.

μ_a is the absorption coefficient of pure water [93] at 632.8nm in this study. Similar to μ_s, this is defined as the probability of photon absorption in a medium per unit path length [8] and is used to calculate the attenuation due to water followed by the *Beer-Lambert* law [8]. The microspheres used in this study are non-absorbing and, therefore, as the absorption coefficient of the pure water is small, there is almost no absorption of photons in the medium.

mfp stands for *Mean Free Path* which is the reciprocal of the scattering coefficient (μ_s) and represents the mean distance over which light will propagate before being scattered [94]. In addition, this is used as the distance unit in the model. Therefore, for

simulating different types of media, a scaling factor to the *mfp*s can be applied. Finally, n_m is the refractive index of the surrounding medium (i.e. water in this study), n_p is the refractive index of the particles or scatterers and λ is the wavelength of light.

In this study, the modified *MC* model is applied to investigate the *ROPI* technique by quantitatively measuring the polarization properties of both linearly dichroic and birefringent targets embedded within a scattering medium. Two different polarizing targets are required, which represent linear dichroism and linear birefringence. By using the Mueller calculus described in chapter 2, for the linear dichroism measurements, an ideal linear polarizer (*LP*) with $T_1=1$, $T_2=0$, gives the maximum linear dichroism signal and is therefore chosen as the target. The Mueller matrix of a *LP* in its general form is shown in equation 2.6 and a *LP* in the ideal case (maximum linear dichroism) is represented in equation 2.8. T_1 and T_2 are the transmittances of the *LP* along the major and minor axes respectively. For the linear birefringence measurements, a half wave plate (*HWP*) is selected as the target for the simulation as this provides the strongest signal. The Mueller matrix of a retarder in its general form is shown in equation 2.7 and that of a *HWP* is shown in equation 2.10.

In accordance with the targets used in the phantom experiments in reflection mode, which will be considered in chapter 4, both simulated targets are set to a width of 14*mfp* (in practice, 0.7*mm* wide). Also, the targets are infinitely thin and infinitely long in the *y* direction. The scattering medium applied is set to semi-infinite in the *z* direction and infinitely wide and long in *x* and *y* directions. In order to fully investigate the sensitivity of the *ROPI* technique, the effects of varying the target's submerged depth and orientation are evaluated. More details about the exact setting of the targets will be given when the appropriate simulations are demonstrated in the next two sections.

3.2.3 Limitation and Verification of the Modified Simulation Model

In this subsection, firstly, a necessary approximation applied to the model is introduced and validated via simulation. Secondly, verification of the modified model is demonstrated.

As discussed in section 3.2.1, each time a photon crosses the target plane, a pair of new photon paths are generated. It is computationally inefficient (in terms of simulation time and storage) to allow this to continue indefinitely as among millions of photons, there is a highly probability for a single photon to cross the target plane a large number of times. This results in a large amount of data that may contribute little to the output due to attenuation on interaction with the target. Statistically speaking, the mean attenuation applied by interaction of a photon with a submerged polariser is 0.5. Therefore, n interactions will result in a reduction in intensity of a photon by a factor of 0.5^n. In order to efficiently implement the model, a limitation applied to restrict the total interactions (n) of a photon with the target plane is necessary.

Based on the computing power available and simulation time consumed, n is conservatively set at 20 for the simulations in this study. In order to investigate if $n=20$ is reasonable, simulations with $n=2, 4, 6 \cdots \cdots 18, 19$ and 20 were implemented. The results represented as *error* vs. n are shown in figure 3.5, where the error for each value of n is calculated as a normalised intensity difference between I_n and I_{20}, i.e. $error_n=(I_{20}-I_n)/I_{20}$. As the figure shows, the error significantly reduces as n increases when $n \leq 8$ and tends to be fairly constant after that. This clearly indicates the simulation results are not significantly changed when $n \geq 8$. Thereby, the setting of $n=20$ is considered reasonable. This will be further improved when the absorption in the medium is high as the contribution from longer pathlength photons will be reduced.
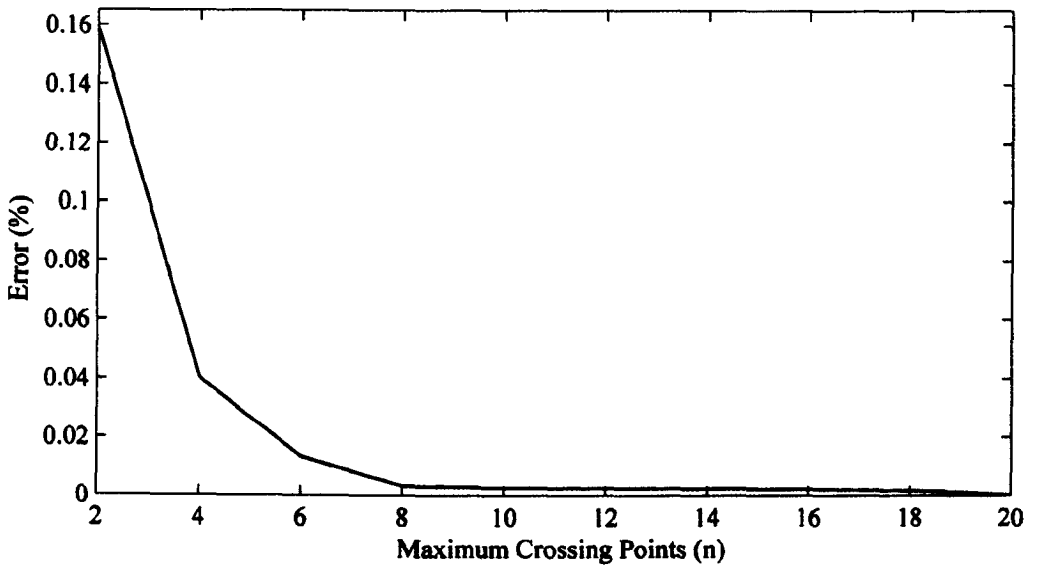
Figure 3.5: Errors of limiting different n in the model by comparing to n=20. n is the total number of interactions of a photon with the target plane. Error is defined as $(I_{20}-I_n)/I_{20}$.

Results verifying that the modified *MC* model can adequately simulate the *ROPI* technique are shown in figure 3.6. The simulations are implemented with full field illumination with 1024^2 illumination points and a separation distance of *mfp/4* between each point. 5 million photons illuminate each point and photons are polarized in the horizontal direction. A linear polarizer, 50*mfps* wide, is located within a scattering medium at a depth of 1.5*mfps* and orientated at $0°$. The properties of the scattering medium are as presented in table 3.1. The backscattered photons are detected in four different channels with polarization states $0°$, $90°$, $45°$ and $-45°$ respectively and the detection area is specified to be 128^2 bins with each bin $1mfp^2$.

Figures 3.6a-d show the images recorded in the four different channels. It is clearly shown that the linear polarizer is imaged within the scattering medium. In the different detection channels, the contrast of the images varies depending on the polarization states of the detectors and the target. The contrast in image a) is poor as the detection and the target are co-polarized while the contrast in b) is high as they are cross-

polarized. The contrast in c) and d) is the same and between that in a) and b) due to a ±45° detection scheme.
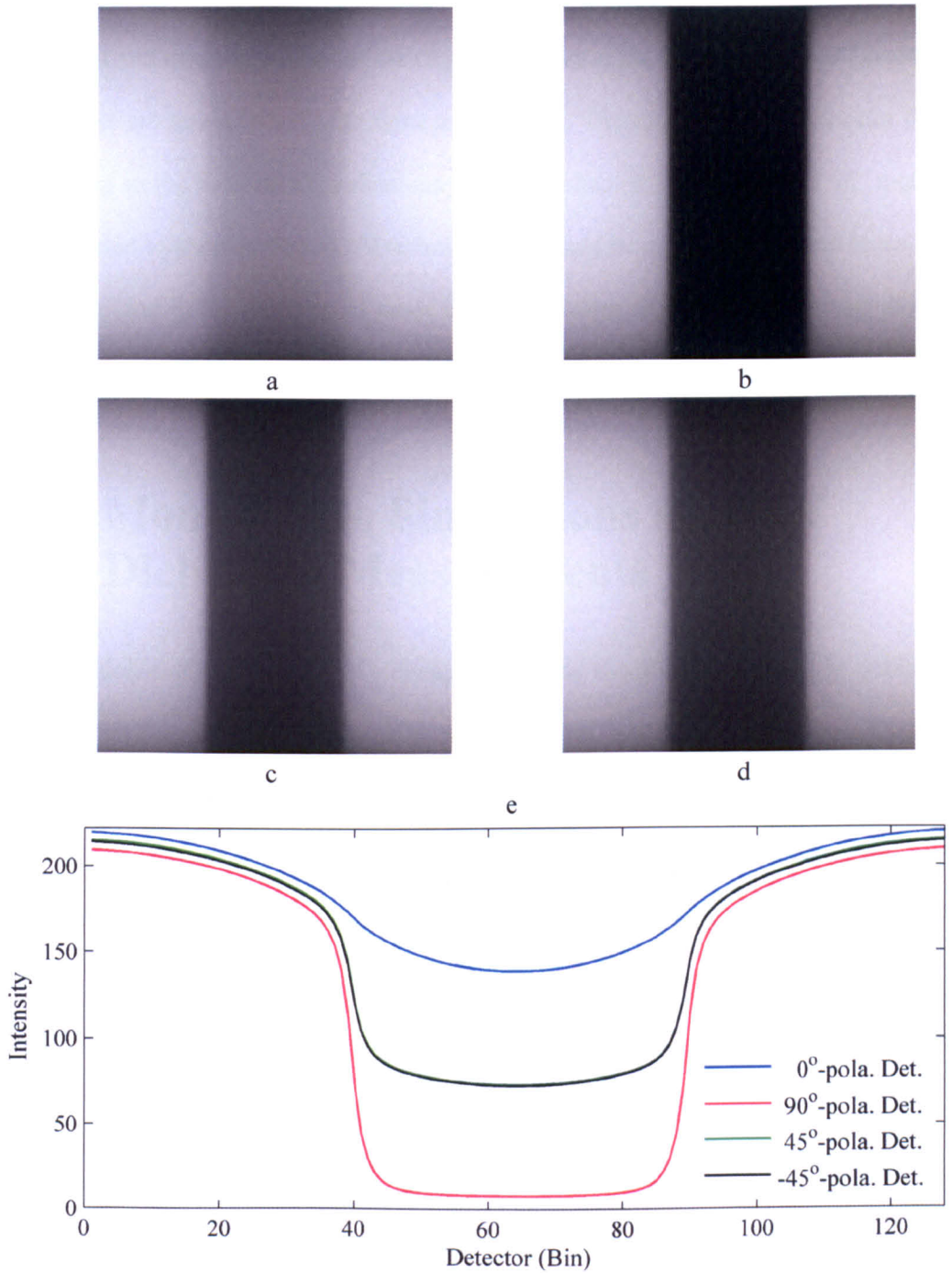
Figure 3.6: Verification of the modified MC model. a) polarizing detection at 0°; b) 90°; c) 45° and d) -45°. e) are the line scans from the images of a), b), c) and d). The target is located at a depth of 1.5mfp and orientated at 0°.

Figure 3.6e illustrates the single line scans from the images, which quantitatively confirm the images contrast. The *co-* and *cross*-polarized quantitative detections are not respectively the same as the background and 0 due to scattering that occurs between the target and medium surface as the target is located at the depth of 1.5*mfp*. The ±45° detections are quantitatively the same as expected. Therefore, this demonstrates that according to the theoretical evaluations shown in chapter 2, the modified *MC* model can be used to simulate the *ROPI* technique. It should be noted that *co-* and *cross-* in this case (and in the majority of cases in the following chapters) refers to the alignment of the detection and target. Illumination and detection are always orthogonal.

3.3   Monte Carlo Simulations of *ROPI* Dichroism Measurements

This section evaluates the *ROPI* technique using the modified *MC* model as outlined in the previous sections. Quantitative measurements are shown of the polarization properties of a linearly dichroic target (linear polarizer) embedded within a scattering medium at different depths and at different orientations. The illumination / detection pairs which are aligned orthogonally at different polarization states are applied.

3.3.1   Overview of the *MC* Simulations and *ROPI* Dichroism Measurements

As described in chapter 1 and equation 2.19 in chapter 2, only two orthogonally polarized illumination / detection pairs are required for measuring linear dichroism when the polarization state of the target is known. In practice, however at least three pairs of illumination / detection are needed when the target orientation is unknown. Therefore,

two *ROPI* channels are used here; illumination at 0° with detection at 90° and illumination orientated at 90° with detection at 0°. The polarizer is located within a scattering medium at the depths of 0, 2, 5, 10, 12, 15 and 17*mfps* with the polarization axis of the target aligned at 0°, 90°, 45° and -45°. In order to further evaluate the *ROPI* technique, illumination / detection polarized at 45° / -45° and -45° / 45° is used to perform the same measurements. To allow comparison of the *MC* simulation and phantom experimental results, which will be given in chapter 7, the design of simulation performed here matches those performed experimentally on the tissue phantoms, which will be given in chapters 5 and 6.

The scattering medium and the polarizing target applied for the simulations are as described previously in subsection 3.2.2. These are consistent with those applied for the same measurements from the phantom experiments described in chapters 5 and 6. The full field illumination area applied for the simulations is 512×512 points in the *x* and *y* directions representing an area of 128*mfps* $\times$ 128*mfps*. Each point is illuminated with 5 million photons and has a distance of *mfp/4* to the next point. The detection is performed over an area of 200*mfps* $\times$ 200*mfps* using an *NA* of 0.1. In order to increase time efficiency, the simulations are implemented on High Performance Computers (*HPC*) within the University of Nottingham, which allow the running of separate simulations in parallel using up to 100 computers at the same time.

According to the Mueller calculus described in chapter 2, linear dichroism is calculated from equation 2.25 using images generated from the pairs of illumination / detection. Depending on the polarization states applied for the pairs of illumination / detection and the target, the maximum dichroism will be measured when the polarization state of the target differs by either 0° or 90° from that of the illumination or detec-

tion. The minimum case (i.e. no dichroism measured) will be obtained with the difference is either 45° or -45°. Therefore, for the two specific sets of illumination / detection pairs and the four specific target states used here, linear dichroism measured at every depth is always at a maximum for one set (illumination / detection pairs) case whilst it is the minimum for the other depending on the target state used.

To avoid showing many similar results, the recorded images and line scans shown in this chapter represent only one of the maximum cases at different depths. The images and line scans in the minimum cases are not shown as there is no dichroism measured. However, two graphs quantitatively showing dichroism obtained at different target states over a range of depths under applying different sets of illumination / detection pairs are respectively shown at the end of the section. These graphs include all the maximum and minimum measurements implemented. Furthermore, in order to find out the depths over which linear dichroism within the scattering medium could be measured by applying the *ROPI* technique, the extended measurement results are presented as well.

3.3.2 Simulation Results

Figures 3.7 to 3.10 show the maximum linear dichroism measurements of a linear polarizer located within a scattering medium orientated at 0° at depths of 0, 2, 5, 10, 12, 15 and 17*mfps*. The illumination / detection pairs linearly polarized at 0°/ 90° and 90° / 0° were used.

Figure 3.7 shows images with the illumination / detection linearly polarized at 90° / 0° for different target depths. In this case the target (0°) is cross aligned to the illumination (90°). Consider initially a depth of 0*mfp* (figure 3.7a). For light that illuminates

the medium directly over the target, this will be completely blocked by the target and will not be able to pass further into the medium. This is the cause of the contrast in the images shown in figure 3.7. As the target moves deeper into the medium (figures 3.7b-g), there is sufficient scattering in the region between the target and the input surface to cause a reduction in contrast.

Figure 3.8 shows images with the illumination / detection orientated at 0° / 90° for the same depths as in figure 3.7. In this case the polarization axes of the target and the detection are cross aligned and there is a different contrast mechanism to that described for figure 3.7. In this case the target (0°) and the detection (90°) are cross aligned. Again, consider a target located at $0mfp$ (figure 3.8a). Unlike figure 3.7, illuminating photons can easily pass through the target (as their orientations are aligned) and contribute to back-illumination of the target. The photons that back-illuminate the target are polarized by the target (0°) in a plane that is orthogonal to the detection (90°) and are not detected. This results in a high contrast image. As with figure 3.7, contrast decreases with increasing target depth due to increased scattering.

Figure 3.9, which is generated by combining the images from figures 3.7 and 3.8 following equation 2.25, shows the maximum linear dichroism images. The contrast in the images reveals linear dichroism measured from the target is different from the background, which is expected. In addition, the measured linear dichroism values reduce as target depth increases. As described, this is due to the effects of scattering between the target and the exit surface of the medium.

Figure 3.10 shows the line scans along the y axis of the dichroism images shown in figure 3.9. These are obtained by averaging in the y direction over rows 10 to 190 in the images and provide quantification of the observed dichroism. It can clearly be

a

b

c

d

e

f

g
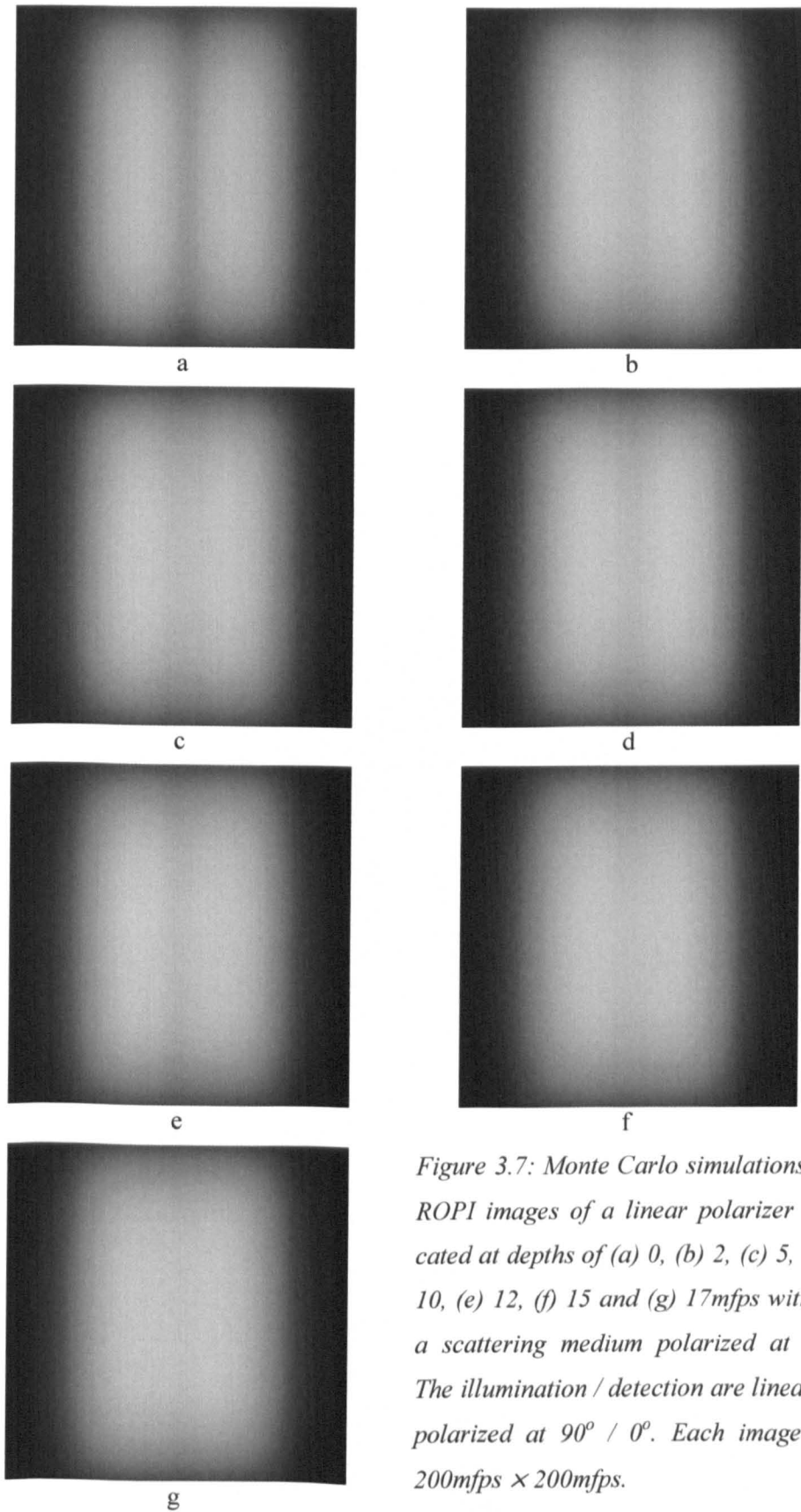
Figure 3.7: Monte Carlo simulations of ROPI images of a linear polarizer located at depths of (a) 0, (b) 2, (c) 5, (d) 10, (e) 12, (f) 15 and (g) 17mfps within a scattering medium polarized at 0°. The illumination / detection are linearly polarized at 90° / 0°. Each image is 200mfps × 200mfps.
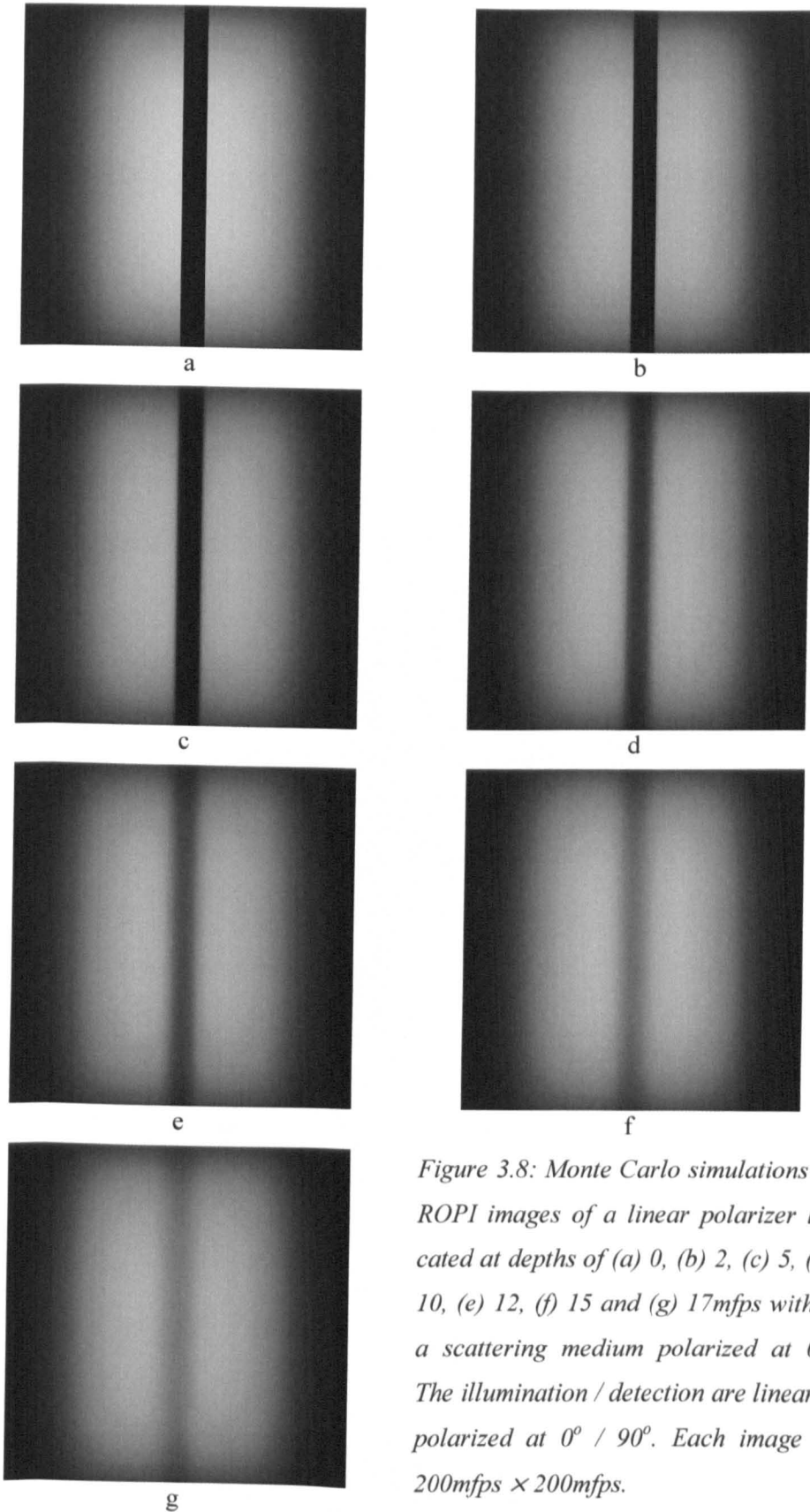
Figure 3.8: Monte Carlo simulations of ROPI images of a linear polarizer located at depths of (a) 0, (b) 2, (c) 5, (d) 10, (e) 12, (f) 15 and (g) 17mfps within a scattering medium polarized at 0°. The illumination / detection are linearly polarized at 0° / 90°. Each image is 200mfps × 200mfps.
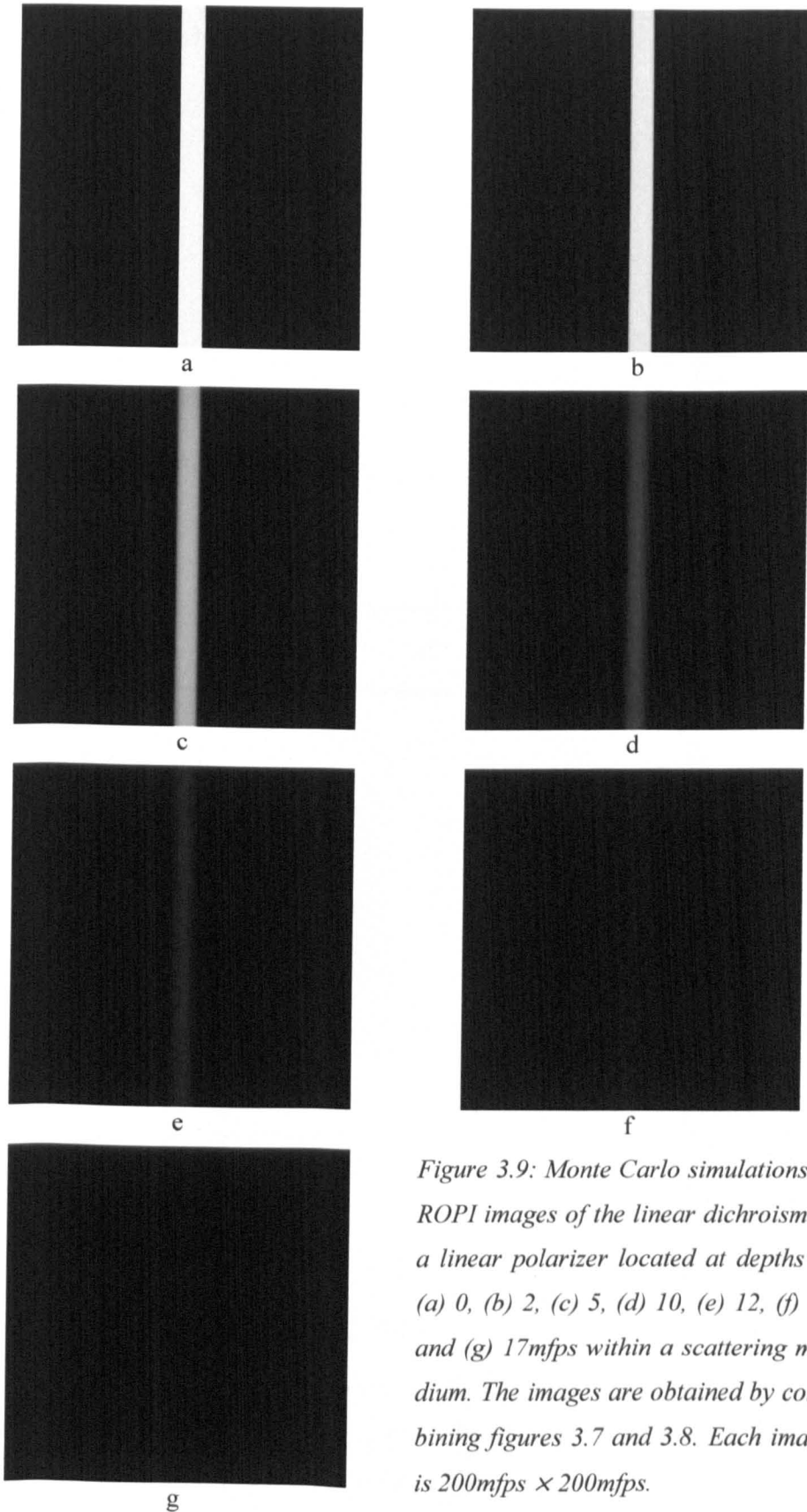
Figure 3.9: Monte Carlo simulations of ROPI images of the linear dichroism of a linear polarizer located at depths of (a) 0, (b) 2, (c) 5, (d) 10, (e) 12, (f) 15 and (g) 17mfps within a scattering medium. The images are obtained by combining figures 3.7 and 3.8. Each image is 200mfps × 200mfps.
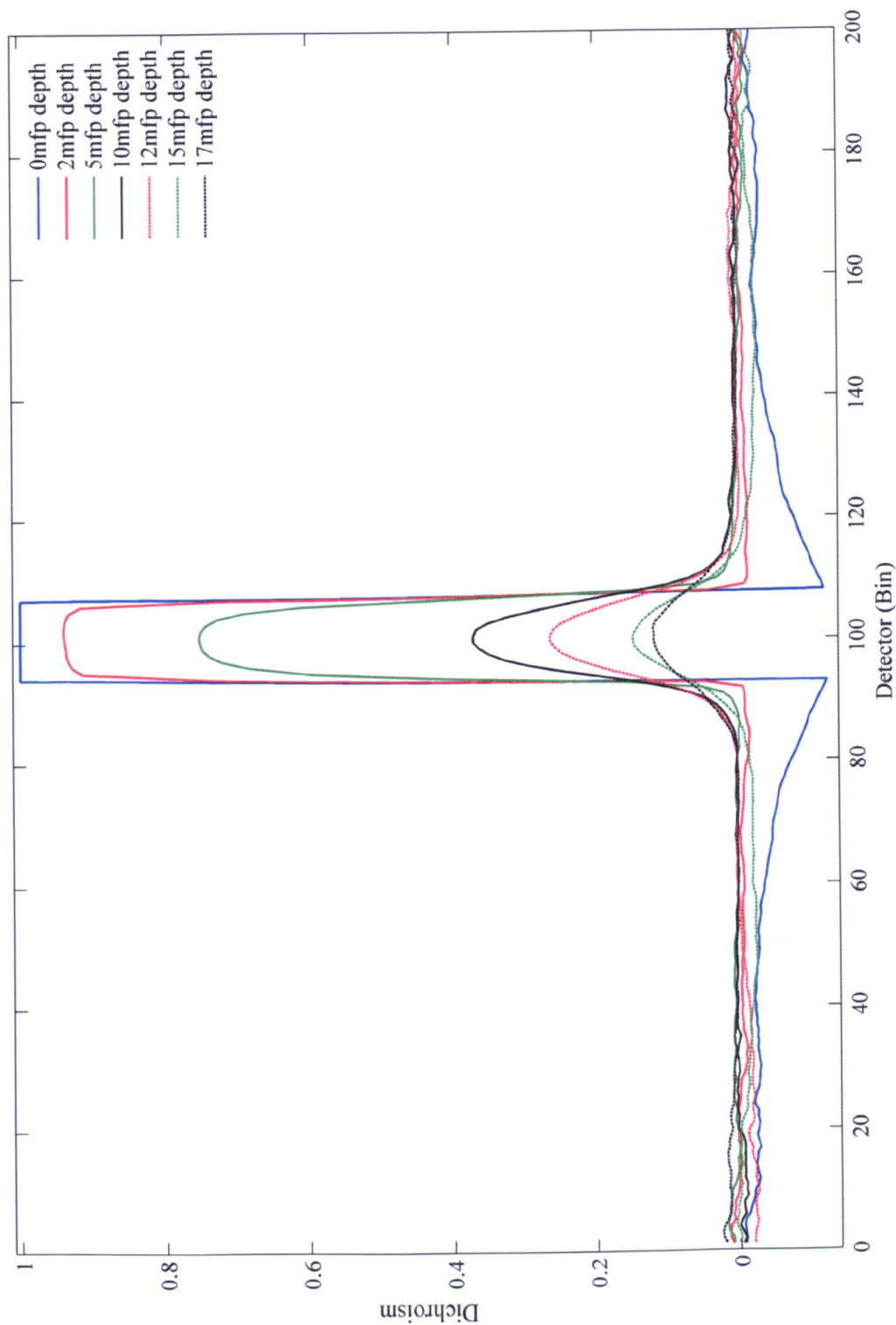
Figure 3.10: Average line scans on y axis of the images in figure 3.9 that quantitatively show the Monte Carlo simulations of the ROPI linear dichroism measurements at different target depths within a scattering medium.
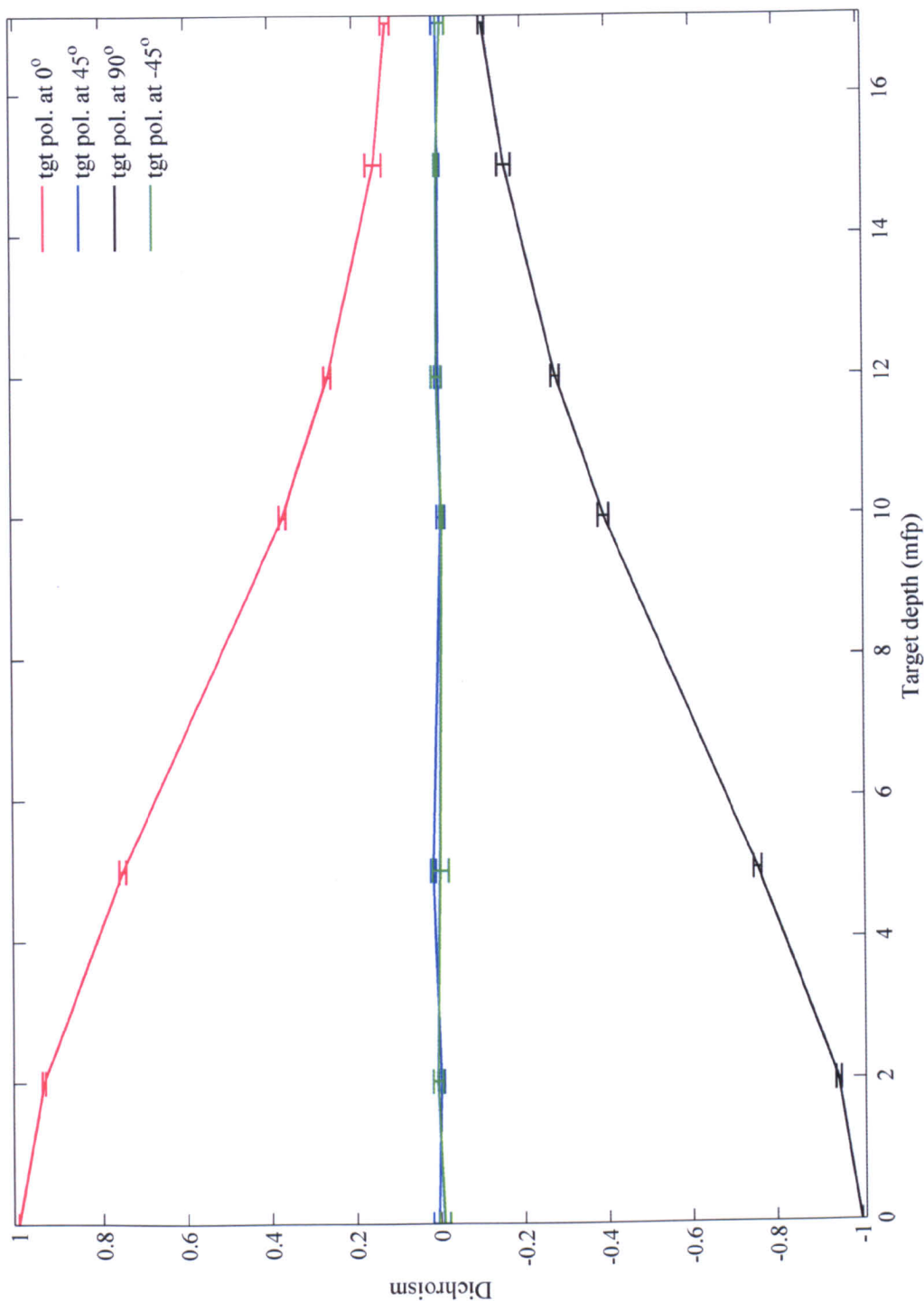
Figure 3.11: Monte Carlo simulations of quantitative ROPI linear dichroism measurements of a linear polarizer located within a scattering medium varying with depths at different polarization states with applying illumination / detection linearly polarized at 0° / 90° and 90° / 0°.
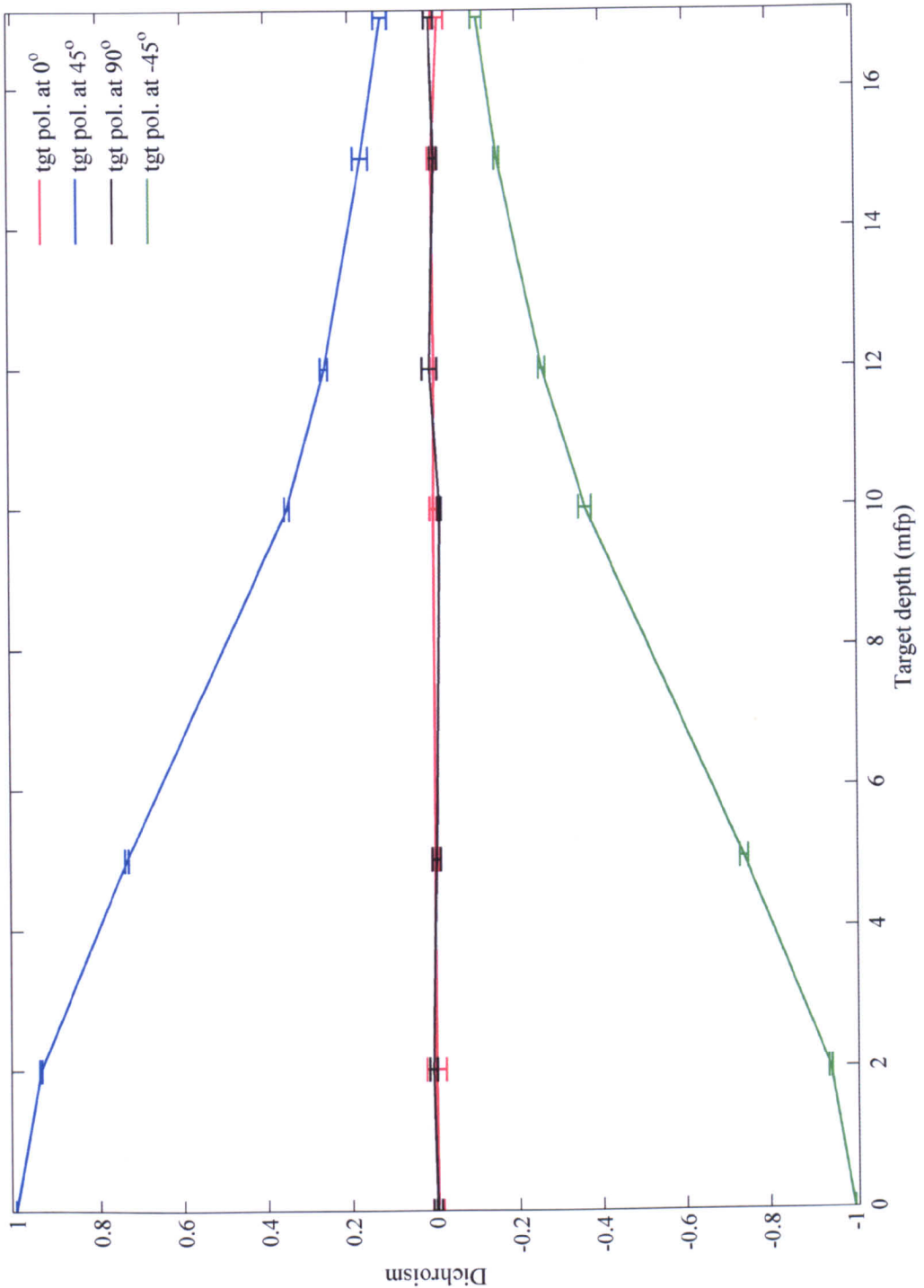
Figure 3.12: Monte Carlo simulations of quantitative ROPI linear dichroism measurements of a linear polarizer located within a scattering medium varying with depths at different polarization status with applying illumination / detection linearly polarized at 45° / -45° and -45° / 45°.
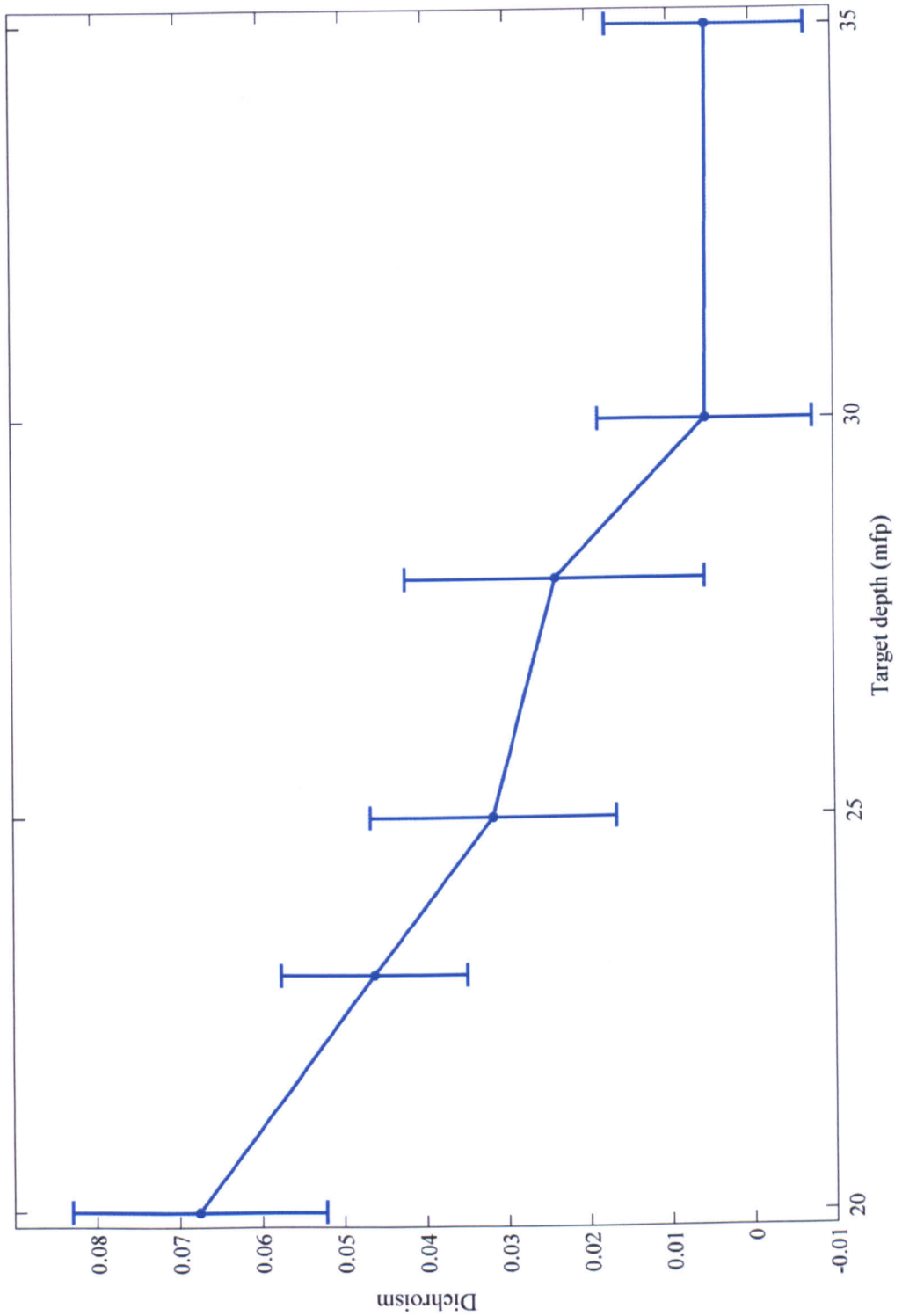
Figure 3.13: Illustration of the sensitivity limit of applying the ROPI technique for ideal measuring linear dichroism of a polarizing target within a scattering medium.

seen that the linear dichroism measurement at the depth of 0*mfp* is 1, which is to be expected from the Mueller calculus shown in chapter 2. As the target depth increases, it can be seen that the measured value decreases gradually towards to 0. As discussed for figure 3.9, this is due to the increase in scattering. Another notable feature of these line scans is the negative value of dichroism for depth=0*mfp* case adjacent to the target. This occurs because the polarization states of the illumination and the target are in one case co-aligned while in the other case are cross-aligned. This results in the photons that pass through the target and into the region behind the medium being different. Different intensities are detected outside the target region for the two images which contributes to a negative dichroism value. Although this feature occurs for all the line scans; it cannot be observed at other depths because it is masked by the effect of the increase in scattering.

Figures 3.11 and 3.12 show quantitatively how the linear dichroism measurement varies with depth with the target linearly polarized at 0°, 90°, 45° and -45° by applying the two sets of illumination / detection pairs linearly polarized at 0° / 90° & 90° / 0° (figure 3.11) and at 45° / -45° & -45° / 45° (figure 3.12) respectively. As the figures show, the maximum measurements are obtained when the target's polarization is set at 0° and 90°. The minimum (i.e. no linear dichroism) is obtained when the target is aligned at 45° and -45° for the illumination / detection pairs at 0° / 90° & 90° / 0°. These are the other way round for the case of using the illumination / detection pairs at 45° / -45° & -45° / 45°. All these results compare well with the expectations discussed based on the Mueller calculus in chapter 2. Depending on the depth, the maximum measurements for both cases vary from 1 towards to 0 due to the effects of the scattering. However, the minimum measurements (i.e. dichroism≅0) are relatively constant for all the depths. The slight variation is an indication of statistical noise. Ef-

fectively, the two cases are the same measurements but with a rotation of the whole system by 45°.

An important parameter to consider in evaluating the technique is the maximum depth to which sensitivity to linear dichroism can be observed. In the limit, the measured linear dichroism will reduce to 0 as the target is situated deeper within the medium. However, it is clear from figure 3.11 and 3.12 that, even for measurement at a depth=17*mfp* this value is greater than 0. To investigate this limit, depth measurements were extended as shown in figure 3.13. As the figure shows, further measurements are made with the target located at depths of 20, 23, 25, 28, 30 and 35*mfps* with the target aligned at 0° and with illumination / detection pairs polarized at 0° / 90° and 90° / 0°. As expected, the measurements reduce further with depth until reaching the depth of 30*mfps*. Nevertheless, although the value reached is not constantly 0 due to noise, it is around 0.005. Therefore, a depth of around 30*mfps* is believed to be the limit that the technique can be used to measure linear dichroism within the scattering medium.

3.4 Monte Carlo Simulations of *ROPI* Bire-fringence Measurements

According to the Mueller calculus given in chapter 2, to achieve measurement of the linear birefringence within a scattering medium using *ROPI*, back-illuminating photons must maintain linear polarization before passing through the target. However, there are only a very small proportion of the backscattered photons that travel within shallow depths that have their polarization state maintained. Therefore, it is difficult to measure linear birefringence using the *ROPI* technique. In this section, in order to

investigate the level of difficulty and further complete the evaluation of the *ROPI* technique, a birefringent target is considered in order to simulate measurement of linear birefringence within a scattering medium.

To measure linear birefringence, the orthogonal illumination / detection pairs must be separated by 45°. For maximum contrast, the target must possess a retardance of 180° and be located with the fast axis aligned to one of the illumination orientations at 0° or 45° or 90°. Therefore, in this study the birefringent target is a half wave plate (*HWP*) located at a depth of 0*mfp* within a scattering medium and orientated at 0° with the illumination / detection pairs linearly polarized at 0° / 90° and 45° / -45°. This provides the maximum birefringence that could be obtained.

In addition, the model is implemented slightly differently from that for the linear dichroism measurements in section 3.3. Here, each simulation runs 5 million photons, the medium is the same as that applied for the linear dichroism measurements, as specified in table 3.1, and the target is 40*mfps* wide. The illumination and detection areas are respectively 2048points × 2048points which corresponds to 512*mfps* × 512*mfps* and 128*bins* × 128*bins* with 1*mfp²* detection bins. The simulated images are shown in figure 3.14.

In figure 3.14, *a)* is the *ROPI* image of the target located at a depth of 0*mfp* and orientated at 0° within a scattering medium with illumination / detection linearly polarized at 0° / 90°; *b)* is the other *ROPI* image with illumination / detection linearly polarized at 45° / -45°; *c)* is the image of linear birefringence combined from images *a)* and *b)* following equation 2.35, and *d)* is the average line scan (averaged over 64 rows) on the *y* axis of the birefringence image in *c)* with error bars which is the standard deviation of the birefringence along the individual rows. This plot quantitatively represents

the maximum possible *ROPI* linear birefringence measured through the model. Each image corresponds to the size of 128*mfps* × 128*mfps*.
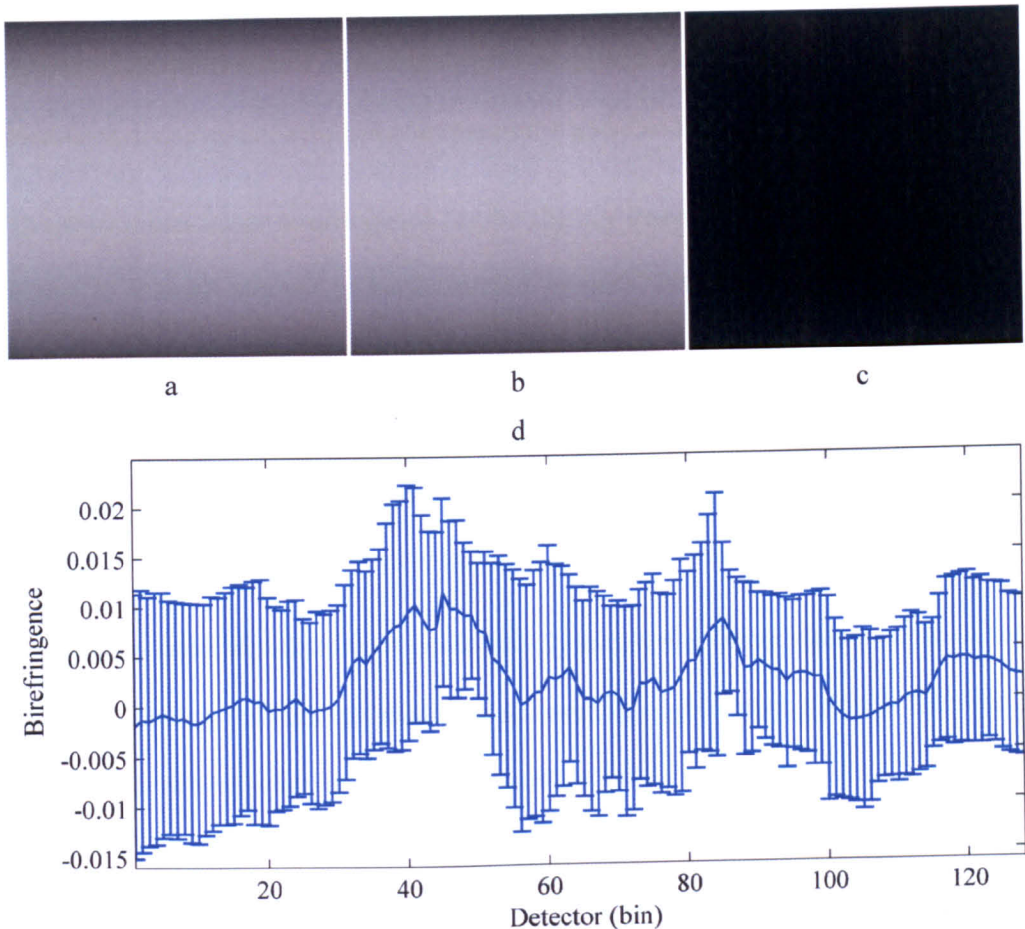
Figure 3.14: Demonstration of the MC simulation of quantitative linear birefringence measurement of a HWP located at the depth of 0mfp within a scattering medium and orientated at 0°. a) imaging with the illumination / detection linearly polarized at 0° / 90°, b) at 45° / -45°, c) the image of linear birefringence combined from a) and b), and d) the average line scan on y axis of the image in c). Each image corresponds to the size of 128mfps × 128mfps.

In both the images *a)* and *b)*, the target can hardly be seen, which indicates that most of the back-illuminating photons detected are randomly polarized and cannot be used to measure linear birefringence according to equation 2.27. However, from image *c)*, it is clear that birefringence signals from both edges of the target are present (ap-

proximately, detector bin = 44 and 84) although signals from the rest of the target are not. Figure 3.14*d)* shows that the maximum birefringence measured on the edges is less than 1% which is very small compared to the theoretical maximum of 100%. Furthermore, as the standard deviations shown are about twice that of the birefringence measured, those quantitative measurements are noisy and the accuracy is very poor.

The reason that linear birefringence can be slightly detected at the edges of the target is due to a small amount of backscattered photons that only travel within shallow depths and maintain their linear polarization as they pass through the target and which they only do once. The reasons that birefringence cannot be obtained from the rest of the target is because photons reaching the centre of the target will have undergone multiple scatters and therefore have lost their original polarization state.

As demonstrated, simulations of quantitatively measuring linear birefringence underlying a scattering medium can hardly be achieved through applying *ROPI*. The results presented here are mainly used for demonstration only.

3.5 Discussion and Summary

This work has involved modifications of a conventional *MC* model to realise a model that is able to simulate *ROPI*. The *ROPI* technique has been evaluated by applying the modified *MC* model to make quantitative measurements of linear dichroism and linear birefringence of a target within a scattering medium at different depths and orientations. In this section, a summary of each of the previous sections in the chapter is given along with a discussion.

Section 3.2 has described the modified *MC* model applied to the ideal study of the *ROPI* technique. The three modifications made are (a) turning the model from single

point illumination into full field illumination; (b) allowing the insertion of a polarizing target which changes the polarization properties and propagation direction of any photon that passes through it by applying a splitting process and (c) addition of the imaging system (i.e. *2-D* detection and imaging lens) to the model to allow imaging of the target within the scattering medium at different depths. The number of times a photon crosses the target plane is limited to 20. This has been shown to provide an appropriate trade-off of sufficient accuracy and computational efficiency.

Section 3.3 presents the evaluation of the *ROPI* technique in terms of quantitatively measuring linear dichroism within a scattering medium through applying the modified *MC* model. The measurements cover both the maximum and the minimum cases and include detecting a polarizing target located the depths up to 35*mfps* and linearly polarized at 0°, 90° 45° and -45° respectively. Results of the maximum measurements provide the variation of linear dichroism over a range of depths while the minimum measurements, which are relatively constant around 0, provide an indication of the noise floor. The depth of 30*mfps* is found to be the limit at which the technique can detect linear dichroism within the scattering medium.

Finally, quantitative measurement of linear birefringence within a scattering medium has been considered in section 3.4. This section illustrates the difficulties of applying the model for measuring linear birefringence with the *ROPI* technique. This is because back-illumination photons have to maintain linear polarization before passing through the target.

There are many research groups using *Monte Carlo* modelling [40; 60; 61; 69]. However, the model developed here, that can be applied for imaging a polarizing target embedded within a scattering medium using polarized light, is possibly unique, although ab-

sorbing and reflecting targets have been modelled [70; 72]. In addition, although the model is not ideal due to the assumption that all of the indexing photons have the same trajectories in order to perform full field illumination and that limited crossing points are applied for every trajectory to avoid computational inefficiency, it is considered reasonable to make these assumptions as described in section 3.2.

The model has been applied for investigating the *ROPI* technique ideally through linear dichroism and birefringence measurements. Results have shown that measurements meet the theoretical expectations based on Mueller calculus. The maximum sensitivity depth of 30*mfps* determined here corresponds to a depth of around 3.0*mm* within tissue according to the typical tissue parameters [95]. Absolute measurements of dichroism are dependent on the depth of the polarizing target within the medium due to scattering effects between the target and the output surface. To enable accurate quantification of the dichroism of the target, the model could possibly be used to provide a look up table for object depth and dichroism. However, determining whether this is a well-conditioned problem is an important area of future research. It is likely that additional measurements such as multiple wavelengths or different illumination conditions will be required to provide a well-conditioned solution.

In order to be able to measure linear birefringence using the *ROPI* technique, back-illuminating photons which maintain their linear polarization are necessary. Previous studies [79] have shown that linearly polarized light can probe depths of 34*mfps* and that deeper propagation (102*mfps*) can be obtained with circularly polarized light. However, the simulations presented here do not suggest this to be a feasible measurement with *ROPI*. Linear birefringence measurements might be achieved by modifying the model to operate in transmission mode although, of course, applications in

transmission mode are not preferred in practice as was discussed in chapter 1. Nevertheless, birefringence measurements will be shown in chapter 5 via experiments on a phantom target.

The *MC* model represents the ideal case of an isolated polarizing target embedded within a scattering medium. This is a reasonable approximation for applications in experiments on phantom targets; however, in practical applications such as the monitoring of collagen alignment within tissue, the situation will be more complicated as the entire volume probed by the light will affect the polarization. This will be the subject of future work to develop an inversion algorithm based on an appropriate model of the forward problem such as that developed by *Wang* and *Wang* [69] although this algorithm will need validation through comparison with histology. For the tissue imaging problem, the focus should be on a more accurate model of the structure of the tissue. Finally, to better simulate the phantom study, further refinements of the model could be performed such as making the polarisers non-ideal, the target of finite thickness or introducing surface reflections at the medium-target boundary. This is worthwhile for applications such as target detection in turbid water or imaging through fog where the model provides an accurate representation of the real world situation.

In conclusion, a modified *MC* model has been introduced to evaluate *ROPI*. This provides an understanding of the technique before moving onto experiments on phantom idealised targets and tissue studies. The model is substantially different from a conventional polarized light *MC* model as it performs imaging from full field illumination and includes the introduction of a target that can modify the polarization state of the light.

Chapter 4

Standard *ROPI* System: Design Characterization and Calibration

4.1 Introduction

As described in chapter 1, precise control of the orthogonal polarization states of illumination and detection is one of the key factors determining the performance of the *ROPI* technique. In this chapter, the standard *ROPI* system with manual control of the polarization states using Glan-Thompson (*GT*) polarisers is introduced.

The system is designed in both reflection and transmission modes and is used to perform the *ROPI* experiments shown in chapter 5. The reflection mode arrangement is preferred in clinical applications and is the main focus of this study. Characterization of the system design in this mode will be provided in detail. This includes describing the experimental setup and the essential calibrations in detail. Furthermore, problems of using conventional polarization difference imaging will also be shown. On the other hand, characterization of the system design in transmission mode will be provided with a description of the differences between those in the reflection mode system only as both the systems are similar but used to perform different experiments for different purposes.

This chapter provides design characterization and calibration of the standard *ROPI* experimental system used in this study. Sections 4.2 and 4.3 describe the system design in reflection and transmission modes respectively. Section 4.4 provides a discussion and conclusions.

4.2 The Reflection Mode System

In this section, the standard *ROPI* experimental system in reflection mode is characterized. Subsection 4.2.1 provides design of the setup that shows how the setup works and discusses all the required optical components. Furthermore, a description of the test sample including how the scattering medium and polarizing target are made is provided. Subsection 4.2.2 provides the system calibration required due to practical alignment issues and non-ideal components. Subsection 4.2.3 shows problems of performing the conventional polarization difference imaging.

4.2.1 Experimental Setup of the System

The standard *ROPI* experimental setup in reflection mode is shown in figure 4.1. Pictures of the real setup and components are shown in appendix C.

For the illumination arm, starting from the light source, a collimated and polarized light beam is emitted from a helium-neon (*He-Ne*) polarized laser (Power = 20*mW*, Wavelength = 632.8*nm*). This is firstly focused to a motor controlled rotating ground glass diffuser by a positive achromatic doublet lens (focal length = 50*mm*). The diffused light is collected by a second positive achromatic doublet lens (focal length = 50*mm*) and a collimated beam is generated. The collimated beam passes through an
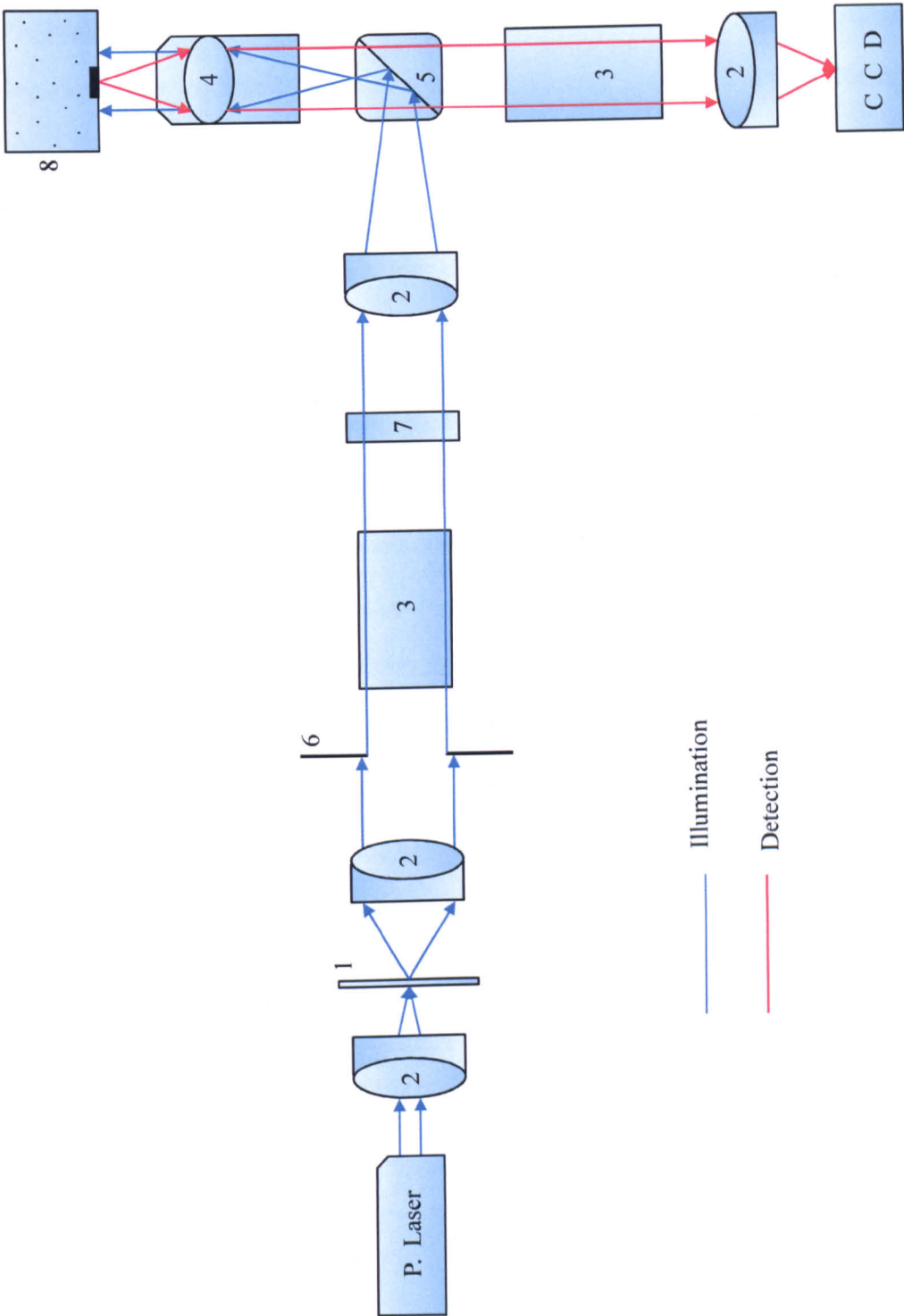
Figure 4.1: *Standard ROPI experimental setup in reflection mode. 1) Ground glass rotating diffuser, 2) Positive achromatic doublet lenses, 3) Glan-Thompson polarisers, 4) Infinite conjugate microscope objective, 5) Cube beam splitter, 6) Iris diaphragm, 7) Half-wave plate, 8) Sample.*

iris diaphragm, a *GT* polarizer and a half-wave plate which produces a linear polariza-

tion state in the required orientation. It is finally focused to the back focal plane of a

×4, numerical aperture (*NA*) = 0.1 infinite conjugate microscope objective via a cube

beam splitter (*BS*) in the reflection direction by the third positive achromatic doublet

lens (focal length = 60*mm*). This provides collimated uniform illumination to the

sample.

For the detection arm, backscattered photons from the sample are firstly collected by

the microscope objective. This light then passes through the same cube *BS* as in the

illumination arm in the transmission direction and through the second *GT* polarizer

which is aligned in the orthogonal polarization state to the illumination. Finally, an

image of the target embedded within the medium is formed on the charge-coupled

device (*CCD*) camera (*Hamamatsu ORCA ERII*) via the fourth positive achromatic

doublet lens (focal length = 50mm). Moreover, as shown in figure 4.2, the collimated

beams after being collected by the objective on the focal plane but not at the focal

point will be bent towards to the optical axis rather than parallel to the optical axis. As

the aperture size of the optical components including the objective, *BS, GT* polariser

and lens are not infinitely large, all those optics are required to be placed as close to

each other as possible in order to detect as many backscattered photons as possible.
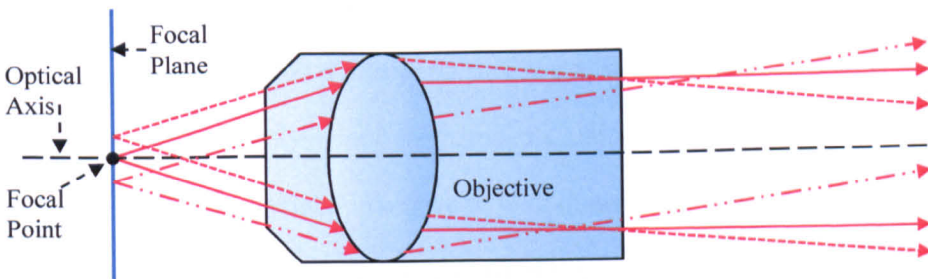
Figure 4.2: Photon paths after being collected by the objective on the focal plane at different positions.

In order to further understand the setup shown in figure 4.1, the rest of this subsection describes the function of each component. In addition, the sample is discussed, which not only provides the properties of the scattering medium and the target but also describes how the medium is made.

Sample

In this study, different samples have been used to investigate *ROPI* using the setup shown in figure 4.1. These include tissue phantoms, engineered tissue and real tissue samples. However, as the investigation is mainly performed by using the phantom sample, this will be described and discussed in detail here. The tissue samples (engineered and *ex-vivo*) will be described with the experiments in chapter 5.

The tissue phantom sample used in this study is an artificial sample which is purposely generated with the property of scattering photons only. Compared to the engineered and real tissue samples, the phantom sample has a much simplified homogeneous structure. This provides an easily controlled sample in terms of both its optical and geometric properties. In order to allow comparison of the experimental phantom results with those obtained from simulations in chapter 3, the tissue phantom has the same optical and physical properties as the simulated sample.

In the reflection mode experiments in this study, the tissue phantom sample is a polarizing target embedded within a scattering medium at different depths. The scattering medium is a mixture of polystyrene microspheres and de-ionized water (governed by *Mie* theory [58; 59]) and contained in a cuvette with dimensions of $45 \times 50mm^2$ (illuminated face) $\times 12mm$ (depth). The optical and physical properties of the medium are summarised by the parameters given in table 4.1. All the parameters have been dis-

cussed in chapter 3 except ρ, which is the density of the polystyrene microspheres and is used to calculate the quantity needed.

Parameters	Values
$g = <cos(\theta)>$	0.938
$\mu_s = N\sigma_s = NQ_sA$	$20\ mm^{-1}$
Q_s	3.373
μ_a	$3.0 \times 10^{-4}\ mm^{-1}$
$mfp = 1/\mu_s$	$0.05\ mm$
n_m	1.332
n_p	1.572
d	$1.4\ \mu m$
ρ	$1.003\ g/cm^3$
λ	$632.8\ nm$

Table 4.1: Optical and physical properties of the scattering medium for ROPI phantom experiments in reflection mode.

The scattering medium is made from 0.555g of polystyrene microspheres suspended in 100*ml* of pure water. These quantities are calculated based on equation 3.1 coupled with the microspheres parameters, d and ρ. Firstly, by using equation 3.1, the number of particles per μm^3 of the medium (N) required for the particular scattering coefficient ($\mu_s = 20mm^{-1}$) can be calculated. Therefore, for the medium volume of 100*ml* needed, the total number of particles required can be obtained. Secondly, by knowing the diameter (d) and density (ρ) of a particle, the volume and weight of a single particle can be calculated. Therefore, the total weight of microspheres can then be obtained. In order to uniformly mix the particles with water, an ultrasonic bath is used.

The test target is a piece of linear polariser with dimensions of $0.75\pm0.05mm$ (thickness) $\times$ 8.5*mm* (length) $\times$ $0.65\pm0.05mm$ (width). This is manually cut from a piece of

linear sheet polarizer (*Comar*) which is plastic laminated and has an extinction ratio

of 1×10^{-4} for the wavelength at 632.8*nm*. The target is embedded at different depths

within the scattering medium and orientated at 0° (horizontally).

To set the appropriate depth of the target within the medium, three adjustable stages

that control the positions of the cuvette and the target to 0.01*mm* resolution in x, y and

z directions are used. However, instead of adjusting the position of the target, the cu-

vette position is adjusted. This is to maintain the target at the focal plane of the objec-

tive in order to form clear images on the *CCD* camera. The target is fixed at the work-

ing distance (22*mm*) of the objective. A picture of this arrangement is shown in ap-

pendix C.

Light Source

There are three key factors that need to be considered when selecting a light source

for the system. These are device type, intensity and wavelength. In addition, safety,

cost and efficiency must also be taken into account.

The first factor regarding the choice of the source is between using a laser or an inco-

herent light source, such as a halogen lamp or LEDs. Comparing these light sources,

application of a laser provides not only monochromatic illumination but also a point

source which allows easier collimation and therefore light efficiency. Firstly, some of

the polarization optics including the scattering sample are strongly wavelength de-

pendent; therefore, monochromatic light is essential. This ensures more predictable

and more easily modelled scattering effects in the sample. In addition, wavelength

dependent effects, such as lens aberrations, variation of the *BS* reflection, transmis-

sion coefficients and variation of the sample's scattering and absorption are removed

by using monochromatic illumination. Secondly, using collimated beams, not only

simplifies alignment, but also can be used to generate a point light source on the diffuser (figure 4.1) and hence provides a collimated beam at the sample. In addition, in order to have high performance from the *BS* and *GT* polarisers, collimated input light is necessary. Therefore, it is clear that having a laser as the light source will increase the performance of the system. However, using a laser increases the cost of the system and more safety protection is required, especially if a technique is intended for clinical application. Nevertheless, the benefits of using a laser outweigh the drawbacks and therefore a laser (*Melles Griot*) is selected as the source.

It is advantageous to use the lowest intensity source possible to alleviate safety issues. However, in order to have enough backscattered light to form images, a reasonably high power laser has to be considered. By taking all the intensity responses of the components in the setup into account, a $20mW$ laser was selected. This provides an intensity of approximately $0.2mW$ over the area of 7.5mm in diameter being delivered to the sample after passing through all of the optics in the illumination path. Discussions about the effects of the components on the intensity will be provided later.

When selecting the wavelength, the absorption spectrum of the sample is of importance. The dominant spectra in skin tissue samples are haemoglobin and melanin. Therefore, to minimise the optical absorption, operation in the near infra red region is most appropriate. However, $632.8nm$ is selected due to the availability of a suitable source and the ease of use of visible light for alignment.

Diffuser

A motor controlled rotating ground glass diffuser is applied in front of the light source in order to break the coherence of the laser beam to remove speckles in the image. The ground glass was located at the focal point which is shared by the first and sec-

ond positive achromatic doublet lenses in order to have a collimated beam after the second lens. To produce the diffuser, diamond paste (particle size in $0.25\mu m$) was used to hand grind the glass. The smaller particles provides larger angles from the diffuser hence it is easier to destroy the coherence. The selected motor rotates at $7600 rpm$.

Positive Achromatic Doublet Lens

As described in figure 4.1, there are in total four positive achromatic doublet lenses used in the experimental setup. From illumination to detection, the first and second lenses are used to expand the collimated laser beam. Thereby, those two lenses have to be separated by a distance equal to the sum of the two focal lengths. However, the distance of the first lens to the laser does not really matter as the laser beam is collimated. The first lens is applied to focus the collimated laser beam onto the diffuser as a new point light source. The second lens is used to collect light from the point source and regenerate a collimated beam as required for the first *GT* polariser and the half-wave plate.

As an infinite conjugate objective is used and uniform illumination to the sample is required, a third lens is used to focus the collimated beam to the back focal point of the objective and generate a collimated beam after the objective. The location of the third lens depends on the back focal length of the objective and the focal length of the lens itself. The distance between the objective and the third lens equals the sum of those two focal lengths. The fourth lens is applied in the detection arm as a tube lens to act in conjunction with the objective lens to form an image on the *CCD* camera. The lens is located in front of the *CCD* camera at the position of one focal length away.

There are three main types of positive lenses to be chosen, which are double-convex lenses, plano-convex lenses and positive achromatic doublet lenses. The main differences between these three types of lenses are their abilities to reduce or eliminate the aberrations introduced by the lenses themselves, which result in different quality images. Figure 4.3 illustrates the ability of the three types of lenses to reduce the spherical aberration which means different rays do not focus at the same point in images [86; 88]. The positive achromatic doublet lenses are selected for imaging to reduce the effect of spherical aberration. In addition, chromatic aberration is also reduced by using achromatic doublets. Although this is not a benefit for this study as monochromatic light is used, later itterations of the system may potentially be multispectral and therefore this would prove highly beneficial.
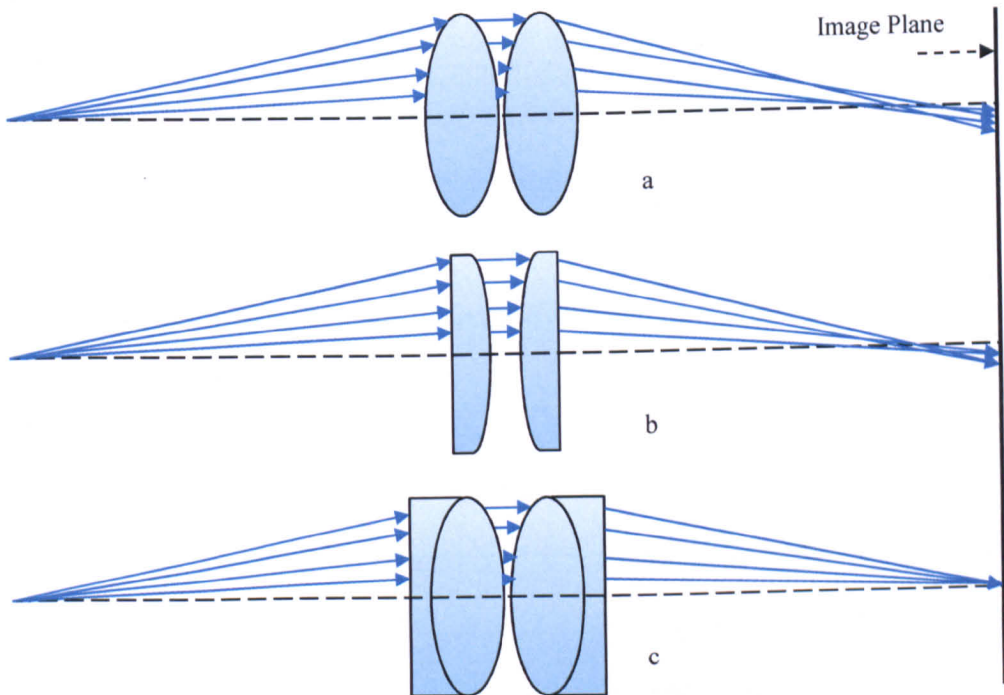
Figure 4.3: Illustrations of spherical aberration from different type of lens combined systems. a) double-convex lenses, b) plano-convex lenses, c) positive achromatic doublet lenses.

Iris Diaphragm

The iris diaphragm applied in the setup has a maximum aperture of 50*mm*. There are two reasons to apply the iris diaphragm in the system. Firstly, it is used to block stray diffused light which is not collected by the second achromatic doublet lens and which could otherwise be detected by the *CCD* camera or passed to the sample. Secondly, it is used to control the beam size to ensure that it passes through the optical components especially the *GT* polarisers as they have the smallest aperture size (8*mm* for clear aperture diameter) in the setup.

Glan-Thompson (GT) Polarisers and Half-Wave Plate (HWP)

As introduced in chapter 1, *ROPI* has the advantage of removing surface reflections from both the sample and the optics. It also removes superficially backscattered photons which do not travel deep enough in the medium to be de-polarized. This is vital for imaging the weak polarization signals from a target. The surface and superficial reflections would be too strong and dominate the images if they are not removed. Therefore, precisely controlling polarization states in the setup is a key aspect of the *ROPI* technique not only for measuring the polarization properties of the sample but also for rejecting surface reflections.

The simplified layout of the polarization controlling components in the experimental setup in reflection mode is shown in figure 4.4. As the figure shows, two *GT* polarisers and a zero order half-wave plate are used in the system to perform the polarization selection. GT_1 is applied to clear up the polarization state of the light emitted from the polarized laser. In a simple characterization experiment, inclusion of GT_1 increases the degree of linear polarization (*DOP*) of light that would be incident on the *HWP* from 0.999574 to 0.999992. This is approximately two orders of magnitude difference

(10^{-6} vs. 10^{-4}) in terms of the ratio of cross-polarized detection to co-polarized detection. The *DOP* is calculated as a ratio of the difference of the co- and cross-polarized detections to their sum. The axis orientation of GT_1 is permanently aligned with that of the laser in order to provide the maximum illumination intensity.
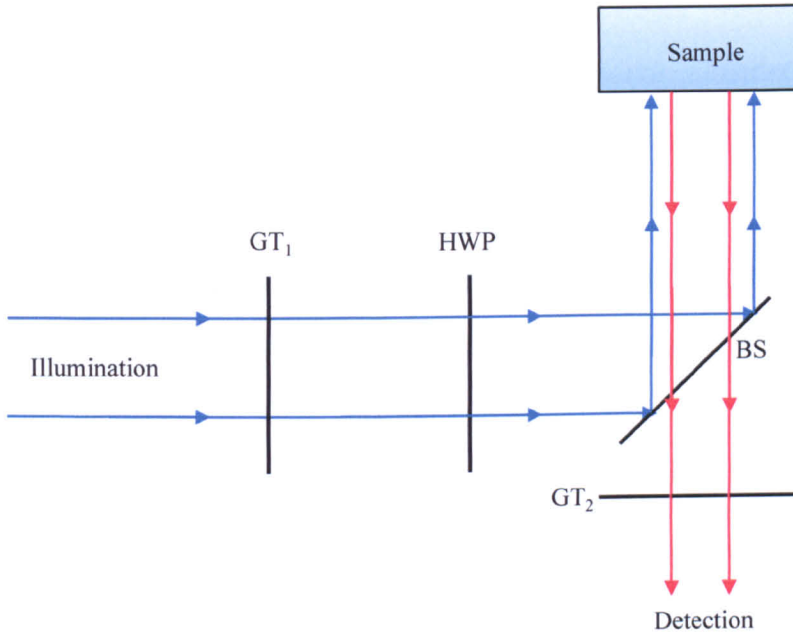
Figure 4.4: The simplified layout of the polarization optics in the standard experimental setup in reflection mode. GT: Glan-Thompson polarizer; HWP: half-wave plate; BS: beam splitter.

HWP delays the phase of one of the polarization components (i.e. resolved wave along either the fast or slow axis) by 180° when linearly polarized light passes through it. The polarization state will be symmetrical by either the fast or slow axis of the *HWP*. Therefore, *HWP* can be used to rotate the linear polarization state over the full range from 0° to 180° by rotating the *HWP* from 0° to 90° [86]. In this study, a *HWP* is applied to select the polarization state of the illumination to be either co-aligned or orthogonally aligned to the polarization state of the target embedded inside the sample.

GT_2 is applied to provide discrimination at the output. Its axis is always rotated to be orthogonal to the polarization state of the illumination (i.e. the polarization states of resultant light after passing through GT_2 and *HWP* are always orthogonal to each other).

In order to achieve good polarization sensitivity whilst effectively removing surface and superficial reflections, a polariser with a good extinction ratio is needed. Both *GT* polarisers (*Linos Photonics, 03-3219*) have a *8mm* clear aperture diameter; extinction ratio = 1×10^{-6}; length = 25.4*mm* and outer diameter = 25*mm*. They are designed for applications in the visible wavelength range. The zero order quartz *HWP* (*Edmund Optics, NT43-701*) has clear aperture = 15*mm* in diameter and operates at 632.8*mm*. Compared to a multiple order wave plate, the zero order wave plate has an increased bandwidth and a lower sensitivity to temperature changes. According to the data sheet, a ±2% change from the design wavelength will cause only a minor change in the retardance of a zero order wave plate. However, with a multiple order wave plate, a ±1% change from the designed wavelength will cause a considerable change in the retardance. Furthermore, a zero order wave plate can provide less than a 10% change in retardance over a range of ±10° incident angles.

Ideally, a collimated beam is supplied to both the *GT* polarisers and *HWP* in order to have optimum performance. As shown in figures 4.1 and 4.2, GT_1 and the *HWP* are under this condition but GT_2 is not as light is diverging from the sample. However, the largest divergence angle is 11.3° (calculated by using the focal length and the *NA* of the objective along with the photon paths shown in figure 4.2). According to the datasheet, the performance is not significantly affected for a pass angle < 15°. Finally, two rotating mounts with a precise control down to 5" (i.e. 0.083°) were chosen (*Melles Griot, 07-HPT-731*) for rotation of *HWP* and GT_2.

Infinite Conjugate Microscope Objective

The objective is used to collect backscattered photons from the sample and, in conjunction with the tube lens, form images of the target embedded within the scattering medium. The *NA* is an important parameter to be considered, which determines the total amount of backscattered photons to be collected and the image resolution. As illustrated in figure 4.5 and using equation 4.1, the *NA* is dependent on the diameter (*D*) of the lenses, the front focal length (*f*) and refractive index (*n*) of the working environment. (It should be noted that figure 4.5 only shows the effective construction of an objective. In reality, there are generally multiple lenses required to construct an objective). As *D* and *n* are usually fixed, a small *f* (hence a small working distance (*WD*)) is required if a high *NA* is needed. This suggests that the distance between the sample and objective is short. As the phantom experiments in this study are investigating a target within a scattering medium at different depths, a relatively long distance is required. Therefore, in order to have long *WD*, a low *NA* objective needs to be used. Although it is possible to have a high *NA* objective with long *WD*, such components are generally expensive.
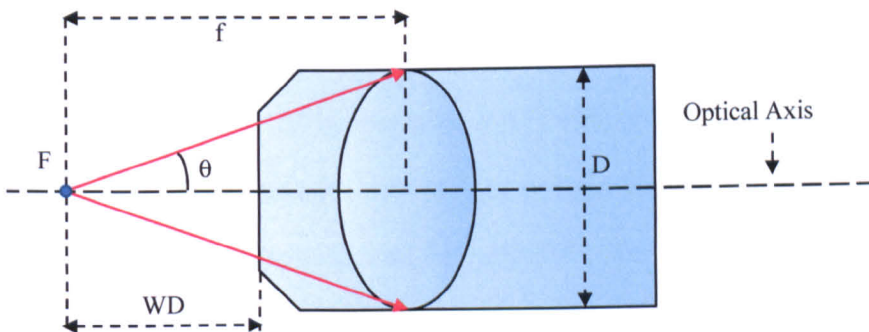
Figure 4.5: Numerical aperture of an objective. F: focal point; f: front focal length; D: diameter of the lenses; θ: half angle of the maximum cone of light that can enter the lenses; WD: working distance of the objective.

$$NA = n\sin(\theta) \simeq n\tan(\theta) = \frac{D}{2f} \qquad (4.1)$$

Another important parameter when selecting an objective is whether it is infinite conjugate or not. Infinite conjugate objectives are optimised to produce a collimated beam while finite conjugate objectives are designed to produce an intermediate image to be reimaged. Infinite conjugate operation is advantageous in this system to minimise the angles incident on GT_2 and the *BS*. By taking all the parameters discussed into account along with cost, an infinite conjugate objective (*Thorlabs, RMS4×*) is used in this study. The main parameters are M (magnification) = 4×, $WD = 22mm$ and $NA = 0.1$.

Cube Beam Splitter (BS)

One of the main advantages of *ROPI* is the ability to significantly reduce surface reflections from both the sample and the optical components. Thereby, instead of using an off-axis system to reduce surface reflections, a compact co-axial system has been designed. However, for a co-axial system, a *BS* has to be applied in order to separate the illumination and detection beams. In this study, a non-polarized cube *BS* with 50:50 splitting ratio is used.

As shown in figure 4.1, the *BS* is orientated at 45° with respect to the optical axis of the setup after the third achromatic doublet. The reasons for orientating the *BS* at 45° are: (i) the design of the *BS* is optimised for operation under the condition of applying perpendicularly collimated illumination, which can only be achieved by locating the *BS* at 45°; (ii) it separates the illumination and detection beams orthogonally, which allows the system to be more compact and easily aligned. However, as shown in figures 4.1 and 4.2, for both illumination and detection arms, neither of them has a col-

limated beam input to the *BS*. This reduces the quality of the experiment measure-
ments as precisely controlled polarization states are important for *ROPI*. Furthermore,
this is also one of the reasons that only $0°$ and $90°$ polarized illuminations are applied
in reflection mode in this study. Calibration of the polarization effects introduced by
the *BS* is discussed in the next subsection.

The differences in beam path for cube, plate and pellicle *BS*s are illustrated in figure
4.6. The transmitted beam direction is co-axial to the input direction except for the
case of the plate *BS*, where a lateral displacement due to refraction occurs.
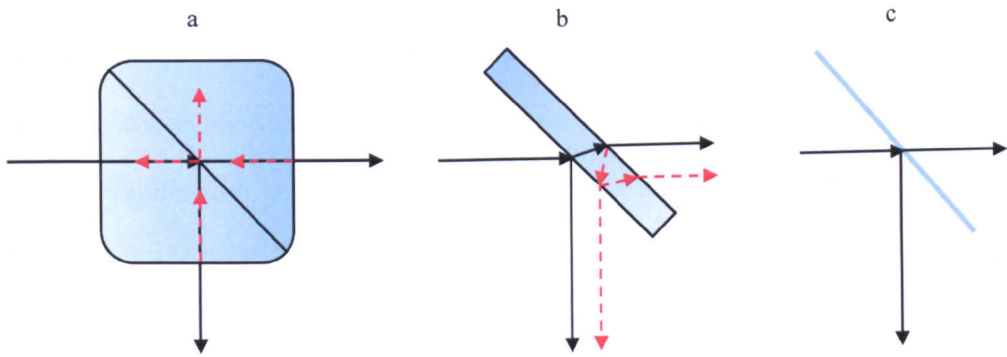
*Figure 4.6: Transmission, reflection (black solid lines) and first-time internal reflec-
tion (red dash lines) beam paths after passing different type of beam splitters located
at 45° (a: cube BS, b: plate BS, c: pellicle BS).*

Different internal reflections exist for all the different types of *BS*. However, the di-
rection of the internal reflections depends on the angle of the surfaces with respect to
the optical axis. For the pellicle component, the internal reflections can be ignored as
it is thin enough so as not to be observed as a separate path. For the cube *BS*, the sur-
face of the *BS* is perpendicular to the input beam, so internal reflection beams will
travel along either the reflection or the transmission direction. For the plate case, as
the surfaces of the *BS* are at $45°$, internal reflections will follow *Snell's* law [86]. Fur-
thermore, as refraction occur for the internal reflection beams as well; another two

beams emerge from the *BS*, which are parallel to the reflection and transmission beams respectively as indicated in figure 4.6b by the red dashed line.

As discussed, a pellicle *BS* seems the best choice for this study as there are no internal reflections and the transmission direction is not changed. However, normally, the pellicle *BS* is made of metal materials (complex refractive index) whilst the cube and plate *BS*s are made of dielectric materials (real refractive index). Therefore, a linear polarization state will be changed slightly to an elliptical one after passing through a pellicle *BS* for both reflection and transmission beams. The imaginary part of the refractive index introduces a phase difference for the *s*- and *p*- polarized components according to *Fresnel's* equations [86]. However, this will not occur for both the cube and plate *BS*s as their refractive indices are real. As careful control of the polarization state of illumination is key to *ROPI*, the pellicle *BS* is not the best choice for this study.

The cube *BS* is chosen as the direction of transmission and the internal reflections are not changed. The plate *BS* is not used as both the directions of transmission and internal reflections are slightly changed, which makes the setup alignment more difficult.

As reflection and transmission coefficients for the *s*- and *p*- polarized components of the *BS* are different; the intensities of the reflection and transmission beams from different polarized inputs will be different as well. Therefore, some form of calibration is needed. The calibration of the system will be described in the next subsection.

Charge Coupled Device (CCD) Camera

In *ROPI*, the main issue with the imaging camera is the ability to measure a small polarization difference signal on a large background. Therefore, the main properties to

be considered when selecting a *CCD* camera are the sensitivity and dynamic range (dictated by the full well capacity and the minimum detectable signal). In addition, the spectral response in terms of quantum efficiency (*QE*) and the range of exposure times are important and must also be considered.

By taking all the design considerations into account and the availability of cameras within the group, the *CCD* camera finally used in the system is the *Hamamatsu ORCA ERII*. The camera has 12-*bit* digitisation and has 1344×1024 *pixels* at a pitch of 6.45*μm*. The well capacity of a single pixel is 18000 *electrons* and the light sensitive area (fill factor) is 100%. The electronic shutter exposure time provided can be controlled between 134*μs* and 10*s*. The dark current is 0.1*electrons/pixel/s* and the read out noise is 6 *electrons*. The spectral response in terms of quantum efficiency (*QE*) vs. wavelength is shown in figure 4.7.
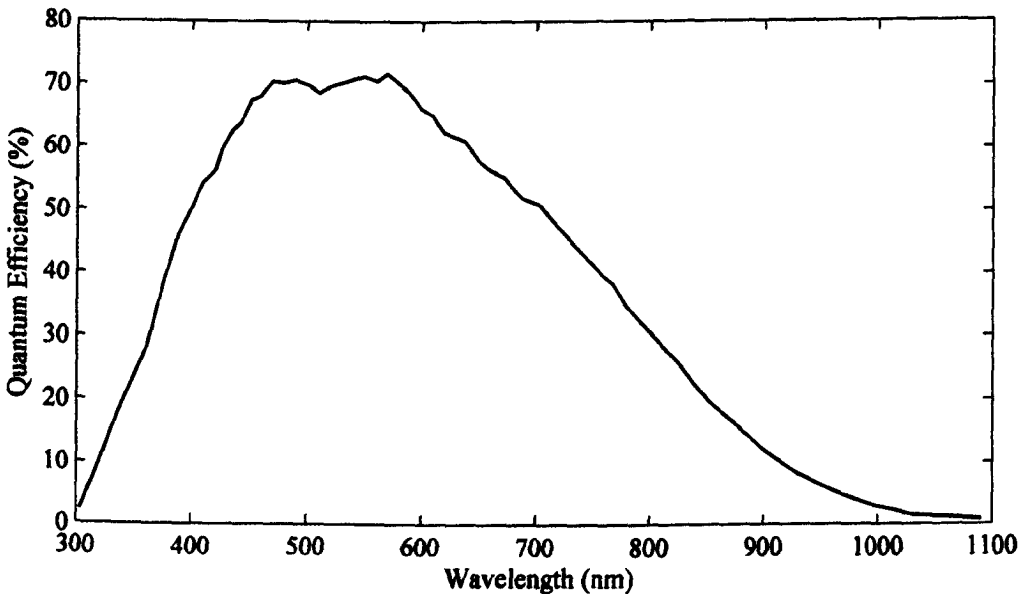
Figure 4.7: Spectral response characteristic of the ORCA CCD camera.

QE is the percentage of photons that are actually detected as not every photon falling onto a detector will actually be detected and converted into an electron. As shown in

figure 4.7, the *QE* of the *ORCA CCD* at the applied wavelength of 632.8*nm* is about

65%. This is considered as a high compared to standard *CCDs* which usually achieve

a *QE* of around 30% [96].

Grey levels is a term used to describe the resolution of the analogue to digital (*A/D*)

converter. This indicates the number of discrete spaces available to actually store ana-

logue photons/signals as digital values after digitalisation into the *CCD* detector, i.e. it

is the actual information that can be stored in the camera. Normally this is represented

by *CCD bits* (*n*) in the form of 2^n as the values are usually stored electronically in bi-

nary form. Thereby, the 12-*bit CCD* camera applied in the system provides 4096 grey

levels. This ensures that there are enough grey levels available to represent the target

without quantization noise becoming too great as the polarization difference signal

from the target is very weak compared to the signal from the surrounding medium.

Full well capacity is the maximum number of electrons that can be stored in a single

pixel before saturation. The full well capacity can be used to estimate the number of

photons required to saturate the camera by dividing the fill factor and *QE*. Fill factor

is the percentage of a pixel area that can be used and it is independent on wavelength.

SNR is used to characterise the detection capability of the *CCD* camera. It is defined

by the ratio of the light signal (*S*) to the sum of the noise signals (*N_{total}*) and is nor-

mally expressed in the unit of decibels (*dB*) as shown in equation 4.2.

$$SNR_{(dB)} = 20\log_{10}\frac{S}{N_{total}} \tag{4.2}$$

S is normally the number of signal electrons generating by the illuminating photons.

N_{total} is composed of shot noise (*N_s*), dark current (*N_d*) and read out noise (*N_r*). *N_s* is an

inherent noise which cannot be overcome. It comes from incoming photons and is normally calculated as the square root of S. N_d comes from thermally generated electrons due to the temperature at which the CCD is operated. This noise can be significantly reduced by cooling. N_r is the noise that originates from the Readout process which is the conversion of the electrons in each pixel to a voltage on the CCD output node. Faster readout speeds will lead to a higher read out noise. [96; 97; 98]

The dynamic range of a CCD detector is usually discussed in terms of the difference between the minimum detectable signal and the maximum number of electrons that can be stored in the same image. For instance, for the extreme case, the maximum number of photons that can be stored in a CCD pixel is the full well capacity. The minimum detectable signal is limited by shot noise and read out noise. The dynamic range quoted by the manufacturer is 3000:1. However, this only considers the read out noise and neglects the fundamental shot noise.

The CCD camera is controlled through a PC using a $Firewire$ interface card. This allows adjustment of many aspects of the camera's functionality including the exposure time and sub-array pixel binning of the detector array. These values can be adjusted for the different wavelengths to ensure that the maximum number of levels are used in forming the detected images. The CCD detector is located at the focal plane of the fourth positive achromatic doublet lens.

For the preliminary $ROPI$ experiments presented in the next chapter (section 5.2), a (*Kodak MegaPlus ES 1.0*) CCD camera was used in the system. The detector has 10-*bit* digitisation and has a resolution of 1008×1018 *pixels* at a pitch of 9μm. The well capacity of a single pixel is 15000 *electrons* and the fill factor is 55%. The electronic shutter exposure time can be controlled between 127μs and 64.872ms. The spectral

response in terms of *QE* vs. wavelength is shown in figure 4.8. The additional *QE*,

well capacity, extended exposure times and bit depth offered by the *ORCA* camera

prompted its replacement with the *Kodak CCD* for the tissue experiments.
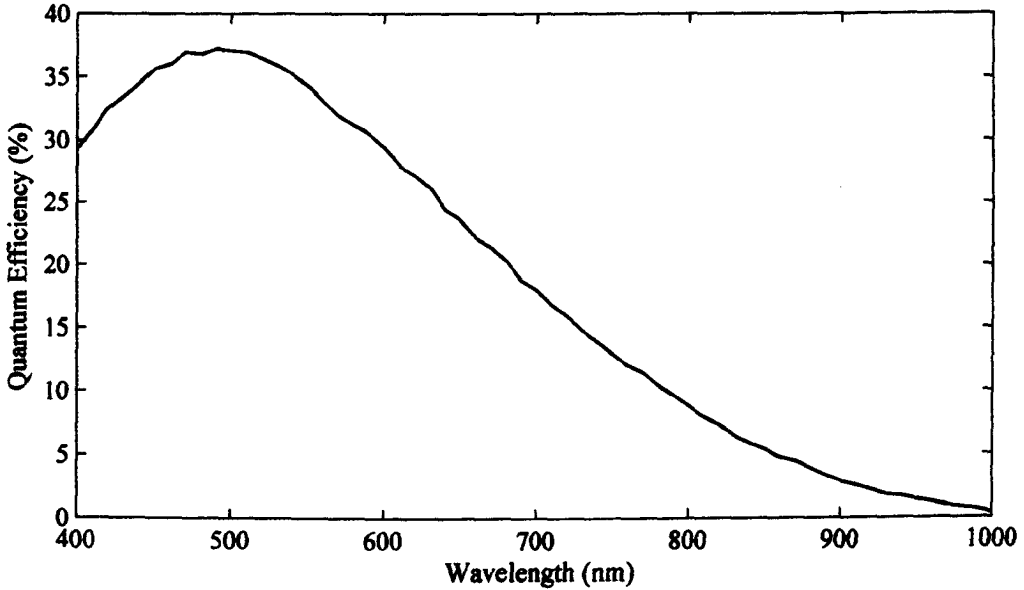
Figure 4.8: Spectral response characteristic of the MegaPlus CCD camera.

4.2.2 Calibration of the System

One of the important issues with the system is the change in beam properties caused

by the *BS*. This subsection discusses the calibration applied to overcome this problem.

Based on *Fresnel's* equations [86; 88], when a linearly polarized beam passes through an

optical component, the polarization state and intensity of the reflected and transmitted

beams are determined by the phase and amplitude differences between the *s*- and *p*-

polarized components of the reflection and transmission coefficients (r_s, r_p, t_s and t_p).

The phase differences between the *s*- and *p*- polarization components cause the po-

larization state to be changed from linear to elliptical. The amplitude differences

cause the polarization state to be changed from one linear state to another linear state

and the overall intensity to be reduced. As the coefficients of the *BS* which is used in the setup shown in figure 4.1 are different (i.e. $r_s \neq r_p$ and $t_s \neq t_p$) in both phase and amplitude, the polarization state and intensity of the illumination after passing through the *BS* are modified.

The modification of intensity and polarization state varies with different incident states. In addition, due to the non-collimated illumination of the *BS* (as the coefficients also vary with input angles); the modifications are not uniform across the beam. Furthermore, when the setup is not ideally aligned, stray internal reflections from optical components also result in the spatial distribution of the intensity being non-uniform. Therefore, in order to perform *ROPI* in the setup, calibrations to account for the modification of the illumination polarization and intensity are needed.

In the remainder of this subsection, the differences in the *Fresnel* coefficients and their variation with input angle and polarization state are discussed. Also, the two stages in the required calibration for polarization and intensity are described.

Investigation and Illustration of the BS' Reflection and Transmission Coefficients

A *BS* is usually constructed by a ground glass substrate coated with different layers[99]. Each layer has a different material and thickness depending on the specifications required. Therefore, the reflection and transmission coefficients for *s*- and *p*-polarized components (r_s, r_p, t_s and t_p) of the *BS* depend on the following layer specifications: thicknesses of the coated layers, $d(s)$, complex refractive indices of the layers $N(s)$, wavelength of the beam, λ, and input angle of the beam, ϕ. For a one layer coated *BS*, where the layer is located between the surfaces of air and the substrate, the relationship between the r_s and the layer specifications can be expressed by equation 4.3[99].

Similarly, r_p, t_s and t_p can be expressed in a similar form. If more coated layers are added; equation 4.3 would be extended to include higher order terms [99].

$$r_s = \frac{r_{01s} + r_{12s}e^{-j2\beta}}{1 + r_{01s}r_{12s}e^{-j2\beta}} \qquad (4.3)$$

$$\beta = 2\pi \left(\frac{d}{\lambda}\right)\left(N_1^2 - N_2^2 \sin\phi\right)^{\frac{1}{2}} \qquad (4.4)$$

$$N = n - jk \qquad (4.5)$$

r_{01s} and r_{12s} are the sub-reflection coefficients between the surfaces of air and the coated layer and between the surfaces of the coated layer and the substrate respectively. These can be generated from *Fresnel's* equations. β is film phase thickness which is expressed by equation 4.4. N_0 and N_1 are the complex refractive indices of air and the coated layer respectively whose general form is expressed as equation 4.5. n is the real part which only results in changing the amplitude. k is the imaginary part (extinction coefficient) which causes changes of both the amplitude and phase of the coefficient due to absorption, surface roughness, anisotropy and inhomogeneities of the layer. k also varies with input polarization state.

Equations 4.3-4.5 show that: (i) from *Fresnel's* equations, as sub-coefficients are different for r_s, r_p, t_s and t_p, clearly, $r_s \neq r_p$ and $t_s \neq t_p$ in terms of both phase and amplitude. This can be seen in figures 4.9 and 4.10 provided by the manufacturer of the *BS*. Figure 4.9 shows the phase shift between *s*- and *p*- components of the reflection and transmission coefficients vary with wavelength. Figure 4.10 shows how the transmittance and reflectance of *s*- and *p*- components, which are calculated as $|r_s|^2$, $|r_p|^2$, $|t_s|^2$ and $|t_p|^2$, vary with wavelength. (ii) Even if all the coated layers are dielectric (i.e.

$N=n$), r_s, r_p, t_s and t_p can still have imaginary parts as they also depend on d, λ and ϕ. (iii) These coefficients vary with different input angles. Therefore, the polarization state and intensity of illumination after passing through the BS will be modified and the distribution is not uniform.
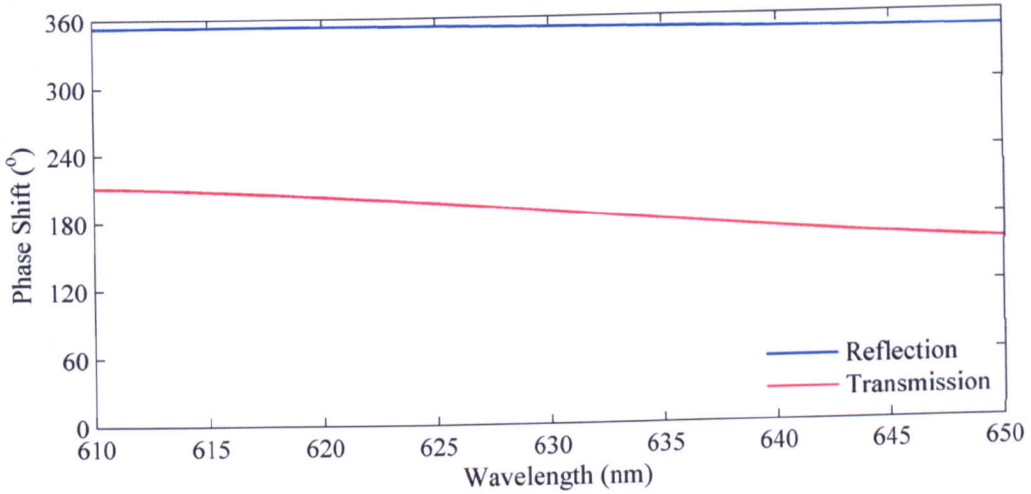
Figure 4.9: Phase differences between s- and p-polarized components of the reflection and transmission coefficients of the BS. (Source: Melles Griot).
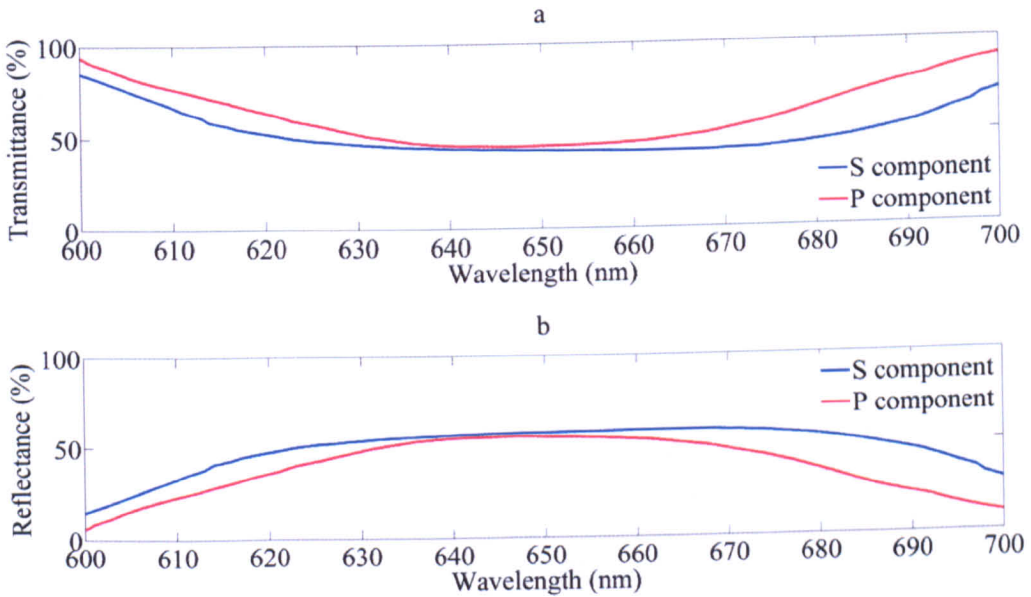
Figure 4.10: Transmittance (a) and reflectance (b) of the s- and p-polarized components of the BS. (Source: Melles Griot).

In order to show how different linear polarization states are modified by passing through the *BS* in both reflection and transmission directions, a test experiment was carried out using the simple setup shown in figure 4.11. GT_1 purifies the illumination polarization state; *HWP* controls the full range of linear polarization states from $0°$ to $90°$ in steps of $10°$. GT_2 is rotated to give the maximum and minimum intensity for every polarization state. The rejection ratio is calculated by the minimum over maximum. Results are shown in figure 4.12.
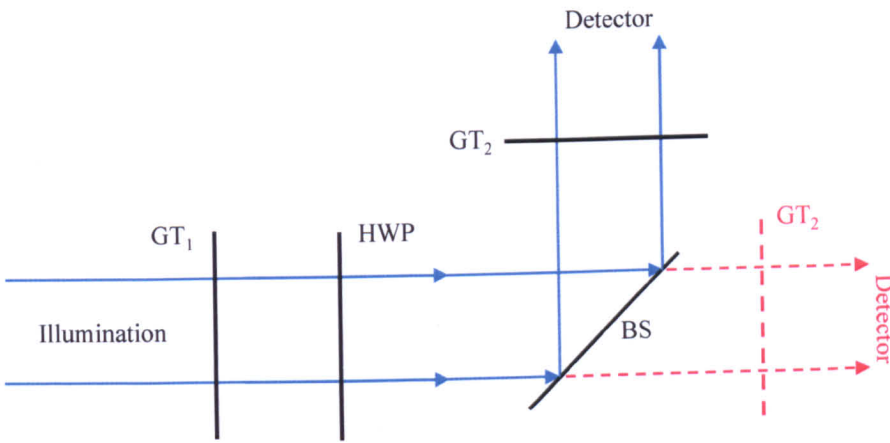
Figure 4.11: Experimental setup for testing the full range of linear polarization states changed by the BS in reflection (solid blue line) and transmission (dash red line) directions. GT, Glan-Thompson polariser; BS, beam splitter; HWP, half-wave plate.

It is clearly shown that at a wavelength of 632.8*nm*, the rejection ratios obtained in both reflection and transmission directions increase from around 10^{-5} at the illumination polarization states of $0°$ and $90°$ to around 10^{-2} at $50°$. As the extinction ratio of the *GT* polarisers is 10^{-6}, the results suggest that (i) different linear input polarization states are modified differently by the *BS*; (ii) the linear polarization states are modified into elliptically polarized states and the effect increases from $0°$ to $45°$ and decreases back to $90°$; (iii) the phases of the coefficients (r_s, r_p, t_s and t_p) of the *BS* vary with input polarization states. Furthermore, as good rejection ratios (small values) are

required for the technique, based on those rejection ratios shown in figure 4.12, only

the linear polarization states of 0° and 90°, which are the least modified by the *BS*, are

used in the setup shown in figure 4.1. This is justified in the phantom experiments as

the alignment of the target is known.
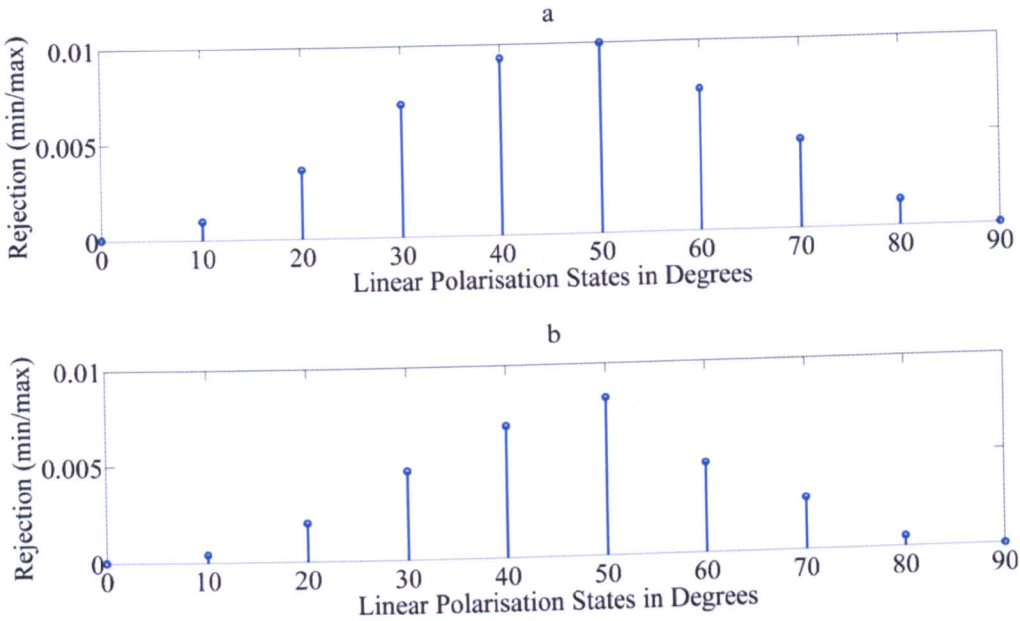
Figure 4.12: Test results of rejections of the full-range of linear polarization states after passing through the BS in reflection (a) and transmission (b) directions.

Calibration of Polarization States

As discussed, although only the linear polarization states of 0° and 90° are used in the

setup, the polarization states are still slightly modified after passing through all the

optical components. In order to find the orientations of the *HWP* and *GT₂* that provide

the highest rejection ratios (smallest values), a calibration is performed. Based on the

setup shown in figure 4.1, the axis orientations of the *HWP*, which are required to

provide the 0° and 90° linearly polarized illuminations, can be firstly obtained before

passing through the rest of the setup. Secondly, by replacing the sample with a mirror,

the orientations of *GT₂*, which are required to provide the highest rejection ratios with

respect to the 0° and 90° illuminations, can be obtained. This is achieved by rotating GT_2 until the minimum intensity is obtained. The calibration results are summarized in table 4.2.

Parameters	Linear Polarization States (illumination / detection)	
	0° / 90°	90° / 0°
Illumination (*HWP*)	51°30"	6°30"
Detection (*GT₂*)	152°50"	61°45"
Rejection Ratio	5.31×10^{-4}	5.78×10^{-4}

Table 4.2: Calibration results of the illumination and detection linear polarization states applied for standard ROPI experiments in reflection mode.

It should be noted that as the optical axes of *HWP* and GT_2 are randomly aligned to the rotating mounts, the degree numbers shown in the table are the reading numbers equivalent to 0° and 90° polarization states. Therefore, comparison can only be performed between either the illumination orientations or the detection orientations (in rows) but cannot be performed between the illumination and detection (in columns). As the table shows, it is clear that the orientations of GT_2 are not exactly 90° different. This further confirms that the polarization states are modified after passing through all the optical components.

Moreover, the rejection ratios for the two cases are slightly different. This is because different polarization states are modified differently as discussed. These rejection ratios are the best that could be obtained in the system. As these rejection ratios will result in a much lower measurement error than the error introduced due to noise on detection (inverse of the *SNR* (due to shot noise) $\cong 10^{-2}$), this performance is deemed adequate.

Calibration of Intensity

As discussed, the effects on the intensity includes: (i) the intensity distribution is non-uniform spatially across the illumination and (ii) different overall intensities are obtained with different input polarization states. The first effect is due to the variation of r_s, r_p, t_s and t_p of the *BS* with incident angle, the second is due to $r_s \neq r_p$ and $t_s \neq t_p$. This is shown by equation 4.6 which is generated based on the measurement definition shown in equation 2.19. k_{co} and k_{cros} are constant coefficients and represent the intensity difference between the *co-* and *cross*-polarized detection images due to variation in the *Fresnel* coefficients. It should be noted that *co-* and *cross-* represent polarization states of the target and detection are aligned or orthogonal respectively, illumination and detection are always orthogonal in *ROPI*.

$$L. \; Dichroism_{before \; cali.} = \frac{k_{co} Im_{co} - k_{cross} Im_{cross}}{k_{co} Im_{co} + k_{cross} Im_{cross}}$$

$$\neq \frac{Im_{co} - Im_{cross}}{Im_{co} + Im_{cross}} \qquad (if \; k_{co} \neq k_{rass})$$

(4.6)

Therefore, in order to accurately perform *ROPI*, an intensity calibration is required. The calibration is performed by normalising the *ROPI* images (Im_{co} and Im_{cross}) by the pure background images (BG_{co} and BG_{cross}) respectively before calculating the measurement value. The background images are obtained from the scattering medium only and taken under the same conditions as those applied for the *ROPI* images (same polarization states of illumination and detection, imaging integration time, and cuvette position). This removes any overall intensity difference and any variation in the lateral intensity distribution. This is further illustrated mathematically by equation 4.7 and graphically by figures 4.13 and 4.14. The calibration is repeated for each *ROPI* image.

$$L.\,Dichroism_{after\ cali} = \frac{\dfrac{k_{co}Im_{co}}{BG_{co}} - \dfrac{k_{cross}Im_{cross}}{BG_{cross}}}{\dfrac{k_{co}Im_{co}}{BG_{co}} + \dfrac{k_{cross}Im_{cross}}{BG_{cross}}}$$

$$= \frac{\dfrac{k_{co}Im_{co}}{k_{co}BG} - \dfrac{k_{cross}Im_{cross}}{k_{cross}BG}}{\dfrac{k_{co}Im_{co}}{k_{co}BG} + \dfrac{k_{cross}Im_{cross}}{k_{cross}BG}} \tag{4.7}$$

$$= \frac{Im_{co} - Im_{cross}}{Im_{co} + Im_{cross}} \qquad \left(\begin{array}{l} BG_{co} = k_{co}BG \\ BG_{cross} = k_{cross}BG \end{array}\right)$$

Equation 4.7 demonstrates the measurement value after the normalised calibration is the same as that calculated from the definition given in equation 2.19. Figure 4.13 demonstrates a pair of pure background images for the calibration. It clearly shows that the intensities from both images are slightly different. Figure 4.14 shows the line scans of the measurement images of a polarizing target before and after the calibration. As shown, the intensity distribution before the calibration is non-symmetrical and after the calibration it is symmetrical.
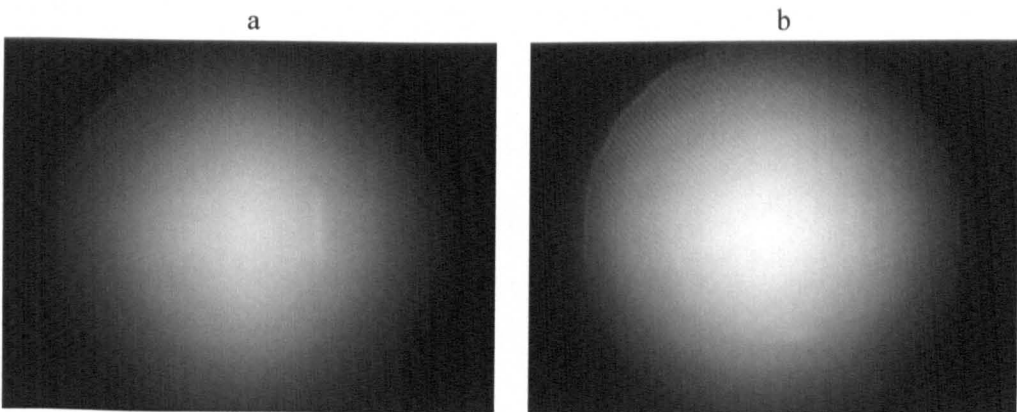
Figure 4.13: Demonstration of the background images applied for the calibration of non-uniform imaging. Polarization states of the illumination / detection pair for a): $90° / 0°$ and b): $0° / 90°$.
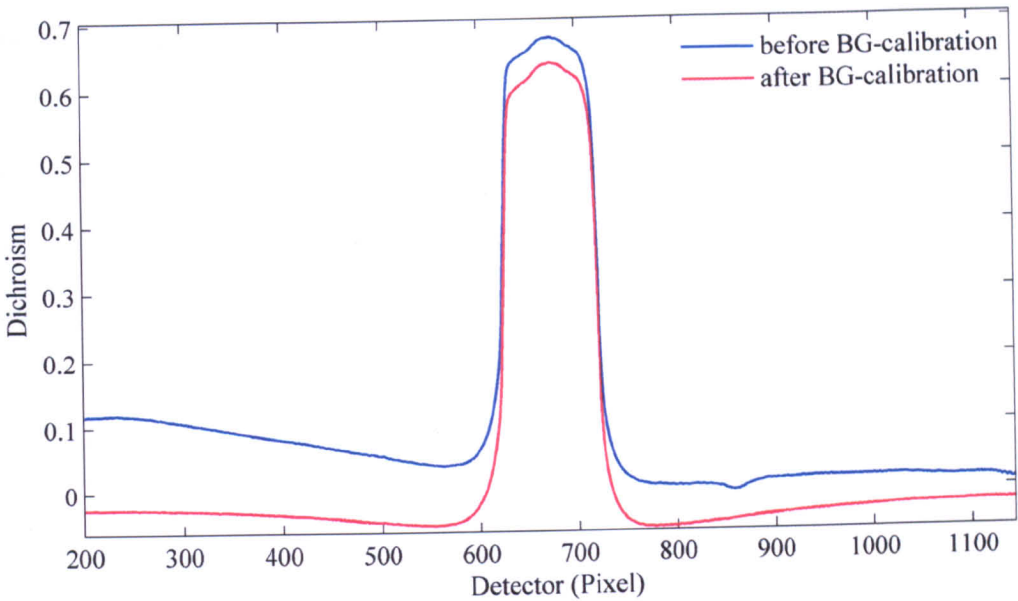
Figure 4.14: Comparison of the line scan results of a linear dichroism measurement in reflection mode at 0mfp depth before and after the calibration of non-uniform intensity.

4.2.3 Conventional Polarization Difference Imaging

In order to show the advantage of *ROPI* over conventional polarization difference imaging, an example is shown here. The conventional measurement of linear dichroism usually involves illumination with a fixed polarization state and employs detection in *co-* and *cross*-polarizations (i.e. the polarization states of illumination and detection are aligned in the *co-* case and orthogonal in the *cross-* case). In order to show the problems caused by surface reflections, the conventional polarization difference imaging of a linear polariser located within a scattering medium is performed using the setup shown in figure 4.1. The target is located at a depth of 0*mfp* and orientated at 0°. The two recorded images are shown in figure 4.15. (a) is obtained with illumination / detection channels polarized at 0° / 0° and (b) is recorded at 0° / 90°. Each image corresponds to an area of 9mm × 9mm.

As the figure shows, although the target is clearly visible in figure 4.15b, the target is completely obscured by surface reflections in figure 4.15a. This is due to the surface of the cuvette being perpendicular to the illumination, which causes large surface reflections to dominate the image. Clearly, this destroys any underlying information and does not provide a reliable method of quantifying the polarization properties of the target. This further indicates the importance of removing surface reflections, which is one of the advantages of *ROPI*.
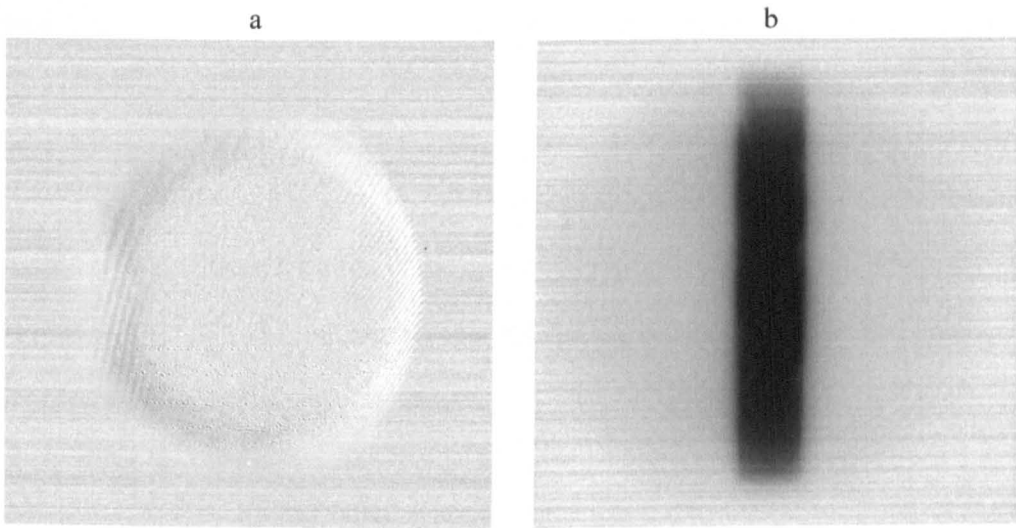
Figure 4.15: Conventional polarization imaging in reflection mode: (a) polarization states of illumination / detection are 0° / 0°; (b) 0° / 90°. The target is embedded at a depth of 0mfp within a scattering medium and polarized at 0°.

4.3 The Transmission Mode System

In the previous chapter, it was demonstrated that the measurement of linear birefringence in reflection mode using *ROPI* is highly challenging due to the small signal levels. A similar approach for measuring linear birefringence in transmission mode is proposed which may be appropriate for certain applications (e.g. engineered tissue samples), where the sample is sufficiently thin to retain a detectable amount of polari-

zation maintaining light. In transmission mode, surface reflections do not present a significant problem; however, the cross-polarized detection (i.e. illumination orthogonal to detection) inherent in *ROPI* will reduce the contributions from multiple component reflections.

The main aim of the transmission mode system is to simulate back-illumination of a birefringent target in reflection mode. The target is placed on the output surface of the cuvette and by varying the amount of scattering in the medium, the amount of polarized light back-illuminating the target can be modified in a controlled way. The experimental results from this transmission mode system will be presented in the next chapter.

In this section, characterization of the system in transmission mode will be presented. However, this will concentrate on the differences between those in the reflection mode system shown in figure 4.1 only.

The standard *ROPI* experimental setup in transmission mode is shown in figure 4.16. By comparing the two systems (figures 4.1 and 4.16), it can be seen that both setups use the same optical components and the layouts of the illumination and detection arms in both setups are the same except for the positions of the arms. As the transmission mode experiments performed here are looking for linear birefringence rather than linear dichroism, the sample used here is different from that discussed in subsection 4.2.1. This includes using a different scattering medium, a different test target and a different way of locating the target.

For the experiments in reflection mode, the scattering medium is required to be strong (i.e. large μ_s) to ensure the illumination photons are randomly polarized and to
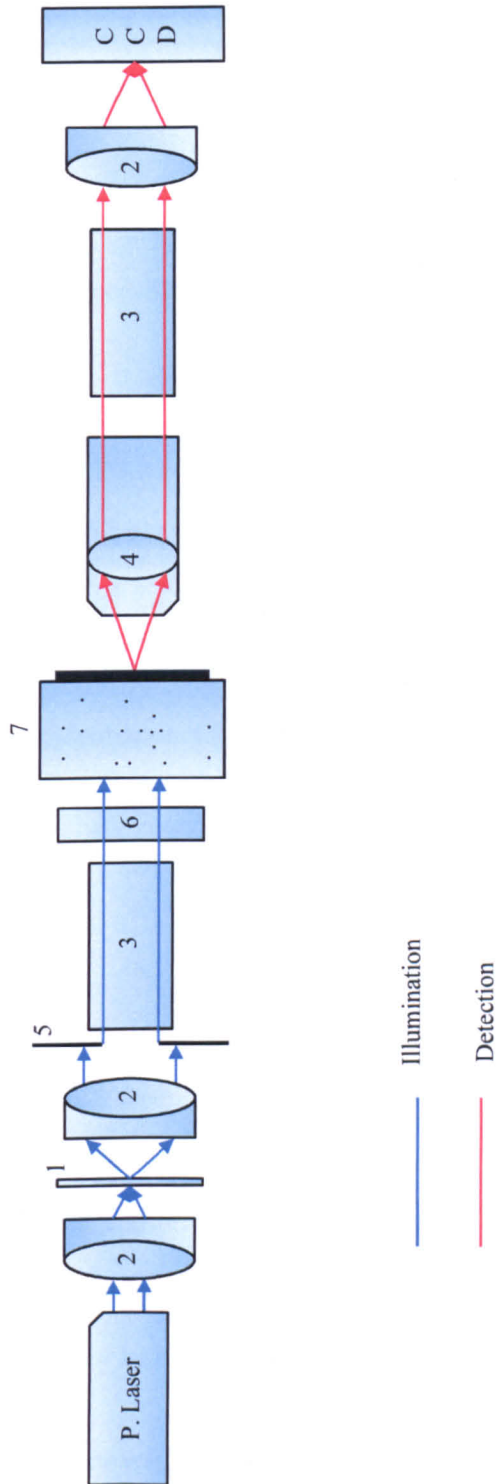
Figure 4.16: Standard ROPI experimental setup in transmission mode. 1) Ground glass rotating diffuser, 2) Positive achromatic doublet lenses, 3) Glan-Thompson po-larisers, 4) Infinite conjugate microscope objective, 5) Iris diaphragm, 6) Half-wave plate, 7) Sample.

approximate a semi-infinite medium in a finite thickness cuvette. In transmission mode, to demonstrate the effects of depolarization of the illumination, the sample must be sufficiently scattering to randomise the light but also must be weak (i.e. small μ_s) enough to allow some propagation through the medium. [80] In order to decide an appropriate μ_s for the medium used in transmission mode, the following estimation is performed.

Firstly, in order to randomly depolarize the illumination photons, generally, at least 10 single scattering events have to occur (for $g = 0.9$) [72]. As a conservative estimate, 40 single scattering events are assumed to be sufficient. Secondly, in order to ensure the photons travel far enough to the end of the medium after 40 scattering events, the total path length of a photon should satisfy equation 4.8 for g being assumed to be 0.9 and with the thickness of the cuvette being 10*mm*.

$$Total\ path\ length\ =\ \frac{4}{\mu_s'}\ =\ 4mfp'\ \cong\ 10mm \tag{4.8}$$

$$\mu_s'\ =\ (1-g)\mu_s\ =\ \frac{1}{mfp'} \tag{4.9}$$

μ_s' is the reduced scattering coefficient and represented in equation 4.9. $1/\mu_s'$ is the distance required to randomise the direction of propagation of a photon. This parameter combines g and μ_s together, which can be more informative than just using μ_s.

Therefore, for a suspension of polystyrene microspheres (diameter = 1.4μm, $g = 0.938$ from *Mie* theory), the μ_s used in the transmission mode experiments has to be greater than 4.0mm^{-1} based on the discussion above. A scattering medium with 1$mfp = 0.2mm$ (μ_s=5.0mm^{-1}) is therefore used for the phantom experiments in transmission mode. All

the other optical and physical properties of the medium are the same as those shown in table 4.1.

The test target used in the transmission mode *ROPI* experiments in this study is a zero order quartz half-wave plate (*HWP*). The *HWP* is identical to that applied in the setup for controlling the illumination polarization state. It is located directly after the cuvette and mounted within a thin (15.5*mm*) rotation mount in order to allow variation of the optical axis of the target. The experiment results will be presented in the next chapter.

4.4 Discussion and Summary

In this chapter, design, characterization and calibration of the standard *ROPI* experimental system in both reflection and transmission modes have been provided in sections 4.2 and 4.3 respectively. The description of the setup includes the system as a whole, all the optical components, the scattering medium and polarizing targets. The calibration process to allow corrections to changes in polarization state and intensity after passing through the system to be made is also presented. These changes result from the non-ideal components, most noticedly the *BS*. In addition, problems of performing the conventional polarization difference imaging for this application are also provided. The problems indicate that quantitatively measuring polarization properties of the underlying target using this method is not possible as surface reflections dominate the co-polar image (i.e. illumination aligned to detection) and the target is obscured.

As figure 4.16 shows, there are no significant surface reflections in the system in transmission mode other than multiple reflections from component surfaces. However,

this layout is not practical in many biomedical applications. In this study, the investigation of *ROPI* concentrates on the system in reflection mode. The system in transmission mode is only used to further complete the investigation of linear birefringence.

As discussed in subsection 4.2.2, different components of polarized light incident onto the *BS* are affected differently; $0°$ and $90°$ polarization states are preferably selected. This is not a problem in the phantom experiments when the polarization axis of the target is known. However, in order to fully apply *ROPI* in practice, the use of other linear polarization states for *ROPI* is necessary. There are three methods that possibly could be researched and applied in the future to achieve this. Firstly, although it is unlikely in practice, the use of a *BS* with $r_s=r_p$ and $t_s=t_p$ is the ideal way to avoid the effect of changing polarization state. Secondly, if two identical *BSs* were used and located with their *s*- and *p*- directions swapped, the effect may be cancelled out. Finally, an appropriate retardance compensator could possibly be used to reduce the effect.

For both of the calibration stages shown in subsection 4.2.2, the effect of changes in both the polarization state and intensity of illumination can be significantly reduced. However, neither calibration is ideal. For the calibration when the polarization state is modified, this is only effective for changes in the polarization state from one linear state to another one due to the amplitude differences between the *Fresnel* coefficients. The introduction of elliptical states due to phase differences is not corrected. However, the observed rejection ratios achieved for the polarization states of $0°$ and $90°$ are still sufficient for *ROPI*.

For the calibration of modified intensity, as figure 4.14 shows, the calibration of non-uniform intensity distribution is incomplete. There is still a very slight difference that can be observed between two sides. This is due to the intensities in the background images not being exactly the same as those in the *ROPI* images when the target is embedded. As the non-uniform distribution can be significantly reduced and this slight difference will be reduced further when the target depth increases, this trade-off when applying the calibration is acceptable. Better methods calibration remains an area for future research.

In conclusion, the standard *ROPI* experimental systems in both reflection and transmission modes have been introduced. These will be used to investigate *ROPI* through the phantom and tissue experiments in chapter 5.

Chapter 5

ROPI Experiments in Standard Mode

5.1 Introduction

In chapters 2 and 3, the *ROPI* technique has been investigated both in theory and with simulations. In this chapter, the technique will be investigated experimentally in both reflection and transmission mode using the standard (i.e. *GT* polariser based) experimental system which was described in chapter 4. As *ROPI* in reflection mode is preferred in clinical applications, this configuration is mainly evaluated in this study. Transmission mode experiments are carried out as an aid to understanding the performance of *ROPI* in reflection mode.

In the reflection mode experiments, the investigation will consist of quantitatively measuring linear dichroism underlying different scattering samples. These include (i) phantom measurements of a polarizing target embedded within a scattering medium at different depths; (ii) preliminary measurements of a variety of real tissues (bovine tendon, lamb tendon, chicken breast and human finger skin); (iii) preliminary measurements of a tissue scaffold orientated in two orthogonal directions. The first investigation experimentally captures results discussed in chapters 2 and 3. The second and third investigations are very preliminary, which are only used to initially demonstrate the results that could be obtained when applying *ROPI* in practice.

Experiments in reflection and transmission modes will be provided in sections 5.2 and 5.3 respectively. Section 5.4 provides discussion and conclusion.

5.2 Experiments in Reflection Mode

In this section, the experiments performed to study *ROPI* using the standard system in reflection mode shown in figure 4.1 are presented. Section 5.2.1 presents the phantom experiments. Sections 5.2.2 and 5.2.3 demonstrate the two different preliminary experiments respectively.

5.2.1 Phantom Experiments of Linear Dichroism Measurements

In this subsection, in order to compare the experimental and simulation results, the linear dichroism measurements performed by *MC* simulations in chapter 3 are repeated using phantom experiments. These involve the measurements for a linear polarizer embedded within a scattering medium at depths of 0, 2, 5, 10, 12, 15 and 17*mfps* and orientated at $0°$ using the illumination / detection pairs orientated at $0°$ / $90°$ and $90°$ / $0°$.

There are two similar setups used sequentially to perform the phantom experiments. The layout is the same as shown in figure 4.1, with mostly the same components except for the *CCD* camera. The original setup with the *MegaPlus* camera is used for the initial studies. Therefore, it mainly shows the initial results and provides the general understanding and difficulties of performing the experiments. After the improvements based on those initial experiments; the final setup with the *ORCA* camera is used to repeat the experiments. This provides improved results which give a more ac-

curate understanding of the *ROPI* technique. In the rest of this subsection, both the initial and improved results will be demonstrated and discussed.

The initial phantom experimental results of the linear dichroism *ROPI* measurements of a polarizer embedded within a scattering medium at different depths and orientated at 0° are shown in figures 5.1 and 5.2. The scattering medium used in the experiments is the same as that specified in table 4.1 in chapter 4. The target is also the same as that introduced in subsection 4.2.1 but with a slight difference in dimensions which with it being 0.75*mm* thick, 6*mm* long and 1*mm* wide. The calibration routine, which is described in subsection 4.2.2 in chapter 4 and used to calibrate non-uniform illumination, is applied for all the images shown here.

In figure 5.1, the images in rows from top to bottom show the target positioned at depths of 0, 2, 5, 10, 12, 15 and 17*mfps* within the scattering medium. The first column shows the images taken with vertically polarized linear illumination (90°) and detection at 0° (i.e. polarization states of illumination and detection are cross-aligned and co-aligned respectively with the target orientation). The second column shows the images taken with horizontally polarized illumination (0°) and detection at 90° (i.e. polarization states of illumination and detection are co-aligned and cross-aligned respectively with the target orientation). The third column shows the linear dichroism images calculated by combining the images from columns 1 and 2 following equation 2.25 (i.e. (column$_1$ − column$_2$) / (column$_1$ + column$_2$)). Each image in the figure is taken once with an integration time of 64.872*ms* and corresponds to an area of 9*mm* × 9*mm*. Figure 5.2 is the average line scan on the *y* axis of the images in column 3 in figure 5.1, which quantitatively represents the linear dichroism at different depths.

Figure 5.1: Initial GT based experimental ROPI images of linear dichroism meas-
urements of a polarizer at different depths in a scattering medium orientated at 0°.
Rows 1 to 7 = 0, 2, 5, 10, 12, 15 and 17mfps. Illumination / detection polarized at
$col_1 = 90^o / 0^o$, $col_2 = 0^o / 90^o$. $col_3 = (col_1 - col_2) / (col_1 + col_2)$. Each image is $9 \times 9mm^2$.
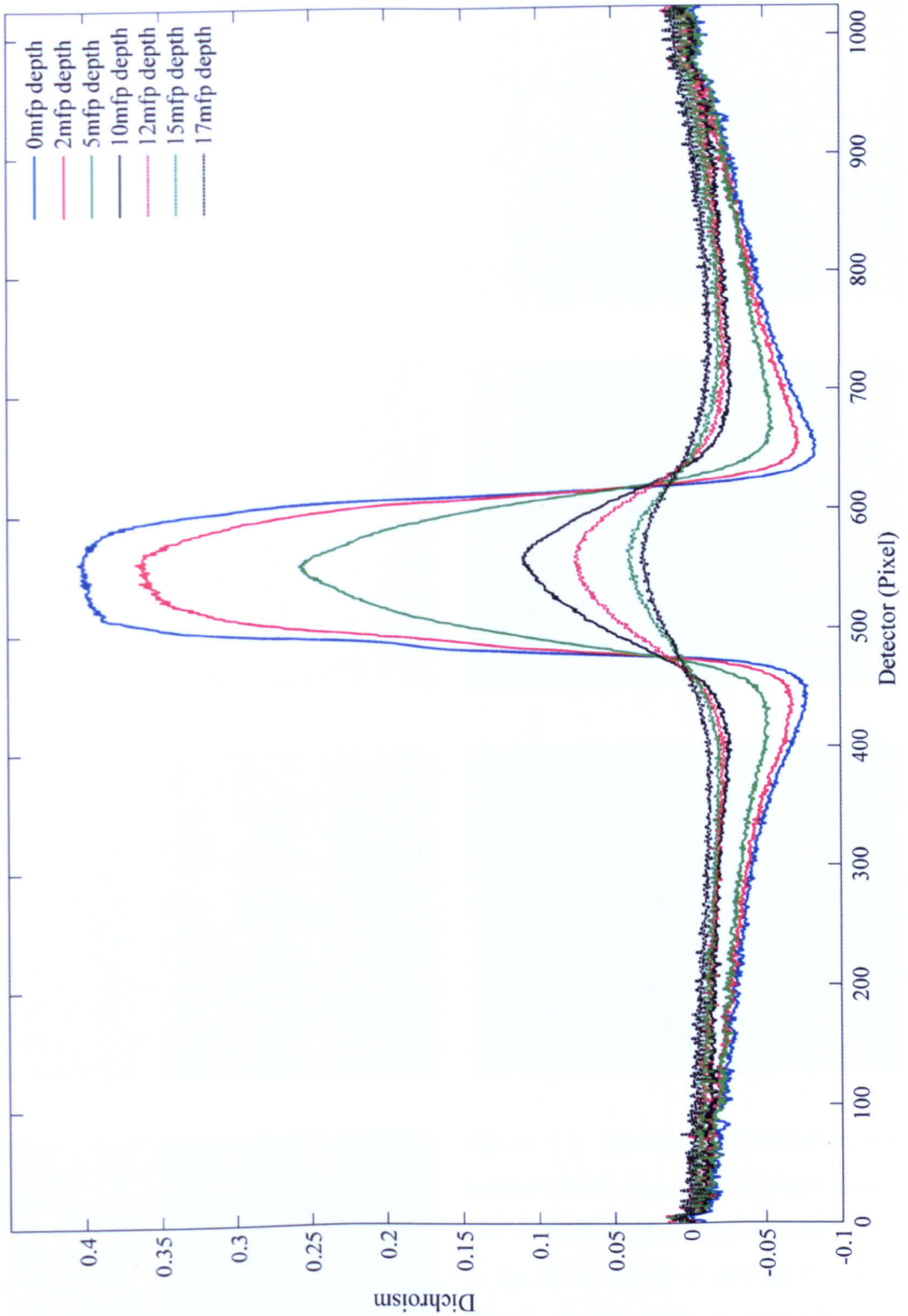
Figure 5.2: Average line scans on the y axis of the initial GT based experimental ROPI linear dichroism images at different target depths within a scattering medium (i.e. images in column 3 in figure 5.1).
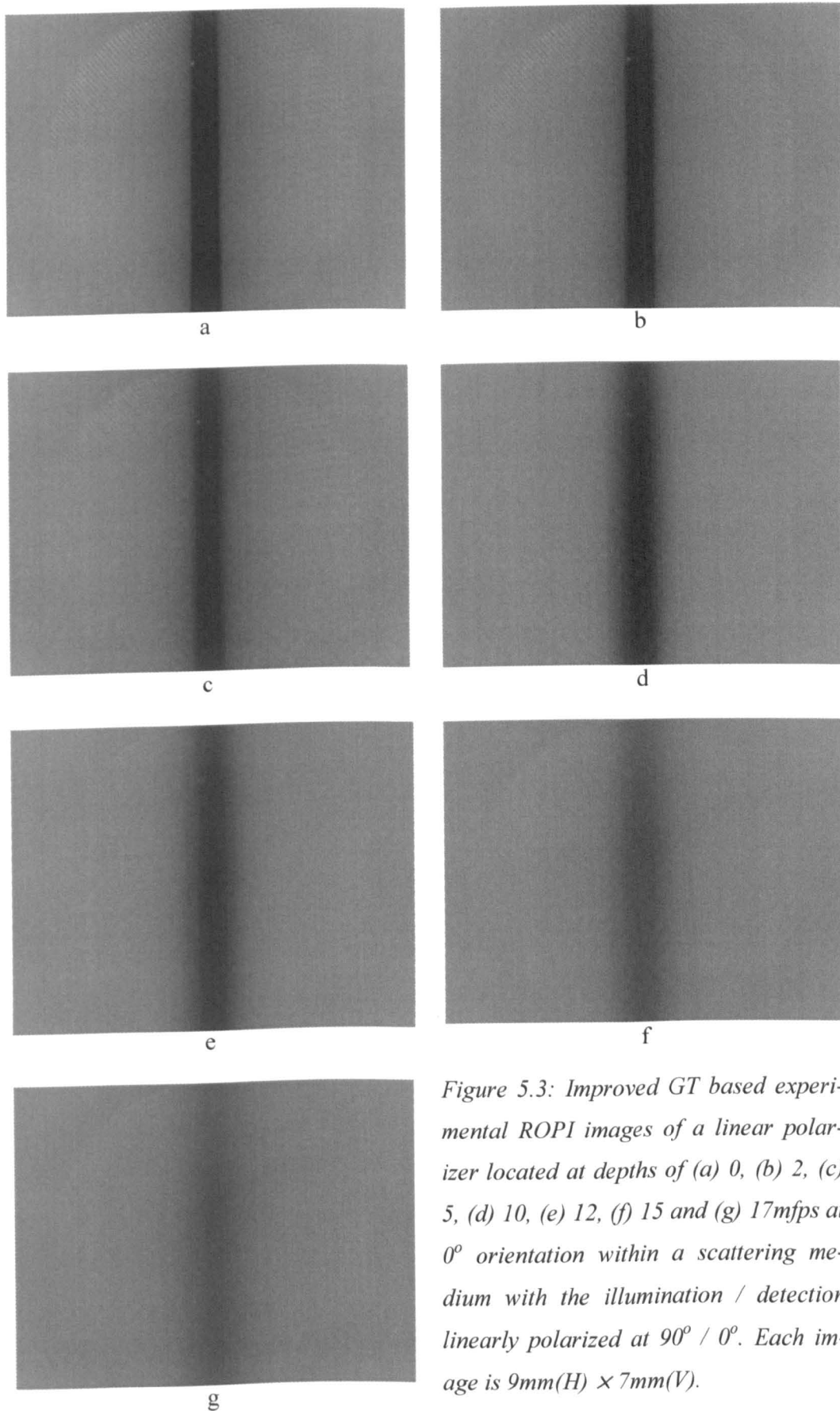
Figure 5.3: Improved GT based experimental ROPI images of a linear polarizer located at depths of (a) 0, (b) 2, (c) 5, (d) 10, (e) 12, (f) 15 and (g) 17mfps at 0° orientation within a scattering medium with the illumination / detection linearly polarized at 90° / 0°. Each image is 9mm(H) × 7mm(V).

a

b

c

d

e

f

g

Figure 5.4: Improved GT based experimental ROP1 images of a linear polarizer located at depths of (a) 0, (b) 2, (c) 5, (d) 10, (e) 12, (f) 15 and (g) 17mfps at 0° orientation within a scattering medium with the illumination / detection linearly polarized at 0° / 90°. Each image is 9mm(H) × 7mm(V).
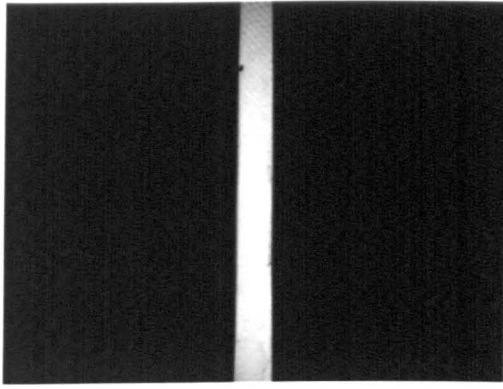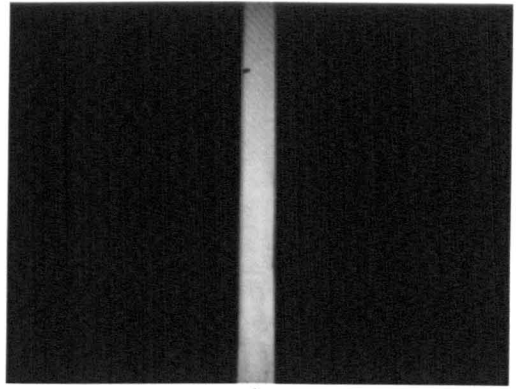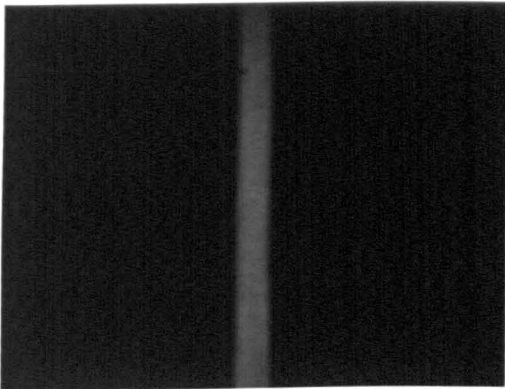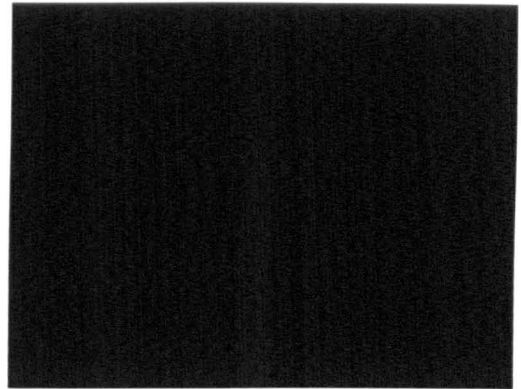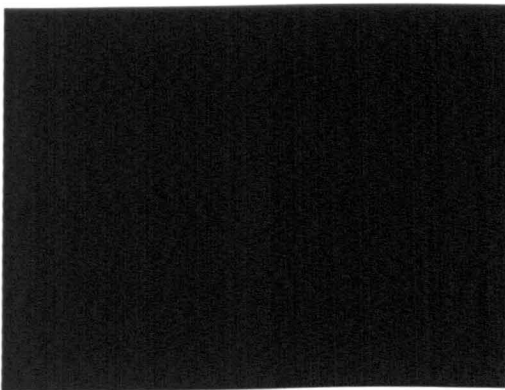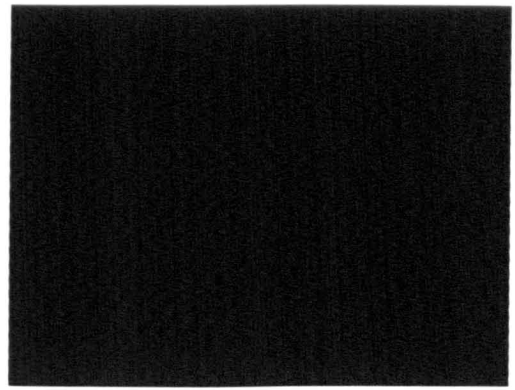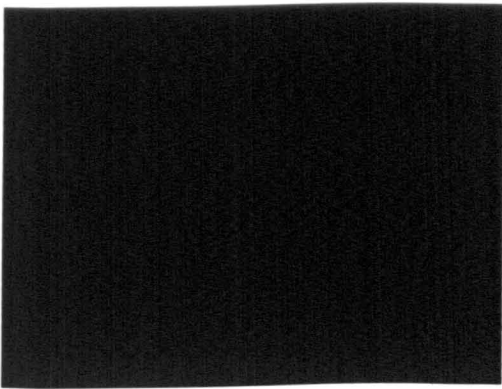
Figure 5.5: *Improved GT based experimental ROPI linear dichroism images of a polarizer located at depths of (a) 0, (b) 2, (c) 5, (d) 10, (e) 12, (f) 15 and (g) 17mfps within a scattering medium. The images are obtained by combining figures 5.3 and 5.4. Each image is 9mm(H) × 7mm(V).*
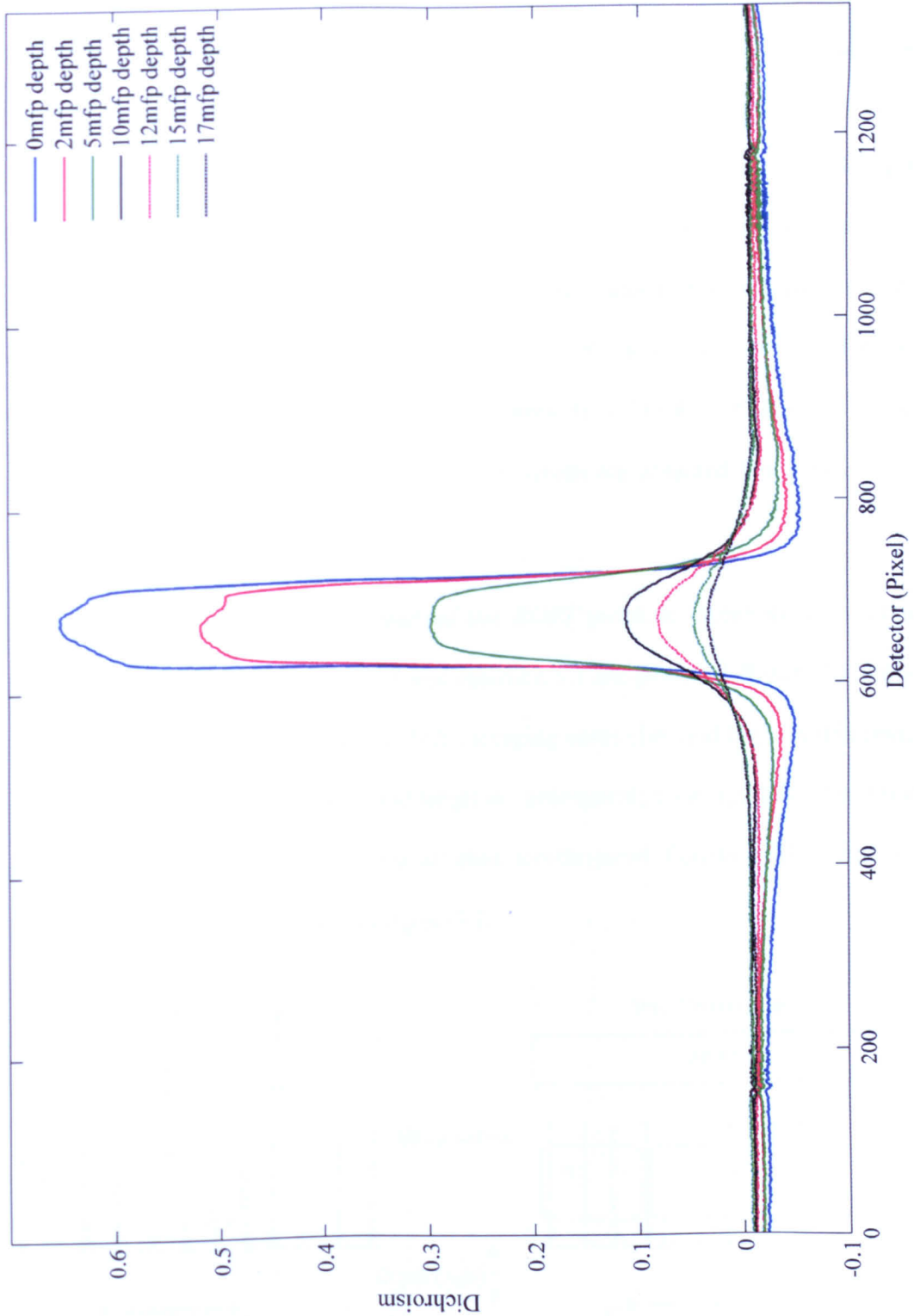
Figure 5.6: *Average line scans on the y axis of the improved GT based experimental ROPI linear dichroism images at different target depths within a scattering medium (i.e. images in figure 5.5).*

The improved results for the same measurements are shown in figures 5.3-5.6. These are performed with the final setup shown in figure 4.1 in chapter 4. The scattering medium and target are described in subsection 4.2.1. The same calibration routine is applied for all the images shown. Figures 5.3-5.5 are the improved normalised images obtained as the same as those shown in the columns 1 to 3 in figure 5.1 respectively. However, instead of only taking each image once, each image here is averaged from 10 single images which are taken sequentially with an integration time of 100ms. Each single image corresponds to the area of 9mm(H) × 7mm(V). Figure 5.6 is the improved line scans of the images in figure 5.5, which are obtained in the same way as those shown in figure 5.2.

In order to clearly describe and analyse the *ROPI* phantom experimental results shown in figures 5.3 to 5.6, figure 5.7 and equation 5.1 are provided. Figure 5.7 illustrates the differences between the two *ROPI* imaging cases (Im_1 and Im_2). In this case, cross imaging is when the detector and target are orthogonal; co imaging is when they are aligned. Illumination and detection are always orthogonal. Equation 5.1 is the specific case of equation 2.19 based on figure 5.7.
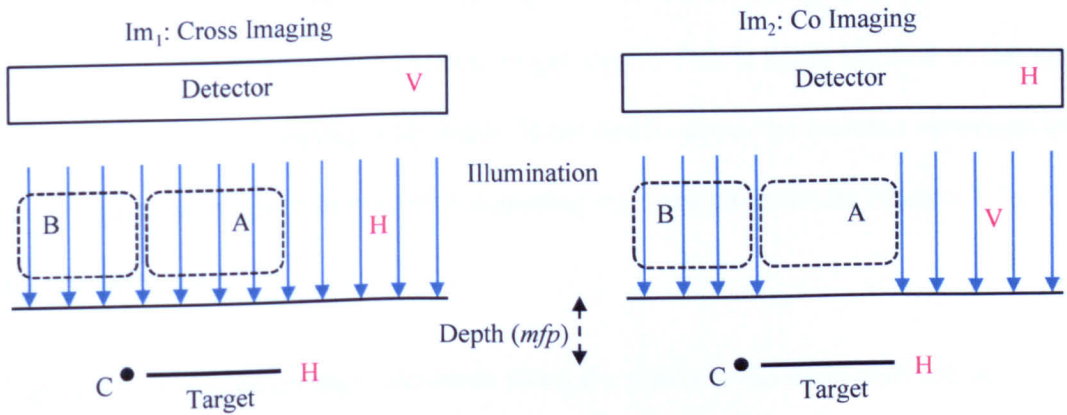
Figure 5.7: *Illustration of differences of the illumination intensities and the polarization states of the illuminations, detections and target between two ROPI imaging cases, Im_1 and Im_2. H is orientated at 0° and V is at 90°.*

$$Linear\ Dichroism = \frac{Co - Cross}{Co + Cross} = \frac{Im_2 - Im_1}{Im_2 + Im_1} \qquad (5.1)$$

Figures 5.3 and 5.4 show the images corresponding to the cases of *co* imaging (Im_2) and *cross* imaging (Im_1) in figure 5.7 respectively. As shown, figure 5.3 is performed with 90° polarized illumination and 0° detection. Contrast of the images can be observed as the illumination is partially blocked by the target as Im_2 shows. This is because the polarization state of the illumination is cross-aligned with the orientation of the target. Figure 5.4 is performed with 0° polarized illumination and 90° detection. Contrast of the images is due to no detection from the target area as the polarization state of the detection is crossed-aligned with orientation of the target. In both cases, contrast gradually reduces as target depth increases due to an increase in scattering. In addition, the contrast of the images is higher in figure 5.4 than that in figure 5.3. This is because the polarization state of detection in Im_1 is orthogonal to the orientation of the target while in Im_2 is co-aligned to the orientation of the target as figure 5.7 shows. Figure 5.5, which is obtained following equation 5.1 by combining the images shown in figures 5.3 and 5.4, represents the images of linear dichroism. Contrast of the images, which gradually reduces as target depth increases, indicates the linear dichroism value obtained reduces with increasing target depth. This is again because of the effects of scattering increasing with depth. More details about the contrast variations in those figures were given in chapter 3 regarding the simulation results (figures 3.7-3.9) for the same setup.

Figure 5.6 shows the average line scans along the *y* axis of the dichroism images over rows 400 to 700 in figure 5.5. These quantitatively represent the *ROPI* linear dichroism measurements at different depths within the scattering medium. It can be clearly

seen that polarization sensitive measurements can still be obtained until a depth of 17*mfps* within the scattering medium. However, the measurement of dichroism is dependent on the target depth within the medium as the mean normalized linear dichroism values within the target are reduced from 0.68 to 0.08 for the depths from 0 to 17*mfps* respectively. In addition, this is obviously dependent on the properties of the target as well. The case of the target embedded at a depth of 17*mfps* is close to the sensitivity limit of the technique for measuring linear dichroism. As discussed, this is because the polarization states detected in both imaging cases are close to fully randomised due to scattering between the target and the detector. This has been validated by preliminary values obtained using *MC* simulations as discussed in chapter 3. Moreover, it is noticed that for each line scan in figure 5.6, the dichroism value is always negative outside the target region and the negative maximum is always at the edges of the target. This is explained below using figure 5.7 and equation 5.1.

As indicated in figure 5.7, considering point C, in the case of *co* imaging (Im$_2$), backscattered photons that contribute to point C due to illumination are only from region B while there are no photons due to illumination from region A. This is because the polarization states of the target and illumination are orthogonal to each other. However, in the case of *cross* imaging (Im$_1$), backscattered photons contributing to point C are now due to illumination from both regions A and B. This is because the polarization states of the target and illumination are co-aligned and the target allows the region A illumination to travel through into the medium. Therefore, backscattered photons that contribute to point C in Im$_1$ are greater than that in Im$_2$. As the equation 5.1 shows, it is clear that at point C (i.e. outside the target region); the linear dichroism calculated is negative as (Im$_2$–Im$_1$) is less than 0. In addition, as point C moves away from the target, the difference between the photons' contributions to point C between from Im$_2$

and Im$_1$ reduces. Therefore, the negative maximum dichroism value is obtained at the edges of the target region. As figure 5.6 shows, these effects reduce as the target depth increases due to an increase in the scattering effect.

By performing the initial experiments, the *ROPI* technique and the experimental setup are tested. As shown in figure 5.1, the technique as initially shown is sensitive to linear dichroism within a scattering medium at different depths, which provides a step forward to applying the technique in practice. However, as shown in figure 5.2, the linear dichroism values obtained are significantly different from the *MC* simulations (figure 3.10) although the trends are the same. After carefully investigating the experiments performed, the following points are believed to be the possible cause of the differences:

1) There are experimental errors in positioning the target at the precise depth required and accurately aligning its orientation at 0°. For positioning at the initial depth (i.e. 0*mfp*), the target is first located at the working distance plane of the objective and then the cuvette was moved towards to the target until the inner surface of the cuvette and the target were next to each other. For setting the polarization state, with a mirror placed behind the target in order to have back illumination, with the *GT$_2$* set at 90°, the target is adjusted until the minimum detection is imaged in the *CCD*. As all these alignments are judged by the naked eye, it is possible the alignments are not accurate enough.

2) In order to have sharp images, the target is required to be accurately located at the focal plane of the objective. However, as this is achieved manually and judged by the naked eye from the image in the *CCD* as well, it is possible that the target is slightly out of focus.

3) There are experimental errors in manually and repeatedly rotating the polarizing components (*HWP* and *GT₂*) to control the orientations of illumination and detection. Firstly, it is not possible to have exactly the same polarization states with manual rotation and secondly it is possible to cause image displacement after manual rotation due to slight changes in optical path [100].

4) The scattering medium used in the experiment has a finite thickness of 12*mm* whereas currently the *MC* model has a medium thickness of only 5*mm* in order to reduce the simulation time.

5) Theoretically, surface reflections within the system including the internal reflections from optical components and surface reflection from the cuvette should be completely eliminated by the crossed polarized detection. However, in experiments, this cannot be achieved ideally as the polarizing components used in the system are not ideal, in particular the *BS*, which modifies the polarization state of illumination (see subsection 4.2.2, chapter 4). Therefore, although those surface reflections can be reduced significantly, it is difficult to completely eliminate them. This is particularly significant in the case when the target and analyzer (*GT₂*) are orthogonally aligned, where the light intensity detected is low.

6) There are side contributions when applying a finite thickness (0.75*mm*) target. Ideally, for both the Mueller calculus and *MC* simulations, the target is applied with zero thickness. Therefore, side contributions (i.e. backscattered photons that might pass through the target via its edges) might contribute to the detected photons. This eventually reduces the measurement values as polarization states detected are not pure due to transmission through a thin target. The error is also particularly significant in the case of *cross* imaging where the light intensity detected is low.

By taking all the points discussed above into account, points 1)-3) are considered as experimental inaccuracies. These can be reduced by re-performing the experiments with better alignment of the target and more accurate control of the polarizing components. However, these errors cannot completely be removed as the alignment is still performed manually. The points 4)-6) cannot be eliminated simply by re-performing the experiments. For point 4), it is found that it only has a very small effect on the linear dichroism values by running a new simulation with the same medium thickness as that applied in the experiments. It can therefore be neglected as a significant source of error. For point 5), in order to remove the surface reflections and increase the measurement values, a further investigation of this error is required. For point 6), theoretically this could be minimized by using a thinner target. However, this is difficult to perform in practice as a thinner target will generate more difficulties in aligning its orientation and initial position within the medium. It is found that the error from surface reflections (point 5)) can be reduced by calibration while the error of side contributions from point 6) cannot. These investigations will be described in chapter 7 in detail.

Figures 5.3-5.5 show the results after performing the improved phantom experiments with the refinements considered for minimizing the errors from points 1)-4). By comparing with the initial results (figure 5.1), the improved *ROPI* and dichroism images are much smoother. This is because the background noise is reduced by averaging over 10 images. Furthermore, as shown in figures 5.2 and 5.6, the linear dichroism value measured at 0*mfp* after these improvements is increased significantly to almost twice of the initial measurement and is also closer as the target depth increases.

Finally, as figure 5.6 also shows, although the linear dichroism values obtained after the refinements are significantly increased, they are still different to those obtained

from the *MC* simulations (figure 3.10). Based on the discussion of the errors provided above, surface reflections and side contributions from points 5) and 6) respectively are believed to be the two main error sources that cause these differences. Therefore, in order to further understand the phantom experimental results, a further calibration of the surface reflections and a further investigation of the side contributions which cannot be calibrated were performed. These will be described and discussed in detail in chapter 7 when a further comparison of the simulation and phantom results is provided.

5.2.2 Tissue Experiments of Linear Dichroism Measurements

In this subsection, in order to initially demonstrate the feasibility of applying *ROPI* in practice, the technique is preliminarily applied for measuring the linear dichroism in various real tissues. These include bovine tendon, lamb tendon, chicken breast and human skin. All the tendons and breasts were bought fresh from a local butcher and the human skin is the left thumb inner skin of the author. As all the measurements in this subsection are preliminary, the results are mainly shown for demonstration and only a brief description and discussion will be provided.

The experiments were performed using the setup shown in figure 4.1 in chapter 4. By imaging with the illumination / detection pairs linearly polarized at $0°$ / $90°$ and $90°$ / $0°$, the two cases of *ROPI* images of different tissues are obtained. Using equation 2.25 to combine the obtained *ROPI* images for each measurement, the respective linear dichroism images for different tissues are obtained. In addition, in order to compare the *ROPI* images with those obtained by using conventional detection which involves the illumination / detection co-aligned (subsection 4.2.3, chapter 4), an image

with illumination / detection polarized at $0°$ / $0°$ is also taken for each measurement. The images of all the measurements are shown in figures 5.8-5.10.

There are three main specifications for the images shown. (i) Each image is averaged from 10 single images taken sequentially and corresponds to an area of $9mm$(H) × $7mm$(V). (ii) The calibration routine of non-uniform illumination (subsection 4.2.2, chapter 4) is applied to all the images taken. (iii) All the images are plotted by using the *imagesc* function in *Matlab*, which automatically scales the images to be shown according to the intensity range of all pixels. This is in order to overcome the problem of using different integration times for different images. Furthermore, in order to enhance the contrast of the images, along with applying the *imagesc* function, a threshold is applied as well to remove the outlying high and low intensity values before plotting the images. From the histogram plot for each image (figures not shown), the outlying high and low intensity values are only about 0.1% of the total pixel values.

Figure 5.8 shows the preliminary images taken for the linear dichroism measurement of a bovine tendon. Figure 5.8a shows the image taken with the conventional detection by applying the illumination / detection polarized at $0°$ / $0°$. It clearly shows that the image is dominated by reflections from the tissue surface and other optical components within the system. The bright central region is a ghost image of the aperture of the *GT* polariser caused by reflections from the optical components in the system. Figures 5.8b and 5.8c show the two *ROPI* cross-polarized images that are taken with the illumination / detection polarized at $0°$ / $90°$ and $90°$ / $0°$ respectively. As shown, both the images are free from surface reflections from both the tissue and the optical components within the system. Figure 5.8d presents the linear dichroism image that is formed by combining the two *ROPI* images.
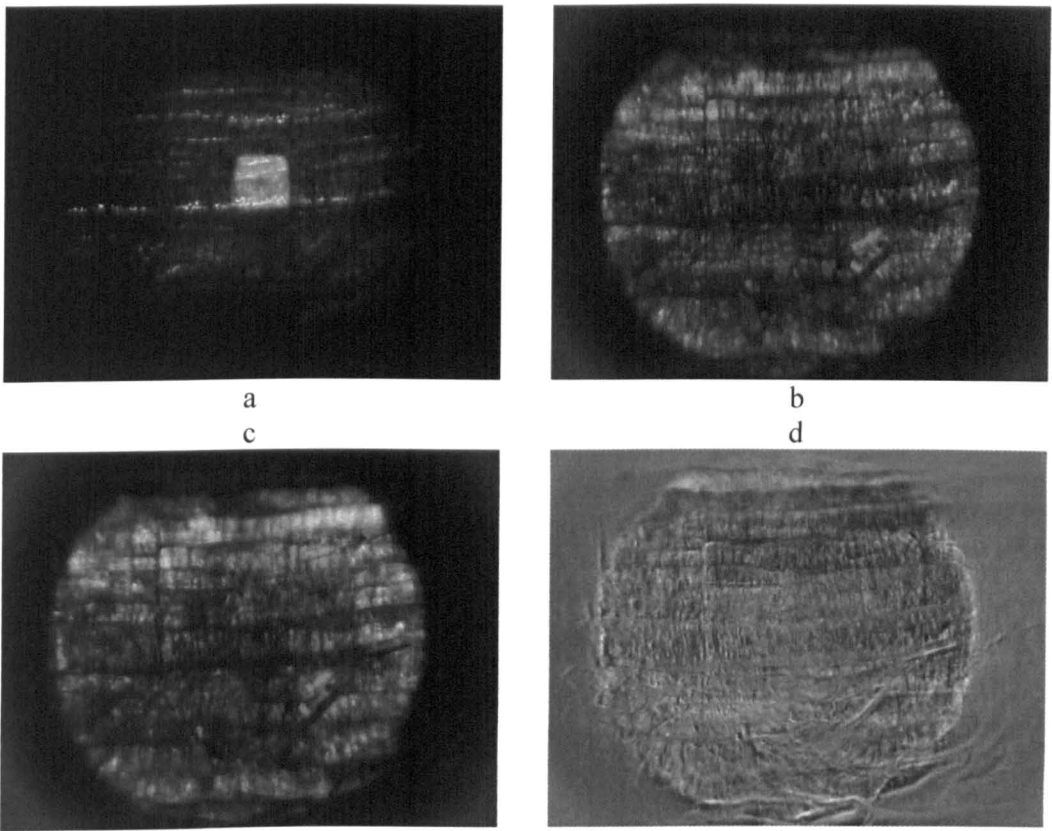
Figure 5.8: Illustration of bovine tendon images taken with illumination / detection polarized at a) 0° / 0°, b) $0°$ / $90°$ and c) $90°$ / $0°$. d) is the ROPI linear dichroism image combined from b) and c). Each image is 9mm(H) × 7mm(V).

Within the images shown in figures 5.8a to 5.8c, horizontal bands can be observed that correspond to structures within the tissue, but the polarization properties cannot be measured without taking a polarization difference image. For conventional polarization difference imaging, a subtraction of the co-polarized image (figure 5.8a) and the cross-polarized image (figure 5.8b) does not provide a useful image for quantifying the polarization properties of the tissue owing to the presence of reflections in the image. The ROPI linear dichroism image (figure 5.8d) is obtained by subtracting and normalizing the figures 5.8b and 5.8c and demonstrates the sensitivity to the polarization properties of the underlying tissue while remaining insensitive to surface reflections. As the underlying tissue contains highly organized fibrous tissue, the polariza-

tion difference image (figure 5.8d) reveals an image which represents the linear dichroism measured with the absolute of the mean value of 0.05. If the tissue exhibits no polarization changes then figure 5.8d would be uniformly zero.

Figure 5.9 shows the same image format as those shown in figure 5.8 but from a chicken breast. The images in the figure provide the same main features as those analysed in figure 5.8. The polarization difference image (fig 5.9d) provides the absolute of the mean value of 0.026, which is smaller than that provided from figure 5.8d. This indicates that chicken breast is not as highly organized as bovine tendon.

a   b

c   d
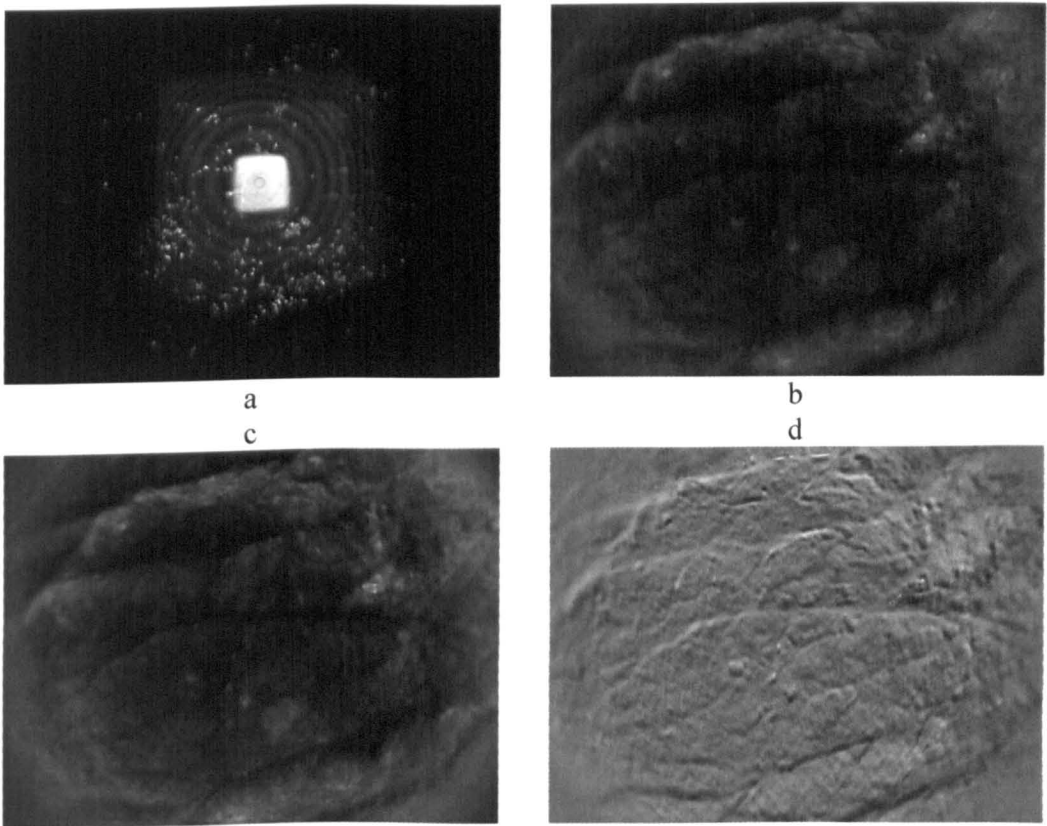
Figure 5.9: Illustration of chicken breast images taken with illumination / detection polarized at a) 0° / 0°, b) $0°$ / $90°$ and c) $90°$ / $0°$. d) is the ROPI linear dichroism image combined from b) and c). Each image is 9mm(H) × 7mm(V).

In order to provide an indication of the dynamic range of the system, the normalized polarization difference images obtained by using the *ROPI* technique for another bovine tendon, lamb tendon, another chicken breast and human skin are shown in figure 5.10a-5.10d respectively. These images represent the polarization properties of the underlying tissues and the absolute of the mean polarization difference value within those tissues shown in the figure are 0.07, 0.03, 0.027 and 0.013 respectively. To provide a comparison, the same absolute mean value for a polystyrene microsphere solution which is a non-polarizing sample and hence does not contain any polarization properties is 0.003. (The polarization difference image of the microspheres is not shown here.)

a   b

c   d
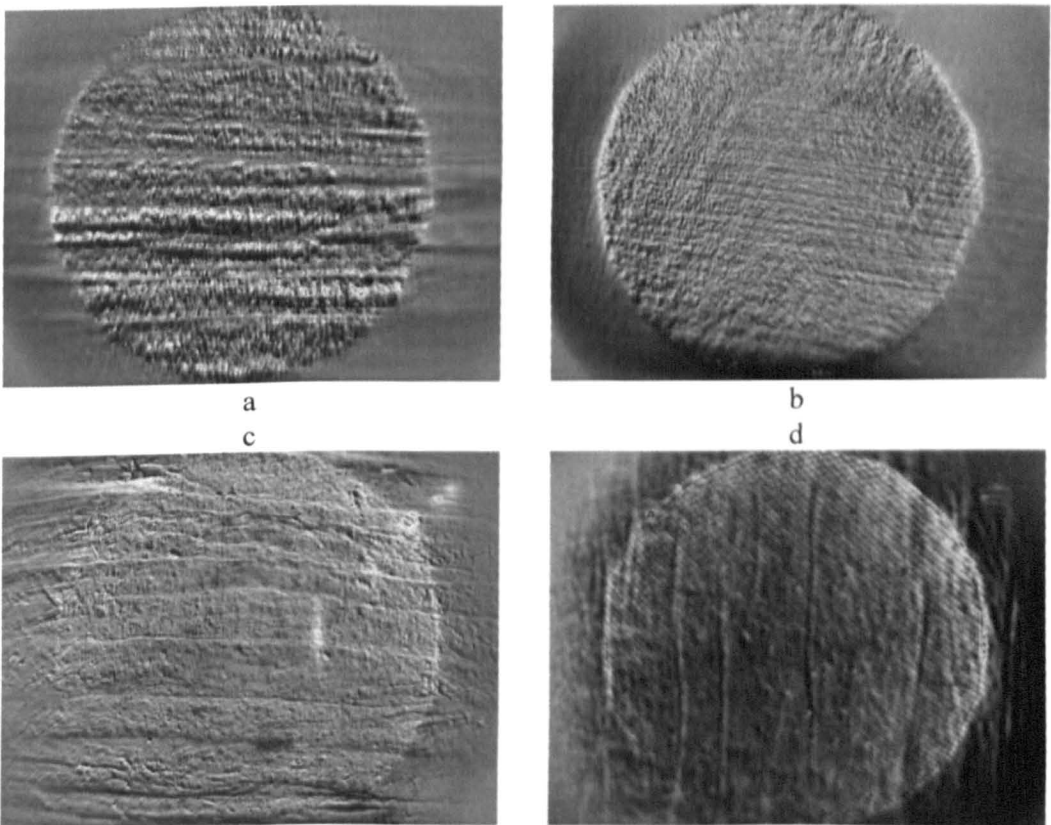
Figure 5.10: Illustration of ROPI normalized polarization difference of tissue images a) bovine tendon, b) lamb tendon, c) chicken breast, d) human left thumb inner skin. Each image is 9mm(H) × 7mm(V).

5.2.3 Scaffold Experiments of Linear Dichroism Measurements

In this subsection, a further initial demonstration of the feasibility of applying *ROPI* in practice is provided. This involves preliminary measurements of the linear dichroism of a tissue engineered tendon specimen orientated at 0° and 90°. These are mainly used to demonstrate how the linear dichroism measurements vary with the change of sample orientation in practice.

The illumination / detection pairs linearly polarized at 0° / 90° and 90° / 0° are used to perform the measurements with the setup shown in figure 4.1 in chapter 4. The specimen is provided by The University of Keele. It is made of rat tenocytes seeded on an aligned collagen [type I scaffold hydrogel ($20mm \times 20mm \times 6mm$)], plastic compressed into a sheet and rolled into a Swiss roll-shape. There are two cuvettes used in experiments. One is used to keep the specimen in saline and the other one contains a scattering medium and is used to provide more backscattered photons. The scattering medium is the same as that applied in the phantom experiments and sits behind the specimen cuvette with the specimen at the working distance of the objective.

The experimental results are shown in figure 5.11. The images in columns 1 and 2 represent the horizontal and vertical measurements of the sample respectively. The reason for rotating the sample is to ensure that changes in dichroism were due to the specimen. Images in row_1 are obtained with the illumination / detection linearly polarized at 0° / 90° while the images in row_2 are at 90° / 0°. Images in row_3 represent the linear dichroism of the specimen obtained by combining the images from row_1 and row_2 following equation 2.25. Each image shown in the figure is averaged from 10 single images taken sequentially with an integration time of $100ms$ and corresponds to

an area of $9mm$(H) $\times$ $5.5mm$(V). The calibration routine for non-uniform illumination (subsection 4.2.2, chapter 4) is applied to the images.
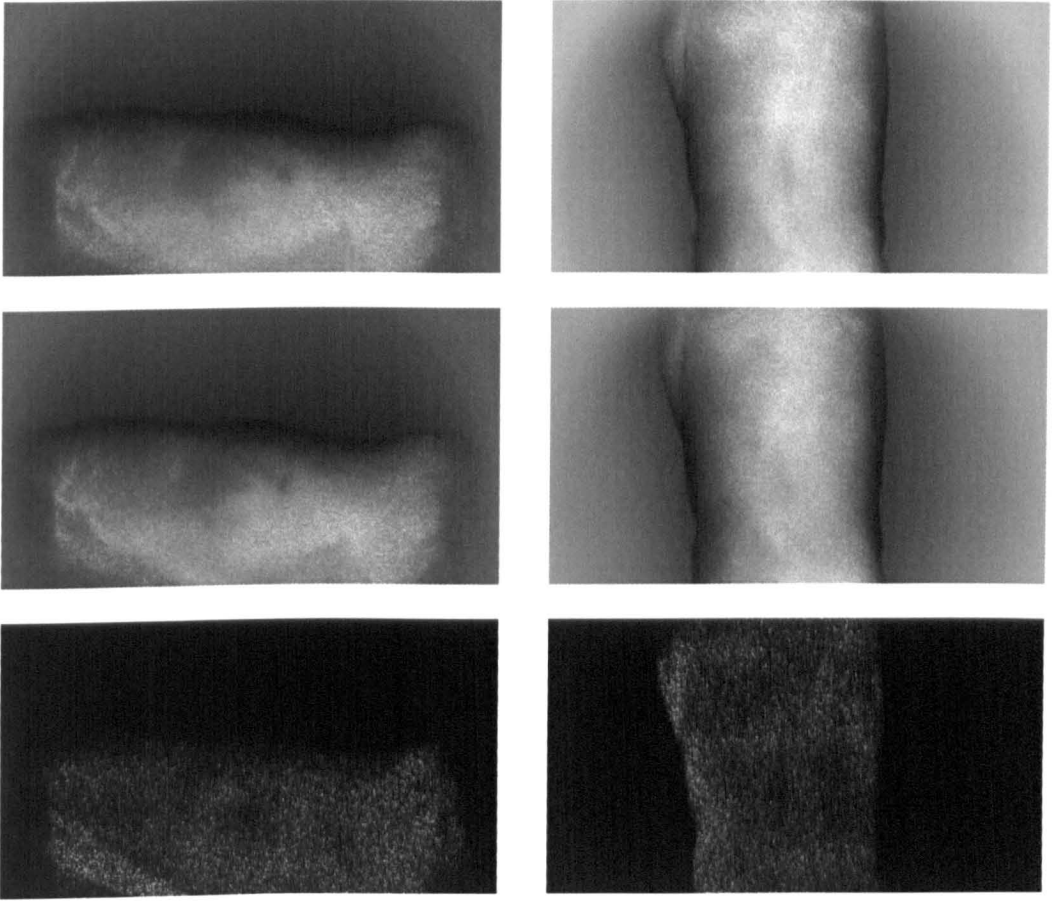
Figure 5.11: ROPI linear dichroism measurements of a tissue engineering tendon specimen orientated horizontally (column₁) and vertically (column₂). Illumination / detection polarized at row₁ = 0° / 90° and row₂ = 90° / 0°. Row₃ are the linear dichroism images calculated as (row₂–row₁) / (row₂+row₁). Each image is 9mm(H) × 5.5mm(V).

Although it is not obvious from figure 5.11, for the case of vertical measurement (column 2), the contrast of the *ROPI* image in row_1 is greater than that in row_2 and vice versa for the case of horizontal measurement (column 1). These are because the orientation of the specimen is co-aligned to the detection in column 2 while it is cross-aligned to column 1. This matches well with the expectation based on the theoretical investigation in chapter 2.

The mean linear dichroism value obtained for the horizontal specimen position is 0.0045 and -0.0049 for the vertical case. The values change from positive to negative whilst remaining similar in absolute value. This shows a good agreement with the theoretical expectation as only the specimen orientation is changed between the two measurements. However, comparing these values with those discussed in subsection 5.2.2, the values here are only slightly higher than that in the microsphere solution (0.003) which contains no polarization properties and are much smaller than those in the real tissues (0.013-0.07). These values indicate the specimen only contains a very small amount of linear dichroism. This was confirmed through discussion with the University of Keele.

5.3 Experiments in Transmission Mode

As *ROPI* in transmission mode is not preferred in practical applications, in this study, experiments in this mode are only performed for further evaluation of the technique. As shown in chapters 2 and 3, the measurement of linear birefringence of a target within a scattering medium is difficult to perform in reflection mode. This is due to the measurement requiring back-illumination with a linear polarization state, which is difficult to achieve in reflection mode, as backscattered photons are randomized with scattering. In this section, in order to experimentally complete the evaluation of the investigations presented in chapters 2 and 3, both the *ROPI* measurements of linear birefringence without and with a scattering medium are presented in transmission mode. This setup is used to simulate back-illumination of a birefringent target in reflection mode. The target is placed on the output surface of the cuvette and by varying the amount of scattering in the medium, the amount of polarized light back-

illuminating the target can be modified. In the extreme cases, the experiments without a scattering medium in subsection 5.3.1 show completely polarized back-illumination and demonstrate how linear birefringence can be measured with *ROPI*. The experiments with a scattering medium in subsection 5.3.2 show completely un-polarized back-illumination and the simulations (chapter 3) are confirmed experimentally.

5.3.1 Experiments of Linear Birefringence Measurements without a Scattering Medium

In this subsection, based on the principles generated in chapter 2, the *ROPI* experiments performed to measure linear birefringence of a retarder without a scattering medium using the standard setup shown in figure 4.16 in chapter 4 are presented. These involve the target orientated at 0°, 11.25° and 22.5° with the illumination / detection pairs polarized at 45° / 135° and 0° / 90°. The target is a *HWP* which provides a retardance of 180° and is 25.4*mm* in diameter. These measurements should provide linear birefringence values varying from the maximum (i.e. 1) to the minimum (i.e. 0). The experimental results are provided in figures 5.12 and 5.13.

Figure 5.12 shows the measurement images. Rows 1 to 3 represent the measurements of the target orientated at 0°, 11.25° and 22.5° respectively. The first column shows the images taken with the illumination / detection linearly polarized at 45° /135° and the second column shows the images taken at 0° / 90°. The third column shows the normalized linear birefringence images obtained by combining the images in columns 1 and 2 following equation 2.35 [i.e. (column$_1$ − column$_2$) / (column$_1$ + column$_2$)]. Each image in the figure is averaged from 10 single images taken sequentially with an integration time of 300*ms* and corresponds to an area of 9*mm*(H) × 7mm(V).
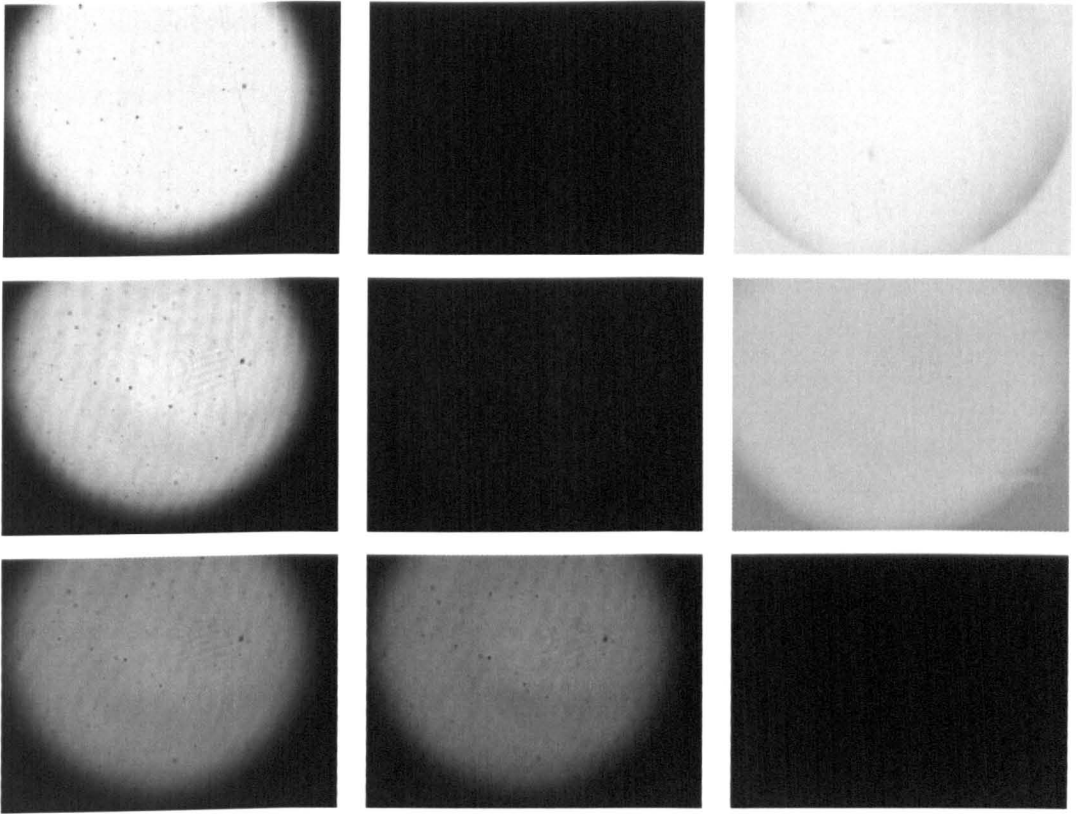
Figure 5.12: Images of ROPI linear birefringence measurements of a HWP orientated at rows 1 to 3 = 0°, 11.25° and 22.5°. Illumination / detection polarized at column₁ = 45° / 135° and at column₂ = 0° / 90°. column₃ = (column₁ − column₂) / (column₁ + column₂). Each image = 9mm(H) × 7mm(V).

In figure 5.12, as the illumination size (about 7.5mm in diameter) is smaller than the target (25.4mm), the photons detected are all filtered by the target. The ring seen in the images represent the detection aperture of the system. From top to bottom, the contrast of the images in column₁ reduces as the target orientation varies from 0° to 22.5°. This is due to the polarization state of the illumination after passing through the target becoming more and more cross-aligned to the detection. On the other hand, the contrast of the images in column₂ increases is because the illumination polarization states after the target become more co-aligned to the detection. The images in column₃, which represent the linear birefringence, vary from bright to dark and indicate

that the measurement values obtained vary from high to low. This qualitatively shows a good agreement with the expectation as discussed.

Figure 5.13 is the average line scan on the y axis of the images over rows 200 to 600 in column$_3$ in figure 5.12. These quantitatively represent the *ROPI* linear birefringence obtained. As shown, the values reduce from approximately 1 to 0 as the target orientation changes from $0°$ to $22.5°$. Although the variation is not ideal, as expected, it is considered a reasonable match as the values differ from the ideal ones by about 0.05 at maximum. The differences are believed to be because the target orientation is not controlled precisely enough as the rotating mount used for the target is only accurate down to around $2°$. The negative values in the $22.5°$ measurement case further indicate that the target orientation is not located precisely and the intensity of the subtracted image in column$_2$ is bigger than that in column$_1$.
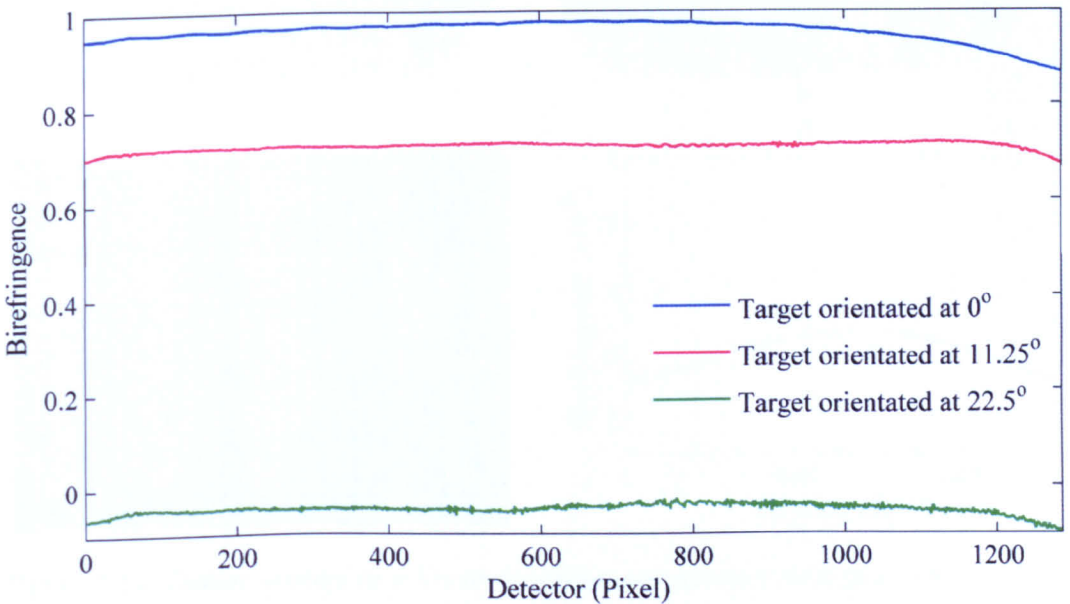
Figure 5.13: Average line scans on the y axis of the ROPI linear birefringence images at different orientations (i.e. images in column$_3$ in figure 5.12).

5.3.2 Experiments of Linear Birefringence Measurements with a Scattering Medium

This subsection shows experimentally the difficulty of measuring linear birefringence within a scattering medium for comparison with section 3.4. This involves measuring linear birefringence of a *HWP* located in front of a scattering medium and orientated at $0°$ using the standard setup shown in figure 4.16. The illumination / detection pairs are linearly polarized at $45°$ / $135°$ and $0°$ / $90°$. The scattering medium and *HWP* are those discussed in section 4.3 in chapter 4.
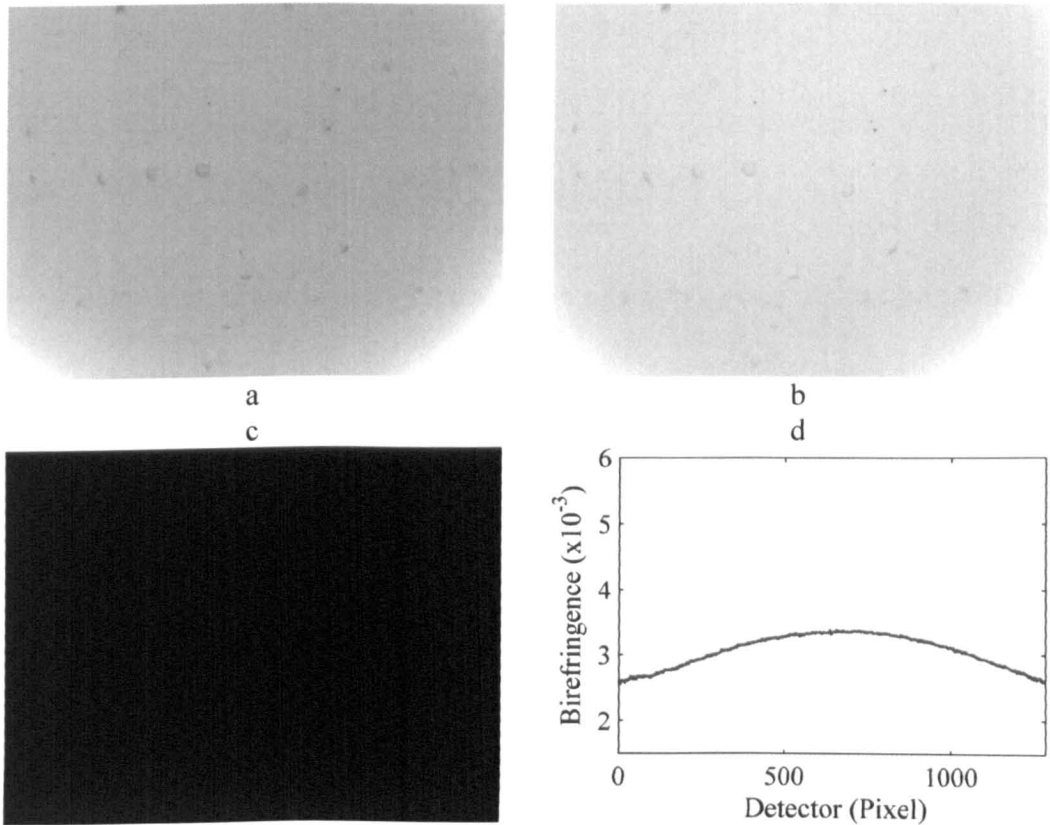
Figure 5.14: Demonstration of a linear birefringence measurement of a HWP located in front of a scattering medium and orientated at $0°$. a) imaging with the illumination / detection polarized at $0°$ / $90°$ and b) at $45°$ / $135°$. c) the image of birefringence combined by a) and b). d) the average line scan on the y axis of the image in c). Each image is 9mm(H) × 7mm(V).

In figure 5.14, a) is the image taken with the illumination / detection polarized at 0° / 90° and b) is the image taken at 45° / 135°. c) is the linear birefringence image obtained by combining a) and b) using equation 2.35. Figure 5.14d) is the average line scan on the y axis of the image over rows 200 to 600 in c), which quantitatively represents the linear birefringence measured. Each image corresponds to an area of $9mm$(H) × $7mm$(V). As the figure shows, as expected, by comparing to those obtained from MC simulations (figure 3.14, chapter 3) in terms of quality and quantity, similar images and values of linear birefringence are observed. These clearly indicate $ROPI$ experiments of measuring linear birefringence underlying a scattering medium cannot be performed when the back-illumination is randomly polarized.

5.4 Discussion and Summary

In this chapter, the experiments performed to study $ROPI$ using the standard (GT polarisers based) system described in chapter 4 in both reflection and transmission modes were presented. As $ROPI$ in reflection mode is preferred in practical applications and mainly evaluated in this study, most of the experiments were performed in this mode. Only the experiments that cannot be performed in reflection mode were investigated in transmission mode to complete the evaluation of $ROPI$.

Section 5.2 presented the $ROPI$ experiments in reflection mode. Firstly, in order to evaluate the investigations discussed in chapters 2 and 3, quantitative phantom measurements of linear dichroism of a polarizer embedded within a scattering medium at different depths were provided. Secondly, in order to demonstrate initially the feasibility of applying $ROPI$ in practice, preliminary measurements of linear dichroism of different real tissues (bovine tendon, lamb tendon, chicken breast and human finger

skin) and a tissue scaffold (tissue engineered tendon) orientated in two orthogonal directions were provided as well. Section 5.3 presented the *ROPI* experiments of measuring linear birefringence of a *HWP* without and with a scattering medium in transmission mode. The experiments without a scattering medium demonstrated how linear birefringence can be measured with *ROPI*. The experiments with a scattering medium show the difficulty of measuring linear birefringence with *ROPI* experimentally.

For the phantom linear dichroism measurements, qualitatively, the images and values over the target depth range show good agreement to those obtained by *MC* simulations (chapter 3). However, quantitatively, the linear dichroism values are still considerably smaller than the simulations. This is due to the effects of surface reflections and side contributions which will be discussed in detail in chapter 7 when further comparisons of all the *ROPI* results are provided.

In addition, it is important to consider how well the phantom experiment and its associated model represent real world applications. The phantom study in reflection mode indicates that the *ROPI* technique can provide sensitivity to polarizing targets down to a depth of 17*mfps*. For typical tissue parameters [95] this corresponds to a depth of 1.7*mm* within tissue, which falls within the correct depth range for polarized light measurement of tissue [95]. Of course, the phantom represents the case of an isolated polarizing target embedded within a scattering medium. This is a reasonable approximation in capillaroscopy in the case of imaging isolated red blood cells in relatively homogeneous tissue for assessment of linear dichroism within cells for applications such as sickle cell anaemia monitoring [6, 101]. It is also reasonable for applications such as targets located in turbid water or in fog [78] (although in both applications the target will have less polarization contrast than an isolated polarizer).

However in other applications such as the monitoring of collagen alignment within tissue, the situation will be more complicated as the entire volume probed by the light will affect the polarization. It will be the subject of future work to develop an inversion algorithm based on an appropriate model of the forward problem such as that developed by *Wang* and *Wang*[69]. This algorithm will need validation through comparison with histology. Even without such an algorithm, the technique provides an indication of collagen alignment as demonstrated by the images shown in subsection 5.2.2, which show polarization difference values for different types of tissue ranging from 0.07 for fibrous tendon down to 0.003 for a microsphere suspension. Through calibration with histology such measurements could be useful for monitoring growth of tissue in bioreactors.

For the preliminary measurements presented in subsections 5.2.2 and 5.2.3, first of all, it can be observed that the values taken from different bovine tendons vary from 0.05 to 0.07. This is due to the fact that the polarization properties of underlying tissues measured by *ROPI* are dependent on the tissue alignment direction. In order to have the maximum measurement, the axes of the tissue have to be properly aligned with those of the illumination or detection. Secondly, it should be pointed out that:

1) The tissue engineered tendon results are consistent with those obtained by using the technique of polarization sensitive optical coherence tomography (*PSOCT*). When *PSOCT* was applied to the same samples, the images demonstrated that the generation of a polarization difference image depends on the density of aligned collagen fibers and only very weak polarization difference signal can be measured [102]. *PSOCT* has the advantage that depth resolved measurements can be obtained; however, *ROPI* offers a simpler imaging system.

2) The real tissue results have not been validated using independent measurements or histology and this will be a subject for future research. They are very preliminary

and are shown mainly to provide an indication that the *ROPI* technique is sensitive to the polarizing properties of the underlying tissue.

3) As discussed in chapter 1, if imaging the alignment of fibrous tissue can be achieved then there will be many uses such as monitoring the healing state of burns and wounds. The results in this thesis demonstrate that the technique has potential but that the method is still far from meeting clinical needs. Further investigations of real tissues' physical and optical properties such as collagen alignment, structures and scattering are necessary in the future research towards taking *ROPI* into clinical applications. Furthermore, an accurate inversion algorithm still needs to be developed.

4) Strictly speaking, the use of *Mie* scattering as a tissue model may not be accurate as the *Mie* scattering conditions such as the assumption that the particles are spherical and widely separated are not present in real tissue. However, it is a reasonable simulation method for the tissue phantom studies in which spherical particles are used. In addition, as a first approximation, it is a widely used simulation method for light propagation in tissue [95]. Development of a more accurate simulation model for tissue will be one of the future challenges for the biomedical optics research community.

5) *ROPI* has the potential to measure the linear dichroism of tissue. Further clinical studies will be required to determine whether this is a useful clinical parameter by evaluating whether it correlates with, for example, the ability of a wound to heal without a skin graft. The mean linear dichroism across the target has been chosen in the tissue phantom studies to reduce the effects of noise. This measurement has been extended to the preliminary tissue experiments and provides an indication of the dichroism across a sample. This may be a useful parameter is some applications e.g. to provide an overall indicator of the alignment of an engineered tissue

in a bioreactor. However, many clinical applications will benefit from imaging the spatial alignment of collagen.

6) It has been reported previously that rotation of the analyzer may result in a spatial shift of the images in different polarization states [100]. In order to investigate whether the images are correctly aligned in different polarization states, a test experiment is performed by imaging a semi-infinite wide absorber in transmission mode. By using the setup shown in figure 4.16, the illumination was polarized at 45° and two images were obtained with the detection polarization states at 0° and 90° respectively. The line scans (averaged along the rows) of the images around the target edge are shown in figure 5.15. As the figure shows, although it is clear that the alignment between those two images is very precise as the edge of the absorber from the red and blue lines are almost accurately overlapped; there is still a very little misalignment between the *ROPI* images. A further detailed investigation is required. The intensity difference between the red and blue lines in the background area might be due to the polarization states being not accurately aligned; however, it allows the alignment problem to be initially investigated.
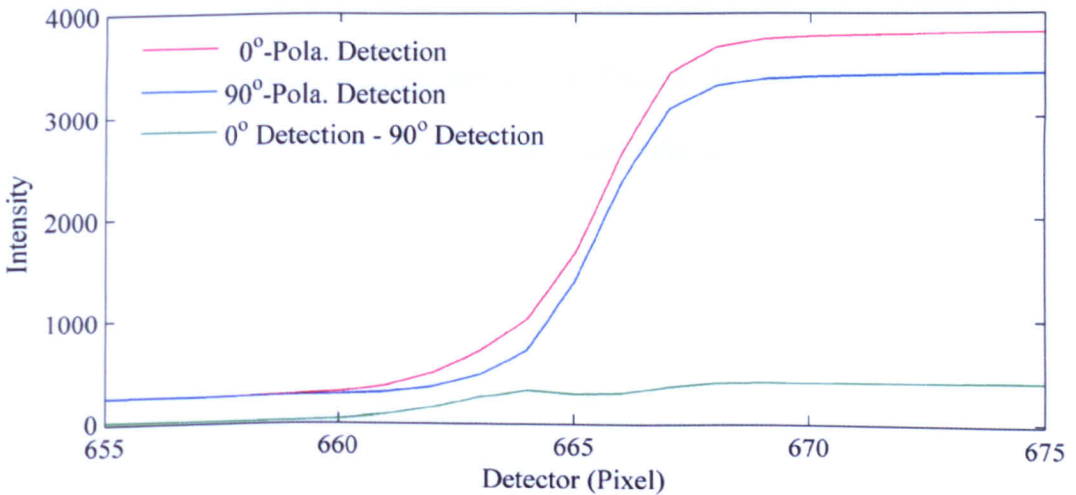
Figure 5.15: Average line scans of the alignment testing images of an absorber, which were obtained in transmission mode with illumination polarized at 45° and detection at 0° and 90°.

For the linear birefringence measurements, the phantom study in transmission mode, the *MC* simulations in chapter 3 and the theoretical Mueller calculus in chapter 2 all indicate that the *ROPI* technique can be applied for achieving the quantity measurements only if the polarization state of the back-illumination is the same as the original illumination before passing through the target. This has been found to be too difficult to be performed in the reflection mode. However, according to previous studies[79], it has been shown that linearly polarized light can probe depths of 34*mfps* and that deeper propagation (102*mfps*) can be obtained with circularly polarized light. It is also interesting to note that aligned structures such as chicken breast may allow polarized light to propagate even further[103], thereby allowing monitoring of birefringence at greater depths than that could be obtained in homogeneous scattering media.

In conclusion, the theoretical and simulated *ROPI* investigations presented in chapters 2 and 3 have been studied experimentally in this chapter. The preliminary *ROPI* measurements of different real tissues and a tissue scaffold have been demonstrated. Rotating both the illumination and detection polarization states to maintain orthogonal detection allows polarization sensitive measurements of the underlying tissue to be obtained that are free from surface reflections. These reflections can be from the air-tissue interface and also from optical components within a co-axial imaging system.

Chapter 6

ROPI Phantom Experiments in Liquid Crystal Mode

6.1 Introduction

One important aspect of successfully applying *ROPI* is the precise orientation of both input polarization states and analysers. This includes maintenance of the orthogonality of illumination and detection. As shown in chapter 4, the standard phantom experimental setup is based on the use of Glan-Thompson (*GT*) polarisers with the polarization states being manually controlled. Although the rotating mounts used to hold the polariser and analyser can be precisely controlled to within 5" (i.e. 0.083°), there are still unavoidable errors due to the accuracy and precision achievable. To a degree, these issues could be addressed through application of motorized stages. In addition, as shown in figure 5.15, there is also a potential error due to the displacement of the images before subtraction arising from slight changes in the optical path [100]. This could be overcome by applying software based image alignment algorithms [104]. However, neither motorized stages nor post-capture correction provides an ideal solution that could be applied easily in clinical practice.

In order to enhance the performance of the technique, a modified approach based on liquid crystal variable retarders (*LCVR*) that permits easy control, in terms of the automatic rotation of the polarization states of the illumination and detection, is inves-

tigated. The *LCVR* based system has no mechanical moving parts and has advantages in terms of its ease of use, speed, repeatability and elimination of errors due to both misalignment of the images and manual alignment. Furthermore, the modified approach is an important step towards taking the technique into routine clinical use.

The incorporation of *LCVR* into polarization microscopy has been an important development in the field of microscopy. For example the *LC Polscope* [100] has been demonstrated to provide results that compare well with conventional polarization microscopy and has resulted in a commercial device that has found widespread application [105; 106]. The main objective of this chapter is to investigate whether the *LCVR* based system is suitable for *ROPI* by performing comparisons with the previous system and *MC* simulations and allow the technique to become more robust and widely used. The phantom experiments in reflection mode described in chapter 5 are repeated with a detailed comparison presented in chapter 7.

Within this chapter, section 6.2 describes the *LCVR* devices and demonstrates the principles of operation over the full range of linear polarization states. The experimental system and related calibration is described in section 6.3. Measurement results are provided in section 6.4, followed by discussion and summary in section 6.5.

6.2 Linear Polarization Operations with *LCVR*

In this section, a preliminary study of the *LCVR* device is provided. Firstly, the *LCVR* device is introduced; secondly, the principles of controlling the full range of linear polarization states using the *LCVR* device are demonstrated schematically and mathematically.

6.2.1 Introduction of *LCVR*

Before introducing *LCVR*, general retarders along with their effect on linearly polarized light are briefly introduced (more details about these can be found elsewhere [86]).

A retarder (or waveplate) is an optical device that resolves a light wave into two orthogonal linearly polarized components (*s*- and *p*-component) and produces a phase shift which is also specified as a retardance (δ) between the components. The phase shift is caused mainly by the orthogonal components being transmitted through the retarder with different velocities since retarders have different refractive indices (n_e and n_o) in orthogonal directions known as the *fast* and *slow* axes respectively. In addition, the phase shift also depends on the thickness of the retarder (*d*) and the wavelength of incident light (λ). The equation for calculating a phase shift (or retardance) of a light wave transmitted through a retarder is given by equation 6.1.

$$\delta = |n_e - n_o| d / \lambda \qquad (6.1)$$

The resulting light wave generally has a different polarization state that depends on the phase shift produced between the orthogonal components and the angle between the retarder fast axis and the input plane of polarization. Table 6.1 provides an overview of different polarization states that could be obtained from horizontal linearly polarized input light over the full range of variations of retardance that could be applied for the retarder.

Ideally, retarders do not polarize and also do not induce an intensity change in the light wave; they just change its polarization state due to the phase shift generated. Therefore, a retarder can be used to change the polarization state of input light. However, as a retarder normally only has one fixed retardance, it is only able to change the

input polarization from one state to another fixed state under the same orientations. Hence, it is difficult to change the retardance and hence change the input polarization state during the experiment, which is an essential condition for applying *ROPI* as at least two orthogonal linearly polarized inputs are required. Thereby, *LCVRs* or phase modulators which have the ability of electrically and sequentially controlling phase delay in the propagating light are introduced for this study.

Linearly Polarized Input	Retardance	Polarized Output
←——→	$\delta = \lambda/2$	↕
←——→	$\lambda/4 < \delta < \lambda/2$	(vertical ellipse)
←——→	$\delta = \lambda/4$	(circle)
←——→	$0 < \delta < \lambda/4$	(horizontal ellipse)
←——→	$\delta = 0$	←——→
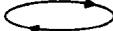
Table 6.1: Output polarization forms from different retardance values of a retarder with a horizontal linearly polarized input.

LCVRs are solid-state, real-time, continuously and electrically variable waveplates which are made by placing a thin nematic liquid crystal layer between parallel windows spaced a few microns apart as illustrated in figure 6.1 [107]. Nematic liquid crystals are materials whose effective birefringence (i.e. the difference between two refractive indices in orthogonal directions) can be changed by varying an applied voltage. The retardance of a *LCVR* can be altered continuously from 0-wave to full-wave by applying a variable low voltage (e.g. $\cong 6.5V$ and $1.4V$ for 0- and full-wave respectively) waveform, thus altering the polarization state of the transmitted light.
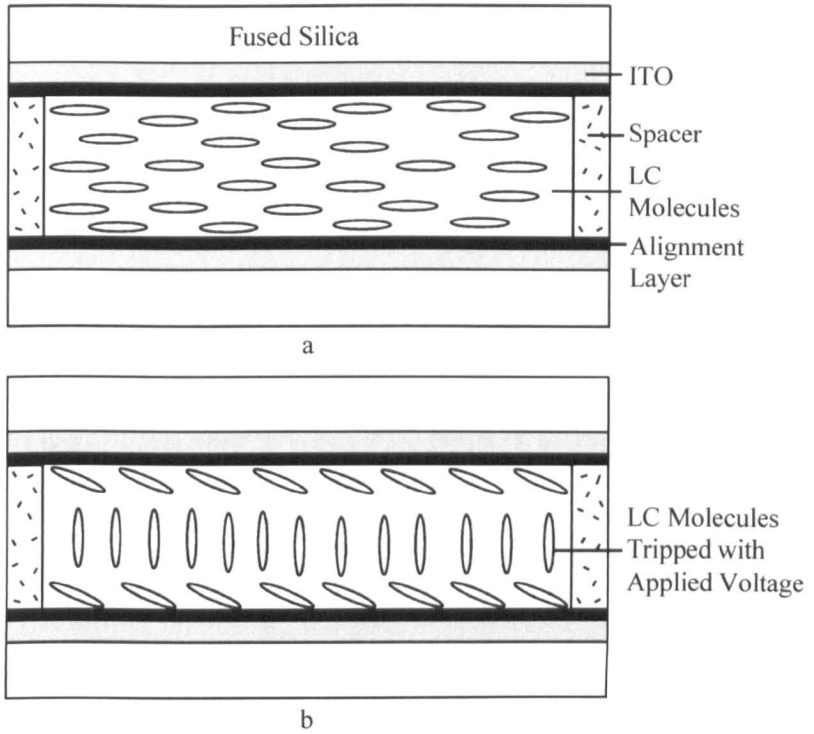
Figure 6.1 [107]: Liquid Crystal Variable Retarder construction showing molecular alignment (a) without and (b) with applied voltage. ITO represents Indium Tin Oxide.

Figure 6.1 shows the structure before and after applying a voltage to one of the most commonly used *LCVRs* made by *Meadowlark Optics*. As the figure shows, a *LCVR* is constructed using optically flat fused silica windows coated with transparent conductive Indium Tin Oxide (*ITO*) which is specially designed for maximum transmission for the wavelength region from 450*nm* to 1800*nm*. A thin dielectric layer is applied over the *ITO* to provide for liquid crystal (*LC*) molecular alignment. Finally, the two windows are then aligned and spaced a few microns apart and the cavity is filled with birefringent nematic *LC* material. As shown in figure 6.1a, with no voltage applied, the *LC* molecules lie parallel to the windows and maximum retardance is obtained. However, as shown in figure 6.1b, when a voltage is applied, the *LC* molecules begin to tip towards the direction perpendicular to the silica windows. As the voltage increases, the *LC* molecules tip further causing a reduction in the effective birefringence and hence, retardance.

In addition to the drive voltage applied, the retardance also depends on the operating wavelength and temperature. Therefore, to precisely obtain a particular retardance, it is important to consider these effects with calibration often employed. By combining the use of *LCVRs* with other optical components, it is possible to implement electrically controllable linear polarization rotation over the full range, as required for *ROPI*.

6.2.2 Full Range Linear Polarization Operations

An optical arrangement applied for electrically controlling linearly polarized light output in the full range from $0°$ to $90°$ from a randomly polarized input light source is shown in figure 6.2. As can be seen, in addition to the *LCVR*, a fixed linear polarizer (*LP*) and a fixed quarter-waveplate (*QWP*) are also required. The position and orientations of the components are determined using Mueller calculus. The *LCVR* is located in the middle between the *LP* and the *QWP*. The slow axis of the *LCVR* is orientated at $45°$ to the fast axis of the *QWP* and the *LP* is orientated in parallel to the fast axis of the *QWP*. It is also possible to orientate the *LP* perpendicularly to the fast axis of the *QWP*; in this case, the polarization of output will be varied from $90°$ to $0°$ rather than from $0°$ to $90°$.

As shown in figure 6.2, the *LP* is first applied to linearly polarize the randomly polarized input light; the *LCVR* is then used to convert the linearly polarized light to elliptically polarized in different forms depending on the retardance applied; and finally the *QWP* transforms the different elliptical polarizations to linear polarizations. Without manually rotating any of the components in the arrangement, the output polarization can be linearly rotated over the full range from $0°$ to $90°$ by electrically controlling the retardance of the *LCVR* from half-wave to 0-wave.
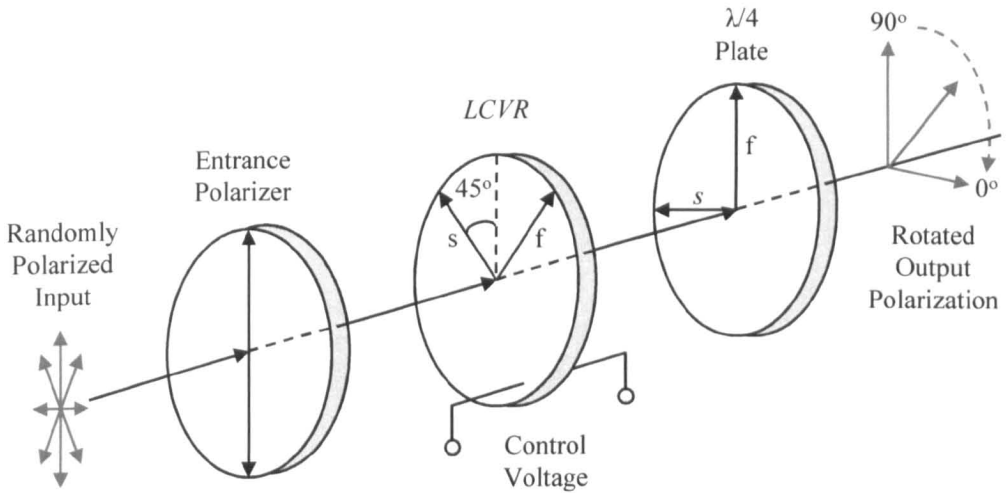
Figure 6.2: Schematic representation of the means of generating the full range linear polarized light from a randomly polarized input by applying a LCVR. 's' and 'f' respectively represent the slow and fast axes of the devices.

By representing the arrangement mathematically using Mueller calculus, it can be directly verified that if the *LCVR* is set with retardance of $0°$ (i.e. 0-wave), the randomly polarized input light will become vertical linearly polarized after passing through the *LP*, and maintain this state after passing through the *LCVR* and *QWP* as both the 0-waveplate and the *QWP* (whose fast axis is orientated at $0°$ with respect to the polarizing direction of input) will not affect the polarization state. If the *LCVR* is set with a retardance of $180°$ (i.e. half-wave), the final output will be horizontally linearly polarized as the input becomes vertically linearly polarized after the *LP*, then horizontally linearly polarized after the half-wave plate and is maintained horizontally linearly polarized again after the *QWP* (as the linear polarization will not be changed as the fast axis of the *QWP* is orientated at $90°$ to the polarizing direction). If the *LCVR* is set with a retardance of $90°$ (i.e. quarter-wave), the final output will be $45°$ linearly polarized as the input is vertically linearly polarized after the *LP*, then circularly polarized after the first *QWP* (as its fast axis is orientated $45°$ to the input linear polarization direction), and finally $45°$ linearly polarized after the second *QWP* (as the fast axes of

the *QWPs* are orientated 45° apart). The Mueller calculus for the generations of other states from the arrangement is shown in appendix D.
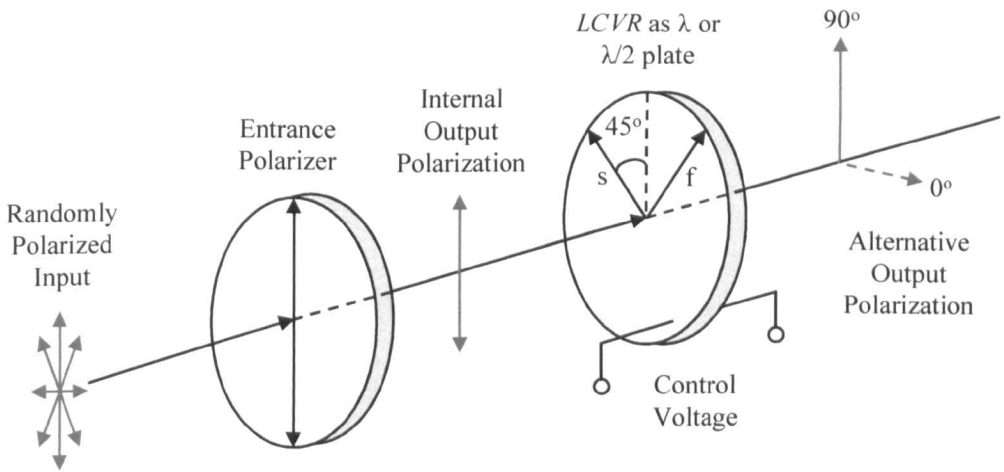
Figure 6.3: Schematic representation of the generation of either horizontally or vertically linear polarized light from a randomly polarized input by applying a LCVR. 's' and 'f' respectively represent the slow and fast axes of the device.

For a simple case where only the generation of horizontally or vertically orientated linearly polarized light is required from a randomly polarized input, a simple arrangement modified from the previous arrangement shown in figure 6.2 can be used as given in figure 6.3. This arrangement is identical to that in figure 6.2 but without a fixed *QWP*. The alternative orthogonal linearly polarized output can be simply achieved by using the *LCVR* as either a half-waveplate or a 0-waveplate (or λ-waveplate).

As described in chapter 1, for the *ROPI* phantom experimental studies, as the polarization state of the target within the scattering medium is known, only two pairs of orthogonal linearly polarized illumination / detection are required to complete a single measurement. Therefore, for the phantom experimental studies presented in this chapter, all of the experiments are performed using the arrangement of polarization optics

shown in figure 6.3. However, for the general case that the polarization state of the target is unknown, as at least three pairs of orthogonal illumination / detection are required. Therefore, the arrangement described in figure 6.2 is required.

6.3 Characterization of the *LCVR* Based *ROPI* Phantom Experiment System

This section describes the characterisation of the *LCVR* based *ROPI* experimental setup in reflection mode. As a similar setup has been presented in detail in chapter 4, the description and calibration will mainly concentrate on the differences between the two systems.

6.3.1 Design of Experimental Setup

The *LCVR* based experimental setup is shown in figure 6.4. Pictures showing the actual setup along with the *LCVRs* are given separately in appendix C. The only difference between figure 6.4 and the previous setup (figure 4.1), where control of the polarization states is manual, is the application of *LCVRs*.

Comparing figure 6.4 and figure 4.1, the difference in the illumination arm is that the *HWP* in figure 4.1 is replaced by a variable retarder *(LCVR₁)* in figure 6.4. In the detection arm, there is an extra variable retarder *(LCVR₂)* inserted between the *BS* and the *GT* polarizer. The orientations of both *LCVRs* are set so that the fast axes are located at 45° with respect to the polarizing directions of the linear polarisers.

With this setup, there are two ways to set the retardance of the *LCVRs* in order to generate two orthogonal linearly polarized illumination / detection pairs dependent on
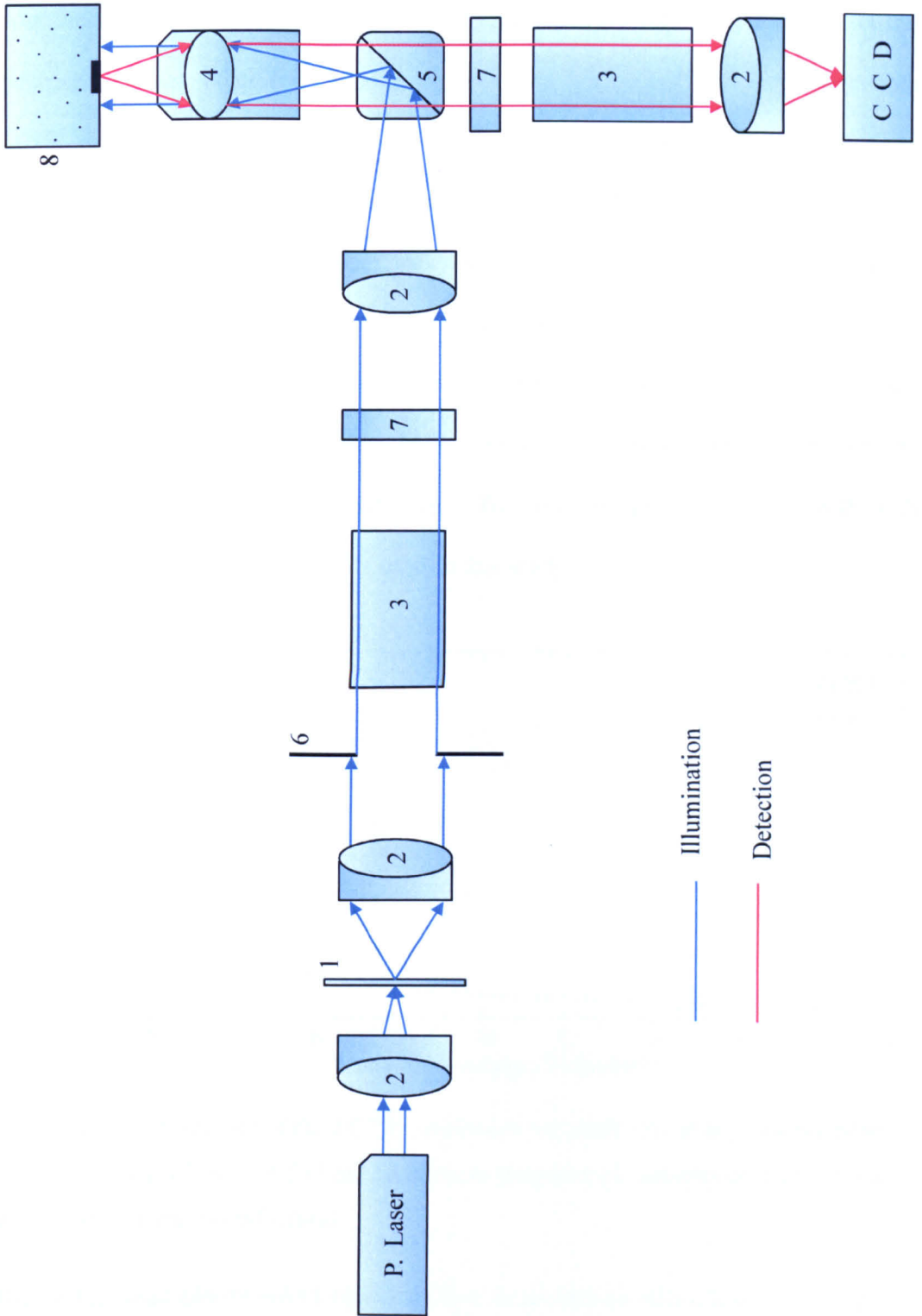
Figure 6.4: ROPI experimental setup in reflection mode for studying phantoms using a LCVR. 1) Ground glass rotating diffuser, 2) Positive achromatic doublet lenses, 3) Glan-Thompson polarisers, 4) Infinite conjugate microscope objective, 5) Cube beam splitter, 6) Iris diaphragm, 7) LCVR, 8) Sample.

how the axes of the linear polarisers are orientated. With both the polarisers set co-polarized to each other (either both are polarized horizontally or vertically); both $LCVR_1$ and $LCVR_2$ can be set as either a $\lambda/2$-waveplate or a λ-waveplate but have to be different from each other. Alternatively, with both the polarisers set cross-polarized to each other (either both are cross-polarized from horizontal to vertical or vice versa); both the $LCVR_1$ and $LCVR_2$ have to be set as either a $\lambda/2$-waveplate or a λ-waveplate simultaneously. However, as the laser applied is vertically polarized, the polarizer in the illumination arm has to be polarized in a vertical direction in order to transmit illumination from the light source. Thereby, the first arrangement with both polarisers set vertically polarized is used in this study.
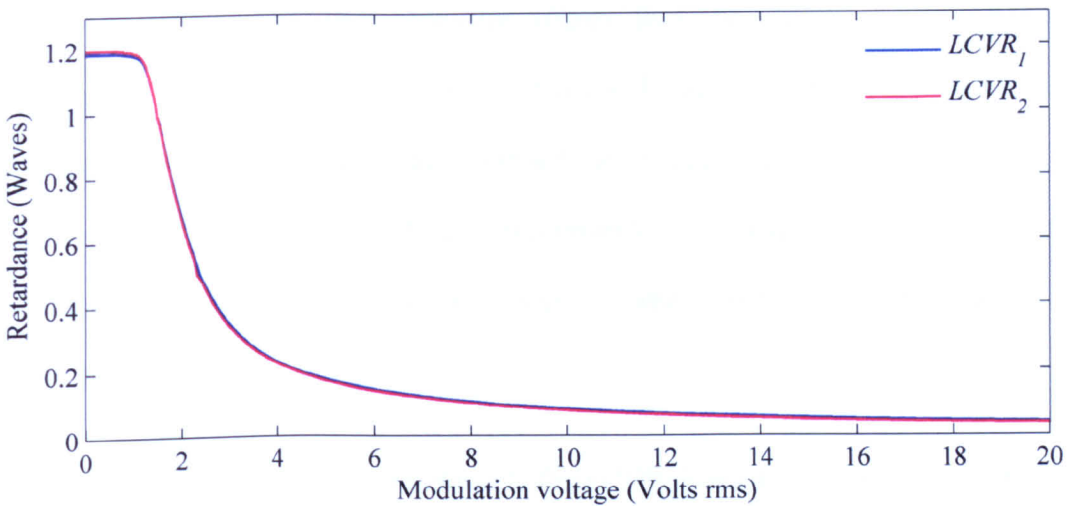
Figure 6.5: Performance of the LCVRs applied in the study versus applied modulation voltage at a wavelength of 632.8nm and room temperature according to the supplied datasheet from the manufacturer.

The *LCVRs* used (*Meadowlark Optics LVR-0.7*), are driven with a $2kHz$ square-wave voltage, with the retardance controlled by changing the amplitude of the signal over the range from 1 to $20V$. Retardance is affected by the operating wavelength and temperature and according to the datasheet, the overall retardance of a *LCVR* decreases

with increasing temperature by approximately 0.4% per ^{o}C. The retardance versus voltage curves of the LCVRs applied in the study at a wavelength of 632.8nm and room temperature are supplied by the manufacturer and shown in figure 6.5. It can be seen that the performance of the LCVRs are slightly different but that the retardances from both curves cover the range from almost a 0-waveplate to more than a full-waveplate. These are sufficient for providing the horizontal and vertical polarization states required for the phantom experimental studies. The 0-waveplate is required if the full range linear polarization from 0° to 180° is required.

The ability of the LCVRs to achieve retardances of a half wave and full wave were tested. Overall, the voltages that have to be applied to both retarders to obtain the specified retardance are not significantly different from the retardance-voltage curves supplied by the manufacturer. However, it is confirmed that temperature affects the retardances obtained, as the voltages applied vary temporally. Therefore, it is necessary to calibrate the system each time experiments are performed and constant temperature operating environments are strongly recommended. Calibration details are given in the next subsection.

The characteristics, indicating retardance, for $LCVR_1$ is shown in figure 6.6. The result for $LCVR_2$ is not shown as it is almost identical. The testing was implemented using the arrangement shown in figure 6.3 with a linear polarizer used to analyze the output polarization. With the retarder set to a half- and a full-waveplate ($2.310V$ and $1.436V$) sequentially, the analyser is rotated from 0° polarized to 180° polarized with a step size of 10°. As the figure shows the intensities measured for both cases vary sinusoidally as expected, and in anti-phase to each other. This indicates the retarder is performing well as the specified waveplates. Furthermore, from the measured values, the

extinction ratio calculated from minimum / maximum is approximately 4×10^{-4}. Although this rejection (value) is not as low as that provided by the *GT* polarisers applied in the previous setup, it is still sufficient for the experiments as the sensitivity of the *CCD* limits the rejection ratio to about 10^{-2}, as discussed in chapter 4.
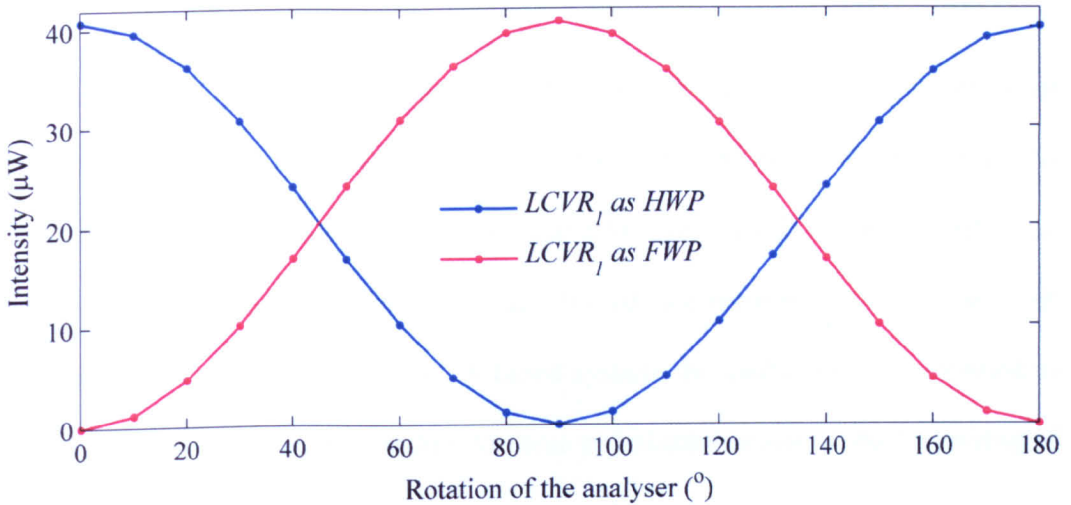
Figure 6.6: Testing performance of the LCVR₁ as a half-waveplate (2.310V) and a full-waveplate (1.436V) through the arrangement shown in figure 6.3 with an analyser applied to analyse the output polarization.

6.3.2 Calibration of the System

One of the key factors in achieving optimum *ROPI* system performance is to control the orthogonality of the illumination and detection channels. Theoretically, this should be easy to achieve by simply using a pair of cross polarised linear polarisers. However in practice, experimental errors; as discussed in chapter 4; are unavoidable and calibration to obtain the optimum polarization states for the illumination and detection within the system is required.

For the *LCVR* based system, the calibration described in chapter 4 is essential. For the system using *GT* polarisers, calibration of the system is only required once; however,

for the *LCVR* based system, as the retardance is temperature dependent, calibration of the system is required each time the system is used (unless the system is located in an environment under a constant temperature). Although this is inconvenient for these experiments, it is not a problem that cannot be overcome and therefore it is worth pursuing as it is an essential step towards clinical application.

As discussed, only linear polarization states at $0°$ and $90°$ are suitable for the phantom experiment studies in this work due to restrictions imposed by the beam splitter. As the target polarization state within the medium is known, only illumination / detection pairs orthogonally polarized at $0°$ / $90°$ and $90°$ /$0°$ are required to implement each measurement. Therefore, for the *LCVR* based system, the calibration is performed to set the *LCVR* voltages corresponding to these polarization states at the beginning of each experiment.

By replacing the sample with a mirror in the setup shown in figure 6.4, the polarization states for illumination and detection are obtained in sequence by changing the retardance of the *LCVRs* step by step until the minimum intensities in the *CCD* position are obtained. The calibration results are summarily shown in table 6.2 and are compared with those obtained from the standard mode from table 4.2. The rejection ratios in both cases are worse in the *LCVR* based mode. This is possibly due to the retardance being temperature dependent and the fact that the voltages applied are not controlled precisely enough as the voltage resolution provided by the controller is only $1mV$. It was also found that the orientation of the *LCVR* optical axis varies with varying voltage and the retardance with time has a small drift under a constant drive voltage [108]. Any of these will result in the *LCVRs* not behaving as $\lambda/2$- and λ-waveplates precisely, which will reduce the rejection ratio significantly.

Finally, although the rejection ratios from the *LCVR* based system are worse than those from the *GT* polarizer based system, it is still sufficient for the experiments. This is due to the sensitivity of the *CCD* which, calculated as the inverse of the *SNR*, is about 10^{-2} and hence dominates the contributions to the rejection ratio of the system in the sense of $\sqrt{A^2 + B^2}$, where *A* and *B* are the errors from *LCVRs* and *CCD* respectively.

Parameters	Linear Polarization States (illumination / detection)	
	0° / 90°	90° / 0°
Illuminations (*GT₁ at 90° + LCVR₁*)	2.354*V* (as λ/2)	1.447*V* (as λ)
Detections (*LCVR₂ + GT₂ at 90°*)	1.464*V* (as λ)	2.301*V* (as λ/2)
Rejection Ratio ($\times 10^{-3}$) (*GT* mode vs. *LCVR* mode)	0.531 vs. 1.89	0.578 vs. 1.91

Table 6.2: Calibration results of linear polarization states applied for illumination and detection with the LCVR based ROPI experimental system.

6.4 *LCVR* Based Phantom Experiments

In this section, *ROPI* experimental phantom studies using the *LCVR* based system are presented. To evaluate the performance, the linear dichroism measurements described in chapter 5 are repeated. This involves quantitative measurements of the maximum linear dichroism of a target orientated at 0° and located at depths of 0, 2, 5, 10, 12, 15 and 17*mfps* within a scattering medium in reflection mode.

The procedures followed are the same as those described in chapter 5. The routine used to calibrate non-uniform illumination is applied and the quantities of the meas-

urements are calculated using equation 2.25. The scattering medium used for these experiments is the same as that specified in table 4.1. The target is also the same as the one applied previously with a slight difference in dimensions which are 0.75*mm* thick with 8.5*mm* long and 0.85±0.05*mm* wide.

6.4.1 Results

The *LCVR* based system shown in figure 6.4 was used to perform reflection mode *ROPI* measurements of linear dichroism of a polarizing target at different depths within the scattering medium. The experimental results are presented in figures 6.7-6.10 and the images shown are generated with calibration for non-uniform illumination as described at the beginning of the section.

Figure 6.7 shows the *ROPI* images formed with the polarization axis of the illumination orientated vertically (i.e. 90°) and that of the target orientated horizontally. The target depths are 0, 2, 5, 10, 12, 15 and 17*mfps* and each image corresponds to an area of about 9*mm*(H) × 7*mm*(V). Figure 6.8 shows the case of *ROPI* images formed with the polarization axes of both the illumination and the target orientated horizontally. As previously discussed, the polarization axis of the detection is always orientated orthogonally to that of the illumination. Each image is averaged from 10 single images taken sequentially with an integration time of 100*ms* for each image. The contrast is greater in figure 6.8 than in figure 6.7 at the same depth because the target and detection polarization axes are orientated orthogonally to each other. The contrast in both the figures is reduced as the target depth is increased due to the increase in scattering effects. Figure 6.9 shows the linear dichroism images calculated at the corresponding depths using the normalized images in figures 6.7 and 6.8 following
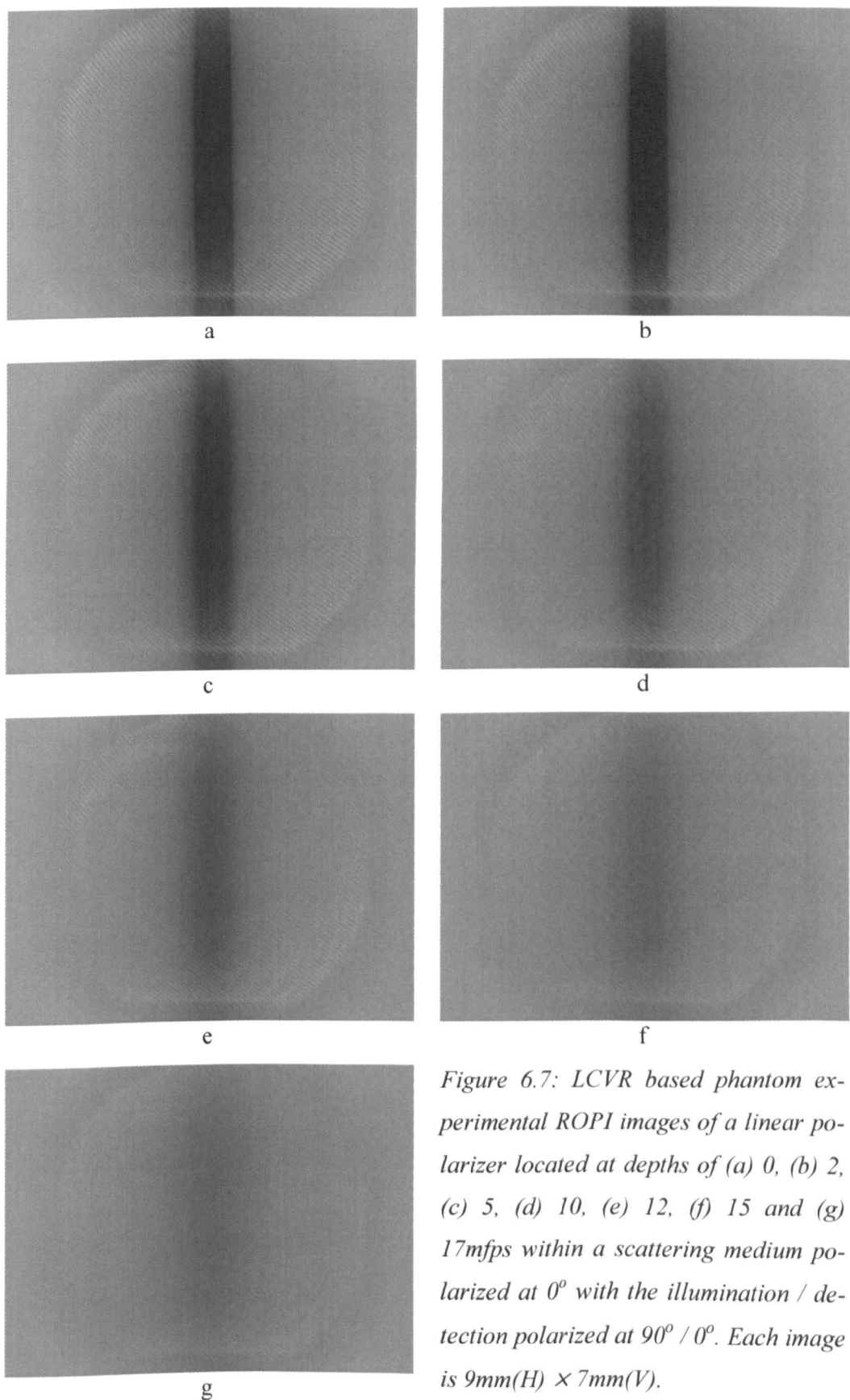
Figure 6.7: LCVR based phantom experimental ROPI images of a linear polarizer located at depths of (a) 0, (b) 2, (c) 5, (d) 10, (e) 12, (f) 15 and (g) 17mfps within a scattering medium polarized at 0° with the illumination / detection polarized at 90° / 0°. Each image is 9mm(H) × 7mm(V).
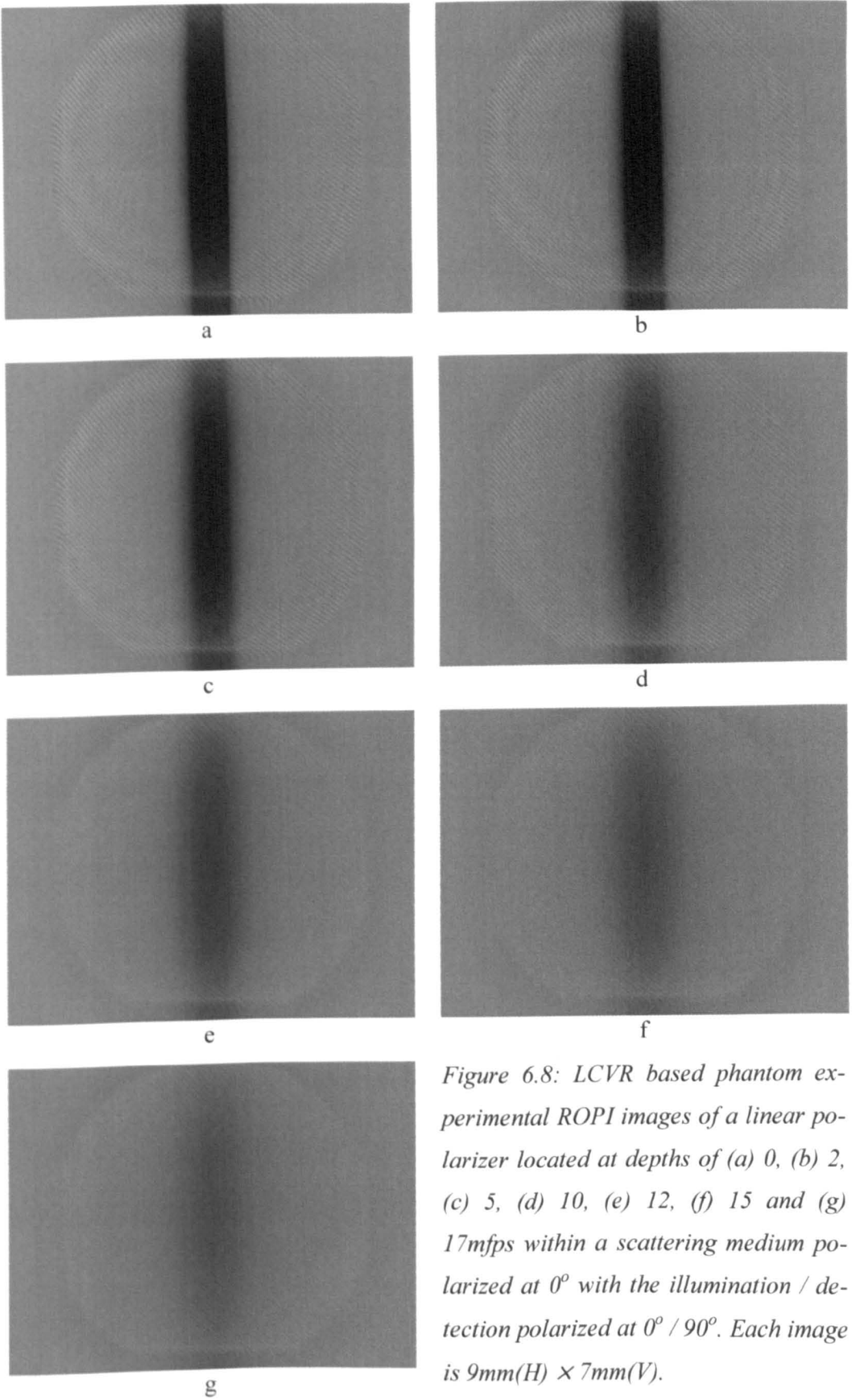
Figure 6.8: LCVR based phantom experimental ROPI images of a linear polarizer located at depths of (a) 0, (b) 2, (c) 5, (d) 10, (e) 12, (f) 15 and (g) 17mfps within a scattering medium polarized at 0° with the illumination / detection polarized at 0° / 90°. Each image is 9mm(H) × 7mm(V).
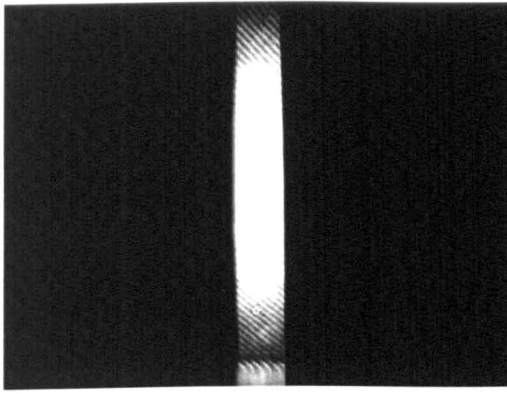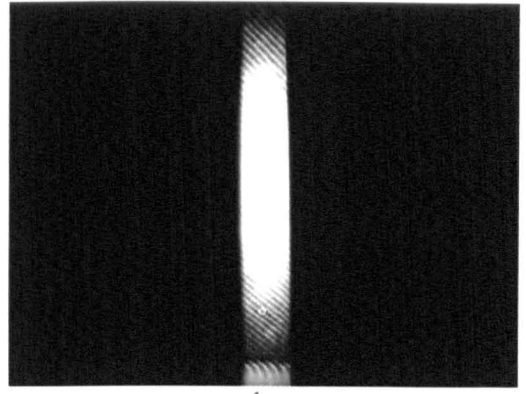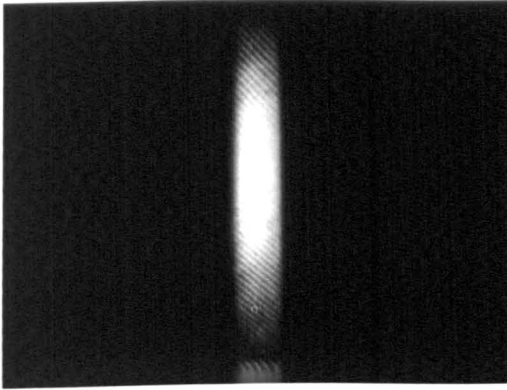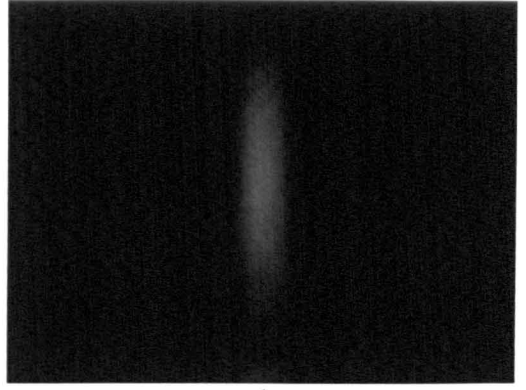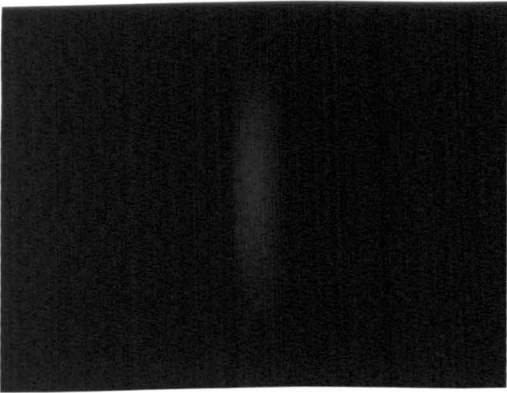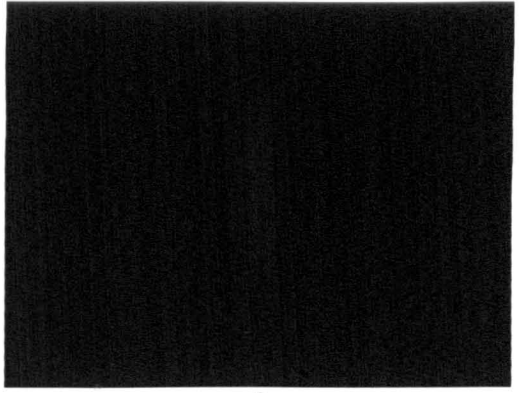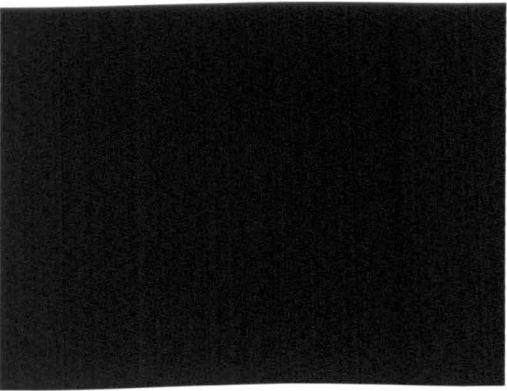
Figure 6.9: LCVR based phantom experimental ROPI images of linear dichroism of the polarizer located at depths of (a) 0, (b) 2, (c) 5, (d) 10, (e) 12, (f) 15 and (g) 17mfps within a scattering medium. The images are obtained by combining figures 6.7 and 6.8. Each image is 9mm(H) × 7mm(V).
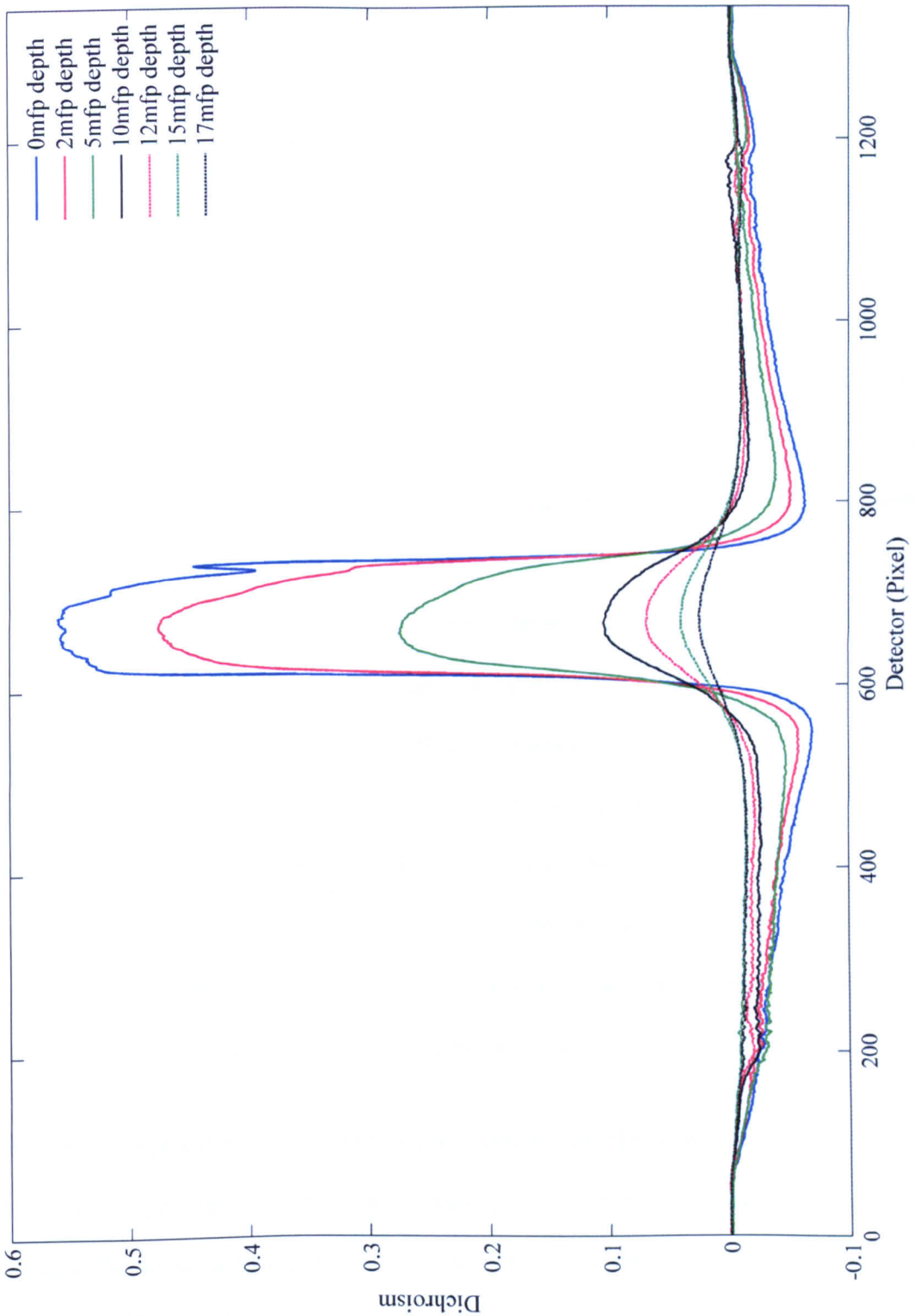
Figure 6.10: Average line scans on y axis of the images in figure 6.9 that quantitatively show the LCVR based phantom experiments of the ROPI linear dichroism measurements at different target depths within a scattering medium.

equation of 2.25. As expected, the contrast of these images also gradually reduces as the target depths increase due to scattering.

The fringes that can be observed in all images in figures 6.7 and 6.8 are the interference pattern caused from surface reflections from the optical components and the cuvette. Theoretically, these surface reflections should be eliminated by cross-polarized detection; however, in practice, due to the polarization controlling components in the system not being ideal and the effects from the *BS* (as discussed in chapter 4), there are always some reflections detected. Furthermore, as a normalisation is performed for calibrating the non-uniform illumination for every image (subsection 4.2.2), these reflections should be cancelled further. However, as the calibration is not ideal as discussed previously in subsection 4.2.2; these reflections still exist and hence the fringes are observed. The fringes change with target depth since the cuvette is moved in order to vary the depth. In figure 6.9, the fringes can hardly be seen in the background area of the dichroism images because the surface reflections are cancelled out when the normalisation is performed (equation 2.25). However, as the rejection ratios shown in table 6.2 are not equal to each other, the cancellation is not exact and the fringes at the target ends where the surface reflections are extra contributed are still visible. This effect reduces as the target depth increases.

By comparing these results with the same phantom experiment results in figures 5.3-5.5 from the previous system, it can be clearly seen that the *ROPI* images from both cases at the same depths compare well. The fringes are more visible in all images from the *LCVR* based system because the rejection ratios given in table 6.2 are not as good as those given in table 4.2 and more surface reflections contribute to the images. Furthermore, this problem also causes the dichroism value to be reduced, which is

clearly indicated in figure 6.10. By comparing to the same simulation results of figures 3.7-3.9 in chapter 3, similar observations can be made.

Figure 6.10 shows the line scans obtained by averaging over the middle 300 rows of the dichroism images in figure 6.9. This quantitatively represents the linear dichroism measurements obtained. Compared with corresponding line scans in figure 5.6 in chapter 5, it clearly shows that the trends of the line scans in both figures vary in the same way in terms of *a)* the measured dichroism being reduced as target depths increase; *b)* the dichroism obtained at a depth of 17*mfps* is very close to 0; *c)* the dichroism value on each line scan is always negative outside the target region and the negative maximum is always at both edges of the target. As discussed in chapter 5, this is mainly because the polarization states applied for the illumination and the target in one case are co-aligned to each other whilst in the other case are cross-aligned to each other, which results in the intensities detected outside the target region in both cases being different. A plot comparing the linear dichroism values shown in figures 5.6 and 6.10 will be presented in chapter 7.

Finally, although the images shown compare well with those from the standard system, the measured dichroism at a depth of 0*mfp* from the *LCVR* based system is substantially smaller than that from the standard system. This is due to the presence of more surface reflections on detection caused by the poorer rejection ratios of the *LCVR* based system. However, as mentioned in chapter 5, these reflections can be significantly reduced by performing a further calibration. This will be described and discussed in more detail in chapter 7 when the results obtained from both systems are compared further. Moreover, further calibrated results will be presented and compared along with an investigation into why the measurements from the phantom ex-

periments after the further calibration still differ from the ideal case from the *MC*

simulations as shown in figure 3.10.

6.5   Discussion and Summary

An important step towards taking the *ROPI* technique into clinical practice is to con-

trol the polarization states for the illumination and detection automatically. This has

been achieved by applying a *LCVR* based system. The ability of the *LCVR* based sys-

tem to perform *ROPI* measurements on phantom samples has been demonstrated.

Section 6.2 introduced an optical system that could be applied for *ROPI* and is built

from a *LCVR*, a fixed linear polarizer and a fixed λ/4-waveplate. It allows the genera-

tion of controlled linear polarization states. A simplified *LCVR* arrangement is also

introduced that uses only a single *LCVR* and a fixed linear polarizer which can be ap-

plied for generation of the 0° and 90° linear polarization states. This arrangement is

applied in the experimental imaging setup for investigating phantom targets as only

two polarization states are required for completing the *ROPI* measurements when the

target orientation is known. Section 6.3 characterizes the *LCVR* based system. It is

found that the rejection ratios of the *LCVRs* are not as good as the *GT* polarisers (table

6.2). Section 6.4 presents the phantom experiments that have been performed using

the *LCVR* based system. The experiments measure the linear dichroism of a polarizing

target whose polarizing axis is orientated at 0° and is located within a scattering me-

dium at different depths. Images are formed with two orthogonal pairs of illumination

/ detection linearly polarized at 0° / 90° and 90° / 0°.

The *LCVR* based system provides results which, qualitatively, compare well with

those obtained from the previous *GT* polariser based system. The imaging results ob-

tained provide confidence that the automatic rotation system may replace the manual rotation system. As tables 6.2 and 4.2 indicate, there is a slight reduction in performance that is because the rejection ratios of the polarizations provided by controlling the *LCVRs* are not as good as those provided by controlling the *GT* polarisers. However, automatically controlling the polarization is preferred as it removes the need for manual or mechanical component rotation. The *LCVR* based system is a significant step forward in the development of a robust device that can be taken into the clinic or biology laboratory. This has been demonstrated in microscopy to be an important step forward to the widespread use of a technique. For example introducing liquid crystals into a polarized light microscope has resulted in a robust commercial microscope, the *LC Polscope*[100].

Imperfections of the *LCVRs* include: (a) that the retardance of the *LCVRs* is temperature dependent and cannot be controlled precisely enough as the controller cannot provide a small enough voltage resolution [107; 109]; (b) the optical axis orientation of the *LCVRs* is found to vary with varying voltage, although theoretically it should not [108; 110] and (c) a small drift of retardance with time is also found under a constant drive voltage [108; 110].

Therefore, for future research into improving the automatically controlled system based on *LCVRs*, the following should be investigated: (1) a constant temperature operating environment, a pre-calibrated temperature-retardance lookup table or use of a temperature controller; (2) a better controller providing better voltage resolution; (3) alternatively, use of an electro-optic modulator which is a more stable and with a precisely controllable phase-shift [108].

In conclusion, the *ROPI* technique had previously been implemented using the *GT* polariser based system with manual rotation of the polarisers to obtain illumination

and analysis of the light. Although the system could be implemented using motorized rotation stages, there are disadvantages in terms of image alignment and ease of use of the system in practical applications. The *LCVR* based system which is introduced and demonstrated in detail in this chapter provides an important step forward in making this technique clinically applicable. Moving parts are removed and the imaging performance is comparable to that obtained with previous systems. A detailed comparison of both will be performed in the next chapter.

Chapter 7

MC Simulation and Phantom Experiment Results: Further Comparisons

7.1 Introduction

In the previous chapters, the *ROPI* technique has been fully investigated through measurement of the polarization properties of a target submerged within a scattering medium. These were provided via mathematical Mueller calculus in chapter 2; ideal *MC* simulations in chapter 3 and practical phantom experiments in two different configurations in chapters 5 and 6 respectively. The same results obtained from different chapters have been briefly compared as the results were presented. As described, although the images obtained are qualitatively comparable, the line scans (figures 3.10, 5.6 and 6.10) indicate quantitative discrepancies between the results. In order to further understand the technique, a more thorough comparison of the results from the different chapters will be presented here.

As eventual applications of the technique in practice are likely to be in reflection mode, this further comparison will focus on these results, and specifically upon the quantitative linear dichroism measurements and resolution of the images. These will be described in sections 7.2 and 7.3 respectively. A discussion and summary is contained in Section 7.4.

7.2 Dichroism Comparison

The results have shown measurements of the linear dichroism of a polariser submerged within a scattering medium at depths of 0, 2, 5, 10, 12, 15 and 17*mfps* using *MC* simulations in chapter 3, phantom experiments with *GT* polarisers and *LCVRs* based systems in chapters 5 and 6 respectively. In this section, a further comparison of the linear dichroism values obtained from those results is performed.

Figure 7.1 shows how linear dichroism varies with target depth for the three different test regimes. The dichroism values are obtained from the mean dichroism along the central band of the target in the dichroism images such as those given in figure 3.9. The error bars in the experimental results represent the standard deviation of measurements from repetition of the experiments. For the *MC* results, the error bars are obtained from the standard deviation of results from running independent simulations.

As the figure shows, qualitatively, the simulated and experimental measurements are well matched. The linear dichroism values obtained reduce as target depth increases with reducing gradients due to reduction of the degree of polarization between the target and sample's surface. The size of the error bars increase as depth increases. This indicates that the quality of measurements is reduced as depth increases, which is due to the effects of scattering between the target and the surface increase with increasing depth. However, quantitatively, the dichroism values obtained in the simulations are significantly higher than those obtained with the experiments and those obtained from the *GT* polarisers based system are slightly higher than those obtained with the *LCVRs* based system across the entire depth range.

As discussed in chapter 5, the two main reasons leading to the differences in measured linear dichroism between the *MC* simulation and phantom experiments are (i)
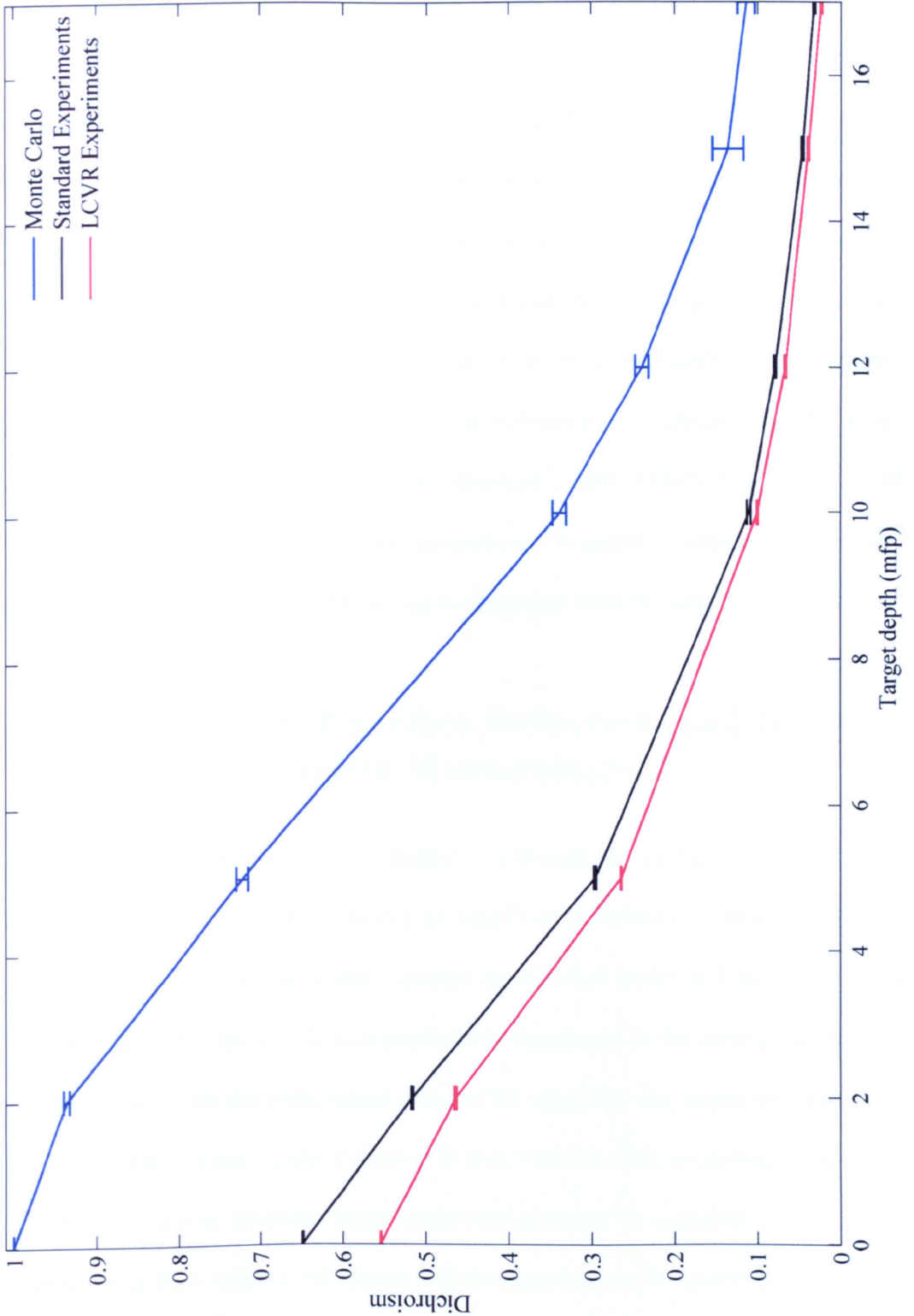
Figure 7.1: Quantitative comparison of linear dichroism measurements of a polarizer embedded at different depths within a scattering medium through applying MC simulations and the phantom experiments in standard and LCVRs based systems.

surface reflections from both the optical components and the cuvette not being completely eliminated by the polarizing components as they are not ideal; (ii) side contributions from the target edges as it is not ideal and has finite thickness. As discussed in chapter 6, the main reason for the differences between the experiments is because the rejection ratios in the *LCVRs* based system are poorer than those in the *GT* polarisers based system and more surface reflections contribute to the images. In order to improve the accuracy of the measured linear dichroism values and further understand the experimental results, the effect due to surface reflections is calibrated and the effect due to side contributions which cannot be calibrated is further investigated. These will be examined in detail in the next two subsections. In addition, experimental results after calibration will be demonstrated and re-compared with the simulation results.

7.2.1 Calibration of Surface Reflections and Its Effect on Dichroism Measurements

As discussed in subsection 5.2.1 in chapter 5, although the surface reflections from the cuvette and optical components can be significantly reduced by orthogonally polarized detection, there is still a small amount of reflection which will be detected and will contribute to the images. This is particularly significant in the cross-polarized imaging case (i.e. where the polarization states of the detection and target are orthogonal to each other) where the signal of interest is low. Theoretically, according to equation 5.1, which is used to calculate linear dichroism (recalled as equation 7.1), with the contribution of these surface reflections (R), the equation can be rewritten as equation 7.2.

$$LD = \frac{Im_{co} - Im_{cross}}{Im_{co} + Im_{cross}} \tag{7.1}$$

$$LD' = \frac{(Im_{co} + R) - (Im_{cross} + R)}{(Im_{co} + R) + (Im_{cross} + R)}$$

$$= \frac{Im_{co} - Im_{cross}}{Im_{co} + Im_{cross} + 2R} \qquad (7.2)$$

By comparing equations 7.1 and 7.2, this clearly indicates that the calculated dichroism (i.e. LD') will be smaller than anticipated (i.e. LD) as $R > 0$, (i.e. $LD' < LD$). Therefore, in order to recover accurate measures of linear dichroism in the presence of surface reflections, calibration is required. It should be noted that it is not possible to easily calibrate surface reflections in the case of co-polar detection in conventional polarization difference imaging as these tend to dominate the image.

In order to clarify the description of the calibration, the following images are firstly defined:

- Im_{co} and Im_{cross}: ROPI images which are taken with the target embedded within the scattering medium with the orientation of the target *co-* and *cross-* aligned to the detection respectively;

- BG_{co} and BG_{cross}: Background images which are taken of the scattering medium without the target present using the same orientations of illumination / detection that are applied for Im_{co} and Im_{cross} respectively;

- R_{co} and R_{cross}: Reflection images which are taken with the target embedded within water (no scattering present) with the orientation of the target co and cross aligned to the detection respectively;

- R_{BGco} and $R_{BGcross}$: Background reflection images which are taken of water in the cuvette without a target present and with the same orientations of illumination / detection that applied to Im_{co} and Im_{cross}.

According to equation 7.2, the removal of surface reflections can be achieved by performing $(Im_{co}+R)-R$ and $(Im_{cross}+R)-R$ before the dichroism is calculated. This suggests that only an image formed solely by R (the image in water) is needed. However, as the intensity of illumination for Im_{co} and Im_{cross} is slightly different (subsection 4.2.2), there are also differences in the surface reflections. Therefore, two reflection images, R_{co} and R_{cross}, are required to calibrate Im_{co} and Im_{cross} respectively. It should be noted that the calibration is not ideal because the R images also contain some reflected light from the back surface of the cuvette which is not present in the Im images.

Background images, BG_{co} and BG_{cross}, are required for normalizing non-uniform illumination (subsection 4.2.2) for Im_{co} and Im_{cross} respectively. Therefore, two more surface reflections images, R_{BGco} and $R_{BGcross}$, are required for calibrating the surface reflections for BG_{co} and BG_{cross}. As an example, the surface reflection images obtained at $0mfp$ from the standard system are shown in figure 7.2. In the figure, the black band in a) and b) is the target. The ring in the images is the field of view of the system. The fringes in the images are an interference pattern due to light not being rejected by cross-polarized detection.

To summarise, surface reflection calibration is performed using the following steps:

- Record images of Im_{co}, Im_{cross}, BG_{co}, BG_{cross}, R_{co}, R_{cross}, R_{BGco} and $R_{BGcross}$;

- Perform $(Im_{co} - R_{co})$, $(Im_{cross} - R_{cross})$, $(BG_{co} - R_{BGco})$ and $(BG_{cross} - R_{BGcross})$;

- Use $(BG_{co} - R_{BGco})$ to calibrate for the non-uniform illumination in $(Im_{co} - R_{co})$ and $(BG_{cross} - R_{BGcross})$ to calibrate for the non-uniform illumination in $(Im_{cross} - R_{cross})$.
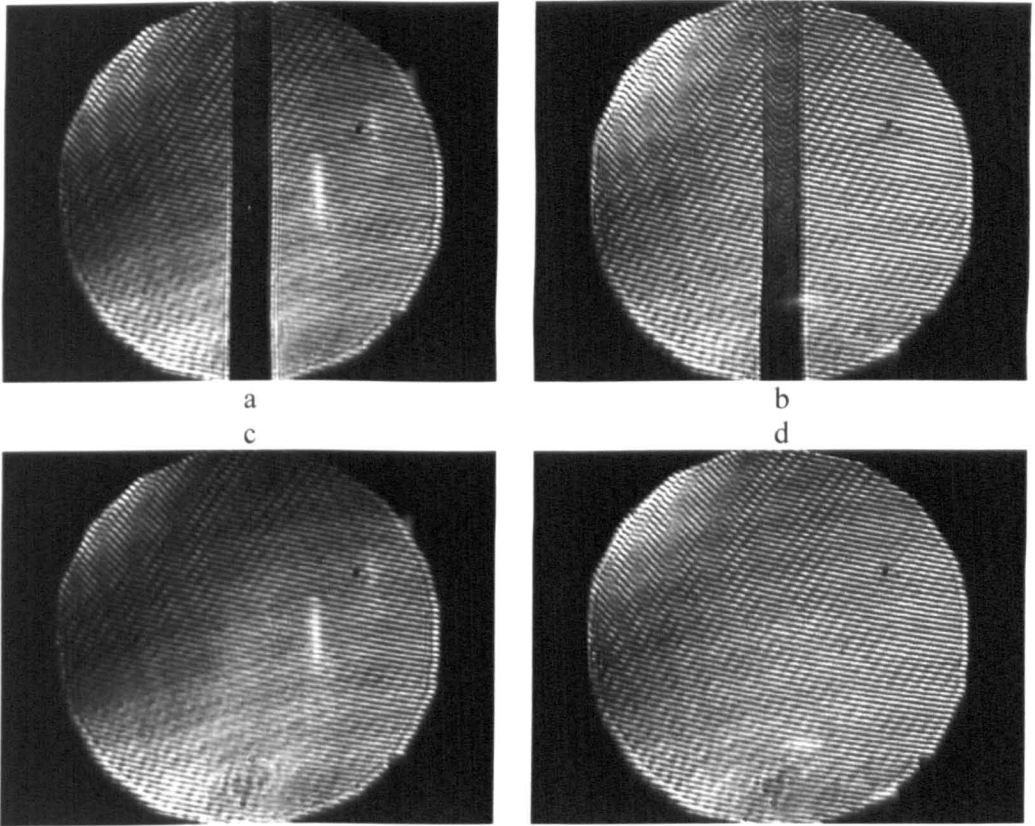
Figure 7.2: Demonstration of the surface reflection images (obtained at 0mfp in the standard system) required for the calibration of surface reflections for a linear dichroism measurement in reflection mode. a) is R_{cross}, b) is R_{co}, c) is $R_{BGcross}$ and d) is R_{BGco}.

After performing calibration, the recorded images and their respective average line scans for a target at a depth of 0*mfp* from both the *GT* polarisers and *LCVR* based systems are shown in figures 7.3 and 7.4 respectively. As the figures show, comparing with those values obtained before performing the calibration (figure 7.3f with figure 5.6 and figure 7.4i with figure 6.10), the dichroism value obtained in figure 7.3f is significantly increased from 0.68 to 0.88 and, from figure 7.4i, from 0.58 to 0.89. This further confirms that contributions from surface reflections are larger in the *LCVRs* based system due to poorer rejection ratios. However, qualitatively, comparing images in figures 7.3abc and 7.4abc with those without the calibration in figures 5.3a-

5.5a and 6.7a-6.9a respectively, the image quality in figures 7.3 and particularly 7.4, is significantly reduced. The poorer quality is because of the poorer rejection ratios in the *LCVRs* system.

a   b   c
d   e   f
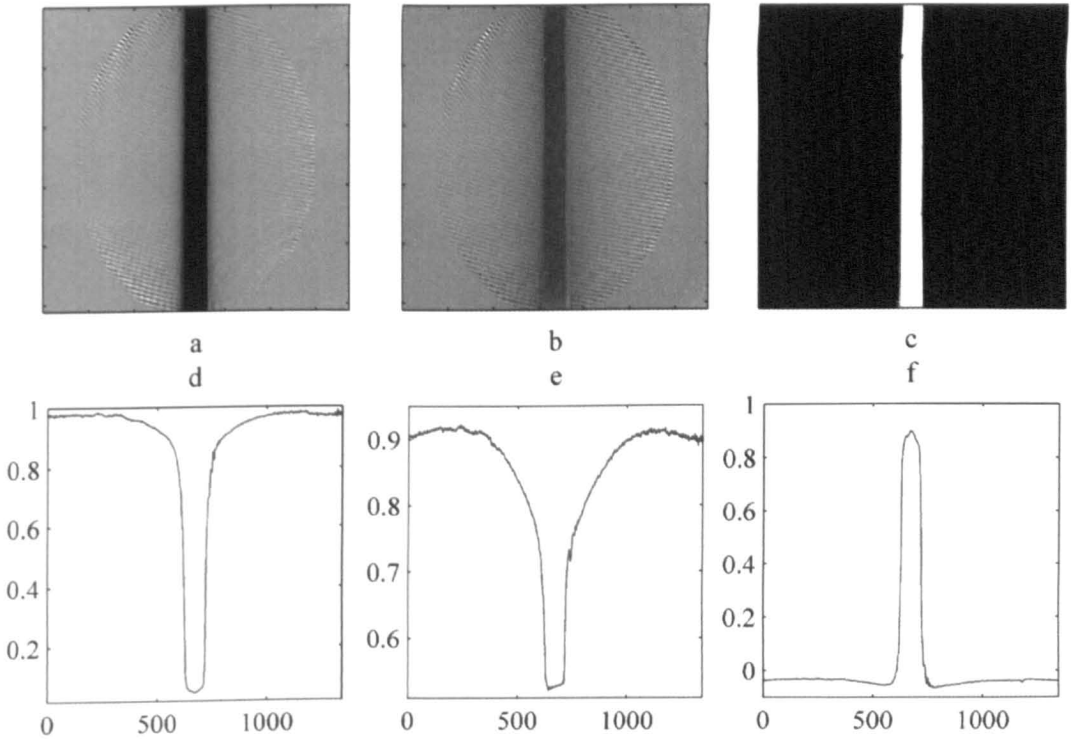
Figure 7.3: GT based experimental results of measuring linear dichroism of a target located within a scattering medium at 0mfp after the calibration of surface reflections. a) image of cross-detection, b) co-detection, c) dichroism, and d), e), f) are the respective average line scans on y axes of the images. Units of x axis is Pixels, y is Intensity for d), e) but Dichroism for f).

As figure 7.3 shows, a ring with fringes in images a) and b) outside the target area is observed. This is due to the calibration not being ideal as the reference images R contain interference fringes. This is especially obvious around the edge areas of the ring where back illumination intensities are weaker. Although the remaining reflections should be further removed when the background normalisation (subsection 4.2.2) is performed, due to the normalisation not being ideal; the remaining reflections remain. This ring is hardly observed from images in figures 5.3a and 5.4a because the surface

reflection intensities are much weaker than those from the back illumination. In figure 7.3c, the ring can hardly be seen because the remaining surface reflections are reduced when normalisation is performed (equation 5.1). However, as the rejection ratios shown in table 4.2 are not equal to each other, the cancellation is not exact and the fringes at the ring edge are still visible.
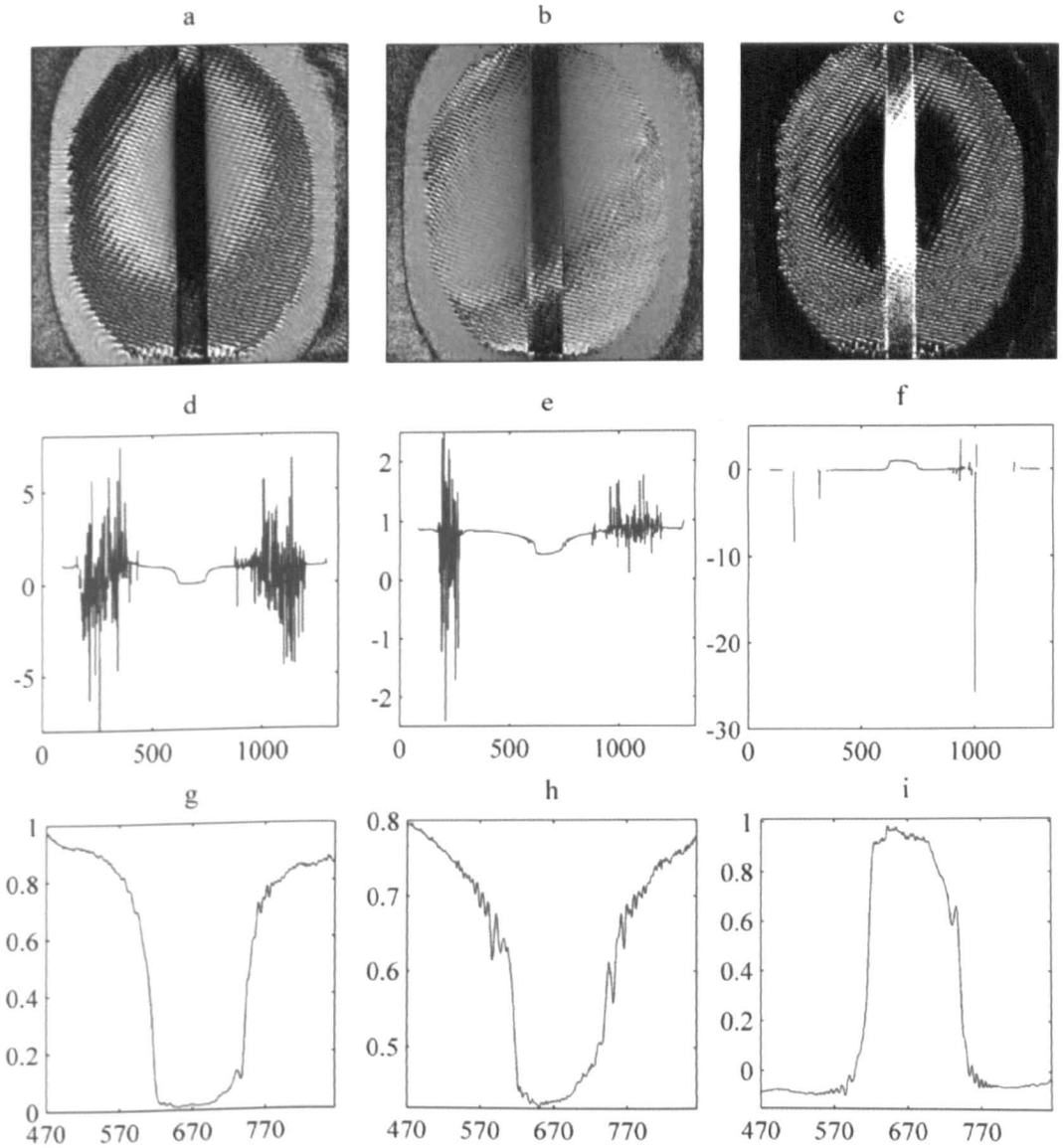
Figure 7.4: LCVR based experimental results of measuring linear dichroism of a target located within a scattering medium at 0mfp after the calibration of surface reflections. a) image of cross-detection, b) co-detection, c) dichroism. d), e) and f) are the respective average line scans on y axes of the images. g), h) and i) are respective the middle part of d), e) and f). Units of x axis is Pixels, y is Intensity for d), e), g) and h) but Dichroism for f) and i).
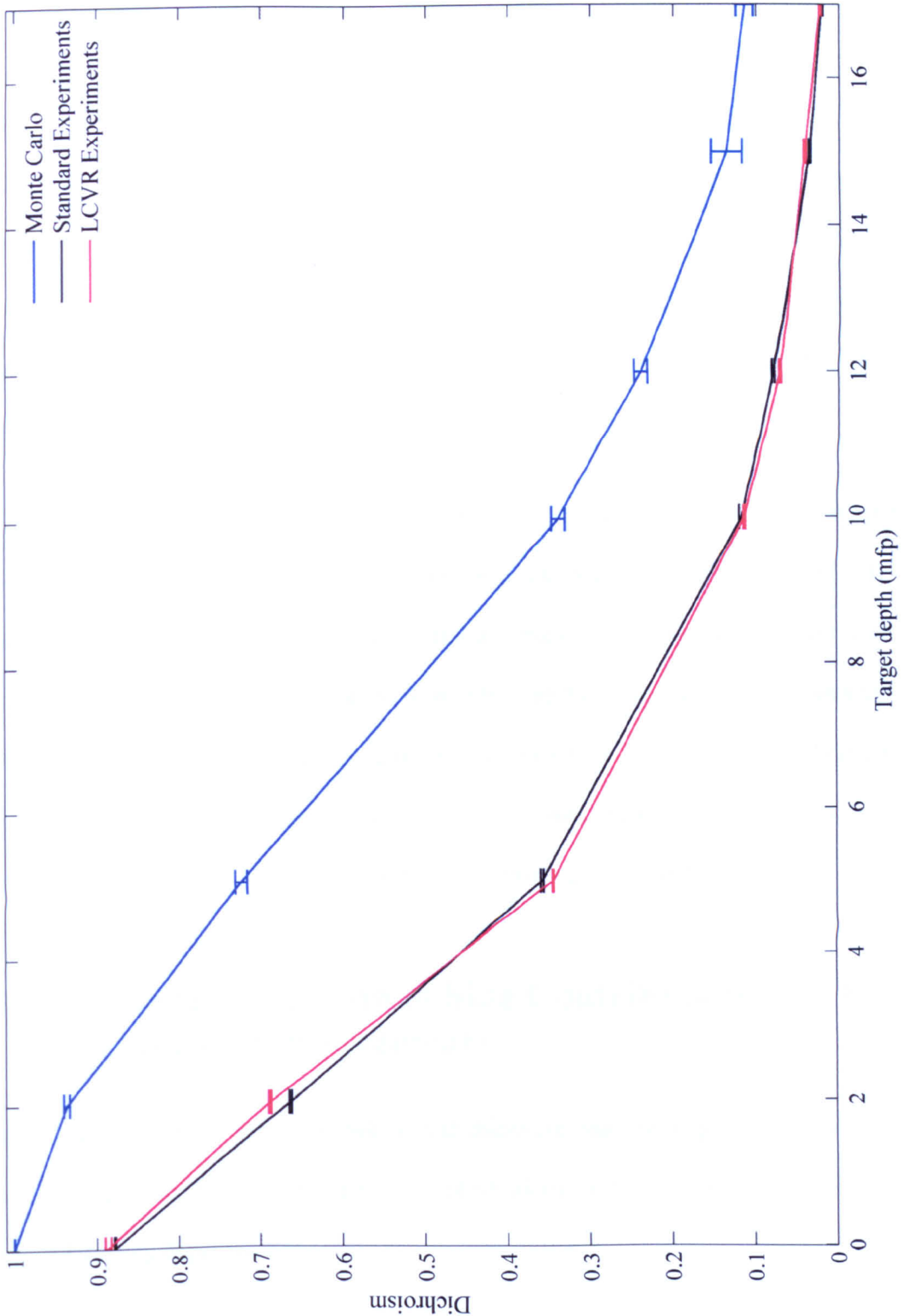
Figure 7.5: Quantitative re-comparison of the linear dichroism measurements shown in figure 7.1 but after applying a calibration of surface reflections for the experimental results.

The image quality is much poorer in the _LCVR_ system (figure 7.4). The outer ring in images a), b) and c) indicates the aperture size of the _LCVRs_ based system. The inner ring (also seen in figure 7.3) is caused by the size of the illuminating beam. The inner ring with fringes is more visible than that in figure 7.3 because of the poorer rejection ratios in the _LCVRs_ system and hence more surface reflections contribute to the images. Due to these effects, as the images in figure 7.4 a), b) and c) show, measurement can only be performed for a small area at the centre of the images where the image quality remains reasonable. These regions of interest are shown in g), h) and i).

The overall dichroism values from both simulation and experiments that have been compared in figure 7.1 without surface reflection calibration are re-compared in figure 7.5 with the calibration. As shown, the accuracy of the dichroism values from both experimental systems is closer to those obtained from theory. This indicates that most of the surface reflections are removed by calibration. The small remaining difference is believed to be due to the effect of the finite thickness of the target (side contributions). This is further discussed in the following subsection.

7.2.2 The Investigation of Side Contributions on Dichroism Measurements

In this subsection, the effect of finite target thickness, leading to photon interactions with the side faces of the target (i.e. side contributions) will be analysed firstly in theory and then by experiments.

Consider the paths of photons in the vicinity of a target shown in figure 7.6. The red line shows a light path through the target even when the target thickness is infinitesimal. The green line shows light would not pass through an infinitesimal thickness tar-

get. For a finite thickness target both paths would not pass through the complete thickness. Light travelling along these paths will be polarized in an unusual manner, which results in the intensity detected in Im_{co} being reduced while in Im_{cross} increased.
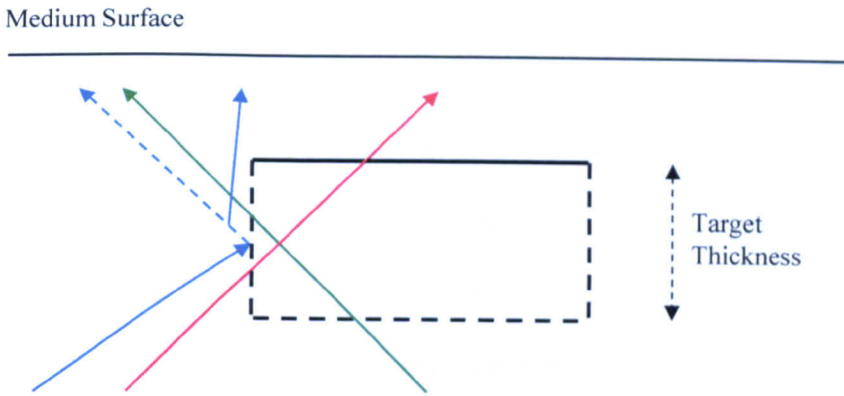
Figure 7.6: Illustration of the likely cases of side contributions within a scattering medium (i.e. the photon interactions with the sides of a target with finite thickness).

An additional effect on image quality by the side contributions is shown as the blue line. This shows light that has reflected from the edge being redirected towards the detector by scattering. This causes the intensity detected at the edges of the target to be increased but reduced in the middle of the target. Both cases affect the overall detected intensities in both Im_{co} and Im_{cross}. It is not clear which is the dominant effect, so further examination was performed by experiment.

Two test *ROPI* phantom experiments on a polarizing target were performed. The target was firstly located in front (i.e. outside) of the cuvette containing a scattering medium and then secondly within the scattering medium at *0mfp*. The experiments were performed using the *GT* polarisers based system. Ideally, dichroism obtained from these two cases should provide the same values as both are performing the same measurement with the target at *0mfp* (i.e. no scatterers in front of the target). However, as the target has finite thickness, the case of locating the target within the medium

will include the effects of side contributions whilst the other case will not. Assuming that surface reflections contribute equally in both cases, comparison of these two measurements will allow examination of the effect.

Results without the calibration are shown (figure 7.7) as these better illustrate the effects of side contributions. As discussed, the results in case A (target within the medium) contain side contributions whereas they should be absent in case B (target in front of the medium). Comparing the cases where target and detection are co-aligned, darker regions can clearly be observed along the targets edges (figures 7.7Ba compared with 7.7Aa) and in the corresponding line scans (figures 7.7Bd and 7.7Ad). Comparing figures 7.7Bd and 7.7Ad, it can be seen that the intensity at the edges of the target in figure 7.7Ad is greater than that in figure 7.7Bd whilst it is the opposite for the intensity in the middle of the target. As discussed previously, these are due to the effects of scattering at the edges of the target and the photons that interact with the target sides being polarized in an unusual manner.

Moreover, comparing figures 7.7Ab and 7.7Bb, the darker regions at the edges cannot be seen due to the cross-polar orientation of the target relative to the analyser. Comparing the line scans shown in figures 7.7Be and 7.7Ae, it can be observed that the intensity over the entire target in figure 7.7Ae is greater than that in figure 7.7Be and the degree of difference at the edges of the target is greater than that in the middle. Comparing the line scans of the dichroism images (figures 7.7Af and 7.7Bf), it can be seen that the measured values are reduced due to the effect of side contributions. Finally, although the line scans in both cases A and B provide a similar shape, the sharpness of the line scans in case A are slightly reduced compared to those in case B due to side contributions and scattering in the vicinity of the edge.
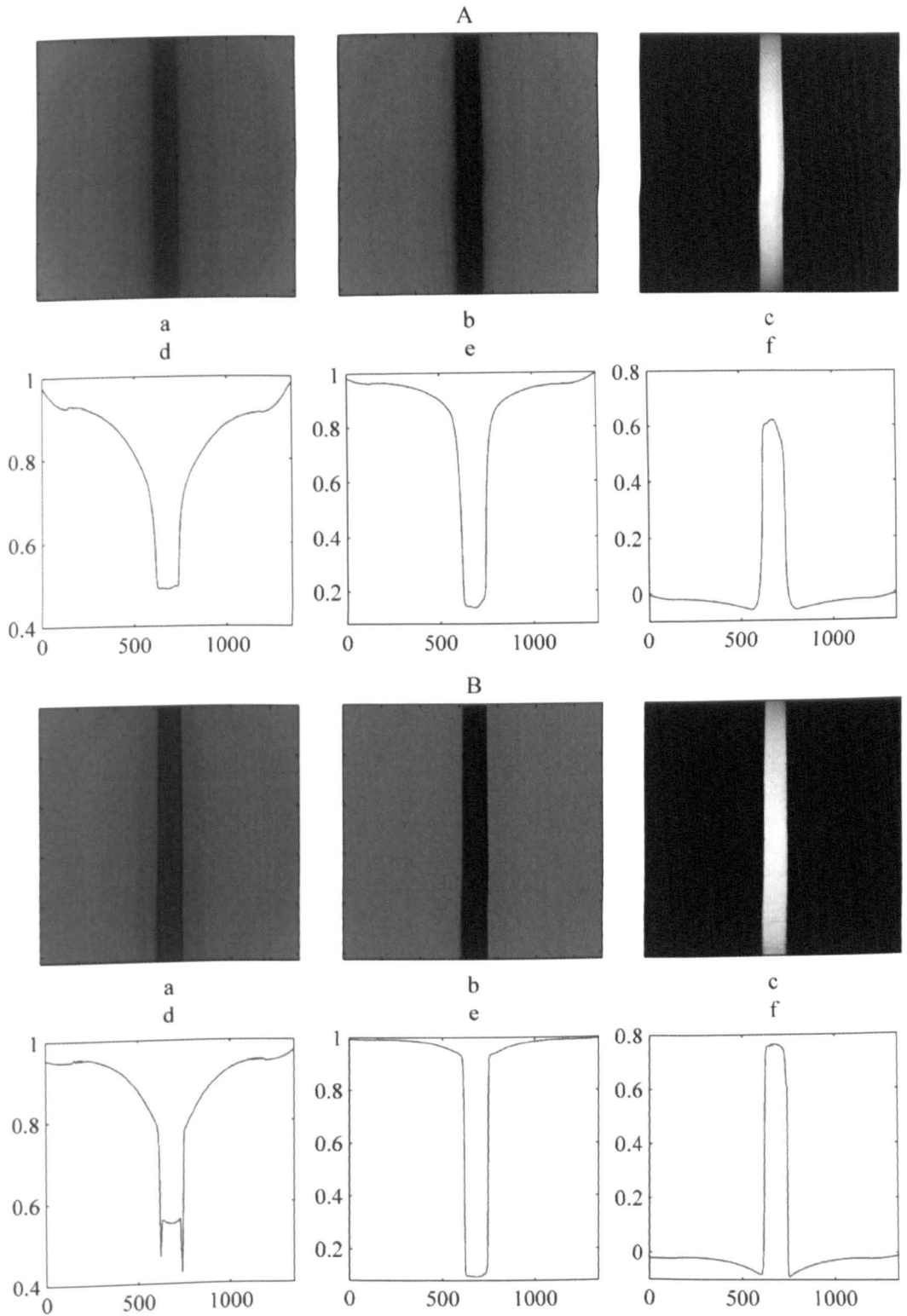
Figure 7.7: Comparison of the GT based experimental results of linear dichroism measurements before the calibration of surface reflections between the target located A) within a scattering medium at 0mfp and B) in front of the cuvette with the same medium. a) image of co-detection, b) cross-detection, c) dichroism. d), e), f) are the respective average line scans on y axis of the images. Units of x axis is Pixels, y is Intensity for d), e) but Dichroism for f).

Figure 7.8 provides the dichroism values of the test measurements as those shown in figures 7.7Af and 7.7Bf but after a calibration for surface reflections. These are used in an attempt to estimate the effect of side contributions. As the figure shows, the value obtained for the target's dichroism from figure 7.8B is 0.97 and from figure 7.8A is 0.88. This suggests the difference due to side contributions is approximately 0.1 in this case. The measurement shown in figure 7.8B is very close to the ideal result obtained from the *MC* simulation (figure 3.10). This further confirms that the main causes of the experimental values differing from the simulation results are due to the surface reflections and the side contributions. The small difference (0.03) is believed to be as a result of other experimental errors such as inaccurate alignment of the target polarization axis.
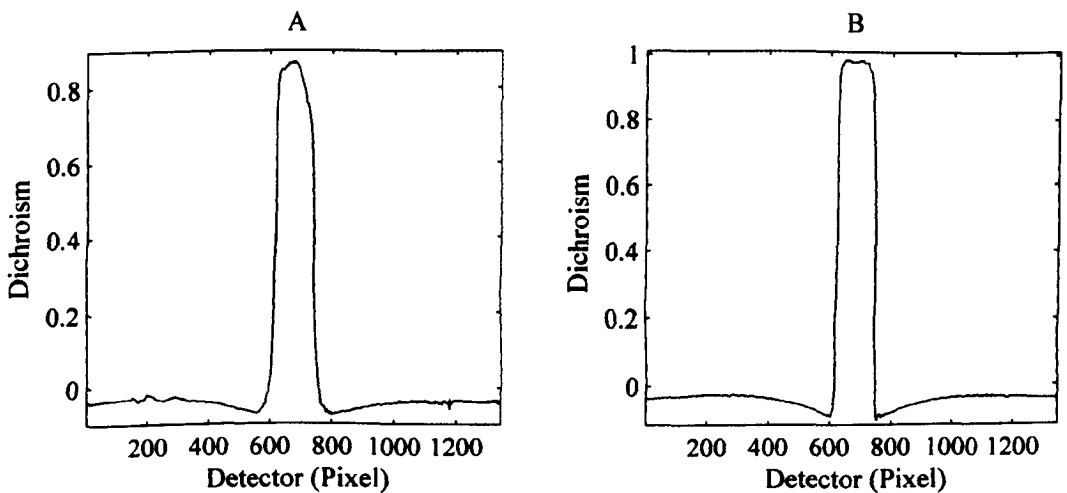
Figure 7.8: Comparison of the GT based experimental results of linear dichroism measurements shown in figure 7.7 but after the calibration of surface reflections.

Finally, comparing figures 7.1 and 7.5 at 0*mfp*, the dichroism difference which is caused by surface reflections is approximately 0.2. Comparing this value to 0.1 which is the dichroism difference caused by side contributions, surface reflections are believed to have a more significant effect than that caused by side contributions. This confirms that good rejection ratios are essential for *ROPI*.

7.3 Resolution Comparison

In this section, comparison will be made between the imaging resolution between simulation and experiments. This is performed over a range of target depths, where imaging resolution is defined as the distance taken for the dichroism value to change from 10% to 90% of its value. A lower transition width (10-90% distance) corresponds to a higher resolution. This can be used as an indication of the imaging performance in terms of responding to the sharpness of the target edges.

Figure 7.9 shows how imaging resolution varies with target depth. The resolution values are calculated from the dichroism average line scans such as those given in figure 3.10. The error bars in the simulation and experimental results are obtained in the same way as that described for figure 7.1. As the figure shows, qualitatively, the simulated and experimental measurements vary in the same way. The transition width increases as target depth increases with increasing gradient. The size of the error bars increase as depth increases. This indicates that the imaging performance is reduced as target depth increases, which is due to more scattering events between the target and the surface. However, quantitatively, the 10%-90% distances in the simulations are lower than those obtained with the experiments and those obtained from the *GT* polarisers based system are slightly lower than those obtained with the *LCVR* based system across the entire depth range.

As discussed in subsections 7.2.1 and 7.2.2, surface reflections and side contributions are the two main reasons that cause measured dichroism differences between the simulation and experiments. The poorer rejection ratio in the *LCVRs* based system is the main reason for the difference between the experiments. Surface reflections can be
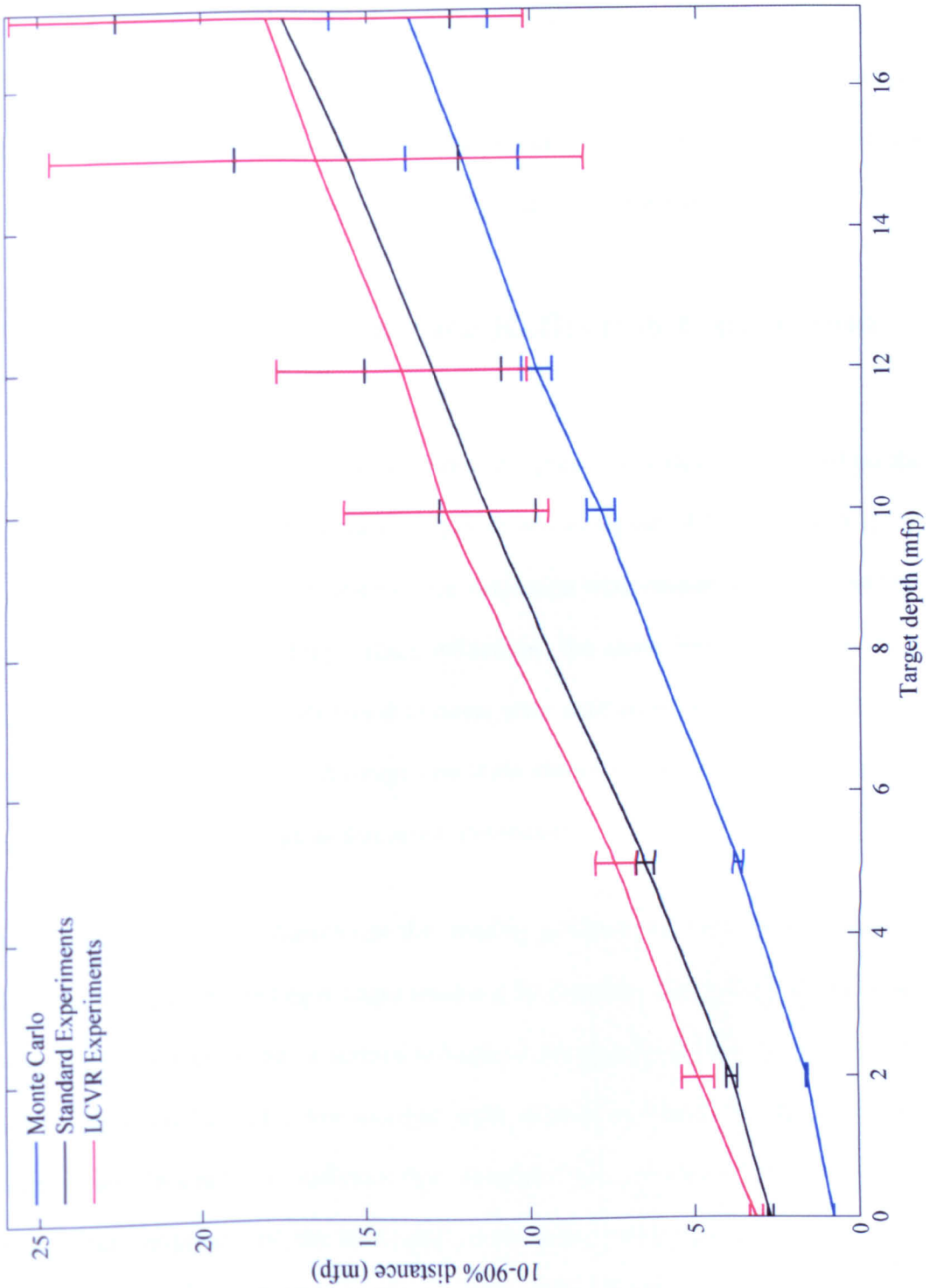
Figure 7.9: Resolution comparison of linear dichroism measurements of a polarizer embedded at different depths within a scattering medium through applying MC simulations and the phantom experiments in standard and LCVRs based systems. Resolution is defined as the distance taken for the dichroism value to change from 10% to 90% of its value.

calibrated and side contributions are shown to cause differences in the experimental and simulated geometries. In order to further investigate the resolution differences shown in figure 7.9; the calibration of surface reflections and the investigation of side contributions are further discussed in the following two subsections.

7.3.1 The Effects of Surface Reflection Calibration on Resolution

As described, the imaging resolution shown in figure 7.9 is calculated based on the average line scans of the dichroism images shown in figures 3.10, 5.6 and 6.10. In order to show whether the accuracy of the resolution measurements can be quantitatively improved by calibrating surface reflections, the same image line scans from both the standard and *LCVRs* based systems after calibration are shown in figures 7.10a and 7.10b respectively. Average line scans shown in figure 7.10b are only provided within the useful range as discussed previously.

As resolution is used to characterise the imaging performance by examination of an edge, the line scan at the target edges must not be distorted during calibration. However, due to the calibration of surface reflections not being ideal for the background areas (subsection 7.2.1), the line scans after the calibration contain oscillations at the target edges. This not only indicates that the edges have been modified, but also results in the maximum and the minimum points being poorly defined. This is especially obvious in figure 7.10b which are obtained from a poorer rejection ratios system leading to stronger detected reflections. For these reasons, the resolution is difficult to be determined with the calibrated images and hence accurately measuring the resolution is difficult.
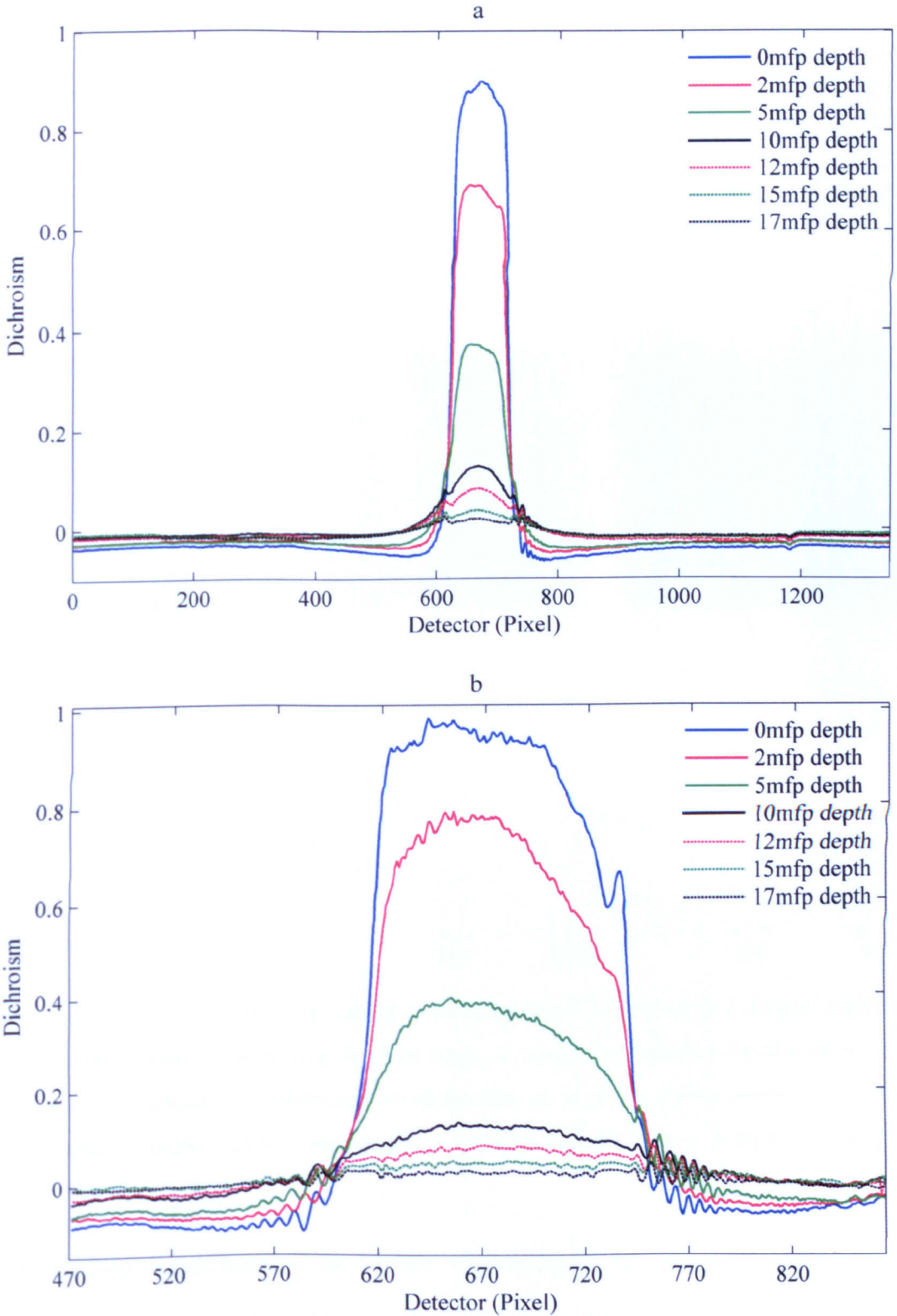
Figure 7.10: Average line scans of the experimental linear dichroism images after the calibration of surface reflections at different target depths within a scattering medium. a) from the GT polarisers based system and b) the LCVRs based system.

7.3.2 The Effect of Side Contributions on Resolution

In order to clarify how the side contributions from target edges result in the resolution differences between the simulation and experiments shown in figure 7.9, experimental results with the effect of side contributions shown in figure 7.7A and *MC* simulation results without the effect shown in figure 7.11 are used.
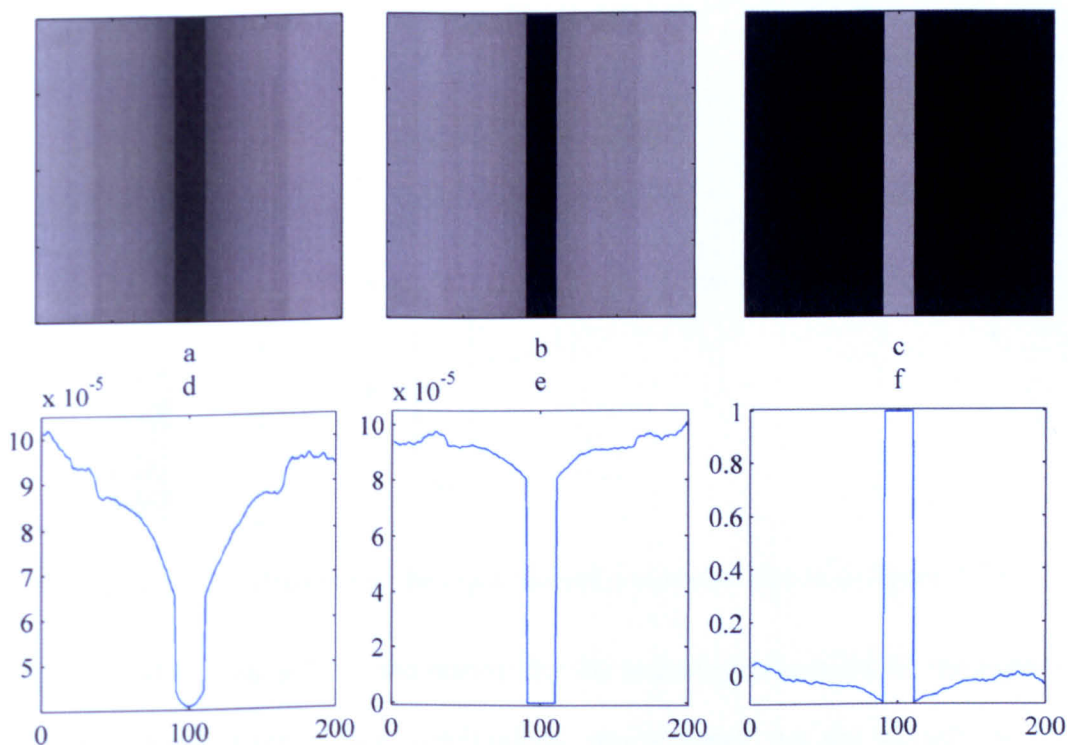
Figure 7.11: MC simulation results of measuring linear dichroism of a target located within a scattering medium at a depth of 0mfp. a) target is aligned to the detection, b) target is orthogonal to the detection, c) dichroism. d), e), f) are the respective average line scans along the y axes of the images. Units of x axis is Pixels, y is Intensity for d), e) but Dichroism for f).

As resolution is calculated as the 10-90% distance based on the line scan of a linear dichroism image, it is essential to identify the position of the maximum value. For the experimental results, the intensity difference between figures 7.7Ad and 7.7Ae is largest at the centre which leads to a maximum dichroism value at this point. For the

simulations, (figures 7.11d and 7.11e), the largest intensity difference occurs at the edge. Therefore, the transition width for the experiment is larger than that for the simulation as shown in figure 7.9. Illustrations of this effect for experiment and simulations are shown in figures 7.12 and 7.13 respectively.
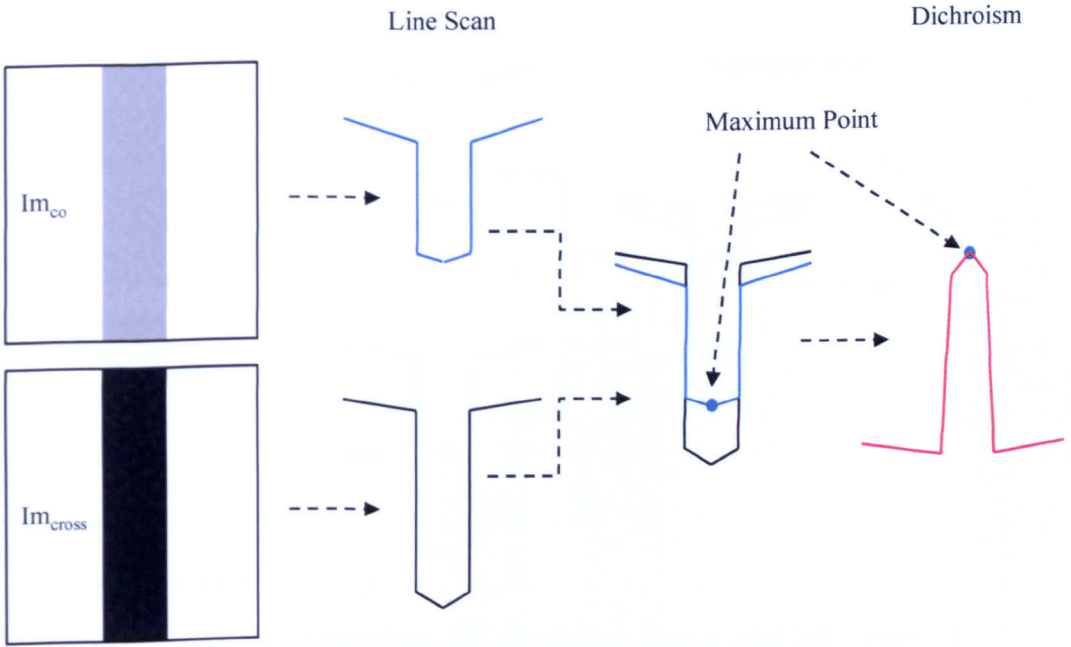
Figure 7.12: Drawing of the experimental test results shown in figure 7.7A.

As discussed in section 7.2.2, the reasons for the intensity differences for the experiment are (i) the effect of side contributions, which means that the intensity at the edges of the target for both figures 7.7Ad and 7.7Ae is greater than at the centre; (ii) as more light is launched into the medium when the target is cross-polarized to the detection (i.e. the target is co-polarized to the illumination), the effect of side contributions in figure 7.7Ae is larger than in figure 7.7Ad. In the simulations, the back-illumination of the target for figure 7.11d (co-polarized detection) is non-uniform while for figure 7.11e (cross-polarized detection) is uniform (figure 5.7).

Finally, the reduction of resolution caused by side contributions for the measurement at $0mfp$ is approximately $1.0mfp$. This is the resolution difference between figure

7.7Af and 7.7Bf, where one case has side contributions and one does not. Resolution differences caused by side contributions for the measurements at other depths cannot be easily quantified due to scattering.
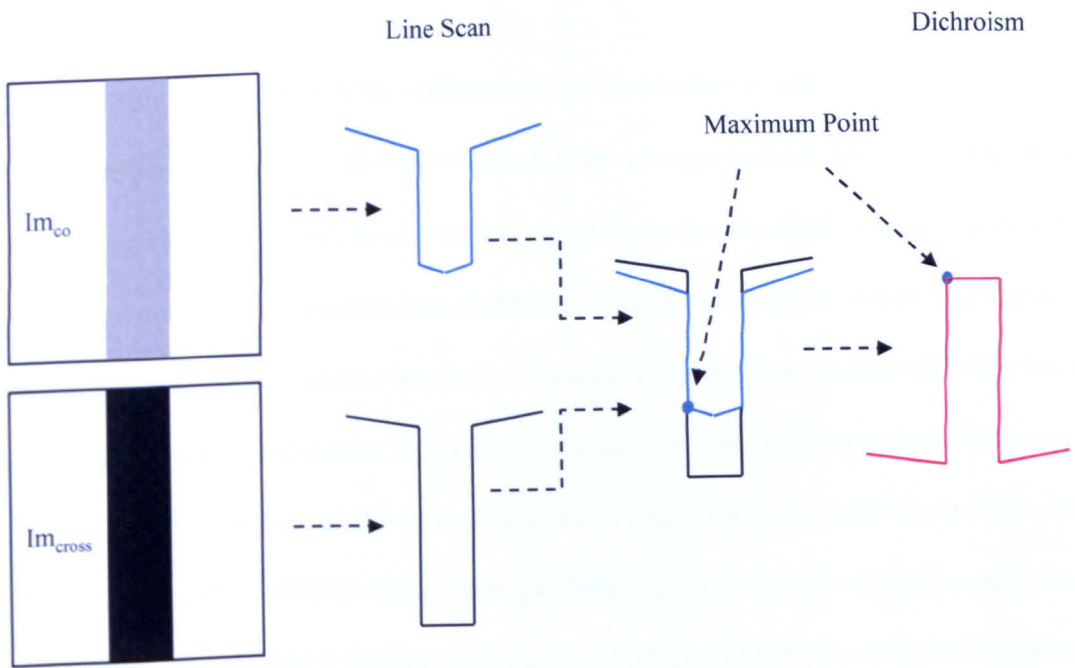
Figure 7.13: Drawing of the MC simulation results shown in figure 7.11.

7.4 Discussion and Summary

In order to complete the investigations of the *ROPI* technique, measurements on a polarizing target located at different depths within a scattering medium have been made through *MC* simulation and phantom experiments using both *GT* polarisers and *LCVRs* based systems. These are compared in terms of both dichroism measurement and resolution in sections 7.2 and 7.3 respectively.

Qualitatively, the simulation and experimental results compare well with each other over the full range of depths. However, quantitatively, both dichroism and resolution values obtained from the *GT* polariser based system are closer to the model than those

from the *LCVRs* based system. The reason for the difference between experiments is poorer rejections ratios of crossed polarizations in the *LCVRs* system. The main reasons that cause the difference between simulations and experiments are the surface reflections and the side contributions from the finite thickness target.

For the dichroism comparison, calibration has been demonstrated to further reduce surface reflections that are not be eliminated by cross-polarized detection. Although the calibration is not ideal, this is mainly a problem for the areas outside the target, which are not used to calculate the dichroism values. It should be noted that for experiments implemented within the study, the surface reflections are directed back into the detection optics due to the flat and orthogonal surfaces. This represents the worst case of this contribution which is anticipated to be lower for practical applications as reflections are often diffuse rather than specular. An extra benefit of performing the calibration is that common channel noise (e.g. offset due to dark current) that is introduced by using the *CCD* camera and contributes to the *ROPI* images can also be removed.

However, for the resolution comparison, the calibration cannot be performed as the background areas which are modified incorrectly by the calibration are required to calculate resolution.

The effect of side contributions which is caused by using a finite thickness target and cannot be calibrated is investigated in terms of showing how the dichroism and resolution are reduced. In addition, it should be pointed out that ideally, for the resolution comparison, surface reflections should only make it harder to measure the resolution but do not actually change it whilst side contributions actually affect the resolution.

Finally, it also should be pointed out that in optics, resolution is the term used to describe the ability of an imaging system to resolve detail in the object that is imaged [86]. In general, two adjacent points in the object give rise to two diffraction patterns, which can be represented by using point spread function. The resolution is the smallest distance between the two patterns where the two points can be distinguished. Often the *Rayleigh* criterion [86] is used where the images of two points are resolved if the maximum in the diffraction pattern of one point coincides with the first minimum of the other. Alternatively, by representing the edge pattern of the object using edge spread function [86], the resolution can also be measured as the distance taken for the intensity to fall from 90% to 10% of its maximum. This approach has been adopted here but for a single edge of an isolated object.

One problem with both this approach and the edge response function is that the maximum signal level needs to be present within the image, or at least known. This is not the case in e.g. figures 3.10, 5.6 and 6.10. Secondly, when using a single edge of an isolated object there is that possibility that the response of the second edge will interact with that of the first. This is particularly true when the resolution is poor and will affect the position of the minimum, hence giving a false impression of the resolution of the system.

In making the comparison between the *MC* simulations and the phantom experiments (e.g. figure 7.9), there is at least consistency in the resolution measurement made, and the trends are similar. However, in future it would be useful to investigate a semi-infinite target so that the edge is isolated, or ideally investigate two adjacent small targets.

The *MC* simulations provide results that qualitatively match those obtained in the phantom experiments while quantitatively there are still slight differences. There are several assumptions made in the model that cannot be accurately achieved in the experiments such as ideal polarisers, precise depth location of the target, precise alignment of optical components, a refractive index match between the target and surrounding medium, an infinitely long and thin target, and uniform illumination. In order to better simulate the phantom studies, for future research on the *ROPI* technique, further refinements of the model could be performed such as making the polarisers non-ideal, the target of finite thickness or introducing surface reflections at the medium-target boundary. This is worthwhile for applications such as target detection in turbid water or imaging through fog where the model provides an accurate representation of the real world situation. However, for the tissue imaging problem, the focus should be on a more accurate model of the structure of the tissue.

In conclusion, from this chapter, further comparisons of the linear dichroism measurements obtained through *MC* simulations and phantom experiments in both *GT* polarisers and *LCVRs* based systems have been presented. It is found that the better the rejection ratios in the system, the better the ability to resolve small changes in polarization properties and to reject the strong surface reflections. This leads to better quality images and hence better linear dichroism measurements.

Chapter 8

Conclusions

8.1 Summary

Non-invasively characterizing the polarization properties of tissues has potential for *in vivo* clinical applications such as monitoring the healing state of wounds and burns. The conventional methods which perform the polarization difference measurements to achieve this, normally involve a co-polarized detection (i.e. polarization states of the illumination and detection are aligned). Therefore, those measurements are either restricted by surface reflections or can only be performed in off-axial systems with the use of matching fluid and a glass plate to the samples' surfaces. In this thesis, the new polarization imaging technique, *ROPI*, has been presented and evaluated. The technique is capable of providing quantitative measurements of the polarization properties of scattering media such as tissue with free surface reflections and allows measurements to be performed in a coaxial system. The evaluation was demonstrated through theoretical calculus, ideal *MC* simulations and phantom and tissue experiments by quantitatively measuring linear dichroism and linear birefringence underlying a scattering medium.

Chapter 1 introduced the background and the technique of *ROPI*. The technique involves illumination in a single polarization state and detection in the orthogonal polarization state. Synchronously rotating both the illumination and orthogonal detection

states can provide a polarization difference image that is free from surface reflections and sensitive to the polarization property of a target embedded within a scattering medium. Depending on whether the polarization property and orientation of the target are known, the synchronously rotating angle and the number of rotations will be different. For the known case of measuring linear dichroism and linear birefringence, only one rotation and a synchronously rotated angle of 90° and 45° are respectively required. For the unknown case, at least three orthogonal polarization detections over the range of [0°, 90°] are necessary. In this study, *ROPI* is evaluated with the known cases only.

In chapter 2, the evaluation of *ROPI* was demonstrated by Mueller calculus with polarized light and polarizing components represented by Stokes vectors and Mueller matrices respectively. This provided the principles to carry out *ROPI* simulations and experiments and also a set of ideal criteria to judge the results by. It was found that maintaining the polarization state of illumination prior to back-illuminating the embedded target is essential for measuring linear birefringence whereas randomly polarized light is required for linear dichroism measurements. In addition, over the range of [0°, 90°], the orientation of the target to one of the illuminations must be 0°, 45° or 90° for the linear birefringence measurements and 0° or 90° for the linear dichroism measurements. The two illuminations must vary by 45° (for measuring birefringence) and 90° (for measuring dichroism) to each other. Both the measurement values would ideally vary from 0 to 1 depending on the targets.

The study of *ROPI* via *MC* simulations was presented in chapter 3. Firstly, three modifications of a conventional *PMC* model to enable the simulation of *ROPI* were introduced. These involved imaging a polarizing target embedded within a scattering medium with full field illumination. Secondly, the evaluation of *ROPI* via quantita-

tively measuring linear dichroism of a polarizing target embedded within a scattering medium at different depths and at different orientations using two different sets of orthogonal illumination / detection pairs were presented. In both quantity and quality, the results decrease as the target depth increases due to the increased effect of scattering. It was found that a depth of 30*mfp* is the limit that the technique can be used to detect linear dichroism within the scattering medium. In addition, a measurement of linear birefringence of a *HWP* embedded within the scattering medium was performed. This was mainly used to demonstrate the difficulties of applying the method to measure linear birefringence with *ROPI* as the back-illumination photons have to maintain linear polarization before passing through the target. All the measurement results were shown to match well the theoretical predictions from chapter 2.

Practically, the *ROPI* technique was evaluated by experiments using two different systems. One is the standard system which is based on *GT* polarisers while the other one is based on *LCVRs*. The main difference between the systems is that the polarization states of illuminations and detections are controlled manually in the standard system but electrically in the *LCVR* one. In chapter 4, the design characterization and calibration of the standard *ROPI* experimental system in both reflection and transmission modes were presented. The design characterization included illustration of the setup principles; discussion of all the optical components and description of the scattering medium and polarizing targets. The calibrations were performed for the modification of polarization state and intensity of the illuminations after passing through the system. These result from the non-ideal setup alignments and components.

In chapter 5, the experiments performed using the standard system in both reflection and transmission modes were presented. As *ROPI* in reflection mode is preferred in

practical applications, and mainly evaluated in this study, most of the experiments were performed in this mode.

For the experiments in reflection mode, in order to evaluate the investigations in chapters 2 and 3, quantitative phantom measurements of the linear dichroism of a polariser embedded within a scattering medium at different depths were presented. It was shown that qualitatively, trends of the linear dichroism values over the entire target depth range matched *well with those obtained by MC* simulations. However, quantitatively, the values were smaller than the simulations. In order to initially demonstrate the feasibility of applying *ROPI* in practice, preliminary measurements of linear dichroism of various real tissues (bovine tendons, lamb tendon, chicken breasts and human finger skin) and a scaffold tissue (tissue engineering tendon) orientated at two orthogonal directions were provided as well. It was shown that the absolute mean values obtained from tissues varied from 0.013 to 0.07 while the same value for a polystyrene microsphere solution which contains no polarization properties was 0.003. The scaffold measurements showed two similar mean values with one positive and the other negative. These provide an indication that the *ROPI* technique is sensitive to the polarizing properties of the underlying tissue.

For the experiments in transmission mode, the *ROPI* experiments of measuring linear birefringence of a *HWP* without and with a scattering medium were demonstrated. The experiments without a scattering medium demonstrated how linear birefringence can be measured with *ROPI* whereas the experiments with a scattering medium showed the difficulty of measuring linear birefringence with *ROPI* in this case. The results were shown to be in good agreement with those predicted based on Mueller calculus and *MC* simulations.

In chapter 6, the experimental evaluation of *ROPI* using the *LCVR* based system was presented. This was mainly to demonstrate an important step towards taking the *ROPI* technique into clinical practice as the system controls polarization states of the illumination and detection electrically. The principles of applying *LCVRs* to control linear polarization states over the full range and the design of the entire *ROPI* system were firstly characterised. This was followed by presenting the same phantom experiments as in chapter 5 in reflection mode. It was found that the rejection ratios provided by the *LCVR* based system are not as good as those provided by the *GT* polariser based system. Therefore, both qualitatively and quantitatively, the results obtained in this chapter were inferior to those from chapter 5. However, these provided confidence that the electric rotation system could replace the manual rotation system. The imperfections of the *LCVR* and possible solutions were also briefly discussed.

In chapter 7, in order to complete the investigation of the *ROPI* technique, further comparisons of the same linear dichroism measurements obtained in chapters 3, 5 and 6 using *MC* simulations and phantom experiments in both *GT* polarisers and *LCVRs* based systems respectively were made. These were provided in terms of dichroism and resolution over a range of depths. Qualitatively, the simulation and experimental results compared well with each other. Both dichroism and resolution comparisons provided the same trend of variation over the entire depth range. However, quantitatively, both dichroism and resolution values obtained from the *GT* polariser based system were better than those from the *LCVR* based system. Those from the simulations were better than those from both the experiments. The reason for the difference between experiments was due to the poorer rejections ratios of cross polarization in the *LCVR* based system. The main reasons that caused the difference between simulations and experiments were the surface reflections and the side contributions.

As demonstrated, the *ROPI* technique has been methodically evaluated through theoretical calculus, ideal *MC* simulations and phantom and tissue experiments in two different systems. Accurate quantification of dichroism is difficult due to scattering that occurs between the target and the exit surface of the medium. Further research into introducing multispectral *ROPI* measurements may allow an inversion to take place and the properties of the target to be accurately measured.

For a birefringent target, measurements can only be performed when the polarization state of the illumination is maintained before it back-illuminates the target. This is difficult to achieve in reflection mode simulation and experiments as a relatively strong scattering medium is required in order to have sufficient back-illumination to produce a high quality image.

In most cases in this thesis, the orientation of the polarization axes of the target have been known and only two illumination and detection pairs have been required. In practical applications these will not be known and three or more pairs will be required. This introduces problems at the beam splitter due to different refection coefficients for *s*- and *p*-polarization components. Calibration of these effects remains a challenge. In addition, the effects of lateral shifting of the image in different polarization states need to be investigated in more detail. In this thesis only very preliminary measurements of tissue were made although encouraging results were obtained, more detailed studies are necessary before the technique can make an impact on clinical practice.

The *ROPI* technique has some advantages and disadvantages over current methods. Conventional polarization difference measurements such as those proposed by *Jacques et al* [1], normally involve co-polarized detection (i.e. the polarization states of the illumination and detection are aligned) and therefore the measurements are ei-

ther restricted by surface reflections or can only be performed in off axial systems with the use of matching fluid and a glass plate applied to the samples' surfaces. *ROPI* has the advantages of performing measurements not only free from surface reflections (without using matching fluid and a glass plate) but also in co-axial detection which often simplifies systems. For instance, in endoscopy, illumination and detection can use the same fiber bundle.

There are some disadvantages when compared with techniques such as optical coherence tomography (*OCT*). For example allows depth resolved polarization measurements. However *OCT* systems are generally more complicated and are used to image a relatively small volume of tissue. *ROPI* is a simpler method and with appropriate inversion algorithms has the potential to be a useful clinical technique. Further *ROPI* can be used to investigate larger areas of tissue than *OCT*.

8.2 Future Work

As discussed, the *ROPI* technique in this study is evaluated mainly via *MC* simulations and phantom experiments. However, there are several assumptions made in the modified *MC* model that cannot be accurately achieved in the experiments such as ideal polarisers, precise depth location of the target, precise alignment of optical components, a refractive index match between the target and surrounding medium, an infinitely long and thin target, and uniform illumination. In order to better simulate the phantom studies, for the future research on *ROPI*, further refinements of the model could be made such as making the polarisers non-ideal, the target of finite thickness or introducing surface reflections at the medium-target boundary. This is worthwhile for applications such as target detection in turbid water or imaging through fog where

the model provides an accurate representation of the real world situation. However, for the tissue imaging problem, the focus should be on a more accurate model of the structure of the tissue.

For the standard *ROPI* system, as discussed in chapter 4, as the polarization states will be modified differently by the *BS*, only linear polarization states at $0°$ and $90°$ can be reliably applied in the setup in reflection mode. In order to fully apply *ROPI* in prac-tice. the use of other *linear polarization* states is necessary as discussed in chapter 1. Therefore, this is one aspect that needs to be investigated in future research. Three possible approaches, which are using a better *BS*, using two identical *BS*s and apply-ing a retardance compensator, have been briefly suggested in chapter 4 (section 4.4). In addition, as discussed in subsection 4.4, both the calibration of the modifications of illumination polarization state and intensity are not ideal. It would be worth investi-gating other calibration methods to completely cover the modifications.

As discussed in chapter 6, for the *ROPI* system based on *LCVRs*, it is found that the polarization rejection ratio provided in the system is poorer than that provided in the *GT* polarisers based system. This is because of the imperfections of the *LCVRs* dis-cussed in section 6.5. Possible future work has been discussed in the same section concerning improvements to the electrically controlled system.

To further evaluate *ROPI*, the next stage that will be of interest is to investigate if the technique is clinically useful. This will include measuring polarization properties of collagen within skin; monitoring the state of healing wounds and burns; capillaro-scopy applications in measuring dichroism of sickle cell polymerization; connective tissue diseases monitoring; applications for plastic surgery and glucose monitoring. In addition, monitoring collagen growth or alignment in bioreactors will also be of inter-est.

8.3 Closing Remarks

To conclude, this thesis has presented a new polarization imaging technique, *ROPI*, which is capable of providing quantitative measurements of the polarization properties of scattering media free from surface reflections.

The technique can be useful in non-invasively characterizing the polarization properties of tissues and has potential for *in vivo* clinical applications such as monitoring the healing state of wounds and burns.

The technique involves illumination in a single polarization state and detection in the orthogonal polarization state. Synchronously rotating both the illumination and orthogonal detection states can provide a polarization difference image that is free from surface reflections and sensitive to the polarization property of a target embedded within a scattering medium.

The evaluation of the technique was demonstrated through theoretical calculus, ideal *MC* simulations and phantom and tissue experiments by quantitatively measuring the linear dichroism and linear birefringence of objects within a scattering medium.

Appendix A

A Further Investigation of Equation 2.34

For equation 2.34 shown in chapter 2 (section 2.4), in order to investigate how the variation of $I_{sig}(\psi_1 - \psi_2)$ is dependent on δ, θ, ψ_1 and ψ_2, the following analysis is performed. Firstly, in order to aid and simplify the analysis, set:

$$I_{sig}Factor = \begin{bmatrix} \left(\cos^2(2\theta) - \sin^2(2\theta)\right)\left(\cos^2(2\psi_2) - \cos^2(2\psi_1)\right) \\ +2\sin(2\theta)\cos(2\theta)\left(\sin(2\psi_2)\cos(2\psi_2) - \sin(2\psi_1)\cos(2\psi_1)\right) \end{bmatrix} \quad \text{(A.1)}$$

This shows the variation of $I_{sig}(\psi_1 - \psi_2)$ with θ, ψ_1 and ψ_2 only and separates the variation with δ. To further aid analysis, taking advantage of the circular symmetry, the three angles, θ, ψ_1 and ψ_2, can be reduced to α and $\Delta\psi$, where:

$$\alpha = \psi_1 - \theta \quad \text{(A.2)}$$

$$\Delta\psi = \psi_2 - \psi_1 \quad \text{(A.3)}$$

As equation 2.34 shows, clearly, the variation of $I_{sig}(\psi_1 - \psi_2)$ with δ is sinusoidal and when $\delta = n\pi$ $(n = 1, 3, 5, 7\cdots)$, $I_{sig}(\psi_1 - \psi_2)$ could be a maximum if α and $\Delta\psi$ are given the appropriate values. Vice versa, if the retardance is fixed to a given value (e.g. $\delta = \pi$), $I_{sig}(\psi_1 - \psi_2)$ only depends upon α and $\Delta\psi$, i.e. $I_{sig}Factor$ as shown

in equation A.1. However, as can be seen, the variation of $I_{sig}(\psi_1 - \psi_2)$ with θ, ψ_1 and ψ_2 (i.e. the variation of $I_{sig}Factor$ with α and $\Delta\psi$) is more complicated.

In order to show this variation and determine the values of α and $\Delta\psi$ to reach the maximum situation for $I_{sig}Factor$, a 3-D plot of how the absolute values of $I_{sig}Factor$ vary with $(0 \le \alpha \le \pi/2)$ and $(0 \le \Delta\psi \le \pi)$ is provided in figure A.1. The reason that applied absolute values for $I_{sig}Factor$ in the plot is the '+' and '−' signs in fact only represent the directions of the phase difference. As discussed in chapter 2, in addition to intensity, the phase issue is not within the scope of this study; therefore, absolute values are applied which simplifies the analysis.
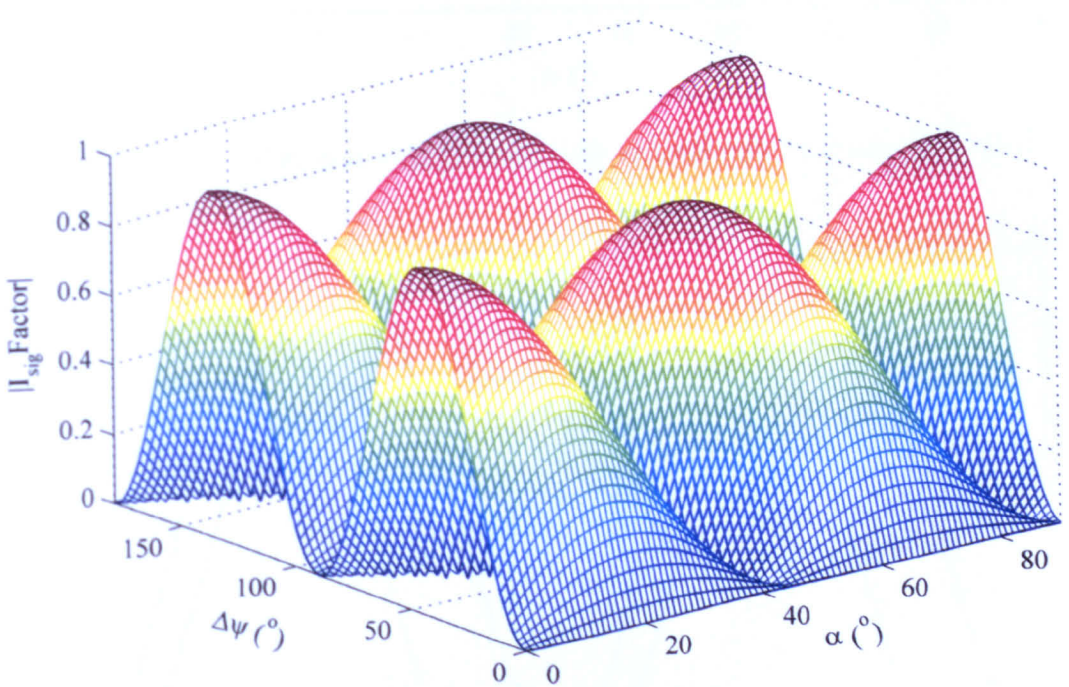
Figure A.1: 3-D illustration of $\left| I_{sig}Factor \right|$ varying with α and $\Delta\psi$.

As figure A.1 shows, both the variations of $\left| I_{sig}Factor \right|$ vs. α and $\left| I_{sig}Factor \right|$ vs. $\Delta\psi$ are sinusoidal. The variation periods are 45° and 90° respectively. It also can be

clearly seen that the absolute values vary from a minimum of 0 to a maximum of 1 depending on the values of α and $\Delta\psi$. However, the values of α and $\Delta\psi$ to reach those maximum situations (i.e. absolute value=1) are not clearly shown.
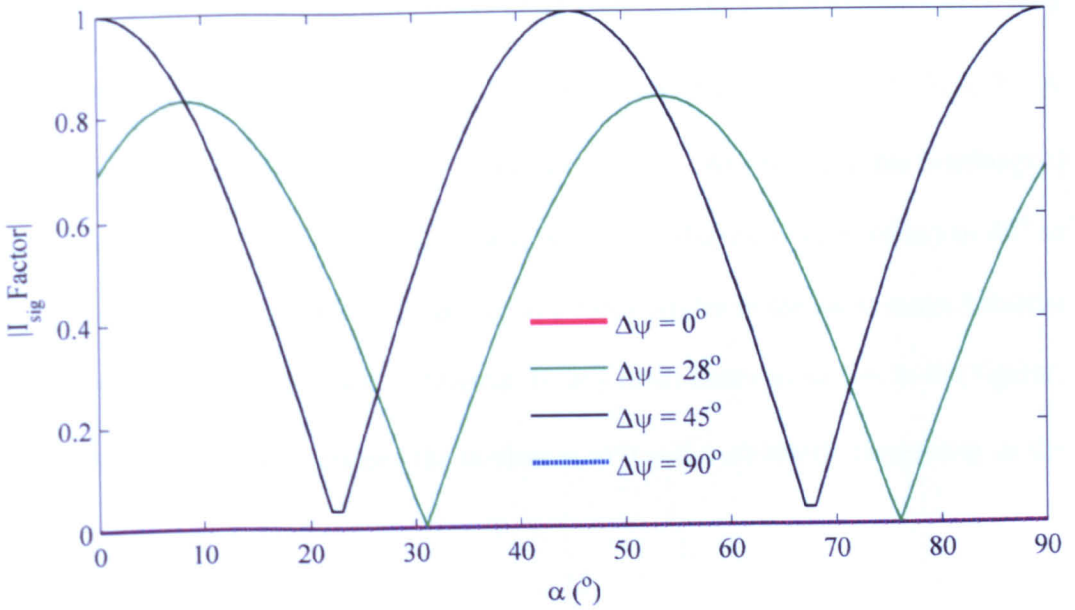
Figure A.2: Variation of $\left|I_{sig}Factor\right|$ with α under different values of $\Delta\psi$.

Figure A.3: Variation of $\left|I_{sig}Factor\right|$ with $\Delta\psi$ under different values of α.

Therefore, figures A.2 and A.3 which represent the specific variations of $\left|I_{sig}Factor\right|$

with α (under different values assigned to $\Delta\psi$ within one period) and with $\Delta\psi$ (under different values assigned to α within one period) are provided respectively. As the figures show, it is clear that $\left|I_{sig}Factor\right|$ would reached a maximum of 1 only when simultaneously $\alpha = n\pi/4$ (n=0, 1, 2, 3 $\cdots$) and $\Delta\psi = n\pi/4$ (n=1, 3, 5, 7 $\cdots$). These indicate the azimuthal angles in the range of [0°, 90°] between the birefringent component and the first illumination must be 0° (i.e. aligned to each other) or 45° or 90° (i.e. crossed to each other) difference and those angles in the same range between two illuminations must be 45° difference. In any other cases as shown in the figures, $\left|I_{sig}Factor\right|$ would vary between the minimum of 0 and 1 arbitrarily depending on the values of α and $\Delta\psi$.

As discussed above, by taking both the absolute variations ($\left|I_{sig}\left(\psi_1-\psi_2\right)\right|$ vs. δ and vs. $\left|I_{sig}Factor\right|$ separately) into account, as both cases vary sinusoidally from the minimum of 0 to the maximum of 1, the combined variation (equation 2.34) will be sinusoidal as well. The maximum value of 1 would be obtained only if simultaneously $\delta = n\pi$ (n=1, 3, 5, 7 $\cdots$), $\alpha = n\pi/4$ (n=0, 1, 2, 3 $\cdots$) and $\Delta\psi = n\pi/4$ (n=1, 3, 5, 7 $\cdots$). In any other cases, the values would vary between the minimum of 0 and 1 arbitrarily depending on δ, α and $\Delta\psi$.

Appendix B

ROPI MC Simulation Algorithm

As discussed in chapter 3, the modified *MC* model used in this study is based on *Mie* scattering theory [58; 59] and consists of two block of codes named '*Polarized Monte Carlo (PMC)*' and '*Analysis*' that are required for the complete simulation (i.e. imaging a polarizing target located at a particular depth and polarizing state within a scattering medium with full field illumination and detection). In this appendix, the main functions of both the *PMC* and the *Analysis* codes are described individually. In addition, the algorithmic flow charts of both codes are provided.

The *PMC* code is used to generate backscattered photons from point source illumination with the splitting process applied for every single photon as described in section 3.2.1 chapter 3 in order to simulate the insertion of a polarizing target within the scattering medium. Every backscattered photon is recorded with multiple trajectories along with each trajectory that has the exclusive information depending on how many times the trajectory passes through the target depth. This information is stored and includes the normalized intensity, polarization state, exiting position and direction and positions of the photon as it passes through the target depth. The algorithmic flow chart of the *PMC* code is given in figure B.1, which details the code step by step from the launch of a photon to the generation of photon that are backscattered with multiple trajectories.
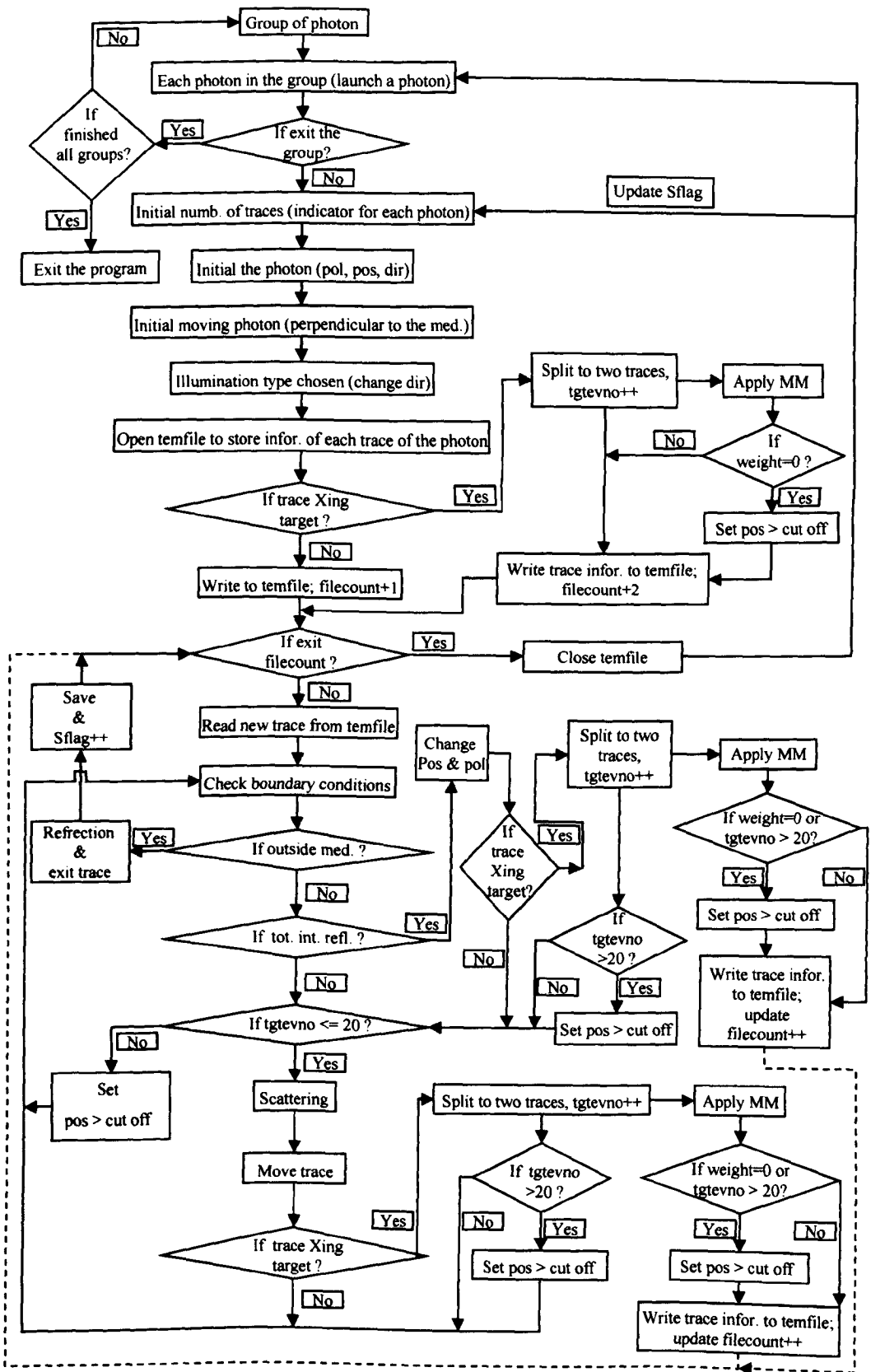
Figure B.1: Algorithmic flow chart of the PMC code.

The *Analysis* code is used to detect the backscattered photons in a particular polarization state. This is achieved through applying the Mueller calculus as described in chapter 2. In addition, the backscattered photons are detected in *2-D* directions in order to form an image of the polarizing target embedded within the scattering medium via the imaging system included in the simulation, as described in detail in section 3.2.1 chapter 3. The indexing process is also implemented from the *Analysis* code in order to achieve full field illumination. In the meantime, as each backscattered photon generated from the *PMC* code has multiple trajectories, the selection of the appropriate trajectory for each detected photon is carried out as well. This depends on the width of the target and the relative position of the illumination point and the target location.

The algorithmic flow chart of the *Analysis* code is given in figure B.2. This illustrates all the functions of the code step by step from obtaining a photon from the *PMC* code with multiple trajectories to detecting the photon in *2-D* directions with a particular polarization state. Also shown in the figure is the process of selecting the appropriate trajectory in the full field illumination and imaging system.

```
                           ┌──────────────────────────────────────────┐
                           │ Generate B.S file (photon information saved)│
                           └──────────────────────────────────────────┘
                                            │
                           ┌──────────────────────────────────────────┐
                           │ Read index infor. (posx and pts)          │
                           └──────────────────────────────────────────┘
                                            │
┌─────────────────────┐     Yes    ◇ If exit back scatt. ◇
│ Apply MM to each    │◀───────────   photons ?
│ detection bin and show│              │ No
│ results.            │     ┌──────────────────────────────────────────────────┐
│ END!                │     │ Read Sflag (indicator of numbers of traces for each photon)│
└─────────────────────┘     └──────────────────────────────────────────────────┘
                                            │
                                ◇ If exit Sflag ? ◇  Yes
                                            │ No
                           ┌──────────────────────────────────────────┐
                           │ Read trace (ray) information              │
                           └──────────────────────────────────────────┘
                                            │
                           ┌──────────────────────────────────────────┐
                           │ Calculate shift distance in x direction   │
                           └──────────────────────────────────────────┘
                                            │
                           ┌──────────────────────────────────────────┐
                           │ Calculate exit angle of the trace (ray)   │
                           └──────────────────────────────────────────┘
                                            │
                   Yes   ◇ If exit the detection angle ◇
                            (i.e. angle filtering) ?
                                            │ No
                   Yes   ◇ If exit the illumination ◇
                            points (i.e. indexing) ?
                                            │ No
                           ┌──────────────────────────────────────────────────┐
                           │ Initial trace status (indicates if trace passing through the target)│
                           └──────────────────────────────────────────────────┘
                                            │
                           ┌──────────────────────────────────────────────────┐
                           │ Calculate distance in x direction after shifting and indexing│
                           └──────────────────────────────────────────────────┘
                                            │
   ┌─────────────────────────┐   No   ◇ If exit the ◇
   │ Calculate distance in x │◀────────  crossing points ?
   │ direction for each      │              │ Yes
   │ crossing points after   │     ◇ If trace status the same ◇  No
   │ indexing                │       as reading from saving?
   └─────────────────────────┘              │ Yes
           │                        ◇ If within ◇  No
   ◇ If the crossing point ◇         detection range ?
     passing through the              │ Yes
  No   target ?   Yes        ┌──────────────────────────────────────────┐
                             │ Calculate absorption in each layer, 0 here.│
 ┌──────────┐ ┌──────────┐   └──────────────────────────────────────────┘
 │ The trace│ │ Update the│            │
 │ (ray)    │ │ trace (ray)│  ┌──────────────────────────────────────────┐
 │ status   │ │ status.   │  │ Calculate bin number, i.e. which bin to   │
 │ remains  │ │ Ex: 100   │  │ save IQUV of the trace (ray)?             │
 │ the same.│ └──────────┘  └──────────────────────────────────────────┘
 │ Ex: 100  │                            │
 └──────────┘               ┌──────────────────────────────────────────┐
                            │ Save IQUV of each trace (ray) to the bin  │
                            └──────────────────────────────────────────┘
```

Calculate 'status' of each trace (ray) at every index point. Ex: 111 / 100

Figure B.2: Algorithmic flow chart of the Analysis code.

Appendix C

Pictures of Experimental Setups

In this appendix, pictures of the actual experimental setups and some components used in this study are illustrated.

<p style="text-align:center;">a   b</p>
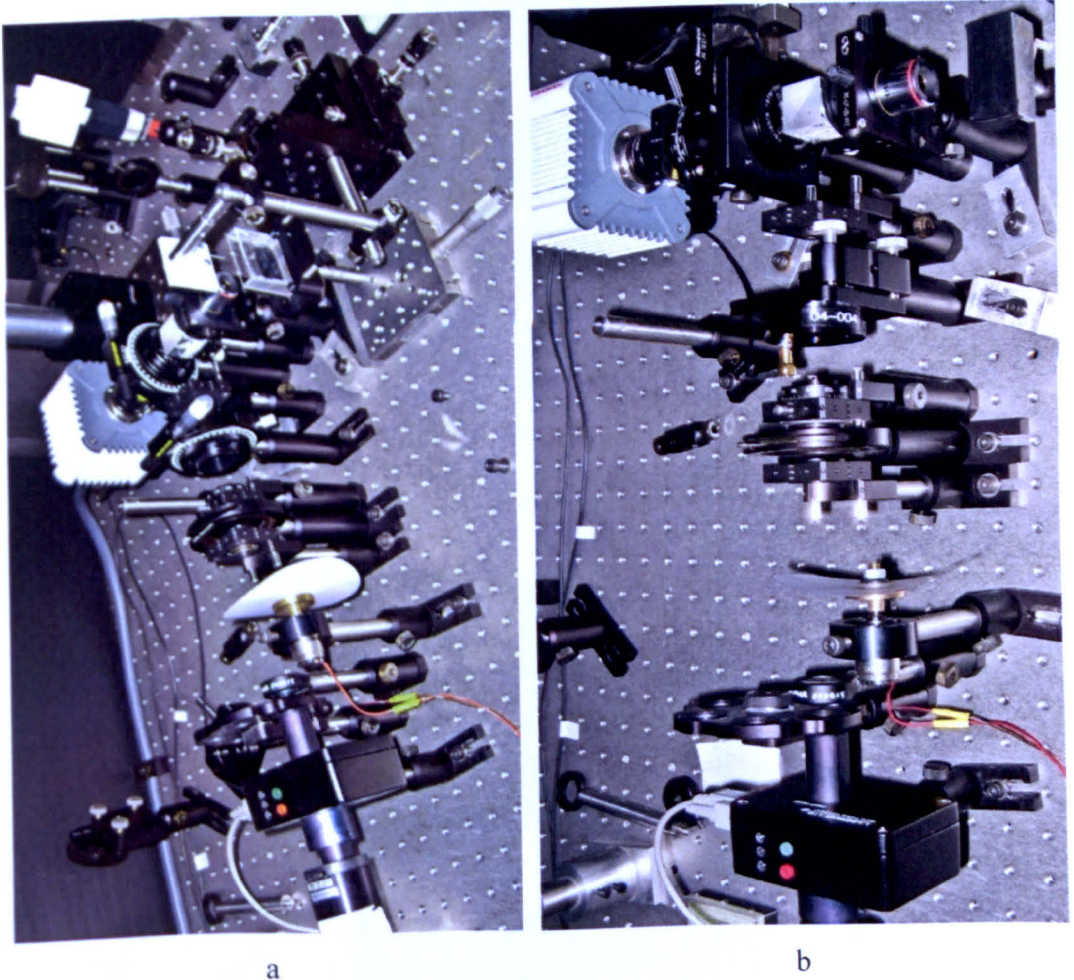
Figure C.1: The experimental setups in reflection mode based on (a) GT polarisers and (b) LCVRs respectively.

Polarizing
Target
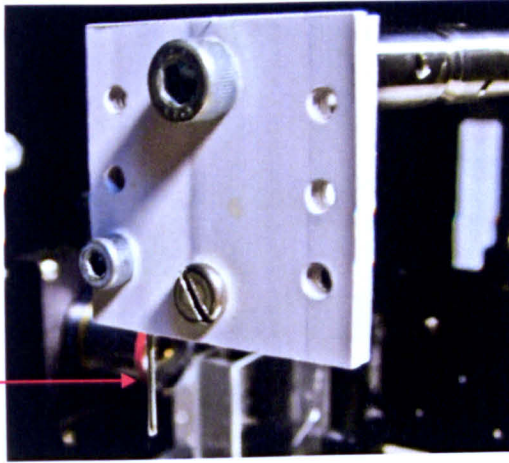
Figure C.2: The target that is used to perform linear dichroism measurements.
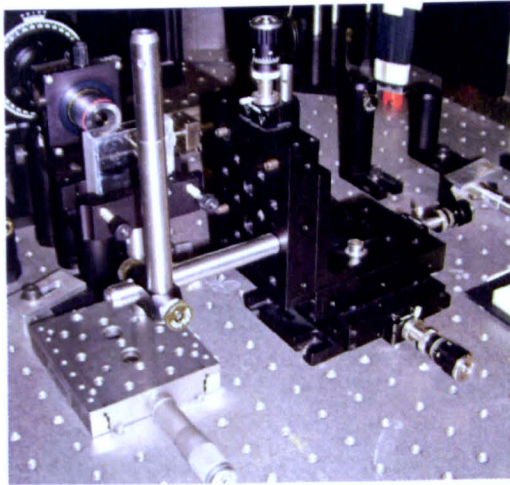
Figure C.3: The xyz stage that is used to control sample positions.
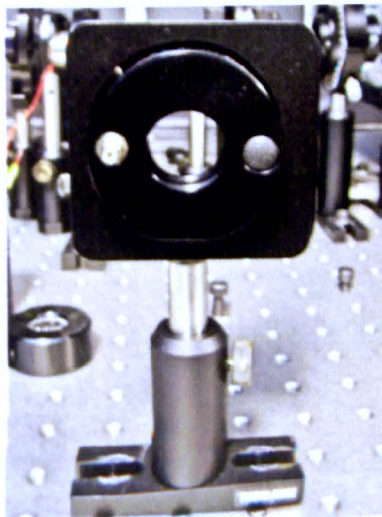
Figure C.4: One of the LCVRs.

Appendix D

Mueller Calculus of Linear Polarization Operations with *LCVR* in the General Case

Referring to figure 6.2 in chapter 6, the arrangement is used to electrically and continuously generate linearly polarized light in the full range from $0°$ to $90°$ from a randomly polarized input light source. The verification of the generation of special states ($0°$, $45°$ and $90°$) has been shown in chapter 6. For all the other general cases, as described, verifications of the arrangement have to be performed via Mueller calculus. For instance, for the case when the *LCVR* is set with retardance of $45°$ (i.e. 1/8-wave), according to the Mueller representation of general retarders given in equation 2.7, the Mueller matrix of the *LCVR* with retardance of $45°$ in the arrangement can be represented as equation D.1, which is obtained by setting both the θ and δ as $45°$ from equation 2.7.

$$\bar{M}_{LCVR(\lambda/8)} = \begin{bmatrix} 1 & 0 & 0 & 0 \\ 0 & \sqrt{2}/2 & 0 & -\sqrt{2}/2 \\ 0 & 0 & 1 & 0 \\ 0 & \sqrt{2}/2 & 0 & \sqrt{2}/2 \end{bmatrix} \tag{D.1}$$

In addition, based on the Mueller representations of *LP* and *QWP* given in equations 2.8 and 2.9 respectively, the specified Mueller matrixes of the *LP* and the *QWP* ap-

plied in the arrangement can be generated in equations D.2 and D.3 separately, which

are achieved by setting φ as 90° in equation 2.8 and setting θ as 0° in equation 2.9.

$$\bar{M}_{LP(\varphi=90°)} = \frac{1}{2} \begin{bmatrix} 1 & -1 & 0 & 0 \\ -1 & 1 & 0 & 0 \\ 0 & 0 & 0 & 0 \\ 0 & 0 & 0 & 0 \end{bmatrix} \tag{D.2}$$

$$\bar{M}_{QWP(\theta=0°)} = \begin{bmatrix} 1 & 0 & 0 & 0 \\ 0 & 1 & 0 & 0 \\ 0 & 0 & 0 & 1 \\ 0 & 0 & -1 & 0 \end{bmatrix} \tag{D.3}$$

$$I_{in} = \begin{bmatrix} 1 \\ 0 \\ 0 \\ 0 \end{bmatrix} \tag{D.4}$$

$$I_{out} = M_{QWP}M_{LCVR}M_{LP}I_{in}$$
$$= \frac{1}{2} \begin{bmatrix} 1 \\ -\sqrt{2}/2 \\ -\sqrt{2}/2 \\ 0 \end{bmatrix} \tag{D.5}$$

Therefore, by representing the un-polarized input light as equation D.4, the arrange-

ment shown in figure 6.2 in the specified case of setting the *LCVR* as a 1/8-waveplate

can be mathematically represented as equation D.5, which shows that the polarization

of the output light obtained is linearly polarized at 22.5°. This is proved by using

equation 2.5 which shows the general form of light with polarization states included.

As $Q=cos(2×22.5°) = U= sin(2×22.5°) = \sqrt{2}/2$, which represents the linear polariza-

tion state is clearly shown in equation D.5, the output polarization states is in 22.5°

linearly polarized. The minus signs in the equation D.5 indicate only the directions apart from horizontal and 45° respectively.

By following the same Mueller calculus but with different retardance assigned for the *LCVR*, it can be shown mathematically that the arrangement shown in figure 6.2 is able to provide the output polarization state linearly polarized in full range from 0° to 90° with retardance of the *LCVR* varied from half-wave to 0-wave.

Bibliography

1. **Jacques, S. L., Roman, J. R. and Lee, K.** Imaging Superficial Tissues with Polarized Light. *Lasers in Surgery and Medicine.* 2000, Vol. 26, pp. 119-129.

2. **Demos, S. G. and Alfano, R. R.** Optical Polarization Imaging. *Applied Optics.* 36, 1997, pp. 150-155.

3. **Backman, V., Gurjar, R., Badizadegan, K., Itzkan, L., Dasari, R. R., Perelman, L. T. and Feld, M. S.** Polarized Light Scattering Spectroscopy for Quantitative Measurement of Epithelial Cellular Structures in Situ. *IEEE Journal of Selected Topics in Quantum Electronics.* 1999, Vol. 5, pp. 1019-1026.

4. **Morgan, S. P., Khong, M. P. and Somekh, M. G.** Effects of Polarization State and Scatterer Concentration on Optical Imaging Through Scattering Media. *Appl. Opt.* 1997, Vol. 36, pp. 1560-1565.

5. **Morgan, S. P. and Stockford, I. M.** Surface-Reflection Elimination in Polarization Imaging of Superficial Tissue. *Optics Letters.* 2003, Vol. 28, 2, pp. 114-116.

6. **Beach, D. A., Bustamante, C., Wells, K. S. and Foucar, K. M.** Differential Polarization Imaging. 3. Theory Confirmation – Patterns of Polymerization of Haemoglobin-S in Red Blood Sickle Cells. *Biophysical Journal.* 1988, Vol. 53, pp. 449-456.

7. **Morgan, M., Kostyuk, O., Brown, R. A. and Mudera, V.** In Situ Monitoring of Tendon Structural Changes by Elastic Scattering Spectroscopy: Correlation with Changes in Collagen Fibril Diameter and Crimp. *Tissue Engineering.* 2006, Vol. 12, pp. 1821-1831.

8. **Wang, L.H. V. and Wu, H. I.** *Biomedical Optics: Principles and Imaging.* Hoboken, New Jersey : Wiley-Interscience, 2007.

9. **McNichols, R. J. and Cote, G. L.** Optical Glucose Sensing in Biological Fluids: An Overview . *Journal of Biomedical Optics.* 2000, Vol. 5, pp. 5-16.

10. **Boulbry, B., Germer, T. A. and Ramella-Roman, J. C.** A Novel Hemispherical Spectro-Polarmetric Scattering Instrument for Skin Lesion Imaging. *Proc. SPIE.* 2006, Vol. 6078, pp. 128-134.

11. **Groner, W., Winkelman, J. W., Harris, A. G., Ince, C., Bouma, G. J., Messmer, K. and Nadeau, R. G.** Orthogonal Polarization Spectral Imaging: A New Method for Study of the Microcirculation. *Nat. Med.* 1999, Vol. 5, pp. 1209-1212.

12. **Anderson, R. R.** Polarized-Light Examination and Photography of the Skin. *Archives of Dermatology.* 1991, Vol. 127, pp. 1000-1005.

13. **Chuh, A. A.** The Use of Digital Epiluminescence Dermatoscopy to Identify Peripheral Scaling in Pityriasis Rosea. *Comput Med Imaging Graph.* 2002, Vol. 26, 2, pp. 129-134.

14. **Lin, S. S., Yemelyanov, K. M., Pugh, E. N. and Engheta, Jr.and N.** Separation and Contrast Enhancement of Overlapping Cast Shadow Components using Polarization. *Optics Express.* 2006, Vol. 14, 16, pp. 7099-7108.

15. **Ince, C.** Sidestream Dark Field Imaging: An Improved Technique to Observe Sublingual Microcirculation. *Critical Care.* 2005, Vol. 9(suppl 4), pp. S13-S19.

16. **Jairo, J. and Monari, M.** Human Capillaroscopy by Light Emitting Diode Epi-Illumination. *Microvascular Research.* 2000, Vol. 59, 1, pp. 172-175.

17. **Kurtz, A. F.** *Wound Healing Monitoring and Treatment.* 2006241495 U.S., 26 Oct. 2006. Patent Application.

18. **Arridge, S. R. and Hebden, J. C.** Optical Imaging in Medicine: II. Modeling and Reconstruction. *Physics in Medicine and Biology.* 1997, Vol. 42, pp. 841-853.

19. **Cheong, W. F., Prahl, S. A. and Welch, A. J.** A Review of the Optical Properties of Biological Tissues. *IEEE Journal of Quantum Electronics.* 1990, Vol. 26, 12, pp. 2166-2185.

20. **Baker, S.** *Optimal Determination of the Optical Coefficients from Scattering Media.* The University of Nottingham. 2002. PhD Thesis.

21. **Flock, S. T., Patterson, M. S., Wilson, B. C. and Wyman, D. R.** Monte Carlo Modelling of Light Propagation in High Scattering Tissues-I: Model Predictions and Comparison with Diffusion Theory. *IEEE Transactions on Biomedical Engineering.* 1989, Vol. 36, 12, pp. 1162-1168.

22. **Nakonrat, P.** *Optical Tomography and Inhomogeneity Localisation in Turbid Media by MC Simulation.* The University of Nottingam. 2007. PhD Thesis.

23. **Ishimaru, A.** *Wave Propagation and Scattering In Random Media.* New York, NY, USA : Academic Press Inc., 1978.

24. **Arridge, S. R.** Optical Tomography in Medical Imaging. *Inverse Problems.* 1999, Vol. 15, pp. R41-R93.

25. **Contini, D., Martelli, F. and Zaccanti, G.** Photon Migration Through a Turbid Slab Decribed by a Model Based on Diffusion Theory. *Applied Optics.* 1997, Vol. 36, 19, pp. 4587-4599.

26. **Gibson, A. P., Hebden, J. C. and Arridge, S. R.** Recent Advantages in Diffuse Optical Imaging. *Phy. Med. Biol.* 2005, Vol. 50, pp. R1-R43.

27. **Patterson, M. S., Chance, B. and Wilson, B. C.** Time Resolved Reflectance and Transmittance for the Non-Invasive Measurement of Tissue Optical Properties. *Applied Optics.* 1989, Vol. 28, 12, pp. 2331-2336.

28. **Boas, D. A., Brooks, D. H., Miller, E. L., DiMarzio, C. A., Kilmer, M., Gaudette, R. J. and Zhang, Q.** Imaging the Body with Diffuse Optical Tomography. *IEEE Signal Processing Magazine.* 2001, Vol. 18, pp. 57-75.

29. **Martelli, F., Bassani, M., Alianelli, L., Zangheri, L. and Zaccanti, G.** Accuracy of the Diffusion Equation to Describe Photon Migration Through an Infinite Medium: Numerical and Experimental Investigation . *Physics in Medicine and Biology.* 2000, Vol. 45, pp. 1359-1373.

30. **Haskell, R. C., Svaasand, L. O., Tsay, T., Feng, T., McAdams, M. S. and Tromberg, B. L.** Boundary Conditions for the Diffusion Equation in Radiative Transfer. *J. Opt. Soc. Am. A.* 1994, Vol. 11, pp. 2727-2741.

31. **van Gemert, M. J. C., Jacques, S. L., Sterenborg, H. J. C. M. and Star, W. M.** Skin Optics. *IEEE Transactions on Biomedical Engineeriing.* 1989, Vol. 36, 12, pp. 1146-1154.

32. **Metropolis, N. and Ulam, S.** The Monte Carlo Method. *Journal of the American Statistical Association .* 1949, Vol. 44, 247, pp. 335-341.

33. **Binder, Ed. K.** *Monte Carlo Method in statistical Physics.* Beilin Heidelberg New York : Springer, 1979.

34. **Kalos, M. H and Whitlock, P. A.** *Monte Carlo Methods.* New York, NY, USA : John Wiley & Sons, Inc., 1986.

35. **Wilson, B.C. and Adam, G.** A Monte Carlo Model for the Absorption and Flux distributions of Light in Tissue. *Med. Phys.* 1983, Vol. 10, pp. 824-830.

36. **Forester, R. A. and Godfrey, T. N. K.** MCNP-A General Monte Carlo Code for Neutron and Photon Transport. [book auth.] R. Alcouffe, et al. *Methods and Applications in Neutronics, Photonics and Statistical Physics.* New York : Springer-Verlag, 1983.

37. **Prahl, S. A.** *Light Transport in Tissue.* University of Texas. Austin : s.n., 1988. PhD Thesis.

38. **Prahl, S. A., Keijzer, M., Jacques, S. L. and Welch, A. J.** A Monte Carlo Model of Light Propagation in Tissue. *Proc. SPIE.* 1989, Vol. 5, pp. 102-111.

39. **Keijzer, M., Jacques, S. L., Prahl, S. A. and Welch, A. J.** Light Distrubutions in Artery Tissue: Monte Carlo simulations for finite-Diameter Laser Beams. *Lasers Surg. Med.* 1989, Vol. 9, pp. 148-154.

40. **Flock, S. T., Wilson, B. C. and Patterson, M. S.** Monte Carlo Modelling of Light in Highly Scattering Tissues-II: Comparison with Measurements in Phantoms. *IEEE Trans. Biomed. Eng.* . 1989, Vol. 36, pp. 1169-1173.

41. **Keijzer, M., Pickering, J. W. and van Gemert, M. J. C.** Laser Beam Diameter for port Wine Stain Treatment. *Lasers Surg. Med.* 1991, Vol. 11, pp. 601-605.

42. **Wang, L. H. and Jacques, S. L.** Monte Carlo Modelling of Light Transport in Multi-Layered Tissues in Standard C. University of Texas M.D. Anderson Cancer Center : s.n., 1992.

43. **Jacques, S. L. and Wang, L. H.** Monte Carlo Modelling of Light Transport in Tissues. [book auth.] A. J. Welch and M. J. C. van Gemert. *OPtical Thermal Response of Laser Irradiated Tissue.* s.l. : Plenum Press, 1995.

44. **Crowe, J. A., Morris, D. E., Woolfson, M., Rodmell, P. I. and Walker, J. G.** Quantitative Spectrophotometry of Scattering Media via Frequency-Domain and Constant-Intensity Measurements. *Journal of the Optical Society of America A.* 2007, Vol. 24, 7, pp. 1969-1974.

45. **Morris, D. E., Stockford, I. M. and Crowe, J. A.** Determination of the Validity of Spectrophotometric Measurements Based upon Cumulants of the Temporal Point-Spread Function. *Optics Letters.* 2008, Vol. 33, 12, pp. 1339-1341.

46. **Wang, L. H., Jacques, S. L. and Zheng, L. Q.** MCML-Monte Carlo Modelling of Photon Transport in Multilayered Tissues. *Computer Methods and Programs in Biomedicine.* 1995, Vol. 47, pp. 131-146.

47. **Wang, L. H. and Wu, H. I.** Monte Carlo Modelling of Photon Transport in Biological Tissue. *BioMedical Optics: Principles and Imaging.* Hoboken, New Jersey : Wiley-Interscience, 2007.

48. **Henyey, L. G. and Greenstein, J. L.** Diffuse Radiation in the Galaxy. *Astrophysics Journal.* 1941, Vol. 93, pp. 70-83.

49. **Kahn, H. and Harris, T. E.** Estimation of Particle Transmission by random Sampling Monte Carlo Method. *National Burean of Standards Applied Mathematics Series.* 1951, Vol. 12 (U.S. Government Printing Office).

50. **Matsumoto, M. and Nishimura, T.** Mersenne Twister: A 623-Dimensionally Equidistributed Uniform Pseudo-Random Number Generator. *ACM Trans. on Modelling and Computer Simulations.* 1998, Vol. 8, pp. 3-30.

51. **Hendricks, J. S. and Booth, T. E.** MCNP Variance Reduction Overview. *Monte-Carlo Method and Applications in Neutronics, Photonics and Statistical Physics.* 1985, Vol. 240, pp. 83-92.

52. **Chatigny, S., Morin, M., Asselin, D., Painchaud, Y. and Beaudry, P.** Hybrid Monte Carlo for Photon Transport Through Optically Thick Scattering Media. *Applied Optics.* 1999, Vol. 38, 28, pp. 6075-6086.

53. **Kirkby, D. R. and Delpy, D. P.** Parallel Operation of Monte Carlo Simulations on a Diverse Network of Computers. *Phys. Med. Biol.* 1997, Vol. 42, pp. 1203-1208.

54. **Kienle, A. and Patterson, M. S.** Determination of the Optical Properties of Tubid Media from a Single Monte Carlo Simulation. *Physics in Medicine and Biology.* 1996, Vol. 41, pp. 2221-2227.

55. **Morris, D. E.** *Quantitative Spectrophotometry on Scattering Media.* The University of Nottingham. 2008. PhD Thesis.

56. **Amdahl, G. M.** Validity of the Single Processor Approach to Achieving Large Scale Computing Capabilities. *AFIPS Conference Proceedings.* 1967, Vol. 30, pp. 483-485.

57. **Bickel, W. S. and Bailey, W. M.** Stokes Vectors, Mueller Matrices, and Polarized Light Scattering. *Am. J. Phys.* 1985, Vol. 53, pp. 468-478.

58. **van de Hulst, H. C.** *Light Scattering by Small Particles.* New York : Dover, 1981.

59. **Bohren, C. F. and Huffman, D. R.** *Absorption and Scattering of Light by Small Particles.* New York : John Wiley & Sons, Inc., 1998.

60. **Rakovic, M. J., Kattawar, G. W., Mehrubeoglu, M., Cameron, B. D., Wang, L. V., Rastegar, S. and Cote, G. L.** Light Backscattering Polarization Patterns from Turbid Media: Theory and Experiments. *Appl. Opt.* 1999, Vol. 38, pp. 3399-3408.

61. **Bartel, S. and Hielscher, H.** Monte Carlo Simulations of the Diffuse Backscattering Mueller Matrix for Highly Scattering Media. *Appl. Opt.* 2000, Vol. 39, pp. 1580-1588.

62. **Tuchin, V. V., Wang, L. V. and Zimnyakov, D. V.** *Optical Polarization in Biomedical Applications.* Berlin : Springer-Verlag, 2006.

63. **Kattawar, G. W. and Plass, G. N.** Radiance and Polarization of Multiple Scattered Light Haze and Clouds. *Appl. Opt.* 1967, Vol. 7, pp. 1519-1527.

64. **Bruscaglioni, P., Zaccanti, G. and Wei, Q. N.** Transmission of a Pulsed Polarized Light Beam Through Thick Turbid Media: Numerical Results. *Appl. Opt.* 1993, Vol. 32, 30, pp. 6142-6150.

65. **Ambirajan, A. and Look, D. C.** A Backward Monte Carlo Study of the Multiple Scattering of a Polarized Laser Beam. *J. Quant. Spectrosc.Radiat. Transfer.* 1997, Vol. 58, pp. 171-192.

66. **Hielscher, A. H., Eick, A. A., Mourant, J. R., Shen, D., Freyer, J. P. and Bigio, I. J.** Diffuse Backscattering Mueller Matrices of Highly Scattering Media. *Optics Express.* 1997, Vol. 1, pp. 441-453.

67. **Kattawar, G. M., Rakovic, M. J. and Cameron, B. D.** Laser Backscattering Polarization Patterns from Turbid Media: Theory and Experiments. [book auth.] J. G. Fujimoto and M. S. Patterson. *Advances in Optical Imaging and Photon Migration.* Washington D.C. : Optical Society of America, 1998, Vol. 21 of OSA Trends in Optics and Photonics Series, pp. 105-110.

68. **Cote, D. and Vitkin, I. A.** Robust Concentration Determination of Optically Active Molecules in Turbid Media with Validated Three-Dimensional Polarization Sensitive Monte Carlo Calculations. *Opt. Express.* 2005, Vol. 13, pp. 148-163.

69. **Wang, X. and Wang, L. V.** Propagation of Polarized Light in Birefringence Turbid Media: A Monte Carlo Study. *Journal of Biomedical Optics.* 2002, Vol. 7, pp. 279-290.

70. **Yao, G.** Differential Optical Polarization Imaging in Turbid Media with Different Embedded Objects. *Optics Communications.* 2004, Vol. 241, pp. 255-261.

71. **Chang, P. C. Y., Walker, J. G., Hopcraft, K. I., Ablitt, B. and Jakeman, E.** Polarization Discrimination for Active Imaging in Scattering Media. *Optics Communications.* 1999, Vol. 159, pp. 1-6.

72. **Stockford, I. M.** *Characterisation of Layered Scattering Media Using Polarized Light.* Electrical and Electronic Engineering, Nottingham University. 2004. PhD Thesis.

73. **Stockford, I. M., Morgan, S. P., Chang, P. C. Y. and Walker, J. G.** Analysis of the Spatial Distribution of Polarized Light Backscattered from Layered Media. *Journal of Biomedical Optics.* 2002, Vol. 7, pp. 313-320.

74. **Lu, B.** *Theoretical Examination of Scattering Media by Temporal Analysis.* Electrical and Electronic Engineering, The University of Nottingham. 2007. PhD Thesis.

75. **Stockford, I. M., Lu, B., Crowe, J. A., Morgan, S. P. and Morris, D. E.** Reduction of Error in Spectrophotometry of Scattering Media Using Polarization Techniques. *Applied Spectroscopy.* 2007, Vol. 61, pp. 1379-1389.

76. **Morgan, S. P., Zhu, Q., Stockford, I. M. and Crowe, J. A.** Rotating Orthogonal Polarization Imaging. *Optics Letters.* 2008, Vol. 33, 13, pp. 1503-1505.

77. **Zhu, Q., Stockford, I. M., Crowe, J. A. and Morgan, S. P.** Experimental and Theoretical Evaluation of Rotating Orthogonal Polarization Imaging. *J. Biomed. Opt.* 2009, Vol. 14, 3, p. 034006.

78. **Lewis, G. D., Jordan, D. L. and Robert, P. J.** Backscattering Target Detection in a Turbid Medium by Polarization Discrimination. *Applied Optics.* 1999, Vol. 38, pp. 3937-3944.

79. **Morgan, S. P. and Ridgway, M. E.** Polarization Properties of Light Backscattered from a Two Layer Scattering Mdium. *Optics Express.* 2000, Vol. 7, 12, pp. 395-402.

80. **MacKintosh, F. C., Zhu, J. X., Pine, D. J. and Weitz, D. A.** Polarization Menory of Multiply Scattered Light. *Phys. Rev. B.* 1989, Vol. 40, pp. 9342-9345.

81. **Mehrubeoglu, M., Kehtarnavaz, N., Marquez, G. and Wang, L.** Skin Lesion Classification Using Reflectance Spectroscopic Imaging with Oblique Incidence. *Applied Optics.* 2002, Vol. 41, 1, pp. 182-192.

82. **Ramella-Roman, J. C., Duncan, D. and Germer, T. A.** Out-of-Plane Polarimetric Imaging of Skin: Surface and Subsurface Effects. *Proc. SPIE.* 2005, Vol. 5686, pp. 142-153.

83. **Gomes, A. J., Turzhitzsky, V. M., Kim, Y., Rogers, J. D. and Roy, H. K.** Measuring Microvascular Blood Supply Using Polarization Gated Spectroscopy to Detect Colonic Neoplasia. *Proc. SPIE.* 2009, Vol. 7186, p. 718609.

84. **Gladish, J. C. and Duncan, D. D.** Spectral Polarimetry for Assessing Cell Alignment in Cultured Tissues. *Proc. SPIE.* 7179, 2009, p. 717909.

85. **Wood, M. F. G., Ghosh, N., Moriyama, E. H. and Wilson, B. C.** Proof-of-Principle Demonstration of a Mueller Matrix Decomposition Method for Polarized Light Tissue Characterization in vivo. *Journal of Biomedical Optics.* 14, 2009, Vol. 1, p. 014029.

86. **Hecht, E.** *Optics.* Third Edition. New York : Addison-Wesley, 1998.

87. **Clarke, D. and Grainger, J. F.** *Polarized Light and Optical Measurement.* Oxford : Pergamon Press, 1971.

88. **Liao, T. B.** *Polarization Optics.* BeiJing : Science Press, 2003.

89. **Lu, S. Y. and Chipman, R. A.** Interpretation of Mueller Matrices Based on Polar Decomposition. *J. Opt. Soc. Am. A.* 1996, Vol. 13, 5, pp. 1106-1113.

90. **Goldstein, D. H.** Mueller Matrix Dual-Rotating Retarder Polarimeter. *Applied Optics.* 1992, Vol. 31, 31, pp. 6676-6683.

91. **Manhas, S., Swami, M. K., Buddhiwant, P., Ghosh, N., Gupta, P. K. and Singh, K.** Mueller Matrix Approach for Determination of Optical Rotation in Chiral Turbid Media in Backscattering Geometry. *Optics Express.* 2006, Vol. 14, 1, pp. 190-202.

92. **Star, W. M., Marijnissen, J. P. A. and van Gemert, M. J. C.** Light Dosimetry in Optical Phantoms and in Tissues: I. Multiple Flux and Transport Theory. *Phys. Med. Biol.* 1988, Vol. 33, pp. 437-454.

93. **Pope, R. M. and Fry, E. S.** Absorption Spectrum (380-700nm) of Pure Water. II. Integrating Cavity Measurements. *Appl. Opt.* 1997, Vol. 36, pp. 8710-8723.

94. **Mackintosh, F. C. and John, S.** Diffusing -Wave Spectroscopy and Multiple Scattering of Light in Correlated Random Media. *Physical Review B.* 1989, Vol. 40, 4, pp. 2383-2406.

95. **Tuchin, V. V.** *Tissue Optics: Light Scattering Methods and Instruments for Medical Diagnosis.* Washington : SPIE Press, 2007.

96. **McFee, C.** *An Introduction to CCD Operation.* MSSL, UCL. Appl. Notes.

97. *SNR-Signal-to-Noise-Ratio.* The Cooke Corporation, PCO.Imaging. Appl. Notes.

98. **Sebastian, R.** *Calculate SNR of CCD Cameras.* ImageJ. 2008. Appl. Notes.

99. **Azzam, R. M. A. and Bashara, N. M.** *Ellipsometry and Polarized Light.* Elsevier North-Holland : North-Holland Pub. Co., 1977.

100. **Oldenbourg, R.** Polarization Microscopy with the LC-PolScope. [book auth.] D. L. Spector and R. D. Goldman. *Living Cell Imaging: A Laboratory Manual.* NY : Cold Spring Harbor Laborotory Press, 2004, pp. 205-237.

101. **Morgan, S. P., Stockford, I. M., Crowe, J. A. and Hayes-Gill, B. R.** Optical Imaging and Spectroscopy of Superficial Tissue. *Journal of Innovative Optical Health Sciences.* 2008, Vol. 1, 1, pp. 85-93.

102. **Yang, Y., Ahearne, M., Wimpenny, I., Torbet, J.** Monitoring the Effect of Magnetically Aligned Collagen Scaffolds on Tendon Tissue Engineering by PSOCT. *Proc. of SPIE.* 2009, Vol. 7179, p. 717903.

103. **Sun, C. W., Wang, C. Y., Yang, C. C, Kiang, Y. W., Lu, C. W., Hsu, I. J. and Lin, C. W.** Polarization-Dependent Characteristics and Polarization Gating in Time-Resolved Optical Imaging of Skeletal Muscle Tissues. *IEEE Journal on Selected Topics in Quantum Electronics.* 2001, Vol. 7, 6, pp. 924-930.

104. **Sawyer, N. B. E., Morgan, S. P., Somekh, M. G., See, C. W., Cao, X. F., Shekunov, B. Y. and Astrakharchik, E.** Wide Field Amplitude and Phase Confocal Microscope with Parallel Phase Stepping. *Rev. Sci. Instr.* 2001, Vol. 72, 10, pp. 3793-3801.

105. **Shribak, M. and Oldenbourg, R.** Techniques for Fast and Sensitive Measurements of Two-Dimensional Birefringence Distributions. *Applied Optics.* 2003, Vol. 16, 42, pp. 3009-3017.

106. **Sun, X. F., Zhang, W. H., Chen, X. J., Xiao, G. H., Mai, W. Y. and Wang, W. H.** Spindle Dynamics in Living Mouse Oocytes During Meiotic Maturation, Ageing, Cooling and Overheating: A study by Polarized Light Microscopy. *Zygote.* 2004, Vol. 12, 3, pp. 241-249.

107. *Retarder Principles & Liquid Crystal Variable Retarders.* Meadowlark Optics. 2008. Appl. Notes.

108. **Ye, C.** Construction of An Optical Rotator Using Quarter-Wave Plate and An Optical Retarder. *Photo-Optical Instrumentation Engineering.* 1995, Vol. 34, 10, pp. 3013-3035.

109. **Heredero, R. L., Uribe-Patarroyo, N., Belenguer, T., Ramos, G., Sánchez, A., Reina, A., Martínez Pillet, V. and Álvarez-Herrero, A.** Liquid-Crystal Variable Retarders for Aerospace Polarimetry Applications. *Appl. Opt.* 2007, Vol. 46, 5, pp. 689-698.

110. **Ye, C.** *Optical Rotator and Rotation-Angle-Variable Half-Waveplate Rotator. 5473465* US, 5 December 1995. Patent.